5-2017

Impedance-Based Stability Analysis and Controller Design of Three-Phase Inverter-Based Ac Systems

Wenchao Cao
University of Tennessee, Knoxville, wcao2@vols.utk.edu

To the Graduate Council:

I am submitting herewith a dissertation written by Wenchao Cao entitled "Impedance-Based Stability Analysis and Controller Design of Three-Phase Inverter-Based Ac Systems." I have examined the final electronic copy of this dissertation for form and content and recommend that it be accepted in partial fulfillment of the requirements for the degree of Doctor of Philosophy, with a major in Electrical Engineering.

Fred Wang, Major Professor

We have read this dissertation and recommend its acceptance:

Leon M. Tolbert, Kevin Tomsovic, James Ostrowski

Accepted for the Council:

Dixie L. Thompson

Vice Provost and Dean of the Graduate School

(Original signatures are on file with official student records.)

Impedance-Based Stability Analysis and Controller Design of Three-Phase Inverter-Based Ac Systems

A Dissertation Presented for the

Doctor of Philosophy

Degree

The University of Tennessee, Knoxville

Wenchao Cao

May 2017

Acknowledgement

First of all, I would like to express my sincerest gratitude to my advisor, Dr. Fred Wang, for his invaluable academic guidance and support throughout my Ph.D. education. His profound knowledge and challenging discussion contributed significantly to my research achievements. He taught me not only the effective methods of doing academic research but also the important skills about leadership, communication and teamwork.

Then, I am very grateful to Dr. Leon M. Tolbert, for teaching me broad knowledge of power electronics in his courses, giving me great advices on my research during the project meetings and offering me meticulous help in paper revisions.

In addition, I would also like to thank other professors in my dissertation committee, Dr. Kevin Tomsovic and Dr. James Ostrowski, for their in-depth discussion and insightful suggestions on my dissertation work.

Meanwhile, I would also like to express my gratitude to Dr. Yilu Liu, Dr. Fangxing Li, Dr. Kai Sun, Dr. Daniel Costinett, Dr. Michael G. Thomason, Dr. Itamar Arel and Dr. Wei Gao for their help in courses and research.

I also want to express my sincere thanks to all my colleagues and friends in the CURENT center for their great help and encouragement. Especially, I would like to thank Mr. Yiwei Ma and Ms. Xingru Yan for helping me in both research and personal life numerous times. I would also like to thank other team members in the same research projects, including Dr. Jingxin Wang, Dr. Lijun Hang, Dr. Jing Wang, Dr. Liu Yang, Dr. Xuan Zhang, Dr. Xiaonan Lu, Dr. Yalong Li, Dr. Xiaojie Shi, Dr. Zheyu Zhang, Mr. Bo Liu, Mr. Shuoting Zhang, Mr. Mingshuo Li, Mr. Ruirui Chen, Dr. Chun Gan, Dr. Shiqi Ji, Mr. Mitch Smith, Ms. Jessica Boles, Mr. Geoff

Laughon, Mr. Surendhar Somasundaram, Ms. Shuyao Wang, Ms. Jingyi Tang and Mr. Mark Nakmali. I also want to appreciate the academic support from Dr. Dong Jiang, Dr. Zhuxian Xu, Dr. Jing Xue, Dr. Ben Guo, Dr. Weimin Zhang, Dr. Ming Li, Dr. Shengnan Li, Dr. Bailu Xiao, Dr. Fan Xu, Dr. Yutian Cui, Dr. Zhiqiang Wang, Dr. Lakshmi Reddy Gopi Reddy, Dr. Mithat Can Kisacikoglu, Ms. Yang Xue, Mr. Bradford Trento, Mr. Edward Jones, Dr. Yiqi Liu, Dr. Sheng Zheng, Mr. Fei Yang, Mr. Ren Ren, Ms. Ling Jiang, Mr. Chongwen Zhao, Mr. Wen Zhang, Dr. Haifeng Lu, Dr. Nan Jin, Dr. Lin Zhu, Dr. Lingwei Zhan, Dr. Jidong Chai, Dr. Fengkai Hu, Mr. Bin Wang, Mr. Wenyun Ju, Mr. Yichen Zhang, Ms. Weihong Huang, Mr. Jiecheng Zhao, Dr. Samir Said Sahyoun and Dr. Liguo Wang.

I would also like to thank all the staff in the CURENT center and the Department of Electrical Engineering and Computer Science, including Mr. Robert B. Martin, Ms. Judy Evans, Ms. Dana Bryson, Dr. Chien-fei Chen, Mr. Erin Wills, Mr. Chris Anderson, Ms. Wendy Smith, and Mr. Adam Hardebeck, for their professional help in miscellaneous ways.

Last, but most importantly, I would like to express my deepest thanks to my parents and other family relatives for their unconditional love and support.

This dissertation was supported primarily by the Engineering Research Center Program of the National Science Foundation and the Department of Energy under NSF Award Number EEC-1041877 and the CURENT Industry Partnership Program.

Abstract

Three-phase voltage-source power inverters are widely used for energy conversion in three-phase ac systems, such as renewable energy systems and microgrids. These three-phase inverter-based ac systems may suffer from small-signal instability issues due to the dynamic interactions among inverters and passive components in the systems. It is crucial for system integrators to analyze the system stability and design the inverter controller parameters during system planning and maintenance periods to guarantee stable system operation. The impedance-based approach can analyze the stability of source-load systems, by applying the Nyquist stability criterion or the generalized Nyquist stability criterion (GNC) to the impedance ratio of the source and load impedances. This dissertation investigates the impedance-based methods for stability analysis and inverter controller design of three-phase inverter-based multi-bus ac systems.

Improved sequence impedance and *d-q* impedance models of both three-phase voltage-controlled inverters and current-controlled inverters are developed. A simple method for sequence impedance measurement of three-phase inverters is developed by using another inverter as the measurement unit, connected in a paralleled structure with common-dc and common-ac sides.

For three-phase radial-line renewable systems with multiple current-controlled inverters, an impedance-based sufficient stability criterion is proposed in the *d-q* frame, without the need for pole calculation of the return-ratio matrices. An inverter controller parameter design method is developed based on the phase margin information obtained from the stability analysis.

For general three-phase multi-bus ac power systems consisting of both voltage-controlled inverters and current-controlled inverters, several impedance-based stability analysis methods

and inverter controller parameter design approaches are further proposed, based on the sequence impedances, the *d*-*q* impedances and the measured terminal characteristics, to avoid the unstable harmonic resonance, the low-frequency oscillation and the oscillation of the fundamental frequency, respectively. All these proposed stability analysis methods enable the system stability assessment without the need for the internal control information of inverters.

Moreover, an impedance-based adaptive control strategy of inverters with online resonance detection and passivity or phase compensation is proposed for stable integration of both voltage-controlled inverters and current-controlled inverters into unknown grid-connected or islanded systems with other existing inverters in operation.

Table of Contents

List of Tables

List of Figures

1 Introduction

1.1 Background and Motivation

Due to the benefits of reduced environmental impacts, better energy security and potential economic aspects, renewable energy sources such as wind and solar are penetrating into the power system with an unprecedented speed. Figure 1-1 shows the installed wind generating capacity for U.S. states at end of 2015. The capacity was nearly 75 GW at the end of 2015 [1]. The U.S. Department of Energy has envisioned that wind power will supply 20% of all U.S. electricity by 2030 [2]. Figure 1-2 shows the solar photovoltaic (PV) installations in U.S. over the past decades. In 2015, over 26 GW of capacity was installed, and 30% of all new electricity generation capacity in the country came from solar [3]. These renewable energy sources are not intrinsically able to connect with the power system directly. A power electronics converter has to act as an interface to convert the dc voltage from the solar panel, and the variable frequency ac voltage from the wind turbine to the grid. Figure 1-3 shows the one-line diagram of multiple PV interface inverters connected to a feeder in a distribution power grid.

Microgrids are localized power networks that incorporate with distributed energy resources (DER), energy storages, and local critical and non-critical loads. With proper control, microgrids can operate in the grid-connected mode with the main power system, or stand-alone in the islanded mode. This can significantly improve reliability of the electricity services. Since the concept was proposed not more than two decades ago [4], microgrids has attracted a lot attentions. Over 13,400.5 MW of operating, under development, and proposed microgrid capacity had been identified over the world as of the end of 2015 [5]. Power converters are essential components in a microgrid. The energy sources and storages like the wind, PV, or

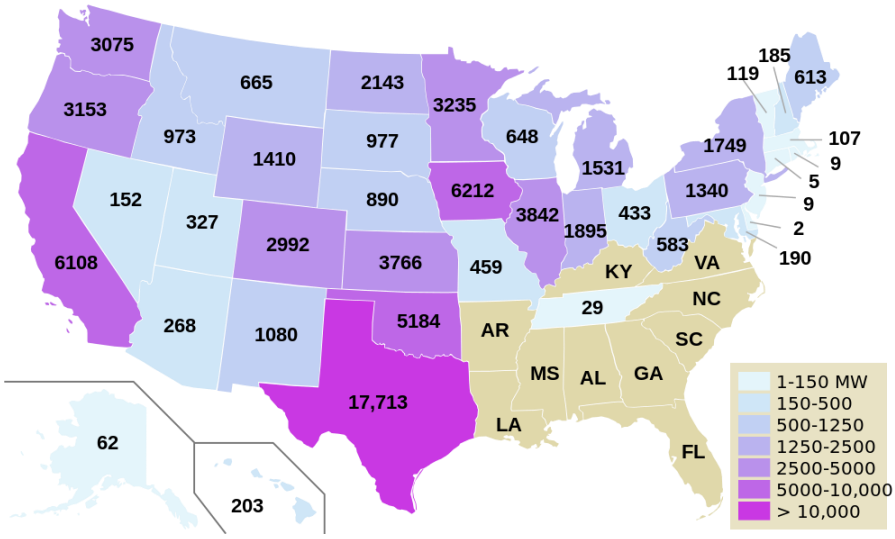

Figure 1-1. Map illustrating installed wind generating capacity for U.S. states at end of 2015.

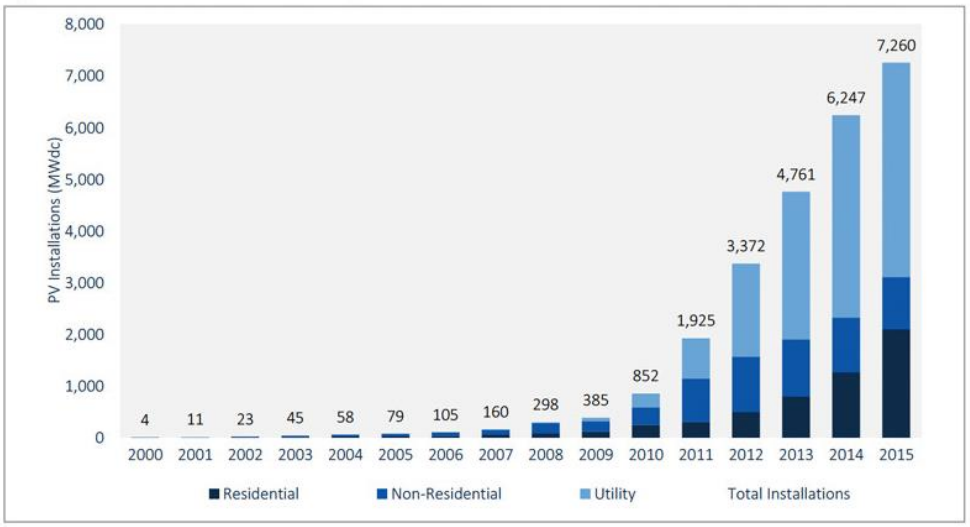

Figure 1-2. Annual U.S. solar PV installation, 2000-2015.

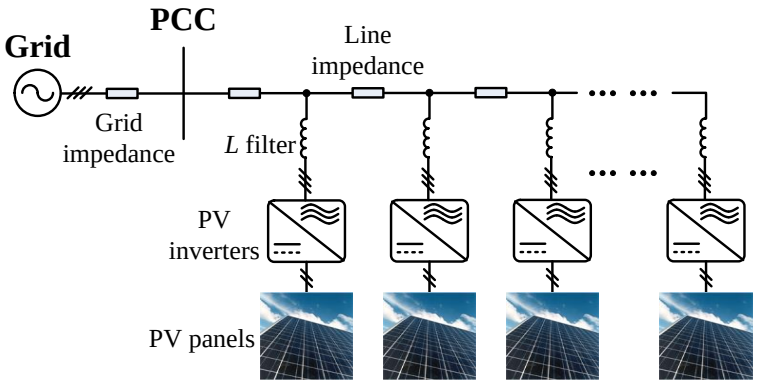

Figure 1-3. Simplified one-line diagram of a grid-connected radial-line PV system with multiple PV inverters.

battery all require power converters to transform electric power to the utility grid.

With a high control bandwidth, power electronic inverters can be controlled to behave like various power system components, by tracking the corresponding models. Figure 1-4 shows the architecture of an inverter-based power grid emulation system, named Hardware Test-bed (HTB) in the CURENT center at the University of Tennessee [6]–[10]. It can emulate the power system performance, by using each of the inverters in parallel to emulate the power system components, such as synchronous generators, induction motor loads, and static loads, etc.

Thanks to the features of controllability, flexibility and high efficiency, three-phase voltage-source inverters are widely used for energy conversion in three-phase ac systems, such as electric railway systems [11], electric aircrafts [12], [13] and modern electric ships [14], [15], in addition to the aforementioned renewable energy systems [16], [17], microgrids [18] and CURENT's power grid emulation system.

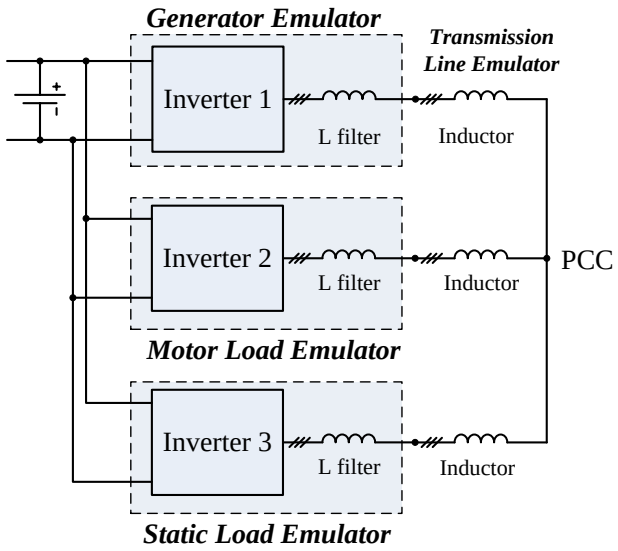

Figure 1-4. Structure of Hardware Test-bed for power grid emulation.

However, these voltage-source inverters based three-phase ac systems may suffer from small-signal instability issues [19]. Due to the high-frequency Pulse Width Modulation (PWM) of semiconductor devices and the dead-time inserted in the duty-cycles of semiconductor devices to avoid shoot-through, the inverters introduce harmonics in a wide spectrum. Passive filters are normally used in inverters for filtering switching frequency harmonics, but the interaction between passive filters and other passive components in the system leads to more resonance frequencies. In addition, because of the high control bandwidth of the inverters, there are dynamic interactions among inverters and the passive components in the system in a wide frequency range. The instability phenomena have been reported in renewable energy systems [20]–[23], microgrids [24] and electric railway systems [11].

These small-signal instability issues in these three-phase inverter-based ac systems can be divided into two categories in different frequency ranges [23]: 1) unstable harmonic resonances,

which result from the interactions among the fast inner current or voltage control loops, converter output filters and network passive components [23]–[26]; 2) low-frequency oscillations, which arise from the interactions among the slow outer power control loops and grid synchronization loops [27]–[29]. It is crucial for system integrators to analyze the system stability and design the converter controller parameters during system planning and maintenance periods to guarantee stable system operation [29], [30].

The impedance-based approach, originally introduced for the stability analysis and design of dc systems, can analyze the stability of systems with interconnections, by applying the Nyquist stability criterion [31]–[33] or the generalized Nyquist stability criterion (GNC) [34]–[36] to the impedance ratio of two subsystems separated at one interface of the whole system. Compared with the state-space-based approach and the transfer-function-based approach for system stability analysis and control parameter design, the impedance-based approach has several advantages.

1) The measured impedances of system components can be directly used to evaluate the system stability, without the need for the detailed physical or control information of the inverter components [37].

2) The impact of individual components or subsystems on the system stability can be clearly interpreted [23].

3) For source-load systems, practical conservative impedance-based stability criteria [38], such as the Middlebrook criterion [39], can be used to define the specifications of the source and load impedances separately.

The impedance-based approach is promising to solve the problems regarding the stability analysis and controller design of three-phase inverter-based ac systems. However, there are still

some challenges in the application of the impedance-based approach.

1) Impedance modeling of three-inverters is important for impedance-based stability analysis and controller design. It is necessary to accurately model the admittance or impedance of both current-controlled inverters and voltage-controlled inverters, with the consideration of the specific applications, such as the static load emulation in CURENT's inverter-based power grid emulation system.

2) The inverter impedance measurement usually requires dedicated equipment, which is not easy to set up. Thus, a simple and effective set up for inverter impedance measurement would be beneficial for system integrators to assess the system stability during the system planning stage.

3) The examination of the right-half-plane (RHP) poles of the impedance ratio is a necessary prerequisite for the application of the Nyquist stability criterion or the GNC. The RHP pole examination can be avoided for the source-load systems with a simple single-bus structure, but it is still inevitable for complicated inverter-based ac systems with multiple buses. The RHP pole calculation requires detailed transfer function models of system components and would result in a heavy computation burden for complicated systems. It is critical to develop impedance-based stability criteria to avoid RHP pole examination for inverter-based ac systems.

4) For inverter-based multi-bus ac systems with definite structures, it is not easy to design the controller parameters of each inverter individually due to the inter-connection of all inverters.

5) When integrating inverters to a weak grid or a microgrid with existing inverters in

operation, the impedance of the existing system is complicated and the information of existing system is not always readily available. This remains an obstacle for controller design of inverters for stable integration to an unknown system.

The objectives of the research are to improve impedance models of three-phase inverters, develop a simple approach for inverter impedance measurement, propose stability criteria to avoid the RHP pole calculation and controller design methods for inverter-based ac systems with definite structures, and propose controller design methods of inverters for stable integration into an unknown system.

1.2 Dissertation Organization

The organization of the chapters in this dissertation is described as follows.

Chapter 2 summarizes and compares the existing stability analysis approaches and explains the selection of the impedance-based approach for stability analysis and controller design of three-phase inverter-based ac systems. The remaining part of this chapter reviews the research activities in the impedance modeling and measurement of three-phase inverters, impedance-based stability analysis and inverter controller design of inverter-based ac systems with definite structure, as well as the impedance-based controller design of inverters for stable integration into an unknown system. Based on the review, the research challenges in these areas and the objectives of this dissertation are pointed out.

Chapter 3 improves the modeling of the sequence impedances and *d-q* impedances for both current-controlled inverters and voltage-controlled inverters, with the consideration of the generator and static load emulation in CURENT's inverter-based power grid emulation system.

Chapter 4 develops a simple method for sequence impedance measurement of three-phase

inverters by using another inverter connected in a paralleled structure with common-dc and common-ac sides.

Chapter 5 proposes an impedance-based sufficient stability criterion, without the need for the pole calculation of return-ratio matrices, for general radial-line renewable systems with multiple current-controlled inverters in the *d*-*q* domain, and a corresponding controller parameter design method based on the phase margin.

Chapter 6 proposes two sequence-impedance-based harmonic stability analysis methods and an inverter controller parameter design approach for stable operation of a three-phase inverter-based two-area system, with the benefits of avoiding the examination of RHP poles of impedance ratios and reducing the computation effort, as compared with the existing impedance-based stability analysis method using the Nyquist stability criterion once.

Chapter 7 proposes a stability analysis method and an inverter parameter design approach, based on the *d*-*q* impedances, the Component Connection Method (CCM) and the determinant-based generalized Nyquist stability criterion (GNC), for the inverter-based two-area system with generator and static load emulation. The examination of RHP poles of the return-ratio matrix is avoided, as compared with the existing impedance-based analysis method using the GNC once.

Chapter 8 proposes a stability analysis method for the low-frequency oscillation of the fundamental frequency in three-phase inverter-based islanded multi-bus ac microgrids, based on the measured terminal characteristics of system components with the fundamental frequency as an additional variable, without the need for the internal information of inverters.

Chapter 9 proposes an impedance-based adaptive control strategy of both voltage-controlled inverters and current-controlled inverters for stable integration into unknown systems. The

proposed strategy is based on the online resonance detection by using the online fast Fourier transform (FFT) and passivity or phase compensation by integrating a BPF or a notch filter into the control loops of inverters.

Chapter 10 summarizes the work that has been done in this dissertation and recommends some future work.

2 Literature Review and Challenges

This chapter reviews the research activities in the corresponding areas of impedance-based stability analysis and controller design of three-phase inverter-based ac systems. The research challenges and objectives are presented to identify the originality of the work.

2.1 Stability Analysis Approaches

This section briefly summarizes different kinds of stability problems, and introduces and compares three major small-signal stability analysis approaches, in order to justify the selection of the impedance-based approach for the small-signal stability analysis of three-phase inverter-based ac systems.

2.1.1 Stability Problems

The stability of a system is the ability to reach and remain at the operating equilibrium point under a disturbance [40]. For example, Reference [41] provided a formal definition of power system stability: "Power system stability is the ability of an electric power system, for a given initial operating condition, to regain a state of operating equilibrium after being subjected to a physical disturbance, with most system variables bounded so that practically the entire system remains intact."

Generally, there are three different kinds of system stability problems, namely, steady-state stability, small-signal stability and large-signal stability problems [40]. The steady-state stability is about the existence of the equilibrium point. The small-signal stability is the ability to go back to the operating equilibrium point under small disturbances, which are sufficiently small so that the linearized system equations are still applicable. The large-signal stability is the ability to

transit from one operating equilibrium point to a new operating equilibrium point after a severe disturbance. The large-signal stability is usually analyzed in the sense of Lyapunov stability [40]. This study only focuses on the small-signal stability of three-phase inverter-based ac systems.

2.1.2 Small-Signal Stability Analysis Approaches

There are several approaches to analyze the small-signal stability of three-phase ac systems, including the state-space-based approach, the transfer-function-based approach and the recently proposed impedance-based approach.

A. The state-space-based approach

The state-space-based approach has been widely used in the stability analysis of the traditional power systems [42]. When using the state-space model of the power system, the system eigenvalues and eigenvectors can be extracted from the system state matrix. The eigenvalues contain the frequency and damping ratio information of the oscillatory modes, while the eigenvectors indicate mode shape, mode composition and participation factors. In addition, for the small-signal stability analysis of traditional power systems, the stability of the system states, such as the synchronous machine rotor angles, bus voltages and system frequency are of great concern. Therefore, the state-space and eigenvalue based approach is more preferable than the transfer-function-based approach, which only describes the input-output relationship but does not reveal the conditions of internal states. Moreover, the small-signal stability analysis of traditional power systems using the state-space-based approach can be readily accomplished with commercial software, such as Power System Simulation for Engineering (PSS/E) and Dynamic Security Assessment Software (DSATools) [9].

The state-space-based approach was introduced to the small-signal stability analysis and

controller parameter design of inverter-based ac power systems [43], [44]. The dynamics of traditional power systems are mainly determined by the synchronous machines, and the frequencies of concerned system oscillatory modes are normally low (less than 10 Hz). However, due to the small time constant and high control bandwidth of power electronics inverters, the dynamic interactions among inverters and grid could occur in a wide frequency range. Therefore, full detailed models of inverters and connection network dynamics are required for the small-signal stability analysis of inverter-based ac systems, such as inverter-based microgrids [27], [43]. Consequently, the state-space-based approach is complicated to use, owing to the high order of the system state matrix, and not flexible in use, considering that the system model needs to be derived again for any change of system physical and control parameters. The modes of the inverter-based ac power systems exhibit a frequency-scale separation [43], [45]. In order to reduce the computational burden, model order reduction techniques, such as the neglect of the inner loop dynamics [46], the singular perturbations technique [47], [48] and the participation analysis [49], are usually adopted to study the stability issues related with either the low frequency modes [46]–[48] or the medium and high frequency modes [49].

A special form of state-space-based approach, the Component Connection Method (CCM) has been proposed to decompose the traditional power systems into components and the connection network and thus simplify the formulation of system state equations thanks to the model sparsity [23], [50]–[53]. The CCM can also reveal the impact of components on the system oscillatory modes [23]. The CCM was recently adopted in the state-space-based harmonic stability analysis of inverter-based ac systems [54]. However, the state-space-based approach requires the detailed internal control information of each inverter in the system, which is not convenient to obtain in practical applications.

B. The transfer-function-based approach

While the state-space-based approach, regarded as the modern control theory, reveals the inner state dynamics using state equations, the transfer-function-based approach, referred to as the conventional control theory, focuses on the input-output relationship [55]. The transfer-function-based approach can analyze the system stability by the Bode plot or Nyquist plot of the open-loop transfer function or the pole-zero maps of the closed-loop transfer function.

Regarding the dynamic control of power electronics inverters, the input-output relationship is a major concern, including the relationship between the reference and the output as well as the relationship between the disturbance and the output, in order to achieve good (voltage, current and power) reference tracking performance and good disturbance rejection performance. In addition, in view of the high control bandwidth of inverters, the frequency response characteristics in a wide frequency range are concerned, which can be easily analyzed using the open loop gain of the feedback control system. Therefore, the transfer-function-based approach is commonly applied to the study of the stability of a power electronics inverter. For example, the open-loop gain and root locus are normally used in the design of passive damping circuits and active damping control parameters, to ensure the current control loop stability of grid-connected inverters with output *LCL* filters [56]–[59].

The transfer-function-based approach is effective in the stability analysis and controller design of a three-phase inverter individually with the assumption of ideal external conditions. However, its application in the stability analysis and controller design of inverter-based ac systems, such as paralleled multiple inverters connected to a weak grid and inverter-based islanded power systems, is complicated, because mutual interactions of system components are embedded in the input-output control loop. A multi-input-multi-output (MIMO) closed-loop

transfer function matrix model of the whole system is normally used, and Bode plots and pole-zero maps of each closed-loop transfer function element are adopted for stability analysis [60]. In order to simplify the stability analysis based on transfer functions, simplification or aggregation of the system structure is usually utilized. Reference [20] uses a simplified passive circuit model to investigate the parallel resonance and series resonance caused by the capacitance and the inductance inside a distribution network, without including the effect of power inverter controllers. An equivalent inverter model of N-paralleled inverter is developed in [61] by assuming the physical and controller parameters of all inverters are identical. Also, an aggregated model of a wind farm is derived in [21] by assuming all the wind turbines are identical and all collector feeders are the same. Although effective in some applications, this simplification process might conceal some instability mechanism of the system.

In addition to the aforementioned limits of the state-space-based approach and the transfer-function-based approach, both approaches require the detailed physical and internal control information of all inverter components in order to formulate the state equation or transfer function matrix of the whole system for stability analysis. However, this proprietary information is not always available from the vendors of inverters, which could hinder the system integrator from system stability assessment [37].

C. The impedance-based approach

The impedance-based approach, originally introduced for the stability analysis and design of dc systems, can analyze the stability of systems with interconnections in a practical way. Different from the reference-to-output relationship of each individual inverter component, which can be regarded as the "internal" stability, in the transfer-function-based approach, the impedance-based approach focuses on the stability caused by the interconnections of system

components, which can be regarded as the "external" stability, by taking advantage of the terminal behaviors, in other words, the impedance or admittance of inverter components [19]. By dividing the system into two subsystems at one interface, the impedance ratio of the impedances of two subsystems represents the minor loop gain of the connection of these two subsystems. In addition, the Nyquist stability criterion can be applied to the impedance ratio to determine the "external" stability related with the connection.

The Nyquist stability criterion can be stated as follows [19], [31]–[33], [36], [55], [62]:

"For a closed-loop system to be stable, the encirclement, if any, of the $(-1, j0)$ point by the Nyquist plot of the open-loop transfer function (as s moves along the Nyquist path) must be anti-clockwise, and the number of such encirclements must be equal to the number of poles of the open-loop transfer function that lie on the right-half-plane (RHP)."

For example, Figure 2-1(a) shows the small-signal impedance-based representation of a grid-connected current-controlled single-phase inverter system [19]. The expression of the inverter current i_t in terms of the inverter current reference i_t^* and the grid voltage v_g is shown in (2-1). The corresponding configuration of the feedback loop can be illustrated in Figure 2-1(b). It can be seen that the inverter current reference to output closed loop gain $G_{cl}(s)$ and the inverter output admittance $Y_{oc}(s)$ represent the "internal" stability of the inverter when connected to an ideal grid, while the impedance ratio $T_m(s)$ defined as (2-2), also called the minor loop gain of the minor feedback loop, indicates the "external" stability related with the grid impedance $Z_g(s)$. The Nyquist plot of the impedance ratio $T_m(s)$ is depicted in Figure 2-2, from which the number of encirclements of the $(-1, j0)$ point as well as the gain margin and phase margin can be obtained. $T_m(s)$ in Figure 2-2(a) is stable without encirclement of the $(-1, j0)$ point, but $T_m(s)$ in Figure 2-2(b) is unstable with two encirclements of the $(-1, j0)$ point.

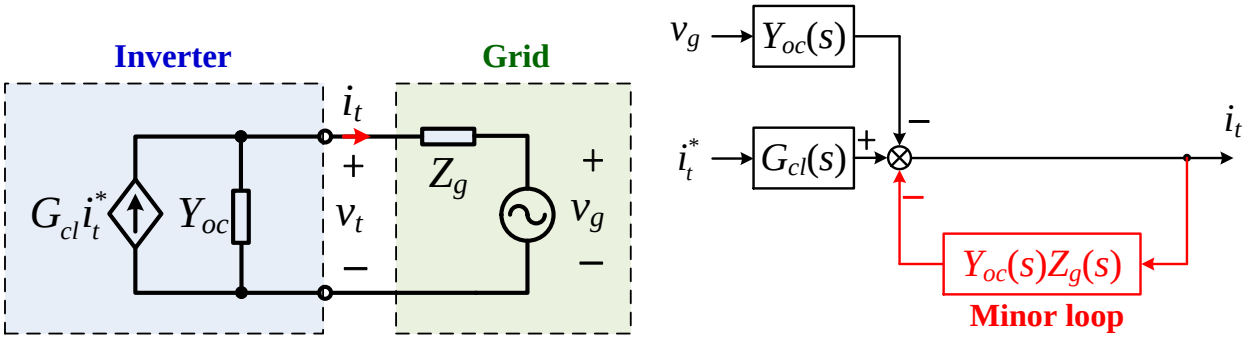

(a) (b)

Figure 2-1. A grid-connected current-controlled single-phase inverter system. (a) Impedance-based equivalent circuit; (b) the feedback control loop.

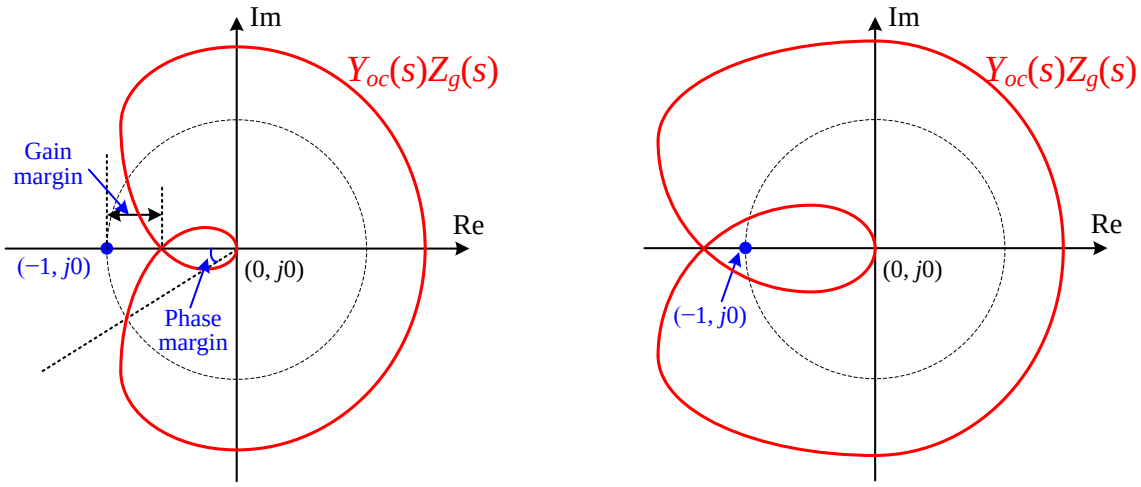

(a) (b)

Figure 2-2. Nyquist plot of the impedance ratio $T_m(s)$: (a) stable; (b) unstable.

$$i_t = \frac{1}{1+Y_{oc}(s)Z_g(s)} G_{cl}(s) i_t^* - \frac{Y_{oc}(s)}{1+Y_{oc}(s)Z_g(s)} v_g \tag{2-1}$$

$$T_m(s) = Y_{oc}(s)Z_g(s) \tag{2-2}$$

As demonstrated in the above example, the impedance ratio can be readily utilized to assess the system stability. As for three-phase ac systems, the inverter impedance can be modeled as sequence impedances and the Nyquist stability criterion can be applied. The inverter impedance can also be modeled as the *d*-*q* impedance in the synchronous *d*-*q* frame, and in this case the generalized Nyquist stability criterion (GNC) for multi-input-multi-output (MIMO) systems should be used.

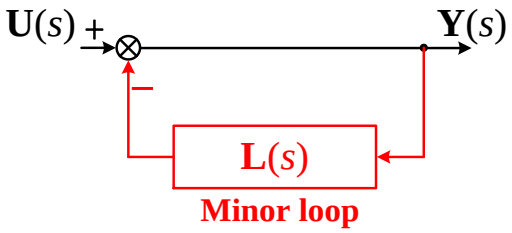

Figure 2-3. Generic multivariable closed-loop configuration.

Consider **L**(s) as the return-ratio matrix of the generic multivariable closed-loop system depicted in Figure 2-3. The eigenvalue-based GNC can be stated as follows [34]–[36]:

"Let **L**(s) have no open-loop uncontrollable and/or unobservable modes whose corresponding characteristic frequencies lie in the right-half plane. The closed-loop system is stable if and only if the net sum of anti-clockwise encirclements of the critical point $(-1, j0)$ by

the set of characteristic loci of **L**(s) is equal to the total number of right-half plane poles of **L**(s).”

The determinant-based GNC can be stated as follows [34]–[36]:

“Let *N* denote the number of open-loop unstable poles in **L**(s). The closed-loop system with loop transfer function **L**(s) and negative feedback is stable if and only if the Nyquist plot of det(**I**+**L**(s)) a) makes *N* anticlockwise encirclements of the origin, and b) does not pass through the origin.”

An impedance-based conservative stability criterion was proposed in [63]–[66], on the basis of the frequency-domain passivity theory, which states that: “a linear, continuous system $G(s)$ is passive if 1) $G(s)$ is stable without RHP poles and 2) the real part of $G(j\omega)$ is non-negative or the angle of $G(j\omega)$ is within [-90 °, 90 °], for the whole range of the frequency ω [19].” For the grid-connected current-controlled single-phase inverter system as shown in Figure 2-1(a), if both the inverter output admittance $Y_{oc}(s)$ and the grid impedance $Z_g(s)$ are passive, the system is stable with the Nyquist plot of the impedance ratio $T_m(s)$ illustrated in Figure 2-4.

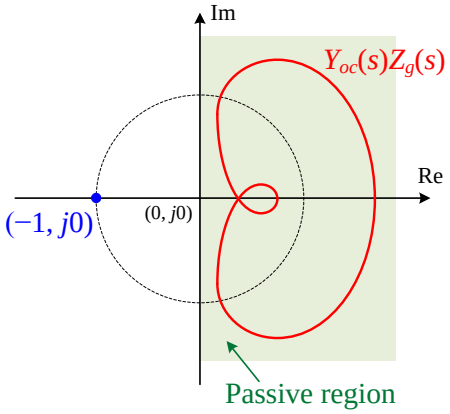

Figure 2-4. Nyquist plot of the impedance ratio $T_m(s)$ when both $Y_{oc}(s)$ and $Z_g(s)$ are passive.

Compared with the state-space-based approach and the transfer-function-based approach, the impedance-based approach, based on the impedance ratio of two subsystems at the interface, has several advantages:

(1) The measured impedances of system components can be directly used to assess the system stability, without the need to know the detailed physical or control information of the inverter components [37]. Thus, it enables the system integrator to easily analyze the stability during the system planning stage without the need for the inverter internal information from the vendors.

(2) This approach can clearly interpret the impact of individual components or subsystems on the system stability [23].

(3) For source-load systems, practical conservative impedance-based stability criteria [38], such as the Middlebrook criterion [39], can be used to define the forbidden regions in the complex plane for the locus of the source and load impedance ratio [37]. Thus, given the source (or load) impedance, the specifications of the load (or source) impedance can be defined to design the controller parameters separately.

Considering the above advantages, the impedance-based approach is adopted in this study to facilitate the stability analysis and controller design of three-phase inverter-based ac systems.

2.2 Impedance Modeling of Three-Phase Inverters

There are generally two kinds of impedance models for three-phase balanced ac systems [66]–[68], that is, the *d-q* impedance matrix model in the synchronous *d-q* frame [69] and the harmonic-linearization-based sequence impedance model [70]. The *d-q* impedance models can be used to assess both the harmonic instability and low-frequency oscillation problems by using

the generalized Nyquist stability criterion (GNC) [34], [71]. As reported in [72] and [73], the positive-sequence and negative-sequence impedances of inverters are decoupled, if 1) only inner current or voltage loops with symmetric structures and equal parameters in *d*- and *q*-axis are considered, and 2) no phase locked loop (PLL) is adopted or the PLL has negligible impact due to a sufficiently low bandwidth. Under these conditions of decoupling, the sequence impedance models have been proven to be effective in analyzing the harmonic stability based on Nyquist stability criterion [23], [25], [31], [70]. While the manipulation of *d-q* impedance matrices is complicated, the scalar computation of decoupled positive-sequence and negative-sequence impedances under above conditions is simpler.

The sequence admittance model of current-controlled three-phase inverters with an output *L* filter is developed in [70], with the consideration of the voltage feed-forward control in the phase domain. Nevertheless, the sequence admittance model of current-controlled inverters with the voltage feed-forward control in the *d-q* frame is not discussed. In addition, the impact of the dead time inserted in duty-cycles of phase-leg switches on the inverter sequence admittance is not considered. Moreover, the sequence impedance modeling of voltage-controlled three-phase inverters has not been studied in the literature yet.

For the small-signal stability analysis in the *d-q* domain, models of system components need to be built in a common *d-q* frame [74]. The *d-q* impedance model of voltage-controlled inverters with droop control in a common *d-q* frame has been developed in [74]. But the output admittance model of current-controlled inverters is usually expressed in the *d-q* frame aligned to the inverter terminal voltage [69], while the model in an arbitrary *d-q* frame has not been discussed in references yet.

In CURENT's power electronics inverter based Hardware Testbed for transmission-level

power grid emulation, static load emulators using current-controlled three-phase inverters are developed for emulation of ZIP loads [6], [7], which are the combination of constant impedance (Z), constant current (I) and constant power (P) loads in both real and reactive power, in order to provide flexible loading conditions for steady-state and transient emulation. The static load emulation changes the dynamic performance of the current-controlled inverters in the low frequency range, and thus the inverter output admittance in the *d-q* frame is also changed and needs to be modeled to assist in the impedance-based stability analysis of the inverter-based systems.

The aforementioned *d-q* impedance models and sequence impedance models assume that the system fundamental frequency ω_1 is a constant value. If the slow dynamics of the fundamental frequency ω_1 is also concerned in three-phase ac systems, such as a microgrid consisting of multiple droop-controlled inverters, the fundamental frequency ω_1 should also be treated as a variable in the terminal characteristics modeling of inverters and system passive components. The terminal characteristics models of three-phase current-controlled inverters and voltage-controlled inverters with the droop control loop were developed in [75] and [76], by further including the transfer function between the fundamental frequency ω_1 and the inverter current. However, the terminal characteristics models of passive components, such as transmission lines, inductive and resistive loads and shunt capacitors, have not been discussed in the literature yet.

2.3 Impedance Measurement of Three-Phase Inverters

Several methods exist for impedance measurement of three-phase ac systems. Generally, the measurement objects include three types: online grid impedance [77]–[79], general three-phase ac source impedance and load impedance [80], [81], and the power converter impedance [82], [83]. The impedance can be measured either in a passive way by utilizing the existing noise [77],

or in an active way by injecting a single-frequency signal [80], [81], [84] and sweeping the frequency or by injecting wide-band signals [78], [82], [85].

As for measurement setup, aside from online grid impedance measurement, which can be implemented by grid-connected inverters [78], the other two types of impedance measurement usually require dedicated equipment [80], [81], [83], such as the frequency response analyzer, power amplifier, isolation transformer and chopper circuit, which are not easy to set up. It has been reported that it is convenient to use existing three-phase inverters in shunt or in series or in grid-connected mode to create perturbations for online source or load impedance measurement [86]–[88]. However, since the inverter only serves as the power amplifier of the injection signal, both the external source and load are needed to create the desired operating point. Therefore, the ratio between the source and load impedance will impact the perturbation distribution and weaken the effective perturbation level. The impedance measurement accuracy also suffers from the background harmonics. On the other hand, most of the existing methods focus on measurement of the impedance in the *d*-*q* domain [89], while the sequence impedance measurement is only discussed in [83], which still uses dedicated equipment.

2.4 Impedance-Based Stability Analysis of Inverter-Based Ac Systems

When using the Nyquist stability criterion or the GNC, not only the encirclement of the Nyquist plot around $(-1, j0)$ should be examined, but also the right-half-plane (RHP) poles of the impedance ratio or return-ratio matrix should be checked [34], [62]. For converter-based ac systems that could be divided into a stable source subsystem and a stable load subsystem, the ratio of two subsystems' impedances does not have RHP poles, and thus the pole examination is avoided in the stability analysis. This applies to the systems with simple structures, such as grids with a single inverter [67], [70] or directly paralleled multiple inverters [25], [29], [90] and

source-load systems with one common ac bus [30], [37], [71], [91]–[94]. However, for complicated inverter-based ac systems with multiple buses, such as meshed power systems [23] and microgrids [27], normally they could not be easily divided into two stable subsystems during the system planning stage, and therefore it is necessary to examine the RHP poles of the impedance ratio when using the Nyquist stability or the GNC for system stability analysis, which requires detailed transfer function models of system components and would result in a heavy computation burden for complicated systems.

A number of research efforts have been made to avoid the pole calculation of the impedance ratio and facilitate the impedance-based stability analysis of inverter-based multi-bus ac systems. The harmonic stability of a three-phase meshed ac power system made up of multiple voltage-controlled and current-controlled converters was evaluated in [23], by analyzing the Nyquist plot of the impedance ratio at each point of connection (PoC) for each component. However, the stability analysis at different PoCs of components could reveal conflictive results [90]. Some stability criteria have also been reported, such as the Impedance-Sum-Type Criterion [95] based on Cauchy's theorem and the Nyquist criterion for multi-loop system [96]. In addition, a sufficient-but-not-necessary stability condition for a radial distribution network with multiple current-controlled converters has been proposed in [97] by analyzing the stability step by step from the simplest entity to the entire network. However, these methods are only applicable to paralleled source-source converter systems with only voltage-controlled converters or only current-controlled converters instead of the mix of both types.

The authors of [95] further considered applying Cauchy's theorem to the stability analysis of single-bus systems, in which both voltage-controlled and current-controlled converters are directly connected to the common bus in parallel [98], [99]. However, the derived two-step

stability criterion is not an extension of the Impedance-Sum-Type criterion. In addition, the application of Cauchy's theorem to a multi-bus general ac system with both voltage-controlled and current-controlled inverters and complicated connections including mesh has not been reported in the existing literature yet. And the underlying principle of the impedance-based stability analysis using Cauchy's theorem has not been clearly described yet.

The CCM has also been reported in the multivariable frequency domain and the eigenvalue-based GNC is applied to the resultant transfer function matrix model to analyze the stability of traditional interconnected power systems [100]. By utilizing the algebraic properties, including Y-symmetry and the ability to be decoupled, of the frequency characteristic matrices of power systems, two uncoupled eigenvalue systems are derived for the original system, and several simplified stability criterion based on the eigenvalue-based GNC have been proposed in [100]. Later on, the small gain theory and the structured singular value (μ)-based analysis have been applied to derive a stability criterion regarding the structure singular value of the connection network and the singular value of each component [101], but such criterion is conservative. The μ-based analysis has also been applied to the stability analysis of a source-load system and a microgrid with multiple inverter-based distributed energy resource (DER) units to establish a robust stability margin in terms of load parameter perturbations in [102], but this method is conservative and not based on the CCM.

In the application of the frequency-domain CCM to conventional power systems [100], all the components are treated as voltage-controlled current sources with voltage as input and current as output, and thus the transfer function matrix (or impedance matrix) of the connection network is simply the inverse of the system nodal admittance matrix. In contrast, in inverter-based autonomous ac systems, the inverter-interfaced power sources and loads could be either

voltage-controlled type or current-controlled type. As a result, the impedance matrix of the connection network could not be obviously obtained. Reference [23] reviewed the application of the CCM in the frequency domain to the harmonic stability analysis of a three-phase inverter-based meshed ac power system in the stationary α-β frame. But the impedance matrix of the connection network was not derived, and thus the application of the CCM was not demonstrated on the studied system. A literature survey indicates that the stability analysis of three-phase inverter-based ac systems based on *d*-*q* impedances and the CCM in the frequency domain has not been demonstrated in the existing literature yet. Moreover, the stability analysis using the CCM and the determinant-based GNC, which is another type of GNC criteria besides the eigenvalue-based GNC [103], has not been discussed in the literature yet.

As for the stability analysis of the low-frequency oscillation of the fundamental frequency in three-phase inverter-based islanded ac microgrids, a stability criterion based on the terminal characteristics of droop-controlled inverters modeled in [75] and [76] was proposed in [104] for a single-bus microgrid with two droop-controlled inverters in parallel sharing a common load. However, such stability criterion cannot be applied to the low-frequency stability of complicated ac micrgrids with multiple buses.

2.5 Impedance-Based Controller Design of Inverters for System Stability

It is important to properly design the controllers of inverters to ensure the stability of an inverter-based ac system with a definite structure, during the system planning stage.

There are several impedance-based methods of inverter controller design for system stability. One way is to shape the converter impedance by emulating virtual impedance [105]–[108] or inserting filters into control loops [109]–[111], which relies on the knowledge of system

impedances or resonance frequency information. Another way is to make the converter impedance passive based on the frequency-domain passivity theory, by adjusting controller parameters or adding special controllers [63]–[66], [112]–[114]. But the passivity-based design requires a trade-off between dynamic performance and passivity. A third way is to select proper controller parameters based on the system stability analysis [37], [115], [116]. Proper controller parameter ranges can be determined to meet the specified stability margin requirements [116], [117], or they can be presented as stability regions and boundaries in the parameter space [28], [40]. For simple source-load systems, given the load-side impedance, it is relatively easy to design the controller parameters of the source side by adjusting its impedance to meet the impedance-based stability criteria, or vice versa [37], [115], [116]. However, for inverter-based multi-bus ac systems, it is not easy to design the controller parameters of each inverter individually due to the inter-connection of all inverters.

2.6 Impedance-Based Controller Design of Inverters for Stable Integration into an Unknown System

Unlike the planning of an inverter-based ac system with a definite structure, there are situations when the inverters need to be integrated into a system with unknown information or a time-varying structure, such as integration of multiple renewable interface inverters into a weak grid, and plug-and-play of inverter-based distributed energy resources (DER) in a microgrid.

There are several impedance-based approaches for controller design of inverters for stable integration into an unknown system. The first approach is to design the inverter impedance to be passive based on the frequency-domain passivity theory. If the potential resonance frequencies of the system are known and time-invariant, such as the sub-synchronous resonances due to the torsional modes of nearby generators [110], the inverter integration can be stable when the

inverter impedance is designed to be passive around these resonance frequencies. However, the resonance frequencies are uncertain in the multiple-inverter-based ac systems due to the wideband dynamic interactions among the inverters and the grid. Thus, the ideal solution is to make the inverter impedance passive in the whole frequency range except the fundamental frequency. Euler-derivative-based control has been proposed in [112] to make the admittances of current-controlled renewable interface inverters passive in the most frequency range. Nevertheless, the voltage feed-forward control, which could contribute to non-passive admittances, is not considered in [112].

The second approach is based on online resonance frequency detection. Reference [111] proposed a self-commissioning notch filter technique through exciting and detecting the *LCL*-filter resonance frequency by using Fourier analysis. But it is only for active damping of the *LCL*-filter resonance, while the low-order harmonic resonance caused by the current/voltage control loops as well as voltage feed-forward control is not discussed. The active damper concept has been put forward in [25], [118], [119] that an additional power converter with a high bandwidth is used to detect the resonance frequencies and reshape the grid impedance at resonance frequencies. However, this method requires additional hardware setup, and it is difficult to design the virtual resistance value due to its dependence on the system structure and location of the active damper [120].

The third approach is based on online grid impedance measurement. There are several methods for online grid impedance measurement in existing literatures [77]–[79], based on single-frequency, or impulse-type or sequence-type current disturbance injection and Fourier analysis. The adaptive control methods based on online grid impedance measurement proposed in existing references [121]–[123], usually simply assumed the grid impedance as a series of

inductance and resistance, and extracted the L and R parameters from the measured frequency response. However, for the inverter-based ac systems, the grid impedance could be rather complicated due to the existence of other inverters, and therefore could not be simplified as pure passive impedance. Reference [124] proposed an impedance-phase compensation strategy by using the phase information of the measured grid impedance. However, a simple inductive grid was used in the verification, and the voltage feed-forward was not included in the current control loop.

Therefore, there are still problems regarding the impedance-based controller design of inverters to stably integrate into a weak grid or microgrid with unknown system information.

2.7 Research Objectives

According to the literature review above, many issues are still unsolved on the impedance-based stability analysis and controller design of three-phase inverter-based ac systems. The main challenges include:

(1) Sequence impedance modeling of three-phase voltage-controlled inverters, and the *d-q* admittance modeling of three-phase current-controlled inverters in an arbitrary *d-q* frame, and the *d-q* admittance modeling of the static load emulator in CURENT's power grid emulation platform.

(2) Lack of a simple setup for sequence impedance measurement of inverters.

(3) Impedance-based stability analysis of ac systems consisting of both voltage-controlled and current-controlled inverters without the need for the RHP pole calculation of the impedance ratio.

(4) Impedance-based controller parameter design of inverters in inverter-based ac

systems with definite structures.

(5) Impedance-based controller design of inverters to stably integrate into an unknown system with existing inverters in operation.

Corresponding to the challenges listed above, the main tasks of this dissertation are identified as follows.

(1) Develop the sequence impedance model of three-phase voltage-controlled inverters, and the *d-q* admittance model of three-phase current-controlled inverters in an arbitrary *d-q* frame, and the *d-q* admittance model of the static load emulator in CURENT's power grid emulation platform.

(2) Propose a simple setup for sequence impedance measurement of three-phase inverters by using an existing inverter connected in a paralleled structure.

(3) Propose impedance-based stability criteria for grid-connected radial-line renewable energy systems and general inverter-based multi-bus ac systems without the need for the RHP pole calculation of the impedance ratio.

(4) Propose a method for controller parameter design of inverters in inverter-based ac systems with definite structures.

(5) Propose an adaptive controller design method of inverters for stable integration to an unknown system with existing inverters in operation.

3 Impedance Modeling of Three-Phase Inverters

In this chapter, the output admittance of current-controlled three-phase inverters and the output impedance of voltage-controlled three-phase inverters are modeled in both the sequence domain and the synchronous rotating *d-q* frame. Only the high-bandwidth inner current or voltage control loops and grid-synchronization phase-locked loop (PLL) are considered in the sequence impedance modeling for the harmonic stability analysis. In contrast, the *d-q* impedance modeling considers all the control loops, including the low-bandwidth outer loops, such as generator and static load emulation loops, which enable the analysis of low-frequency stability.

The block diagram of the three-phase inverter with an output *L* filter is shown in Figure 3-1, where i_t is the inverter output current, v_M is the inverter output voltage and v_t is the inverter terminal voltage. In this study, it is assumed that the dc-link voltage v_{dc} is regulated by a front-end converter and can be regarded as a constant value V_{dc}.

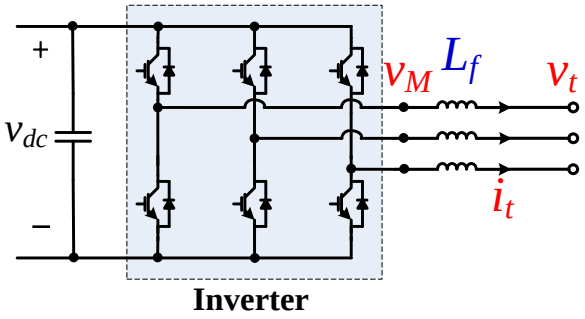

Figure 3-1. Block diagram of a three-phase inverter with an output *L* filter.

3.1 Sequence Admittance of Current-Controlled Inverters with Voltage Feed-Forward Control in the D-Q Frame and Dead Time

Reference [70] presented the sequence admittance modeling of current-controlled three-phase inverters with an output *L* filter, considering the voltage feed-forward control in the phase domain. However, the case with voltage feed-forward control in the *d-q* frame is not discussed. In addition, the dead time inserted in duty-cycles of phase-leg switches is not considered. Following the modeling method in [70], this section improves the sequence admittance models of current-controlled three-phase inverters by including the voltage feed-forward control in the *d-q* frame and the impact of the dead time [125].

A. Modeling of the current control loop with the voltage feed-forward control

For current-controlled inverters, the inverter output current i_t is usually controlled with a proportional-resonant (PR) controller in the stationary α-β frame or a proportional-integral (PI) controller in the synchronous *d-q* frame. In addition, a phase-locked loop (PLL) unit is adopted to obtain the angle θ_1 and frequency ω_1 information of the inverter terminal voltage v_t. The block diagram of the commonly used synchronous rotating reference frame PLL (SRF-PLL) is shown in Figure 3-2. For the current control in the α-β frame, the angle θ_1 is used to transform the current references i_t^* from the *d-q* frame to the α-β frame. For the current control in the *d-q* frame, the angle θ_1 is used to transform the inverter terminal voltage v_t, the output current i_t and controller output v_c between the three-phase *abc* frame and the *d-q* frame.

The block diagram of the current control loop in the sequence domain can be generally depicted in Figure 3-3, for the inverters with a PR current controller and the voltage feed-forward control in α-β frame, or a PI current controller and the voltage feed-forward control in *d-q* frame.

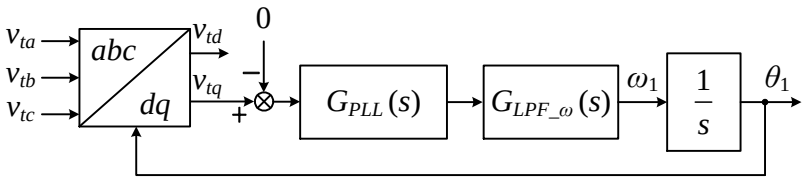

Figure 3-2. Block diagram of the PLL loop.

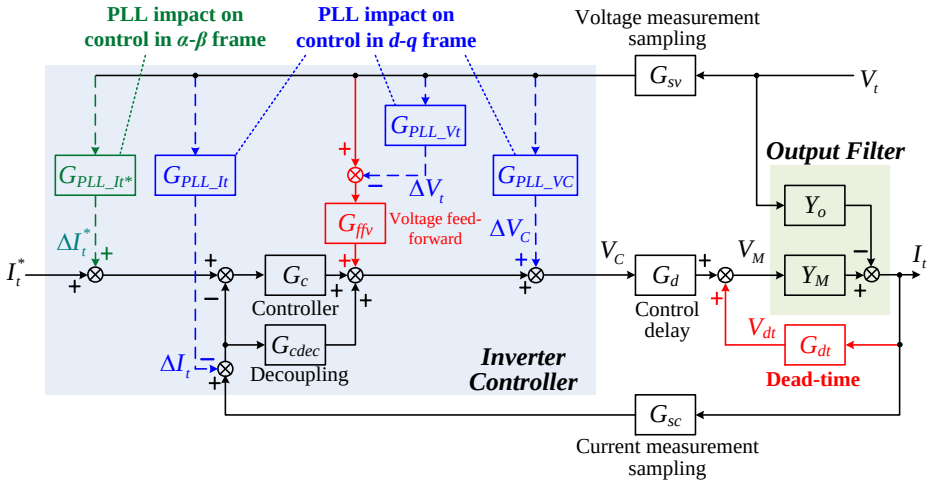

Figure 3-3. Block diagram of the current control loop in the sequence domain with the PLL impact on both the control in *d-q* frame and the control in *α-β* frame.

Assuming I_t is the inverter output current, V_M is the inverter output voltage and V_t is the inverter terminal voltage in the sequence domain, the frequency behavior of the output L filter can be modeled by two admittances Y_M and Y_o represented by (3-1), where L_f and R_{Lf} are the inductance and resistance of the L filter. Both the voltage and current are sampled four times in equal time intervals in each switching period (T_s) and the average of the four samples is used as the final measurement value. So the sampling processes of the voltage and current are modeled approximately as a $0.5T_s$ delay unit as shown in (3-2). The approximately 1.5 switching period

delay, including the computation delay of T_s and the PWM generation delay of $0.5T_s$, is introduced in the digital control and modeled in (3-3). These delay units can be represented by a second-order Pade approximation as shown in (3-4).

$$Y_M = Y_o = \frac{1}{L_f s + R_{Lf}} \tag{3-1}$$

$$G_{sv} = G_{sc} = \left(1 + e^{-0.25T_s s} + e^{-0.5T_s s} + e^{-0.75T_s s}\right) \Big/ 4 \approx e^{-0.5T_s s} \tag{3-2}$$

$$G_d = e^{-1.5T_s s} \tag{3-3}$$

$$e^{-T_d s} \approx \frac{1 - T_d s/2 + (T_d s)^2/12}{1 + T_d s/2 + (T_d s)^2/12} \tag{3-4}$$

The transfer functions of the control gains inside the "Inverter Controller" block are explained as follows. The transfer function of the PR or PI controller $G_c(s)$ is expressed in (3-5), where K_{cp} is the proportional gain and K_{ci} is the resonant or integral gain. The transfer function of the decoupling term $G_{cdec}(s)$ used in the control in the *d*-*q* frame is represented by (3-6). A first-order low-pass filter is used as the voltage feed-forward gain $G_{ffv}(s)$ in (3-7), where ω_{ffv} is the cut-off frequency. In the block diagram of the PLL shown in Figure 3-2, $G_{PLL}(s)$ is a PI controller with the proportional gain K_{PLLp} and the integral gain K_{PLLi} as expressed in (3-8), and G_{LPF_ω} is a low-pass filter with the cut-off frequency ω_{PLL}, as expressed in (3-9). The open-loop gain $H_{PLL}(s)$ and the closed-loop gain $T_{PLL}(s)$ of the PLL loop are expressed in (3-10) and (3-11).

$$\text{PR}: \quad G_c(s) = K_{cp} + \frac{K_{ci} s}{s^2 + \omega_1^2}; \quad \text{PI}: \quad G_c(s) = K_{cp} + \frac{K_{ci}}{s} \tag{3-5}$$

$$G_{cdec}(s) = \omega_1 L_f \tag{3-6}$$

$$G_{ffv}(s) = \frac{1}{1 + s/\omega_{ffv}} \tag{3-7}$$

$$G_{PLL}(s) = K_{PLLp} + \frac{K_{PLLi}}{s} \tag{3-8}$$

$$G_{LPF\_\omega}(s) = \frac{1}{1 + s/\omega_{PLL}} \tag{3-9}$$

$$H_{PLL}(s) = V_{t1} \cdot G_{PLL}(s) \cdot G_{LPF\_\omega}(s) \cdot \frac{1}{s} \tag{3-10}$$

$$T_{PLL}(s) = \frac{H_{PLL}(s)}{1 + H_{PLL}(s)} \tag{3-11}$$

To derive the output admittance of the inverter in the sequence domain, all the control gains with transfer functions in the *d-q* frame need to be converted to their corresponding transfer functions in the sequence domain. Therefore, for current control in the *α-β* frame, the transfer functions of the control gains are expressed in (3-12) in the positive sequence domain and in (3-13) in the negative sequence domain. Similarly, for the current control in the *d-q* frame, the control gains are expressed in (3-14) in the positive sequence domain and in (3-15) in the negative sequence domain.

$$G_c = G_c(s); \quad G_{ffv} = G_{ffv}(s); \quad T_{PLL} = T_{PLL}(s - j\omega_1) \tag{3-12}$$

$$G_c = G_c(s); \quad G_{ffv} = G_{ffv}(s); \quad T_{PLL} = T_{PLL}(s + j\omega_1) \tag{3-13}$$

$$G_c = G_c(s - j\omega_1); G_{cdec} = j\omega_1 L_f; G_{ffv} = G_{ffv}(s - j\omega_1); T_{PLL} = T_{PLL}(s - j\omega_1) \quad (3\text{-}14)$$

$$G_c = G_c(s + j\omega_1); G_{cdec} = -j\omega_1 L_f; G_{ffv} = G_{ffv}(s + j\omega_1); T_{PLL} = T_{PLL}(s + j\omega_1) \quad (3\text{-}15)$$

The PLL impact on the current control in the α-β frame can be seen as the additional voltage feed-forward component to the current reference (ΔI_t^*), and the feed-forward gain G_{PLL_It*} is expressed in (3-16) in the positive sequence domain. The PLL impact on the current control in the *d-q* frame can be seen as the additional voltage feed-forward components to the inverter terminal voltage measurement (ΔV_t), the current feedback (ΔI_t) and the controller output (ΔV_C), and the feed-forward gains are defined as G_{PLL_Vt}, G_{PLL_It} and G_{PLL_VC} respectively, as expressed in (3-16) in the positive sequence domain. In these equations, $\mathbf{V}_{t1}$, $\mathbf{I}_{t1}$and $\mathbf{V}_{C1}$ are the steady-state phasors at the fundamental frequency of V_t, I_t and V_C, with V_{t1}, I_{t1} and V_{C1} as the magnitudes and ϕ_{t1}, ϕ_{t1} and ϕ_{C1} as the phases, respectively, as expressed in (3-17). In the negative sequence domain, $\mathbf{V}_{t1}^*$, $\mathbf{I}_{t1}^*$, and $\mathbf{V}_{C1}^*$ should be used in (3-17), which are the complex conjugates of $\mathbf{V}_{t1}$, $\mathbf{I}_{t1}$and $\mathbf{V}_{C1}$, respectively. By neglecting the impact of measurement and delay, $\mathbf{V}_{C1}$ can be approximately expressed as (3-18).

$$G_{PLL\_It*} = \frac{T_{PLL}}{V_{t1}}\mathbf{I}_{t1}; G_{PLL\_Vt} = \frac{T_{PLL}}{V_{t1}}\mathbf{V}_{t1}; G_{PLL\_It} = \frac{T_{PLL}}{V_{t1}}\mathbf{I}_{t1}; G_{PLL\_VC} = \frac{T_{PLL}}{V_{t1}}\mathbf{V}_{C1} \quad (3\text{-}16)$$

$$\begin{cases} \mathbf{V}_{t1} = \dfrac{V_{t1}}{2}e^{j\phi_{Vt1}}; \quad \mathbf{I}_{t1} = \dfrac{I_{t1}}{2}e^{j\phi_{It1}}; \quad \mathbf{V}_{C1} = \dfrac{V_{C1}}{2}e^{j\phi_{VC1}} \\ \mathbf{V}_{t1}^* = \dfrac{V_{t1}}{2}e^{-j\phi_{Vt1}}; \quad \mathbf{I}_{t1}^* = \dfrac{I_{t1}}{2}e^{-j\phi_{It1}}; \quad \mathbf{V}_{C1}^* = \dfrac{V_{C1}}{2}e^{-j\phi_{VC1}} \end{cases} \quad (3\text{-}17)$$

$$\mathbf{V}_{C1} = \mathbf{V}_{t1} + \mathbf{I}_{t1} \cdot \left(j\omega_1 L_f + R_{Lf} \right) \tag{3-18}$$

B. Modeling of the dead time effect

In real applications, a dead time is usually introduced in the PWM signals to prevent a shoot-through condition across the dc link. The dead-time effect will create a voltage difference (v_{dt_ph}) on the inverter output phase voltage, the value of which depends on the direction of the inverter output current i_{t_ph} in each phase. Assuming the voltage drops of the power semiconductors are negligible and the dc link voltage V_{dc} is constant, v_{dt_ph} can be expressed as:

$$v_{dt\_ph} = -\frac{T_{dt} + T_{don} - T_{doff}}{T_s} \cdot \frac{V_{dc}}{2} \cdot \mathrm{sgn}\left(i_{t\_ph} \right) \tag{3-19}$$

where T_{dt}, T_{don} and T_{doff} are the dead time, turn-on time and turn-off time of the power semiconductors. By approximating i_{t_ph} with its fundamental component i_{t1_ph}, the output of the signum function will be a square waveform in the steady state, which can be further approximated with its fundamental component [126]:

$$\mathrm{sgn}\left(i_{t\_ph} \right) \approx \mathrm{sgn}\left(i_{t1\_ph} \right) \approx \frac{4}{\pi} \cdot \frac{i_{t1\_ph}}{I_{t1}} \approx \frac{4}{\pi} \cdot \frac{i_{t\_ph}}{I_{t1}} \ . \tag{3-20}$$

Assuming all three phases are affected by the dead time, in the sequence domains, the relationship between the inverter output voltage difference V_{dt} caused by the dead time and the inverter output current I_t can be derived as

$$V_{dt} \approx -\frac{T_{dt} + T_{don} - T_{doff}}{T_s} \cdot \frac{V_{dc}}{2} \cdot \frac{4}{\pi} \cdot \frac{1}{I_{t1}} \cdot I_t = G_{dt} \cdot I_t \tag{3-21}$$

where G_{dt} is the transfer function. It can be seen that the dead-time effect can be approximated as

a virtual series resistor of the L filter, and the resistance value is $-G_{dt}$, which is dependent on the magnitude of the inverter output current. The block diagram of the current control loop with the dead-time effect is shown in Figure 3-3. By considering the dead-time effect, the two admittances Y_M and Y_o represented by (3-1) in the model of the output L filter should be modified as

$$Y_M = Y_o = \frac{1}{L_f s + R_{Lf} - G_{dt}} \ . \tag{3-22}$$

C. Modeling of the sequence admittance

According to the above analysis, the open-loop gain T_c and the closed-loop gain G_{clc} of the current-control loop as defined in (3-23) and (3-24), respectively, as well as the closed-loop output admittance Y_{oc} of the inverter, as defined in (3-25) for the current control in the α-β frame and in (3-26) for the current control in the d-q frame, can be derived from the block diagram shown in Figure 3-3 in both the positive sequence domain and the negative sequence domain. The Norton equivalent circuit of a current-controlled inverter is depicted in Figure 3-4. Then the positive sequence admittance $Y_{oc\_p}(s)$ and the negative sequence admittance $Y_{oc\_n}(s)$ of the current controlled inverter can be derived for both the current control in the α-β frame and the current control in the d-q frame.

$$T_c = \left(G_c - G_{cdec}\right) G_d Y_M G_{sc} \tag{3-23}$$

$$G_{clc} = \frac{I_t}{I_t^*} = \frac{G_c G_d Y_M}{1 + T_c} \tag{3-24}$$

$$Y_{oc} = -\frac{I_t}{V_t} = \frac{Y_o - G_{sv} G_d Y_M \left(G_{ffv} + G_c G_{PLL\_It^*} \right)}{1 + T_c} \tag{3-25}$$

$$Y_{oc} = -\frac{I_t}{V_t} = \frac{Y_o - G_{sv} G_d Y_M \left[G_{ffv} \left(1 - G_{PLL\_Vt} \right) + \left(G_c - G_{cdec} \right) G_{PLL\_It} + G_{PLL\_VC} \right]}{1 + T_c} \tag{3-26}$$

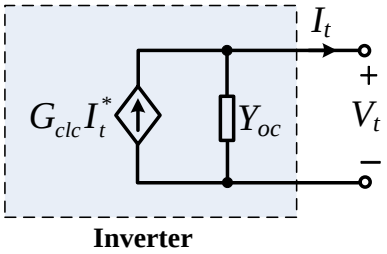

Figure 3-4. The Norton equivalent circuit of a current-controlled inverter in the sequence domain.

D. Examples

For the inverter under study in this chapter, the electrical parameters are summarized in Table 3-1, and the main controller parameters are listed in Table 3-2. The analytical results of the sequence admittances of the inverter with PR control in the α-β frame are shown in Figure 3-5(a) for the current output (I_d = 15 A, I_q = 0 A) and Figure 3-5(b) for the current output (I_d = –15 A, I_q = 0 A). The sequence admittances of the inverter with PI control in the *d*-*q* frame under the same conditions of current outputs are shown in Figure 3-6. In Figure 3-5 and Figure 3-6, red curves are positive sequence admittances $Y_{oc\_p}(s)$ and blue curves are negative sequence admittances $Y_{oc\_n}(s)$. $Y_{oc\_p}(s)$ and $Y_{oc\_n}(s)$ are different due to the different transfer functions of control gains.

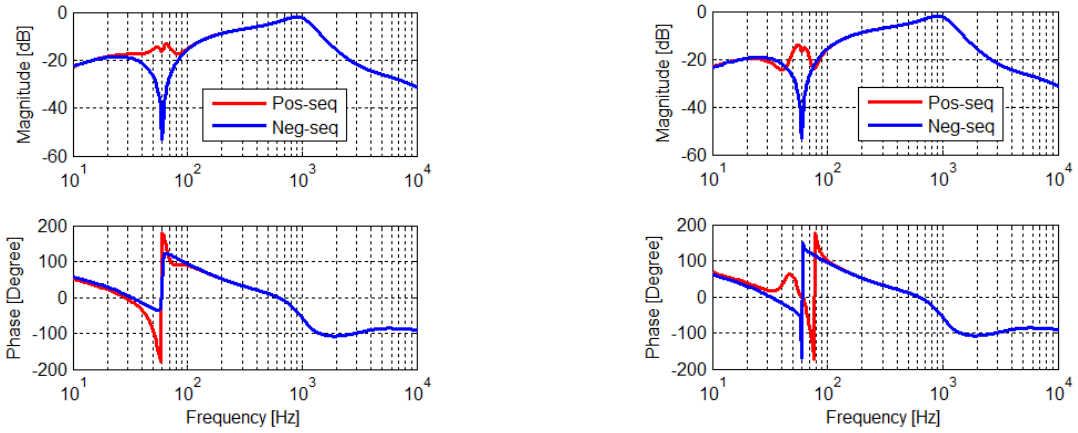

(a) (b)

Figure 3-5. Sequence admittances of the inverter with PR control in the α-β frame. Output current is (a) I_d=15 A, I_q=0 A; (b) I_d= –15 A, I_q=0 A.

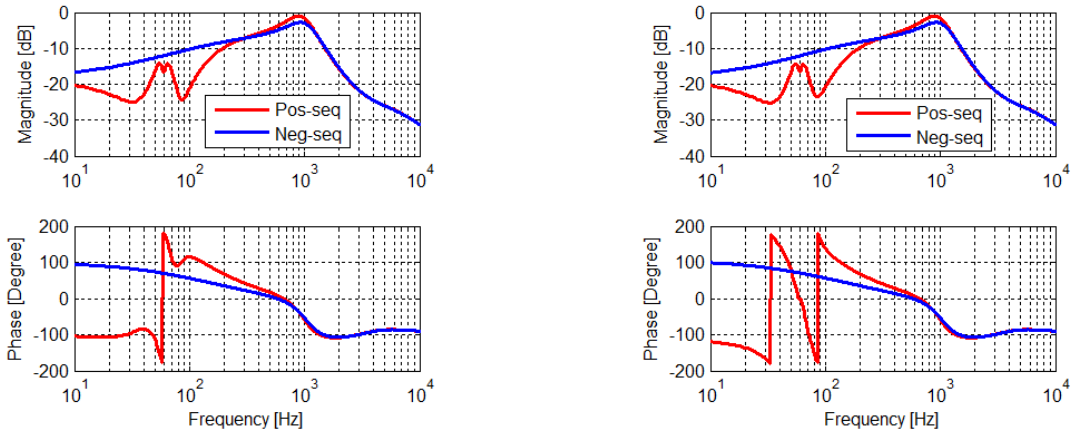

(a) (b)

Figure 3-6. Sequence admittances of the inverter with PI control in the *d*-*q* frame. Output current is (a) I_d=15 A, I_q=0 A; (b) I_d= –15 A, I_q=0 A.

Table 3-1. Electrical parameters of the inverter.

Electrical Parameters		**Values**
L filter	L_f	0.575 mH
	R_{Lf}	0.2 Ω
Dc-link voltage	V_{dc}	130 V
Ac voltage base	V_{base}	50 V (phase peak)
Ac current base	I_{base}	17.36 A (phase peak)
Ac power base	S_{base}	1302 W
Fundamental frequency	ω_1	60×2π rad/s

Table 3-2. Controller parameters of current-controlled inverters.

Controller Parameters		**Values**
Switching frequency	f_s	10 kHz
Switching period	T_s	100 μs
Current controller	K_{cp}	2.6
	K_{ci}	2275
Voltage feed-forward	ω_{ffv}	50×2π rad/s
PLL	K_{PLLp}	1.06
	K_{PLLi}	18
	ω_{PLL}	25×2π rad/s
Dead time	T_{dt}	1.5 μs

3.2 Sequence Impedance of Voltage-Controlled Inverters

The sequence impedance modeling of voltage-controlled three-phase inverters have not been studied in literature yet. This section develops the sequence impedance model of voltage-controlled three-phase inverters.

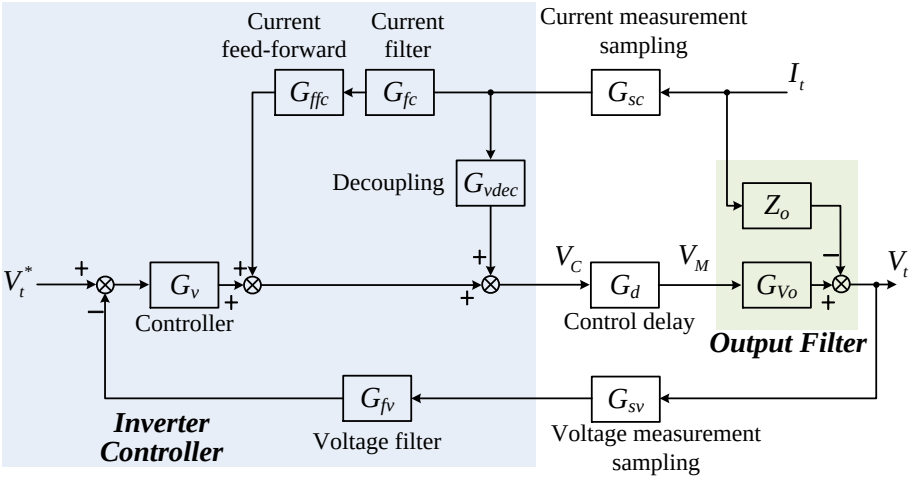

Figure 3-7. Block diagram of the voltage control loop in the sequence domain.

For voltage-controlled three-phase inverters with a PI voltage controller and the current-feedforward control in the synchronous *d*-*q* frame [8], the block diagram of the voltage control loop in the sequence domain can be illustrated in Figure 3-7. The output *L* filter can be modeled by a voltage gain G_{Vo} and an impedance Z_o represented by (3-27) and (3-28). The transfer functions of the control gains inside the "Inverter Controller" block in the *d*-*q* frame are explained as follows. The transfer function of the PI voltage controller $G_v(s)$ is modeled by (3-29), where K_{vp} is the proportional gain and K_{vi} is the integral gain. The transfer function of the decoupling term $G_{vdec}(s)$ is represented by (3-30). The first-order low-pass voltage filter $G_{fv}(s)$

and current filter $G_{fc}(s)$ are expressed as (3-31) and (3-32), with ω_{fv} and ω_{fc} as the cut-off frequencies respectively. The current feed-forward gain $G_{ffc}(s)$ is represented by (3-33). The corresponding transfer functions of these control gains are expressed in (3-34) in the positive sequence domain and expressed in (3-35) in the negative sequence domain.

$$G_{Vo} = 1 \tag{3-27}$$

$$Z_o = L_f s + R_{Lf} \tag{3-28}$$

$$G_v(s) = K_{vp} + \frac{K_{vi}}{s} \tag{3-29}$$

$$G_{vdec}(s) = \omega_1 L_f \tag{3-30}$$

$$G_{fv}(s) = \frac{1}{1 + s/\omega_{fv}} \tag{3-31}$$

$$G_{fc}(s) = \frac{1}{1 + s/\omega_{fc}} \tag{3-32}$$

$$G_{ffc}(s) = L_f s \tag{3-33}$$

$$G_v = G_v(s - j\omega_1); G_{vdec} = j\omega_1 L_f; G_{fv} = G_{fv}(s - j\omega_1); G_{fc} = G_{fc}(s - j\omega_1); G_{ffc} = G_{ffc}(s - j\omega_1) \tag{3-34}$$

$$G_v = G_v(s + j\omega_1); G_{vdec} = -j\omega_1 L_f; G_{fv} = G_{fv}(s + j\omega_1); G_{fc} = G_{fc}(s + j\omega_1); G_{ffc} = G_{ffc}(s + j\omega_1) \tag{3-35}$$

Based on the above analysis, the open-loop gain T_v and the closed-loop gain G_{clv} of the voltage-control loop as well as the closed-loop output impedance Z_{ov} of the inverter can be derived as (3-36), (3-37) and (3-38), respectively, in both the positive sequence domain and the

negative sequence domain. The Thevenin equivalent circuit of a voltage-controlled inverter is shown in Figure 3-8. For an inverter with parameters listed in Table 3-1 and Table 3-3 and output voltage V_{td}= 50 V, V_{tq}= 0 V, Figure 3-9 shows the analytical results and simulation measurement results of the positive-sequence impedance $Z_{ov\_p}(s)$ and negative-sequence admittance $Z_{ov\_n}(s)$. The difference between $Z_{ov\_p}(s)$ and $Z_{ov\_n}(s)$ is mainly due to the different transfer functions of control gains in the positive- and negative- sequence domains.

$$T_v = G_v G_d G_{Vo} G_{sv} G_{fv} \tag{3-36}$$

$$G_{clv} = \frac{V_t}{V_t^*} = \frac{G_v G_d G_{Vo}}{1 + T_v} \tag{3-37}$$

$$Z_{ov} = -\frac{V_t}{I_t} = \frac{Z_o - G_{sc} G_d G_{Vo} \left(G_{vdec} + G_{fc} G_{ffc} \right)}{1 + T_v} \tag{3-38}$$

Table 3-3. Controller parameters of voltage-controlled inverters.

Controller Parameters		**Values**
Switching frequency	f_s	10 kHz
Switching period	T_s	100 μs
Voltage controller	K_{vp}	1.04
	K_{vi}	325
Current filter in current feed-forward	ω_{fc}	$1000 \times 2\pi$ rad/s
Voltage filter	ω_{fv}	$300 \times 2\pi$ rad/s
Dead time	T_{dt}	1.5 μs

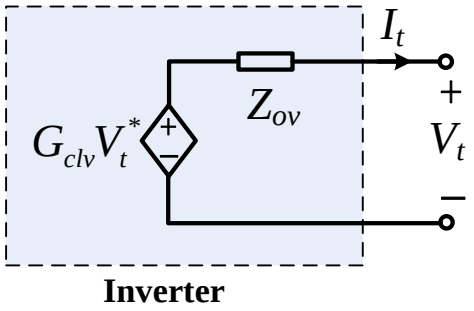

Figure 3-8. The Thevenin equivalent circuit of a voltage-controlled inverter in the sequence domain.

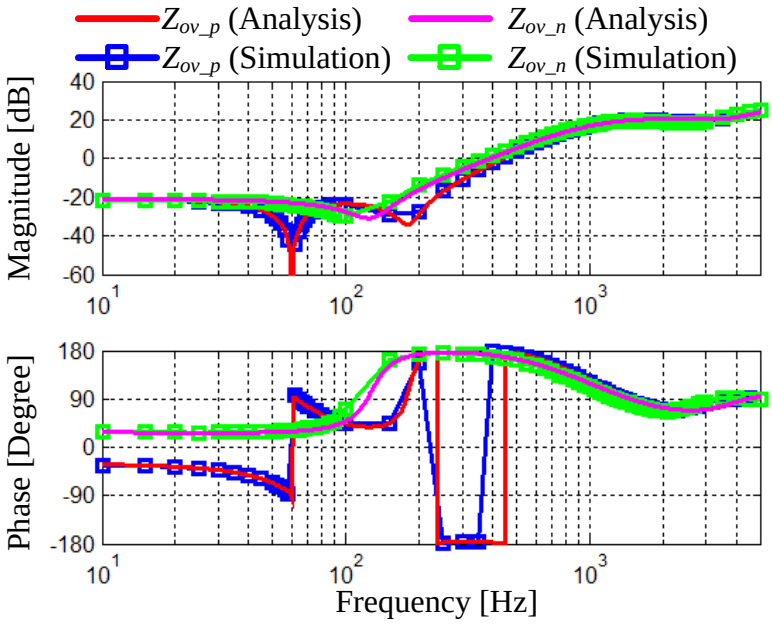

Figure 3-9. Positive and negative sequence impedances of an inverter with PI voltage control in the *d*-*q* frame.

3.3 Discussion on Sequence Impedance Models

3.3.1 Coupling in Balanced Systems

It was reported recently in [72] and [73] that there are couplings between positive-sequence and negative-sequence impedances with a shift of twice the fundamental frequency even in three-phase balanced systems, but the positive-sequence and the negative-sequence are decoupled if the inverters meet the following conditions: 1) with only inner current or voltage loops and no outer loops, 2) current or voltage controllers with symmetric structures and equal parameters in *d*- and *q*-axis, 3) without PLL. Since the voltage-controlled inverters investigated in this study for the harmonic stability analysis meet all the above conditions, their positive- and negative- sequence impedances are decoupled. The only violation is the adoption of the PLL in current-controlled inverters. Nevertheless, as pointed out in [72] and [73], the coupling terms are directly proportional to the closed-loop gain of PLL, T_{PLL}. Therefore, if the PLL bandwidth is very small (such as 10 Hz used in this study, as shown in Figure 3-10), the PLL has a negligible impact on the sequence admittances of current-controlled inverters in the frequency range above 100 Hz, as shown in Figure 3-11. In addition, when the focus is only on the harmonic instability issues instead of the low-frequency oscillation problems, the positive- and negative- sequence impedances or admittances of inverters can be regarded as decoupled for harmonic stability analysis.

3.3.2 Sequence Impedance Models in the Full Frequency Range

As expressed in (3-25), (3-26) and (3-38), the positive-sequence and negative-sequence admittances ($Y_{oc\_p}(s)$ and $Y_{oc\_n}(s)$) or impedances ($Z_{ov\_p}(s)$ and $Z_{ov\_n}(s)$) of inverters are complex transfer functions.

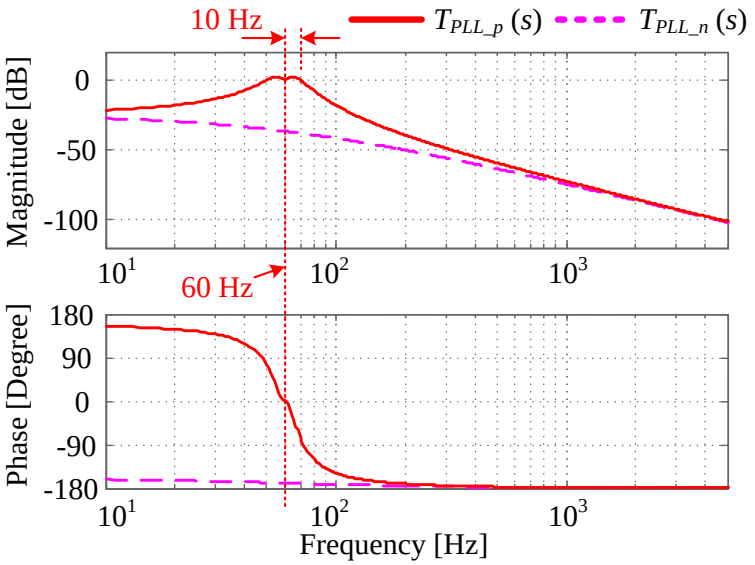

Figure 3-10. Bode plots of the closed-loop gains of PLL: $T_{PLL\_p}(s)$ in the positive-sequence domain and $T_{PLL\_n}(s)$ in negative-sequence domain.

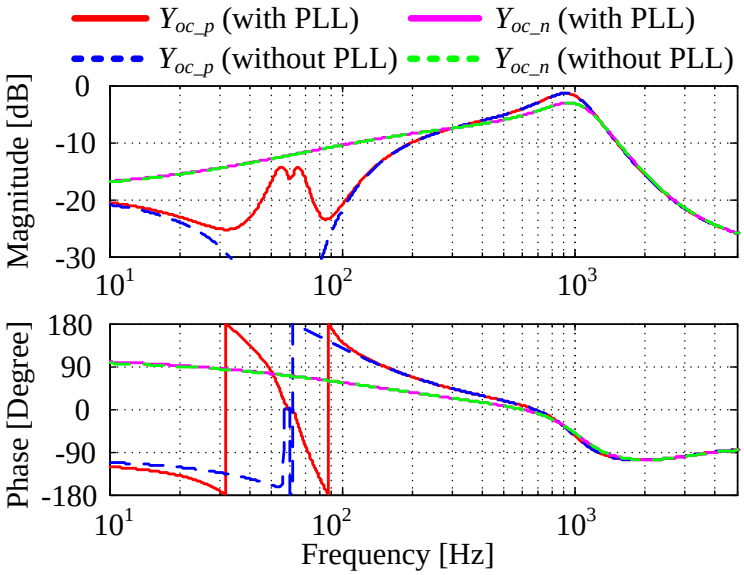

Figure 3-11. Positive and negative sequence admittances of a current-controlled inverter with and without PLL.

Figure 3-5, Figure 3-6 and Figure 3-9 only show the Bode plots of sequence admittances or impedances of inverters in the positive frequency range (0, +∞). Figure 3-12 and Figure 3-13 further depict the sequence admittances or impedances of inverters in the full frequency range (−∞, +∞). It can be observed that the Bode plot of each of $Y_{oc\_p}(s)$, $Y_{oc\_n}(s)$, $Z_{ov\_p}(s)$ and $Z_{ov\_n}(s)$ is approximately anti-symmetric in the full frequency range (−∞, +∞), with approximately equal magnitudes but opposite phases. For the harmonic stability analysis, Nyquist diagrams of an impedance ratio in the sequence domains can be drawn in the full frequency range (−∞, +∞), in order to clearly illustrate the encirclement of the critical point (−1, *j*0). Nevertheless, considering the approximate anti-symmetric Bode plots of sequence impedances, Bode plots of a function of sequence impedances can be drawn only in the positive frequency range (0, +∞), to clearly demonstrate the net phase change or the encirclement of the origin point (0, *j*0).

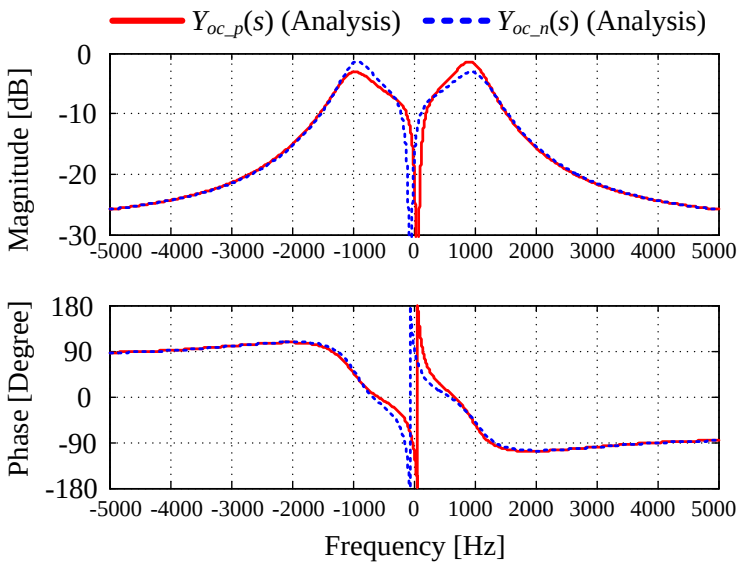

Figure 3-12. Positive- and negative- sequence admittances of a current-controlled inverter in the full frequency range.

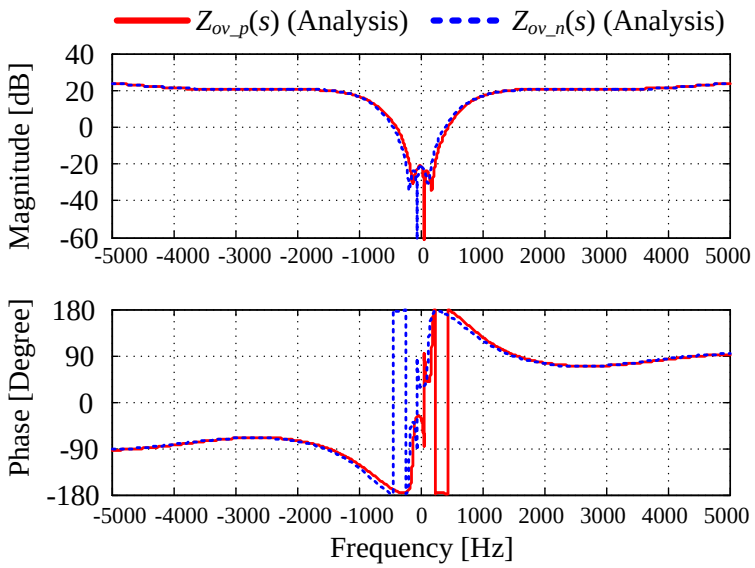

Figure 3-13. Positive- and negative- sequence impedances of a voltage-controlled inverter in the full frequency range.

3.3.3 Coupling Due to Unbalanced Filters

As reported in [127], if the three-phase systems are unbalanced, the positive- and negative-sequence impedances are also coupled, and 2-by-2 sequence admittance or impedance matrices, $\mathbf{Y_{oc}}$ and $\mathbf{Z_{ov}}$, are expressed in (3-39). The three-phase filters might have slight unbalance, due to the toleration of about 10% in physical inductors. Figure 3-14 shows the analytical results and simulation measurement results of sequence-admittance magnitudes of current-controlled inverters with (a) three-phase balanced L filters and (b) unbalanced L filters where phase-A is 100%, phase-B is 110% and phase-C is 90% of the rated value. Even with ±10% deviations in the L filters, the coupling terms Y_{oc_pn} and Y_{oc_np} are still at least 20 dB smaller than Y_{oc_p} and Y_{oc_n} . Therefore, the small couplings introduced by slightly unbalanced filters can be neglected.

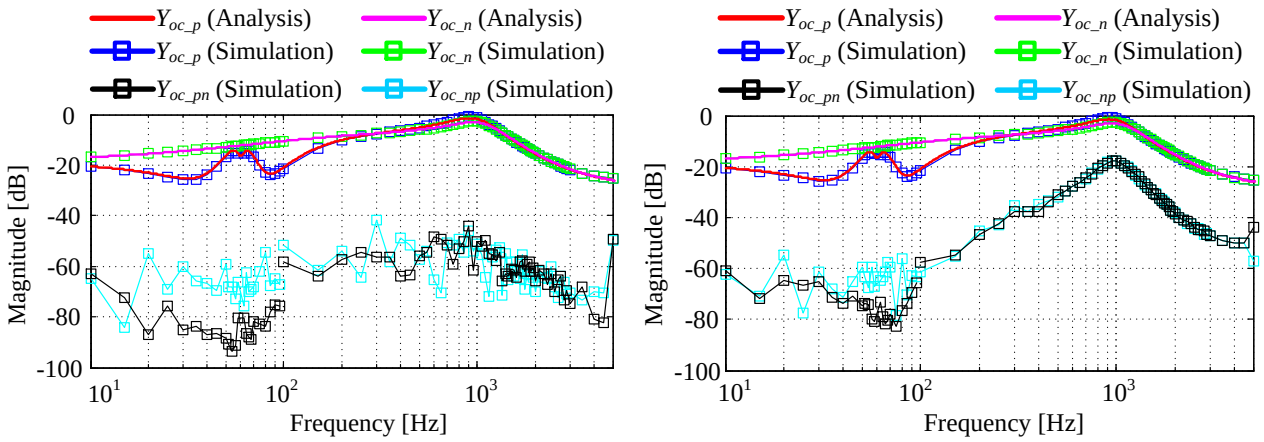

Figure 3-14. Analytical results and simulation measurement results of sequence admittances of current-controlled inverters with (a) balanced *L* filters and (b) unbalanced *L* filters (phase-A: 100%, phase-B: 110%, phase-C: 90%).

$$\mathbf{Y_{oc}} = \begin{bmatrix} Y_{oc\_p} & Y_{oc\_pn} \\ Y_{oc\_np} & Y_{oc\_n} \end{bmatrix}, \quad \mathbf{Z_{ov}} = \begin{bmatrix} Z_{ov\_p} & Z_{ov\_pn} \\ Z_{ov\_np} & Z_{ov\_n} \end{bmatrix} \tag{3-39}$$

3.3.4 With LCL Filters

Due to the actual experimental setup, only the *L* filters are considered in this dissertation. Other high-order filters with small volumes, such as *LCL* filters, are also commonly used in practice. The output sequence impedance models of inverters with *LCL* filters are different from the models presented here, but they were studied in the existing literature [23], [128]. In addition, the focus of this chapter is on the system-level harmonic stability analysis, the analysis and parameter design methods developed in the chapter are applicable to the systems consisting of inverters with *LCL* filters.

3.4 D-Q Admittance of Current-Controlled Inverters in an Arbitrary D-Q Frame

The output admittance model of current-controlled inverters in an arbitrary *d-q* frame is derived in this section to facilitate the system stability analysis in a common *d-q* frame.

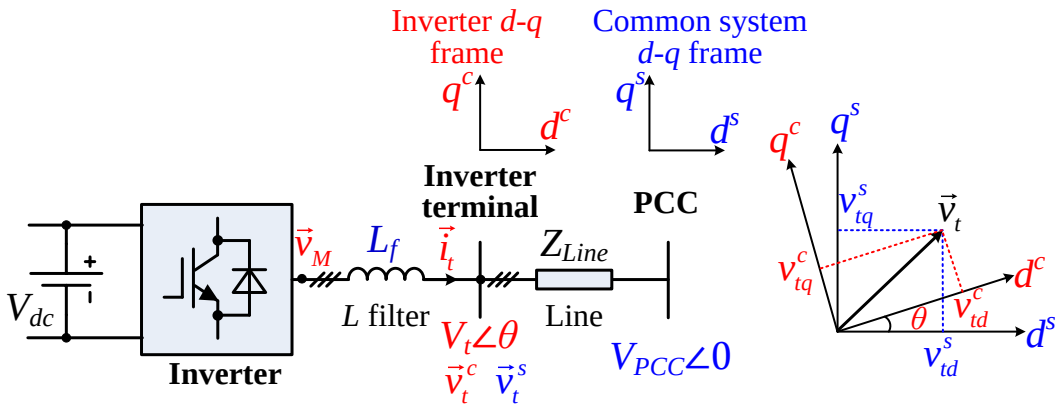

Figure 3-15. Block diagram of a three-phase inverter with an output *L* filter, and the relationship between different d-q frames.

Take a PV inverter connected to the point of common coupling (PCC) through a feeder line as an example, as shown in Figure 3-15. Assume the arbitrary *d-q* frame is chosen to be aligned with the voltage at PCC v_{PCC}, and it is selected as the common system *d-q* frame with the superscript *s*. In the following analysis, the dc-link voltage V_{dc} is assumed constant. The inverter *d-q* frame with the superscript *c* is aligned with the inverter terminal voltage v_t. Let the angle between the inverter terminal voltage v_t and v_{PCC} be θ, then the relationship between $\vec{v}_t^{\,c}$ and $\vec{v}_t^{\,s}$ can be expressed as (3-40). By adding small-signal perturbation and considering $\cos\tilde{\theta} \approx 1$ and $\sin\tilde{\theta} \approx \tilde{\theta}$, the small-signal model is derived in (3-41), where the symbol ~ denotes small-signal variables. Considering the open-loop relationship (3-42) and the closed-loop relationship (3-43)

of the conventional phase-locked loop (PLL) in the synchronous reference (*d*-*q*) frame (SRF) as shown in Figure 3-16, the small-signal model can be further derived as (3-44) and (3-45). Similarly, the relationships for currents ($\vec{\tilde{i}}^{\,c}$ and $\vec{\tilde{i}}^{\,s}$) and inverter controller outputs ($\vec{\tilde{v}}_c^{\,c}$ and $\vec{\tilde{v}}_c^{\,s}$) can be obtained in (3-46).

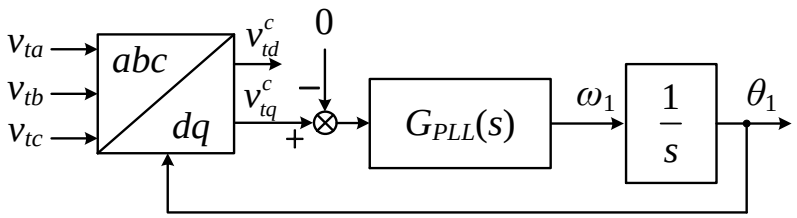

Figure 3-16. Block diagram of the SRF PLL loop.

$$\begin{bmatrix} v_{td}^c \\ v_{tq}^c \end{bmatrix} = \mathbf{T}_{\boldsymbol{\theta}} \begin{bmatrix} v_{td}^s \\ v_{tq}^s \end{bmatrix} \quad \text{with} \quad \mathbf{T}_{\boldsymbol{\theta}} = \begin{bmatrix} \cos\theta & \sin\theta \\ -\sin\theta & \cos\theta \end{bmatrix} \tag{3-40}$$

$$\begin{bmatrix} \tilde{v}_{td}^c \\ \tilde{v}_{tq}^c \end{bmatrix} = \mathbf{T}_{\boldsymbol{\theta}} \begin{bmatrix} \tilde{v}_{td}^s \\ \tilde{v}_{tq}^s \end{bmatrix} + \begin{bmatrix} V_{tq}^c \\ -V_{td}^c \end{bmatrix} \tilde{\theta} \tag{3-41}$$

$$\begin{cases} \tilde{\theta} = \tilde{v}_{tq}^c G_{PLL} \dfrac{1}{s} \\ G_{PLL} = K_{PLLp} + \dfrac{K_{PLLi}}{s} \end{cases} \tag{3-42}$$

$$\tilde{\theta} = \frac{G_{PLL}}{s + V_{td}^c G_{PLL}} \mathbf{T}_{\boldsymbol{\theta}} \begin{bmatrix} \tilde{v}_{td}^s \\ \tilde{v}_{tq}^s \end{bmatrix} = T_{PLL} \mathbf{T}_{\boldsymbol{\theta}} \begin{bmatrix} \tilde{v}_{td}^s \\ \tilde{v}_{tq}^s \end{bmatrix} \tag{3-43}$$

$$\begin{bmatrix} \tilde{v}_{td}^{c} \\ \tilde{v}_{tq}^{c} \end{bmatrix} = \mathbf{T}_{\theta} \begin{bmatrix} \tilde{v}_{td}^{s} \\ \tilde{v}_{tq}^{s} \end{bmatrix} + T_{PLL} \begin{bmatrix} 0 & V_{tq}^{c} \\ 0 & -V_{td}^{c} \end{bmatrix} \mathbf{T}_{\theta} \begin{bmatrix} \tilde{v}_{td}^{s} \\ \tilde{v}_{tq}^{s} \end{bmatrix} = \mathbf{G}_{\mathbf{vt}} \mathbf{T}_{\theta} \begin{bmatrix} \tilde{v}_{td}^{s} \\ \tilde{v}_{tq}^{s} \end{bmatrix} \tag{3-44}$$

$$\vec{\tilde{v}}_{t}^{\,c} = \mathbf{G}_{\mathbf{vt}} \mathbf{T}_{\theta} \vec{\tilde{v}}_{t}^{\,s} \quad \text{with} \quad \mathbf{G}_{\mathbf{vt}} = \mathbf{I} + T_{PLL} \begin{bmatrix} 0 & V_{tq}^{c} \\ 0 & -V_{td}^{c} \end{bmatrix} \tag{3-45}$$

$$\begin{cases} \vec{\tilde{i}}^{\,c} = \mathbf{T}_{\theta} \vec{\tilde{i}}^{\,s} + \mathbf{G}_{\mathbf{i}} \mathbf{T}_{\theta} \vec{\tilde{v}}_{t}^{\,s} \quad \text{with} \quad \mathbf{G}_{\mathbf{i}} = T_{PLL} \begin{bmatrix} 0 & I_{q}^{c} \\ 0 & -I_{d}^{c} \end{bmatrix} \\ \vec{\tilde{v}}_{c}^{\,c} = \mathbf{T}_{\theta} \vec{\tilde{v}}_{c}^{\,s} + \mathbf{G}_{\mathbf{vc}} \mathbf{T}_{\theta} \vec{\tilde{v}}_{t}^{\,s} \quad \text{with} \quad \mathbf{G}_{\mathbf{vc}} = T_{PLL} \begin{bmatrix} 0 & V_{cq}^{c} \\ 0 & -V_{cd}^{c} \end{bmatrix} \end{cases} \tag{3-46}$$

Then the control block diagram of the current-controlled inverter can be depicted in Figure 3-17.

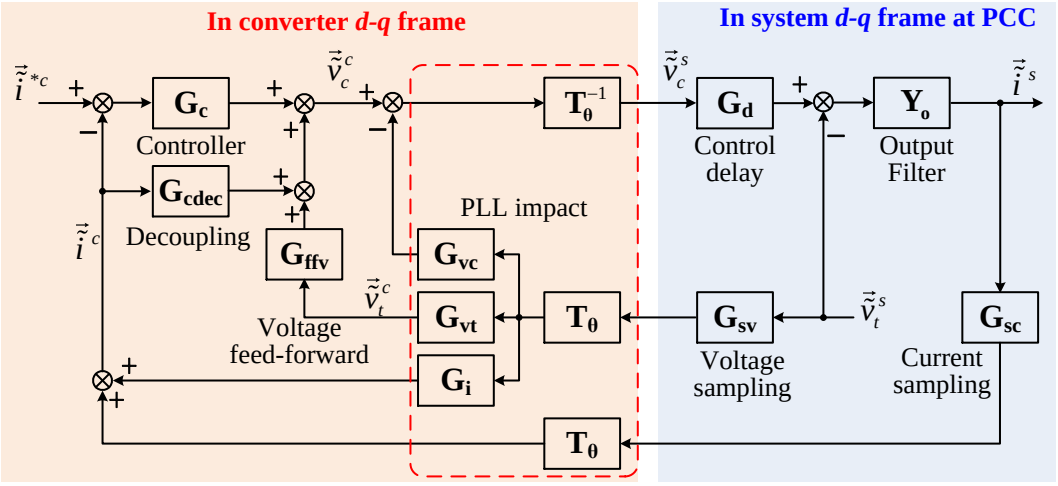

Figure 3-17. Control block diagram of the current-controlled inverter.

$\mathbf{Y_o}$ is the admittance matrix of the inverter output L filter. $\mathbf{G_c}$ represents the proportional plus integral (PI) current controller matrix and $\mathbf{G_{cdec}}$ is the decoupling term. A first-order low-pass filter with the cut-off frequency ω_{ffv} is adopted in the voltage feed-forward transfer function matrix $\mathbf{G_{ffv}}$. The PWM modulation and the computation delay are modelled as a delay component $\mathbf{G_d}$. $\mathbf{G_{sc}}$ and $\mathbf{G_{sv}}$ are the transfer function matrices for current and voltage measurement. The current open-loop gain $\mathbf{T_c}$, closed-loop gain $\mathbf{G_{clc}}$ and output admittance $\mathbf{Y_{oc}}$ in the arbitrary d-q frame can be derived. Figure 3-18 illustrates the Bode plots of $\mathbf{Y_{oc}}$ for the inverter with parameters listed in Table 3-4 and Table 3-5, ω_{ffv}=20×2π rad/s and the output current (I_d =10 A, I_q =0 A) in its own inverter d-q frame, considering three different values of θ (namely, 0 °, 10 ° and 20 °). It can be seen that the inverter terminal voltage angle θ mainly affects the inverter admittances in the low frequency range.

$$\mathbf{Y_o} = \begin{bmatrix} L_f s + R_{Lf} & -\omega_1 L_f \\ \omega_1 L_f & L_f s + R_{Lf} \end{bmatrix}^{-1} \tag{3-47}$$

$$\mathbf{G_c} = \left(K_{cp} + \frac{K_{ci}}{s} \right) \mathbf{I} \tag{3-48}$$

$$\mathbf{G_{cdec}} = \begin{bmatrix} 0 & -\omega_1 L_f \\ \omega_1 L_f & 0 \end{bmatrix} \tag{3-49}$$

$$\mathbf{G_{ffv}} = \frac{1}{1 + s/\omega_{ffv}} \mathbf{I} \tag{3-50}$$

$$\mathbf{G_d} = e^{-T_d s} \mathbf{I}, \quad \mathbf{G_{sc}} = \mathbf{G_{sv}} = e^{-0.5 T_s s} \mathbf{I} \tag{3-51}$$

$$\mathbf{T_c} = \mathbf{Y_o G_d T_\theta^{-1}} \left(\mathbf{G_c} - \mathbf{G_{cdec}} \right) \mathbf{T_\theta G_{sc}} \tag{3-52}$$

$$\mathbf{G_{clc}} = \left(\mathbf{I} + \mathbf{T_c} \right)^{-1} \mathbf{Y_o G_d T_\theta^{-1} G_c} \tag{3-53}$$

$$\mathbf{Y_{oc}} = \left(\mathbf{I} + \mathbf{T_c} \right)^{-1} \mathbf{Y_o} \cdot \left\{ \mathbf{I} - \mathbf{G_d T_\theta^{-1}} \left[\mathbf{G_{ffv} G_{vt}} - \left(\mathbf{G_c} - \mathbf{G_{cdec}} \right) \mathbf{G_i} - \mathbf{G_{vc}} \right] \mathbf{T_\theta G_{sv}} \right\} \tag{3-54}$$

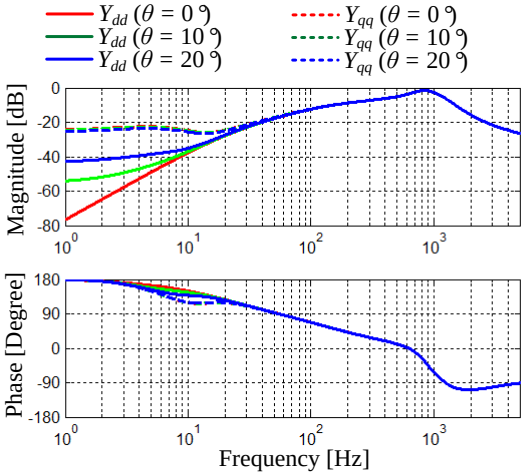

(a)

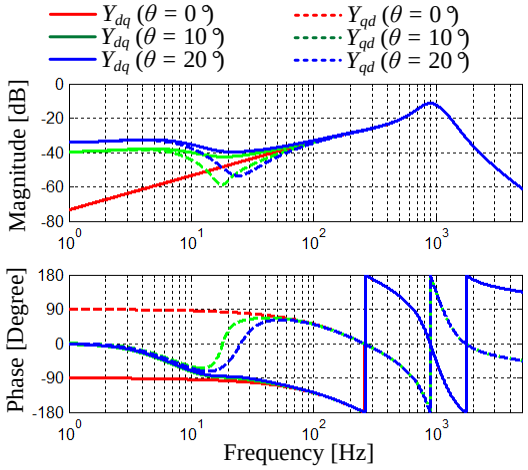

(b)

Figure 3-18. Output admittances of the inverter: (a) Y_{dd}, Y_{qq}; (b) Y_{dq}, Y_{qd}.

Table 3-4. Electrical parameters of the inverter.

Electrical Parameters		**Values**
L filter	L_f	0.575 mH
	R_{Lf}	0.2 Ω
Dc-link voltage	V_{dc}	400 V
Ac voltage base	V_{base}	170 V (phase peak)
Fundamental frequency	ω_1	60×2π rad/s

Table 3-5. Controller parameters of current-controlled inverters.

Controller Parameters		**Values**
Switching frequency	f_s	10 kHz
Switching period	T_s	100 μs
Current controller	K_{cp}	2.6
	K_{ci}	2275
PLL	K_{PLLp}	0.312
	K_{PLLi}	5.294
Delay time	T_d	150 μs

3.5 D-Q Admittance of Current-Controlled Inverters with Static Load Emulation

The output admittance of the current-controlled inverters with static load emulation in the *d-q* frame is modeled in this section to assist in the impedance-based stability analysis of the inverter-based systems in CURENT's Hardware Testbed.

The mathematical equations of ZIP loads are expressed as (3-55) and (3-56), considering the effects of minor grid voltage fluctuation and frequency variation. P_0, Q_0 and V_0 represent the real and reactive power base values and nominal grid voltage value, respectively. P_{ZIP} and Q_{ZIP} represent actual real and reactive power values of the ZIP load, respectively, in terms of the load voltage v and grid frequency deviation Δf. The coefficients (k_{p1}, k_{p2}, k_{p3}) and (k_{q1}, k_{q2}, k_{q3}) are for constant impedance (Z) portions, constant current (I) portions and constant power (P) portions for voltage-dependent real and reactive power, respectively, while the coefficients k_{pf} and k_{qf} stand for the frequency-dependent characteristics, which are neglected in the following admittance modeling considering the small frequency variation in the steady-state.

$$P_{ZIP} = P_0 \cdot \left[k_{p1}\left(\frac{v}{V_0}\right)^2 + k_{p2}\left(\frac{v}{V_0}\right) + k_{p3} \right]\left(1 + k_{pf}\Delta f\right) \tag{3-55}$$

$$Q_{ZIP} = Q_0 \cdot \left[k_{q1}\left(\frac{v}{V_0}\right)^2 + k_{q2}\left(\frac{v}{V_0}\right) + k_{q3} \right]\left(1 + k_{qf}\Delta f\right) \tag{3-56}$$

Taking into account the definition of the current direction as flowing out of the inverter as shown in Figure 3-1, the values of P_0, Q_0, P_{ZIP} and Q_{ZIP} are negative for power assumption and positive for power generation from the load. According to the power equations in terms of the load currents and voltages in the *d-q* frame as described in (3-57), the expression of load currents

can be derived with the power and voltages as the inputs, as shown in (3-58). By applying small perturbation to (3-58), the linearized small-signal model can be achieved as in (3-59), where $\mathbf{Y_{ZIP}}$ and $\mathbf{G_{ZIP}}$ are the *d-q* admittance matrix and the current gain matrix of the ZIP load, respectively, and they are functions of P_0, Q_0, V_0 as well as steady-state voltages (V_d and V_q) and currents (I_d and I_q) in the *d-q* frame. Four elements of $\mathbf{Y_{ZIP}}$ are expressed in (3-60), (3-61), (3-62) and (3-63), respectively.

$$\begin{bmatrix} P_{ZIP} \\ Q_{ZIP} \end{bmatrix} = \frac{3}{2}\begin{bmatrix} v_d & v_q \\ v_q & -v_d \end{bmatrix}\begin{bmatrix} i_d \\ i_q \end{bmatrix} \tag{3-57}$$

$$\begin{bmatrix} i_d \\ i_q \end{bmatrix} = \frac{2}{3}\cdot\frac{1}{v_d^2+v_q^2}\begin{bmatrix} v_d & v_q \\ v_q & -v_d \end{bmatrix}\begin{bmatrix} P_{ZIP} \\ Q_{ZIP} \end{bmatrix} \tag{3-58}$$

$$\begin{bmatrix} \tilde{i}_d \\ \tilde{i}_q \end{bmatrix} = \mathbf{Y_{ZIP}}\begin{bmatrix} \tilde{v}_d \\ \tilde{v}_q \end{bmatrix} + \mathbf{G_{ZIP}}\begin{bmatrix} \tilde{P}_0 \\ \tilde{Q}_0 \end{bmatrix}, \quad \mathbf{Y_{ZIP}} = \begin{bmatrix} Y_{ZIPdd} & Y_{ZIPdq} \\ Y_{ZIPqd} & Y_{ZIPqq} \end{bmatrix} \tag{3-59}$$

$$Y_{ZIPdd} = \frac{2}{3}P_0\cdot\left[\frac{k_{p1}}{V_0^2} + \frac{k_{p2}V_0V_q^2\sqrt{V_d^2+V_q^2} + k_{p3}V_0^2\left(V_q^2-V_d^2\right)}{V_0^2\left(V_d^2+V_q^2\right)^2}\right] - \frac{2}{3}Q_0\cdot\frac{k_{q2}V_0V_dV_q\sqrt{V_d^2+V_q^2} + 2k_{q3}V_0^2V_dV_q}{V_0^2\left(V_d^2+V_q^2\right)^2} \tag{3-60}$$

$$Y_{ZIPdq} = -\frac{2}{3}P_0\cdot\frac{k_{p2}V_0V_dV_q\sqrt{V_d^2+V_q^2} + 2k_{p3}V_0^2V_dV_q}{V_0^2\left(V_d^2+V_q^2\right)^2} + \frac{2}{3}Q_0\cdot\left[\frac{k_{q1}}{V_0^2} + \frac{k_{q2}V_0V_d^2\sqrt{V_d^2+V_q^2} + k_{q3}V_0^2\left(V_d^2-V_q^2\right)}{V_0^2\left(V_d^2+V_q^2\right)^2}\right] \tag{3-61}$$

$$Y_{ZIPqd} = -\frac{2}{3}P_0\cdot\frac{k_{p2}V_0V_dV_q\sqrt{V_d^2+V_q^2} + 2k_{p3}V_0^2V_dV_q}{V_0^2\left(V_d^2+V_q^2\right)^2} - \frac{2}{3}Q_0\cdot\left[\frac{k_{q1}}{V_0^2} + \frac{k_{q2}V_0V_q^2\sqrt{V_d^2+V_q^2} + k_{q3}V_0^2\left(V_q^2-V_d^2\right)}{V_0^2\left(V_d^2+V_q^2\right)^2}\right] \tag{3-62}$$

$$Y_{ZIPqq} = \frac{2}{3} P_0 \cdot \left[\frac{k_{p1}}{V_0^2} + \frac{k_{p2} V_0 V_d^2 \sqrt{V_d^2 + V_q^2} + k_{p3} V_0^2 \left(V_d^2 - V_q^2 \right)}{V_0^2 \left(V_d^2 + V_q^2 \right)^2} \right] + \frac{2}{3} Q_0 \cdot \frac{k_{q2} V_0 V_d V_q \sqrt{V_d^2 + V_q^2} + 2 k_{q3} V_0^2 V_d V_q}{V_0^2 \left(V_d^2 + V_q^2 \right)^2} \quad (3\text{-}63)$$

In the implementation of the static ZIP load emulation, the measured and filtered inverter terminal voltage vector $\tilde{\vec{v}}^c$ in the *d-q* domain and the external real and reactive load power commands P_0 and Q_0 are used as the inputs to the ZIP load emulation model. The output current vector of the ZIP load emulation is filtered through a first-order low pass filter $\mathbf{G_{fZIP}}$ as expressed in (3-64) with the cut-off frequency ω_{fZIP}, and the filter current vector is set as the inverter current reference $\tilde{\vec{i}}^{*c}$, which will be achieved by the inner current control loop. Figure 3-19 depicts the block diagram of the control loop with ZIP load emulation for the current-controlled three-phase inverter in the common system *d-q* frame. Consequently, the *d-q* admittance of a current-controlled inverter with static ZIP load emulation can be derived as (3-65), according to Figure 3-19. The total model of the inverter with ZIP load emulation can be expressed as (3-66).

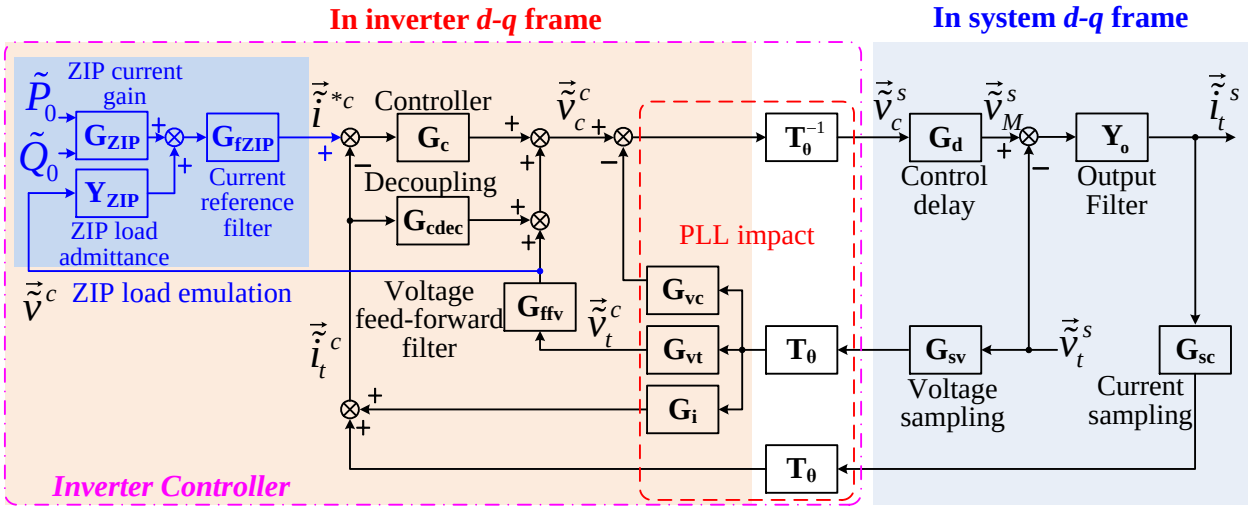

Figure 3-19. Control block diagram of the current-controlled inverter with ZIP load emulation.

$$\mathbf{G_{fZIP}} = \frac{1}{1 + s/\omega_{fZIP}}\mathbf{I} \tag{3-64}$$

$$\mathbf{Y_{oc}} = \left(\mathbf{I} + \mathbf{T_c}\right)^{-1}\mathbf{Y_o}\cdot\left\{\mathbf{I} - \mathbf{G_d}\mathbf{T_\theta^{-1}}\left[\left(\mathbf{I} + \mathbf{G_c}\mathbf{G_{fZIP}}\mathbf{Y_{ZIP}}\right)\mathbf{G_{ffv}}\mathbf{G_{vt}} - \left(\mathbf{G_c} - \mathbf{G_{cdec}}\right)\mathbf{G_i} - \mathbf{G_{vc}}\right]\mathbf{T_\theta}\mathbf{G_{sv}}\right\} \tag{3-65}$$

$$\vec{\tilde{i}}_t^{\,s} = \mathbf{G_{clc}}\left(\mathbf{G_{fZIP}}\mathbf{G_{ZIP}}\begin{bmatrix}\tilde{P}_0 & \tilde{Q}_0\end{bmatrix}^{\mathrm{T}}\right) - \mathbf{Y_{oc}}\vec{\tilde{v}}_t^{\,s} \tag{3-66}$$

The electrical and control parameters of the current-controlled inverter are shown in Table 3-1 and Table 3-2. Assume the inverter terminal voltage magnitude is 49.3 V and the angle difference between the inverter terminal *d-q* frame and the system common *d-q* frame is −22.4 °. With the parameters of the ZIP load emulation as listed in Table 3-6 and load power commands (P_0 = −1393.1 W, Q_0 = 481.7 Var) as well as the voltage base V_0 = 50 V, the steady-state values of current and voltage are expressed in (3-67), and the admittance of the ZIP load can be calculated as (3-68), and the Bode plots of the inverter output *d-q* admittance in both the inverter terminal *d-q* frame and the common system *d-q* frame are illustrated in Figure 3-20. The Bode plot of the *d-q* admittance of the inverter without the ZIP load emulation but with the equivalent current reference as expressed in (3-69) in the inverter terminal *d-q* frame, is also drawn in Figure 3-20. The ZIP load emulation mainly changes the *d-q* admittance below 200 Hz.

$$\begin{bmatrix}V_d, V_q\end{bmatrix}^{\mathrm{T}} = \begin{bmatrix}49.3\,\mathrm{V}, 0\,\mathrm{V}\end{bmatrix}^{\mathrm{T}};\quad \begin{bmatrix}I_d, I_q\end{bmatrix}^{\mathrm{T}} = \begin{bmatrix}-18.7\,\mathrm{A}, -6.5\,\mathrm{A}\end{bmatrix}^{\mathrm{T}} \tag{3-67}$$

$$\mathbf{Y_{ZIP}} = \begin{bmatrix}0.155 & 0.131\\ 0.054 & -0.379\end{bmatrix} \tag{3-68}$$

$$\begin{bmatrix}I_d^*, I_q^*\end{bmatrix}^{\mathrm{T}} = \begin{bmatrix}-18.7\,\mathrm{A}, -6.5\,\mathrm{A}\end{bmatrix}^{\mathrm{T}} \tag{3-69}$$

Table 3-6. Parameters of ZIP load emulation.

Parameters	Values	Parameters	Values
k_{p1}	0.2	k_{q1}	0.2
k_{p2}	0.2	k_{q2}	0.2
k_{p3}	0.6	k_{q3}	0.6
k_{pf}	0	k_{qf}	0
ω_{fZIP}	300×2π rad/s		

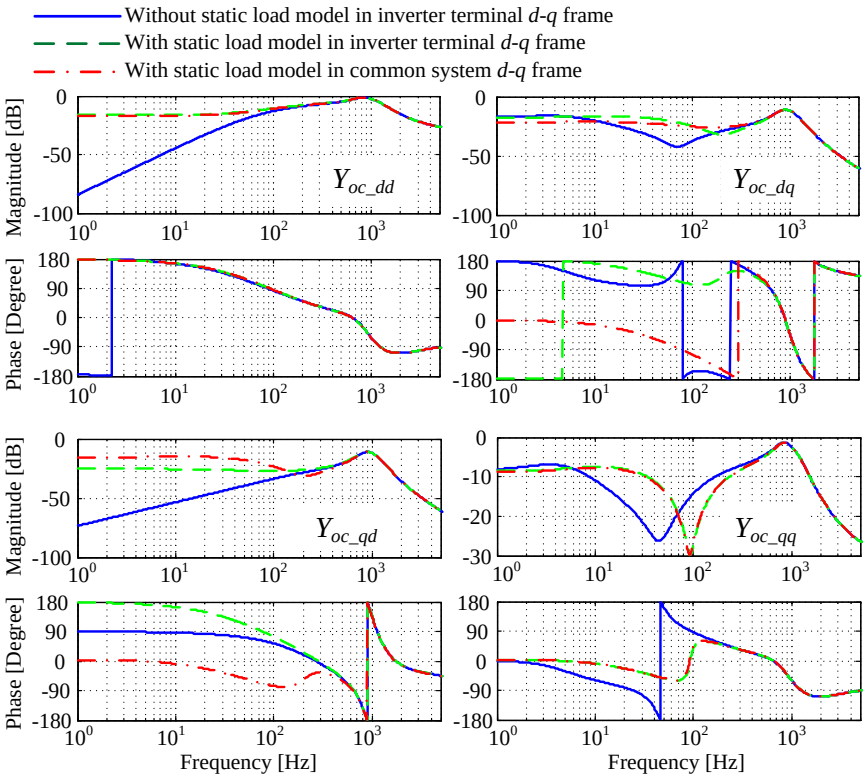

Figure 3-20. Bode plot of *d-q* admittance of the inverter with ZIP load emulation.

3.6 D-Q Impedance of Voltage-Controlled Inverters with Generator Emulation

The synchronous generator (SG) emulator in CURENT's Hardware Testbed is developed using a voltage-controlled three-phase inverter. The *d-q* impedance of a voltage controlled-inverter with the generator emulation has been analyzed in [8], [9], and thus it is briefly described in this section, in order to assist in the impedance-based stability analysis of the inverter-based two-area power system implemented in the power grid emulation platform.

The fourth-order SG model in the generator rotor reference *d-q* frame with the quadrature axis leading the direct axis by 90 degrees, which is widely used in large-scale power system calculation, are expressed in (3-70), where i_d, i_q, v_d and v_q are SG stator currents and terminal voltages, respectively, E_{fg} is the field voltage, R_a is the armature resistance per phase, X_d and X_q are self-reactance, X'_d and X'_q are transient reactance, T'_{d0} and T'_{q0} are transient open-circuit time constants, $\mathbf{G_{gf}}$ is the voltage gain and $\mathbf{Z_g}$ is the generator output impedance.

$$\begin{bmatrix} v_d \\ v_q \end{bmatrix} = \mathbf{G_{gf}} E_{fd} - \mathbf{Z_g} \begin{bmatrix} i_d \\ i_q \end{bmatrix} = \begin{bmatrix} 0 \\ \dfrac{1}{T'_{d0}s+1} \end{bmatrix} E_{fd} - \begin{bmatrix} R_a & -\dfrac{X'_q T'_{q0} s + X_q}{T'_{q0}s+1} \\ \dfrac{X'_d T'_{d0} s + X_d}{T'_{d0}s+1} & R_a \end{bmatrix} \begin{bmatrix} i_d \\ i_q \end{bmatrix} \tag{3-70}$$

It should be noted that the generator emulation also includes governor, droop control, automatic generation control (AGC), power system stabilizer (PSS), and excitation system with automatic voltage regulator (AVR) [8], [9]. The bandwidths of these control loops are usually very low (below 10 Hz). The focus of this study is on the small-signal instability issues due to the interactions among inverters and passive connection networks in the power grid emulation platform, instead of the small-disturbance rotor angle stability or voltage stability of the emulated power system. Considering the frequency-scale separation among system modes [45] and mode

reduction techniques [49], the generator mechanical model and generator control loops are neglected in the *d-q* impedance modeling of inverters with SG emulation. The system fundamental frequency ω_1 is assumed as constant.

The control block diagram of the voltage-controlled inverter with the fourth-order SG emulation is depicted in Figure 3-21. A first-order LPF $\mathbf{G_{fcg}}$ with the cut-off frequency ω_{fcg}, as expressed in (3-71), is applied to the current input of the SG electrical model. $\mathbf{G_{fv}}$, $\mathbf{G_{fc}}$ and $\mathbf{G_{ffc}}$ are the voltage filter, current filter and current feed-forward gain, respectively, as expressed in (3-72). $\mathbf{G_v}$, $\mathbf{G_{vdec}}$, $\mathbf{G_{Vo}}$ and $\mathbf{Z_o}$ are shown in (3-73). The open-loop gain $\mathbf{T_c}$ and closed-loop gain $\mathbf{G_{clv}}$ of the voltage-control loop are expressed in (3-74) and (3-75), respectively. The *d-q* output impedances of the voltage-controlled inverter without generator emulation ($\mathbf{Z_v}$) and with generator emulation ($\mathbf{Z_{ov}}$) in the common system *d-q* frame are expressed in (3-76) and (3-77), respectively. The total model of the inverter with generator emulation is expressed in (3-78).

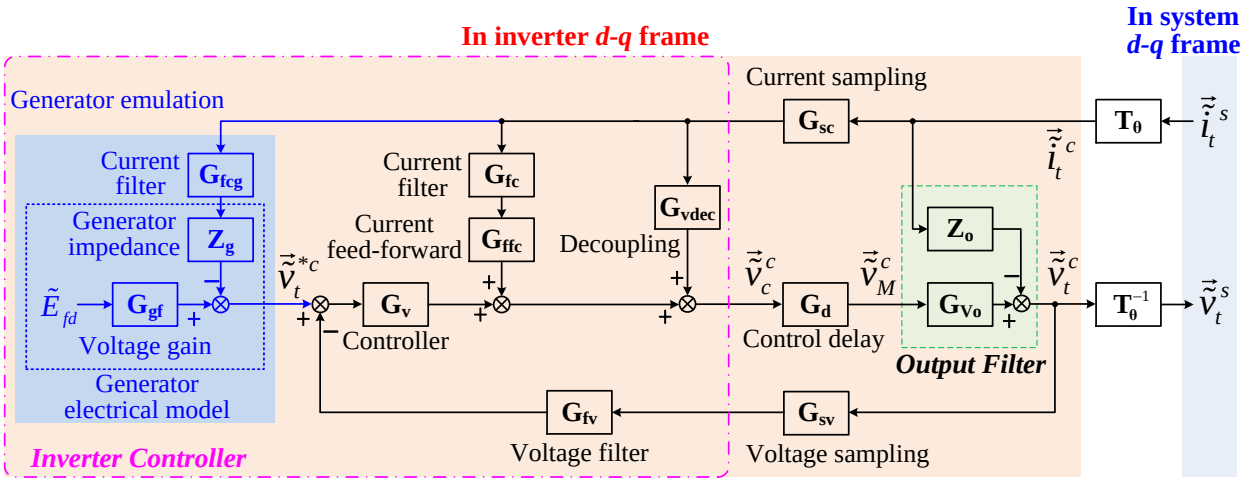

Figure 3-21. Control block diagram of the voltage-controlled inverter with generator emulation.

$$\mathbf{G_{fcg}} = \frac{1}{1 + s/\omega_{fcg}}\mathbf{I} \tag{3-71}$$

$$\mathbf{G_{fv}} = \frac{\omega_{fv}}{s + \omega_{fv}}\mathbf{I}, \quad \mathbf{G_{fc}} = \frac{\omega_{fc}}{s + \omega_{fc}}\mathbf{I}, \quad \mathbf{G_{ffc}} = L_f s\mathbf{I} \tag{3-72}$$

$$\mathbf{G_v} = \left(K_{vp} + K_{vi}/s\right)\mathbf{I}, \quad \mathbf{G_{vdec}} = \mathbf{G_{cdec}}, \quad \mathbf{G_{Vo}} = \mathbf{I}, \quad \mathbf{Z_o} = \mathbf{Y_o^{-1}} \tag{3-73}$$

$$\mathbf{T_v} = \mathbf{G_{Vo}G_dG_vG_{fv}G_{sv}} \tag{3-74}$$

$$\mathbf{G_{clv}} = \mathbf{T_\theta^{-1}}\left(\mathbf{I} + \mathbf{T_v}\right)^{-1}\mathbf{G_{Vo}G_dG_v} \tag{3-75}$$

$$\mathbf{Z_v} = \mathbf{T_\theta^{-1}}\left(\mathbf{I} + \mathbf{T_v}\right)^{-1}\left[\mathbf{Z_o} - \mathbf{G_{Vo}G_d}\left(\mathbf{G_{ffc}G_{fc}} + \mathbf{G_{vdec}}\right)\mathbf{G_{sc}}\right]\mathbf{T_\theta} \tag{3-76}$$

$$\mathbf{Z_{ov}} = \mathbf{Z_v} + \mathbf{G_{clv}Z_gG_{fcg}G_{sc}T_\theta} \tag{3-77}$$

$$\vec{\tilde{v}}_t^{\,s} = \mathbf{G_{clv}}\left(\mathbf{G_{gf}}\tilde{E}_{fd}\right) - \mathbf{Z_{ov}}\vec{\tilde{i}}_t^{\,s} \tag{3-78}$$

The parameters of the scaled-down emulated generator with the same per unit (p.u.) values as those in the original two-area system [42] are listed in Table 3-7. The parameters of the voltage-controlled inverters are listed in Table 3-1 and Table 3-3. The Bode plots of *d*-*q* output impedances of the voltage-controlled inverter without generator emulation ($\mathbf{Z_v}$) and with generator emulation ($\mathbf{Z_{ov}}$) as well as the generator impedance ($\mathbf{Z_g}$) are depicted in Figure 3-22. As observed, the output impedance ($\mathbf{Z_{ov}}$) of the generator emulator can track the generator impedance in the low frequency range.

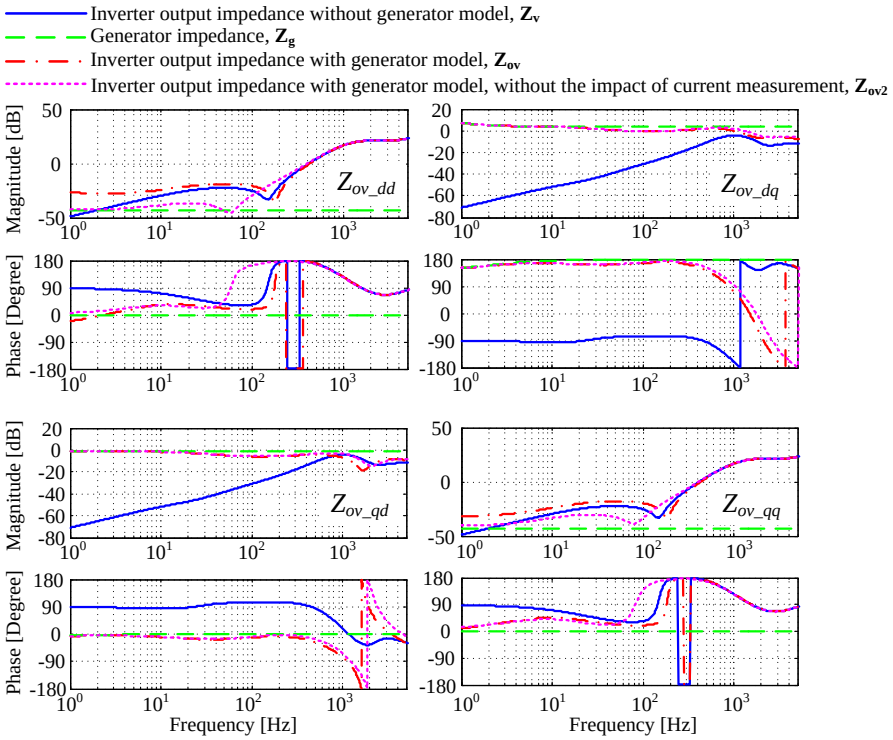

Figure 3-22. Bode plot of *d-q* impedance of the inverter with generator emulation.

Table 3-7. Parameters of generator emulation

Parameters	**Values**	**Parameters**	**Values**
Original power P_{gen}	900 MVA	R_a	0.0025 p.u.
Original voltage V_{gen}	20 kV	X_d	1.8 p.u.
f_{base}	60 Hz	X_q	1.7 p.u.
Rescaled power P_{gen}	1302 W	X'_d	0.3 p.u.
Rescaled voltage V_{gen}	61.2 V	X'_q	0.55 p.u.
Impedance base Z_{base}	2.88 Ω	T'_{d0}	8 s
H	6.5 p.u. for G1, G2 6.175 p.u. for G3, G4	T'_{q0}	0.4 s
		ω_{fcg}	1000×2π rad/s

There are some minor discrepancies between ($\mathbf{Z_{ov}}$) and ($\mathbf{Z_g}$) in the *d-d* channel and the *q-q* channel, due to the delay effect introduced by the current measurement $\mathbf{G_{sc}}$. The *d-q* output impedance of the voltage-controlled inverter with generator emulation ($\mathbf{Z_{ov2}}$) neglecting the impact of the current measurement is also plotted in Figure 3-22. It can be seen that ($\mathbf{Z_{ov2}}$) can track ($\mathbf{Z_g}$) very well in the *d-d* channel and the *q-q* channel.

3.7 Conclusion

The sequence-admittance model of current-controlled three-phase inverters is improved, considering the voltage feed-forward control in the *d-q* domain and the dead time effect. The sequence-impedance model of voltage-controlled three-phase inverters is also developed. Sequence impedance models can facilitate the harmonic stability analysis of three-phase inverter-based ac systems. However, in order to analyze the low-frequency oscillation problems in three-phase inverter-based ac system, the *d-q* impedances in the synchronous rotating *d-q* frame are preferred. Since the system model should be established in a common system *d-q* frame, the *d-q* admittance model of current-controlled inverters in an arbitrary *d-q* frame is developed. In addition, the *d-q* admittance model of current-controlled inverters with static load emulation and the *d-q* impedance model of voltage-controlled inverters with generator emulation are presented.

4 Sequence Impedance Measurement of Three-Phase Inverters Using a Paralleled Structure

For the only consideration of the impedance measurement of three-phase inverters, this chapter proposes a sequence impedance measurement method by using another inverter connected in a paralleled structure with common-dc and common-ac sides. The measurement setup is simple, because the inverter as the measurement unit not only injects perturbations but also serves as the voltage source or the current load at the fundamental frequency to create the desired operating conditions for the inverter under test. Several issues about this measurement setup are discussed and solved, including the zero-sequence circulating current and the discrepancy due to the voltage drop on the output filter. Simulation and experimental results demonstrate the effectiveness of this approach.

4.1 Sequence Impedance Measurement

4.1.1 Impedance Measurement Setup

In order to measure the impedance of inverters in an easy way without the need of additional equipment or a complicated setup, this chapter proposes to use another inverter with the same design or similar power rating, which can be easily obtained in the laboratory, to measure the impedance of the inverter under test, by connecting these two inverters in parallel with common-dc and common-ac sides [8], [129]. The impedance measurement setup is depicted in Figure 4-1. The inverter as the measurement unit not only serves as the power amplifier of the injection signal for impedance measurement, but also serves as the voltage source (for current-controlled inverter under test) or current load (for voltage-controlled inverter under test) at the fundamental

frequency to run at the desired operating point. This chapter focuses on the sequence admittance measurement of the current-controlled inverters, and thus the inverter as the measurement unit is controlled as a voltage source.

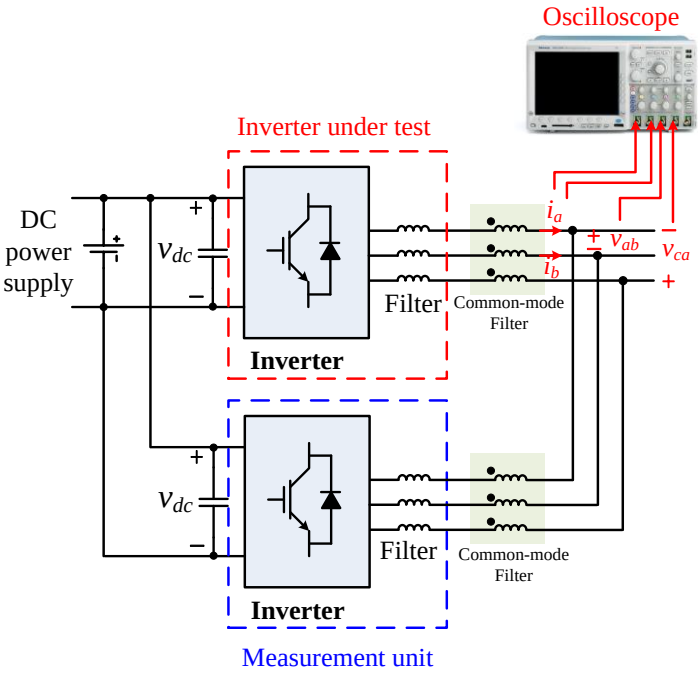

Figure 4-1. Impedance measurement setup with a paralleled structure.

Due to the limited switching frequency f_s (e.g. 10 kHz) and limited control bandwidth of the measurement unit, open-loop control is used and the injection signal $V^*_{t\_inj}$ is directly added to the fundamental voltage reference V^*_{t1}, as shown in Figure 4-2. The identifiable frequency can be up to the half of the switching frequency (e.g. 5 kHz).

An oscilloscope is adopted to acquire the response data of the output phase currents and the

line-to-line terminal voltages of the inverter under test during the measurement process, and the sampling rate is set as 1 MS/s. The data from the oscilloscope is processed offline in MATLAB using FFT to get the impedance or admittance.

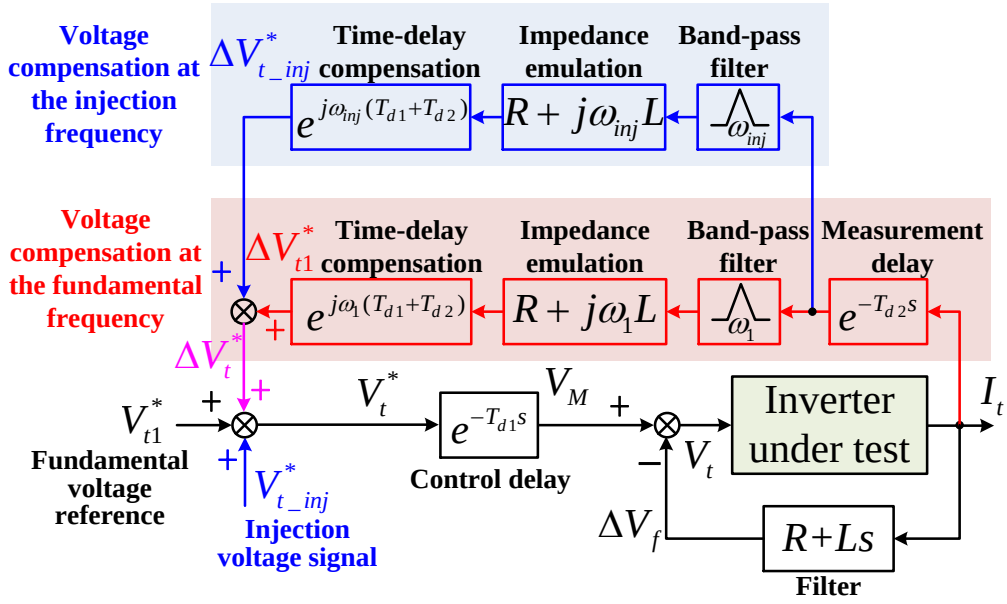

Figure 4-2. The open-loop voltage control with voltage compensation in the inverter as the measurement unit.

4.1.2 Injection and Sequence Impedance Measurement

The relationships between the phase components and the sequence components of both the current and the voltage are expressed in (4-1) and (4-2), where $\mathbf{a} = e^{j2\pi/3}$. For a balanced three-phase ac system, there are no couplings among sequence components, and each sequence impedance can be calculated independently, as shown in (4-3).

$$\begin{bmatrix} \mathbf{I}_0 \\ \mathbf{I}_p \\ \mathbf{I}_n \end{bmatrix} = \frac{1}{3}\begin{bmatrix} 1 & 1 & 1 \\ 1 & \mathbf{a} & \mathbf{a}^2 \\ 1 & \mathbf{a}^2 & \mathbf{a} \end{bmatrix}\begin{bmatrix} \mathbf{I}_a \\ \mathbf{I}_b \\ \mathbf{I}_c \end{bmatrix} = \mathbf{A}\begin{bmatrix} \mathbf{I}_a \\ \mathbf{I}_b \\ \mathbf{I}_c \end{bmatrix} \tag{4-1}$$

$$\begin{bmatrix} \mathbf{V}_0 \\ \mathbf{V}_p \\ \mathbf{V}_n \end{bmatrix} = \mathbf{A}\cdot\frac{1}{3}\begin{bmatrix} 1 & 0 & -1 \\ -1 & 1 & 0 \\ 0 & -1 & 1 \end{bmatrix}\begin{bmatrix} \mathbf{V}_{ab} \\ \mathbf{V}_{bc} \\ \mathbf{V}_{ca} \end{bmatrix} \tag{4-2}$$

$$\begin{bmatrix} \mathbf{Z}_0 \\ \mathbf{Z}_p \\ \mathbf{Z}_n \end{bmatrix} = \begin{bmatrix} \mathbf{V}_0/\mathbf{I}_0 & 0 & 0 \\ 0 & \mathbf{V}_p/\mathbf{I}_p & 0 \\ 0 & 0 & \mathbf{V}_n/\mathbf{I}_n \end{bmatrix} \tag{4-3}$$

The sinusoidal signal injection method is used here, due to its higher noise immunity over wide-band signal injection methods, such as impulse signal, binary sequence signal and chirp signal. By using another inverter as the measurement unit, the positive sequence voltage disturbance signals in (4-4) can be injected solely for positive sequence impedance measurement, and similarly the negative sequence voltage disturbance signals in (4-5) can be injected solely for the negative sequence impedance measurement.

Further, if there is no zero-sequence current during either the positive sequence injection or the negative sequence injection, then the positive/negative sequence impedance or admittance is equal to the phase-A impedance or admittance, as shown in (4-6). That means only phase-A current measurement (i_a) along with two line-to-line voltage measurements (v_{ab}, v_{ca}), which are used for phase-A voltage calculation, are necessary to identify the sequence impedance or admittance.

$$\begin{cases} v_a(t) = V_1\cos(\omega_1 t) + V_p\cos(\omega_{inj} t) \\ v_b(t) = V_1\cos(\omega_1 t - \frac{2\pi}{3}) + V_p\cos(\omega_{inj} t - \frac{2\pi}{3}) \\ v_c(t) = V_1\cos(\omega_1 t + \frac{2\pi}{3}) + V_p\cos(\omega_{inj} t + \frac{2\pi}{3}) \end{cases} \quad (4\text{-}4)$$

$$\begin{cases} v_a(t) = V_1\cos(\omega_1 t) + V_n\cos(\omega_{inj} t) \\ v_b(t) = V_1\cos(\omega_1 t - \frac{2\pi}{3}) + V_n\cos(\omega_{inj} t + \frac{2\pi}{3}) \\ v_c(t) = V_1\cos(\omega_1 t + \frac{2\pi}{3}) + V_n\cos(\omega_{inj} t - \frac{2\pi}{3}) \end{cases} \quad (4\text{-}5)$$

$$\begin{cases} Y_p(j\omega_{inj}) = \dfrac{I_a(j\omega_{inj})}{V_a(j\omega_{inj})}, & \text{for pos-seq} \\ Y_n(j\omega_{inj}) = \dfrac{I_a(j\omega_{inj})}{V_a(j\omega_{inj})}, & \text{for neg-seq} \end{cases} \quad (4\text{-}6)$$

4.1.3 Zero-sequence Circulating Current Reduction

There are different types of unnecessary circulating current in this common-dc and common-ac paralleled structure [129], which will influence the impedance measurement. The switching period circulating current can be minimized by synchronizing the carrier waves of the inverters. The dc component of the zero-sequence circulating current can be mitigated by the zero-sequence current control with a PI controller. The third order and other low order harmonic zero-sequence circulating current can be reduced by inserting common-mode (CM) filters in series with the original inverter filters, as shown in Figure 4-1. The CM filters can be regarded as large zero-sequence impedances in the current path between two inverters, and thus help mitigating the zero-sequence current. The parameter L_{cm} of the CM filters is 17.73 mH. The

injected sinusoidal voltage signals at the measurement frequencies f_{inj} will also induce additional frequency components in the zero-sequence circulating current. However, it is observed that the frequencies of the additional components are ($f_{inj} - f_1$) and ($f_{sw} - f_{inj} + f_1$), so the magnitude of the phase current and inverter admittance at the injection frequency f_{inj} will not be influenced. For instance, when the injection frequency is f_{inj} = 1000 Hz, two frequency components of 940 Hz and 9060 Hz show up in the spectrum of the zero-sequence current, according to the simulation results as shown in Figure 4-3. The CM filters can also reduce the magnitudes of these two frequency components, compared with the spectrum without using the CM filters. Therefore, they will not cause additional difference between the phase admittance measurement result and the sequence admittance measurement result. For example, based on the simulation results as shown in Figure 4-4, the differences between the phase admittances (Y_a, Y_b and Y_c) and the positive sequence admittance (Y_p) are very small with above zero-sequence circulating current reduction methods, so the phase admittance (Y_a) can be measured to represent the sequence admittances (Y_p and Y_n).

4.1.4 Open Loop Control with Voltage Compensation

Since open-loop control of the measurement unit is used for impedance measurement, there is a voltage drop on the output filter of the measurement unit. It will change the fundamental terminal voltage, which makes the inverter under test away from the desired operating point. And it will also cause the injected voltage amplitudes of the terminal voltage different for different injection frequencies. Therefore, a voltage compensation method is proposed here, by adding compensation voltage components at both the fundamental frequency (ΔV_{t1}^*) and the injection frequency ($\Delta V_{t\_inj}^*$) to the open-loop voltage reference (V_t^*) as shown in Figure 4-2, where L and

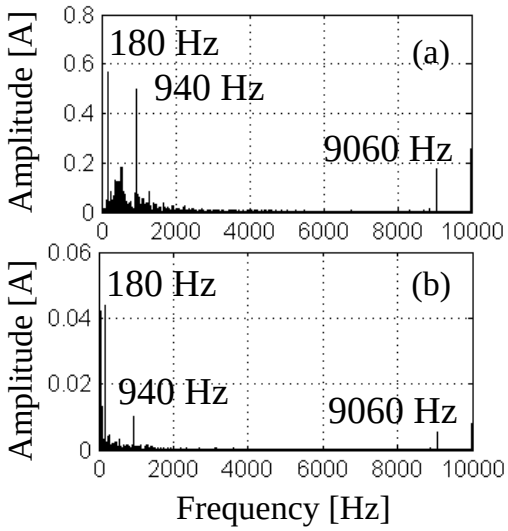

Figure 4-3. Spectrum of zero-sequence current in simulation: (a) without and (b) with CM filters.

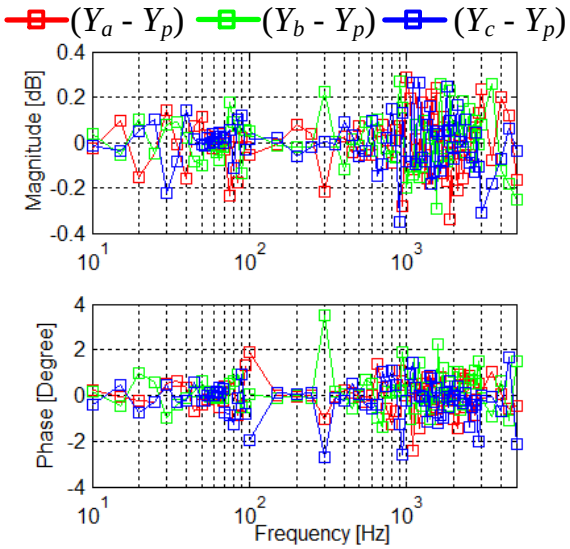

Figure 4-4. Difference between the simulation measurement results of phase admittances (Y_a, Y_b and Y_c) and the simulation measurement result of positive-sequence admittance (Y_p).

R are the inductance and resistance of the *L* filter of the inverter as the measurement unit.

Fundamental and injection-frequency components of the output current of the measurement unit are extracted based on the multiple reference frame (MRF)-based band-pass filters [130]. The impedance emulation is implemented by the multiplication of space vectors [131]. The time-delay compensation is achieved through a frequency-dependent constant phase lead during the *d*-*q* to *α*-*β* transformation [132]. For example, according to the simulation results of the terminal voltage of the inverter under test during the frequency injection from 100 Hz to 5 kHz as shown in Figure 4-5, without the voltage compensation the fundamental terminal voltage is away from the desired value (50 V), while by only enabling the voltage compensation at the fundamental frequency, the terminal voltage can be controlled to be the desired value during the injection.

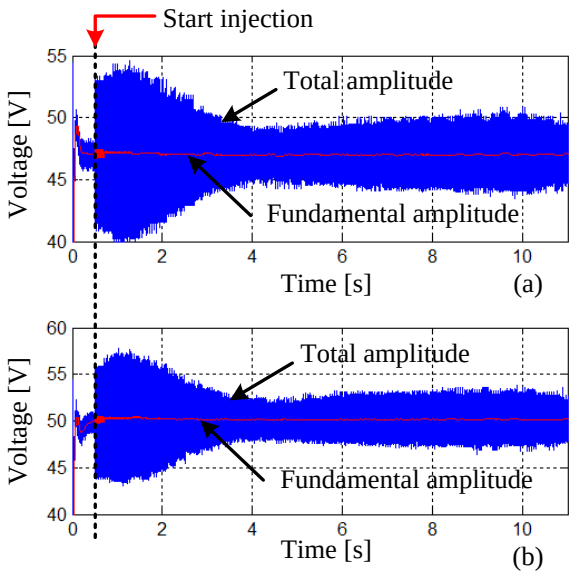

Figure 4-5. Effect of the voltage compensation at the fundamental frequency: (a) without and (b) with compensation.

4.2 Practical Considerations

A. Fundamental frequency component and background harmonics

Since the inverter under test is running under a certain operating condition during the admittance measurement process, if the injection frequency is the fundamental frequency, the injected voltage and the current response cannot be differentiated from the operating positive-sequence voltage and current at the fundamental frequency [83]. Therefore, the fundamental frequency is omitted, and the sequence admittances at the fundamental frequency can be approximately interpolated by using the measurement results at the nearby frequency points. Because the additional ac source, such as power supply and utility grid, or ac load banks are not needed in the proposed measurement setup, the proposed method is not obviously affected by the background harmonic issue.

B. Level of injection and selection of dc-link voltage

To avoid deviation from the required operating condition during the measurement process, the injected voltage magnitude should not be too large. The injected voltage magnitude is selected as 10% of the normal operating voltage (50 V) for both the simulation and the experiments. As for compensating the impact of the output filter of the measurement unit, for simplicity, the voltage compensation at the injection frequency is not adopted in the experiments, while the injected voltage magnitude is simply increased to 30% for high frequency injection (above 2 kHz).

Because both the normal operating voltage at the fundamental frequency and the injected voltage for admittance measurement are provided by the paralleled inverter with a common dc-link, the dc-link voltage should be high enough for the measurement unit to generate the required

voltage V_t^* as shown in Figure 4-1. The dc-link voltage is increased from the normal value 130 V as listed in Table 3-1 to 160 V during the measurement process. In addition, according to the analysis in 3.1, the dc-link voltage value does not affect the sequence admittances of the inverter under test, except through the dead time effect.

C. Period selection of the injected signals

In this experimental setup, the currents and voltages are measured by probes and the measurement data is acquired through an oscilloscope, the data precision of which is usually limited. Therefore, multiple periods of the sinusoidal signal at each injection frequency are used to improve the measurement accuracy. By also considering the FFT calculation accuracy, in the simulation and experiments, 1 second of signal injection is used for each frequency point in the range of [10 Hz, 95 Hz], while 0.2 seconds of signal injection is used for each frequency point in the range of [100 Hz, 5 kHz].

D. Measurement of coupled sequence impedances

In the above description of the proposed sequence impedance measurement method, only uncoupled sequence impedance measurement is considered. However, this proposed measurement setup can be extended to measure the coupled sequence impedances as express in (4-7). At least two different tests are required to measure the two-by-two impedance matrix [83]. Therefore, the inverter as the measurement unit can inject one positive sequence signal and another negative sequence signal, or it can inject two sets of unbalanced voltage signals. In this case, assuming the zero-sequence current can also be mitigated, two phase currents instead of one should be measured in addition to the measurements of two line-to-line voltages.

$$\begin{bmatrix} \mathbf{V}_p \\ \mathbf{V}_n \end{bmatrix} = \begin{bmatrix} \mathbf{Z}_p & \mathbf{Z}_{pn} \\ \mathbf{Z}_{np} & \mathbf{Z}_n \end{bmatrix} \begin{bmatrix} \mathbf{I}_p \\ \mathbf{I}_n \end{bmatrix} \tag{4-7}$$

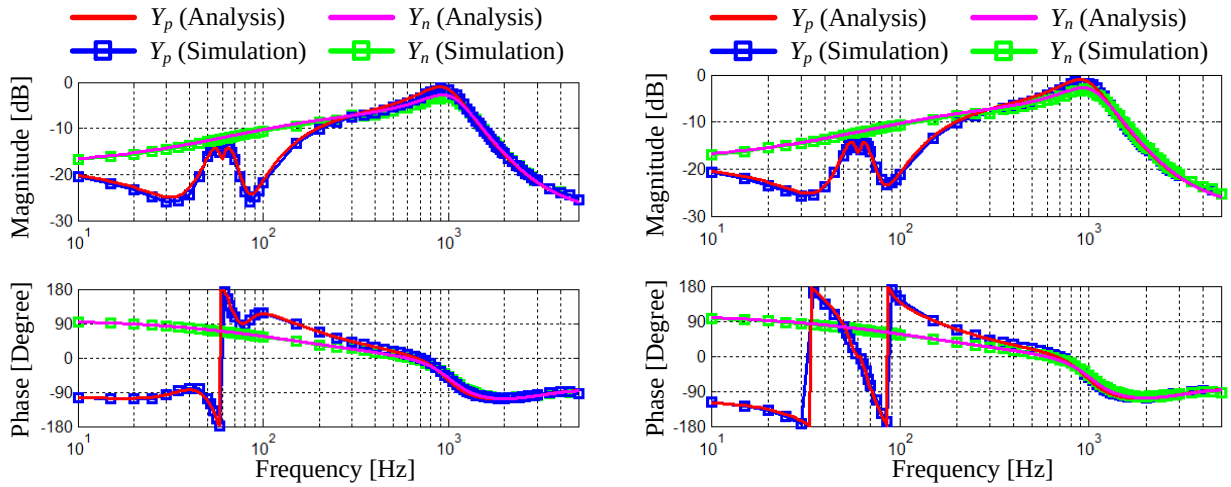

Figure 4-6. Simulation measurement results of the sequence admittances of the inverter with PI control in the *d*-*q* frame, for (a) the operation with the current output (I_d = 15 A, I_q = 0 A) and (b) the operation with the current output (I_d = –15 A, I_q = 0 A)

4.3 Simulation and Experimental Verification

The parameters and operating conditions of the inverter under test in the simulation and experiments are the same with those of the inverter analyzed in Section 3.1. The dead time is not modeled in the simulation model, but a 1.5 μs dead time is set in the experiments. Figure 4-6 shows the simulation measurement results of the positive and negative sequence admittances of the inverter with PI control in the *d*-*q* frame, for the operation with the current output (I_d = 15 A, I_q = 0 A) and the operation with the current output (I_d = –15 A, I_q = 0 A), respectively. The

simulation measurement results match with the theoretical analysis very well, which verifies the effectiveness of the proposed sequence impedance measurement method by using a paralleled structure.

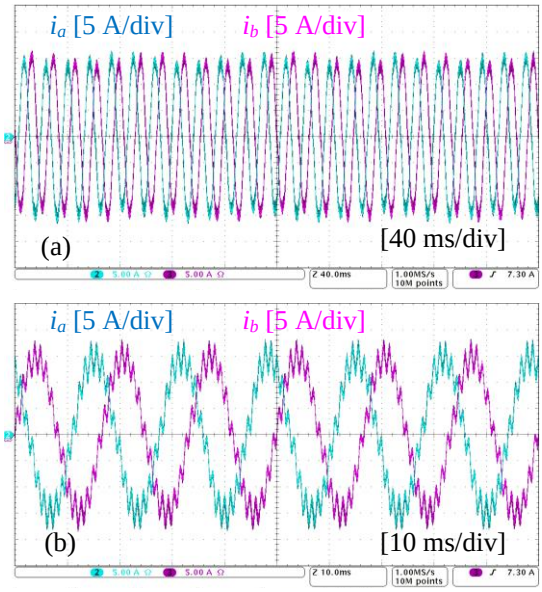

Figure 4-7. Phase currents of the inverter under test during (a) low frequency injection and (b) high frequency injection.

As for sequence admittance measurement in experiments, Figure 4-7 shows the inverter output current waveforms acquired in a Tektronix oscilloscope during the injections of both the low frequency signals and the high frequency signals. Figure 4-8(a) shows the experimental measurement results of the positive sequence admittance and the negative sequence admittance of the inverter with PI control in the *d*-*q* frame with the current output (I_d = –15 A, I_q = 0 A). Figure 4-8(b) shows the experimental measurement results of the positive sequence admittance and the negative sequence admittance of the inverter with PR control in the α-β frame with the

current output (I_d = –15 A, I_q = 0 A). The analytical results of the sequence admittances are re-calculated by including the model of the dead-time effect, and are drawn in Figure 4-8 for comparison with the experimental measurement results. These experimental results match with the theoretical analysis very well, except some small differences around 1 kHz, which might be due to the assumptions and approximations made in the model of the dead-time effect.

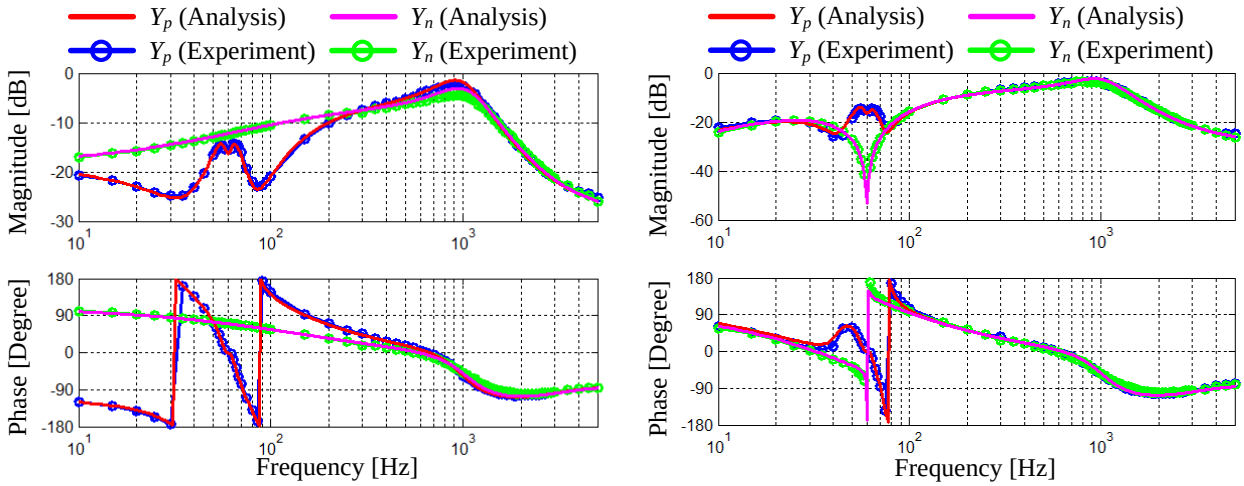

Figure 4-8. Experimental measurement results of the sequence admittances of the inverter with (a) PI control in the *d*-*q* frame and (b) PR control in the *α*-*β* frame, for the operation with the current output (I_d = –15 A, I_q = 0 A).

To further demonstrate the effect of the dead time on the sequence admittances and verify the validness of the proposed sequence impedance measurement method, two more experiments are carried out. The three-phase inverter is controlled with the PI current controller in the *d*-*q* frame under two different operating conditions: (I_d = 2 A, I_q = 0 A) and (I_d = 15 A, I_q = 0 A). The

same controller parameters as in Table 3-2 are used, except that voltage feed-forward cut-off frequency is a little different (ω_{ff} = 25×2π rad/s). The experimental measurement results of the positive sequence admittances in the frequency range of [100 Hz, 2 kHz] for both operating conditions are shown in Figure 4-9. The analytical results with and without the dead-time effect are also drawn in Figure 4-9 for comparison. It can be seen that the dead time brings more obvious damping effect when the output current is lower (I_d = 2 A), which is consistent with the dead-time model. The experimental results further verified the effectiveness of the proposed sequence impedance measurement method.

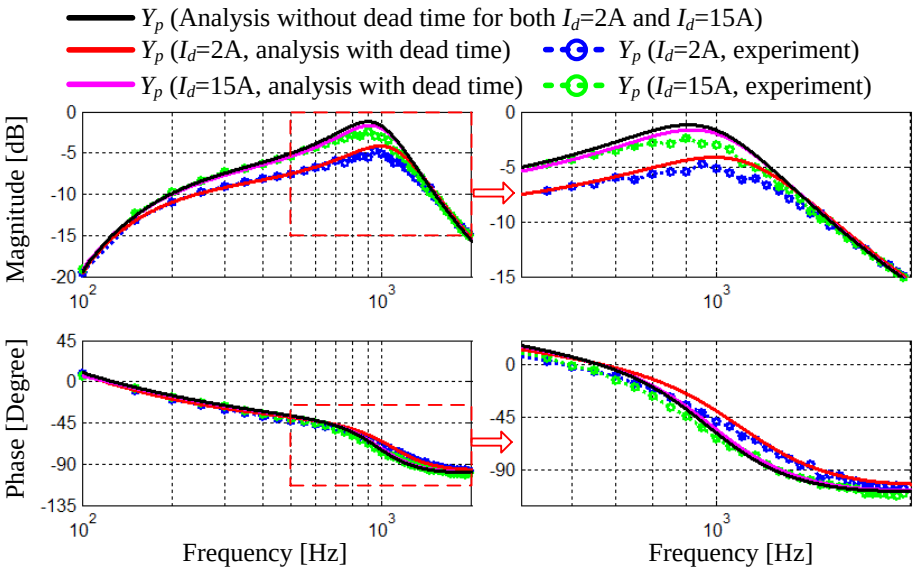

Figure 4-9. Experimental measurement results of the positive sequence admittances of the inverter with PI control in the *d-q* frame, for two operation conditions: (I_d = 2 A, I_q = 0 A) and (I_d = 15 A, I_q = 0 A).

4.4 Conclusion

In this chapter, a sequence impedance measurement method of three-phase inverters by using another inverter connected in parallel with common-dc and common-ac sides has been proposed. Zero-sequence circulating current reduction and open-loop voltage compensation improve the measurement accuracy. The proposed method is verified by both simulation and experiments.

5 Stability Analysis and Controller Parameter Design of Radial-Line Renewable Systems

In this chapter, an impedance-based sufficient stability criterion of general radial-line renewable systems with multiple current-controlled inverters in the *d-q* domain is proposed. The system stability can be examined by checking the encirclements of the point (−1, *j*0) by the characteristic loci of the return-ratio matrix at each bus successively from the farthest bus to the PCC, without the need for pole calculation of the return-ratio matrices. The phase margin of the system can also be obtained while applying the proposed stability criterion, based on which some design rules of the controller parameters are proposed.

5.1 Calculation of the Steady-State Point

Assume the arbitrary *d-q* frame is chosen to be aligned with the voltage at PCC v_{PCC}, and it is selected as the common system *d-q* frame with the superscript *s*. The steady-state point regarding bus voltage v_n, inverter current i_n and current i_{Ln} through the line impedance $\mathbf{Z_n}$ (with inductance L_n and resistance R_n) in this common *d-q* frame can be obtained by solving the steady-state equations of the radial-line system as shown in Figure 5-1, including KCL equation (5-1), feeder line equation (5-2), inverter output current and voltage equations (5-3) and (5-4) (assuming unity power factor), PCC voltage equation (5-5) as well as the grid voltage equation (5-6). Then, the bus angle θ_n can be calculated in (5-7).

$$\begin{bmatrix} I_{Lnd} \\ I_{Lnq} \end{bmatrix} = \begin{bmatrix} I_{L(n+1)d} \\ I_{L(n+1)q} \end{bmatrix} + \begin{bmatrix} I_{nd} \\ I_{nq} \end{bmatrix} \tag{5-1}$$

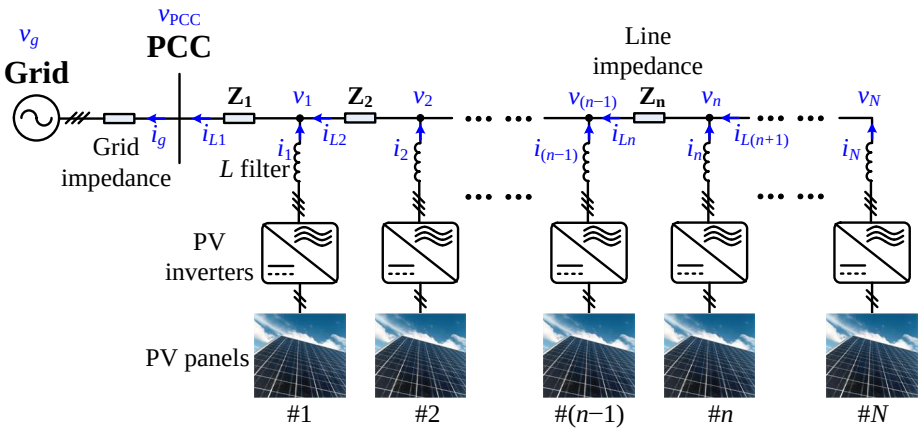

Figure 5-1. Simplified one-line diagram of a grid-connected radial-line PV system with multiple PV inverters.

$$\begin{bmatrix} R_n & -\omega L_n \\ \omega L_n & R_n \end{bmatrix} \begin{bmatrix} I_{Lnd} \\ I_{Lnq} \end{bmatrix} = \begin{bmatrix} V_{nd} \\ V_{nq} \end{bmatrix} - \begin{bmatrix} V_{(n-1)d} \\ V_{(n-1)q} \end{bmatrix} \tag{5-2}$$

$$\sqrt{I_{nd}^2 + I_{nq}^2} = I_n^* \tag{5-3}$$

$$\frac{I_{nd}}{I_{nq}} = \frac{V_{nd}}{V_{nq}} \tag{5-4}$$

$$V_{PCCq} = 0 \tag{5-5}$$

$$\sqrt{V_{gd}^2 + V_{gq}^2} = V_g \tag{5-6}$$

$$\theta_n = \arctan \frac{V_{nq}}{V_{nd}} \tag{5-7}$$

Table 5-1. System electrical parameters.

Electrical Parameters		**Values**
L filter	L_f	0.575 mH
	R_{Lf}	0.2 Ω
Dc-link voltage	V_{dc}	400 V
Ac grid voltage	V_g	170 V (phase peak)
Inverter rated current	I_{rated}	10 A (phase peak)
Fundamental frequency	ω_1	60×2π rad/s
Grid impedance	L_g	0.575 mH
Each line impedance	L_{Line}	0.7 mH

5.2 Small-Signal Stability Criterion

The parameters of the radial-line system with three current-controlled inverters under study in this chapter are listed in Table 3-5 and Table 5-1. Three inverters have the same electrical and controller parameters. The impedance-based system equivalent circuit can be obtained in the system *d-q* domain, as shown in Figure 5-2. The grid current $\mathbf{I_g}$ can be expressed as (5-8), and the system stability can be examined by analyzing the poles of the transfer function matrices **A**, $\mathbf{B_1}$, $\mathbf{B_2}$ and $\mathbf{B_3}$.

$$\mathbf{I_g} = \mathbf{A}\mathbf{V_g} + \mathbf{B_1}\mathbf{I_1^*} + \mathbf{B_2}\mathbf{I_2^*} + \mathbf{B_3}\mathbf{I_3^*} \tag{5-8}$$

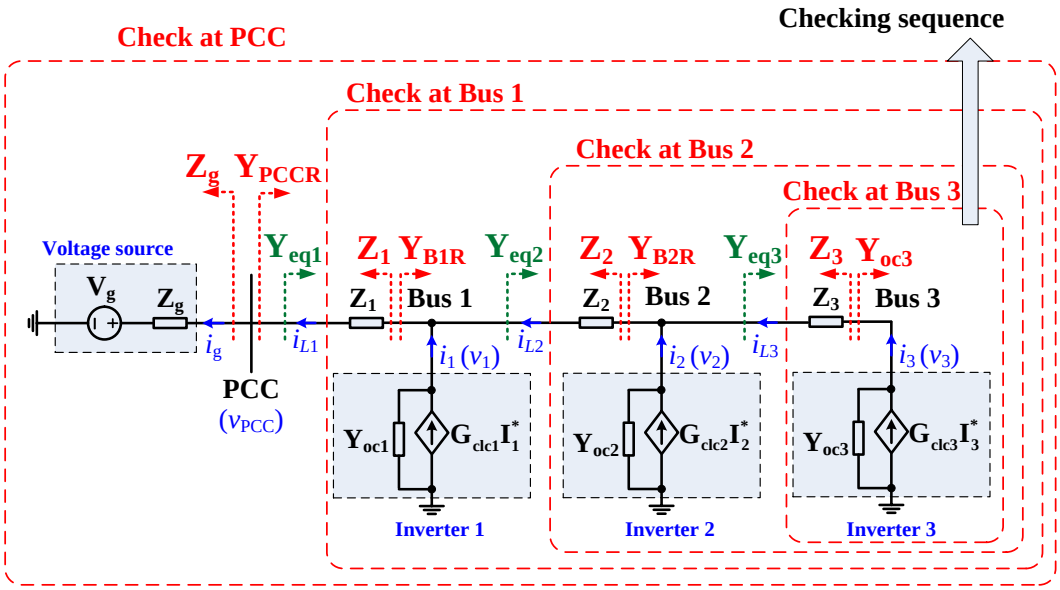

Figure 5-2. Impedance-based system equivalent circuit showing stability check at each bus.

These matrices can be obtained by deriving the equivalent Norton circuit at each bus and simplifying the system structure successively from the farthest point (Inverter 3) to the PCC (Inverter 1), as shown in Figure 5-3.

The result is expressed in (5-9), where the equivalent admittances are defined in (5-10) and the return-ratio matrix $\mathbf{T}_{\mathbf{m\_x}}$ and its closed-loop gain $\mathbf{T}_{\mathbf{clm\_x}}$ at each bus are defined in (5-11). The grid or line impedance $\mathbf{Z}_{\mathbf{n}}$ is expressed in (5-12).

$$\begin{aligned}\mathbf{I}_{\mathbf{g}} = {} & \mathbf{T}_{\mathbf{clm\_PCC}}\mathbf{Y}_{\mathbf{PCCR}}\mathbf{V}_{\mathbf{g}} - \mathbf{T}_{\mathbf{clm\_PCC}}\mathbf{T}_{\mathbf{clm\_B1}}\mathbf{G}_{\mathbf{clc1}}\mathbf{I}_{\mathbf{1}}^{*} \\ & - \mathbf{T}_{\mathbf{clm\_PCC}}\mathbf{T}_{\mathbf{clm\_B1}}\mathbf{T}_{\mathbf{clm\_B2}}\mathbf{G}_{\mathbf{clc2}}\mathbf{I}_{\mathbf{2}}^{*} \\ & - \mathbf{T}_{\mathbf{clm\_PCC}}\mathbf{T}_{\mathbf{clm\_B1}}\mathbf{T}_{\mathbf{clm\_B2}}\mathbf{T}_{\mathbf{clm\_B3}}\mathbf{G}_{\mathbf{clc3}}\mathbf{I}_{\mathbf{3}}^{*}\end{aligned} \tag{5-9}$$

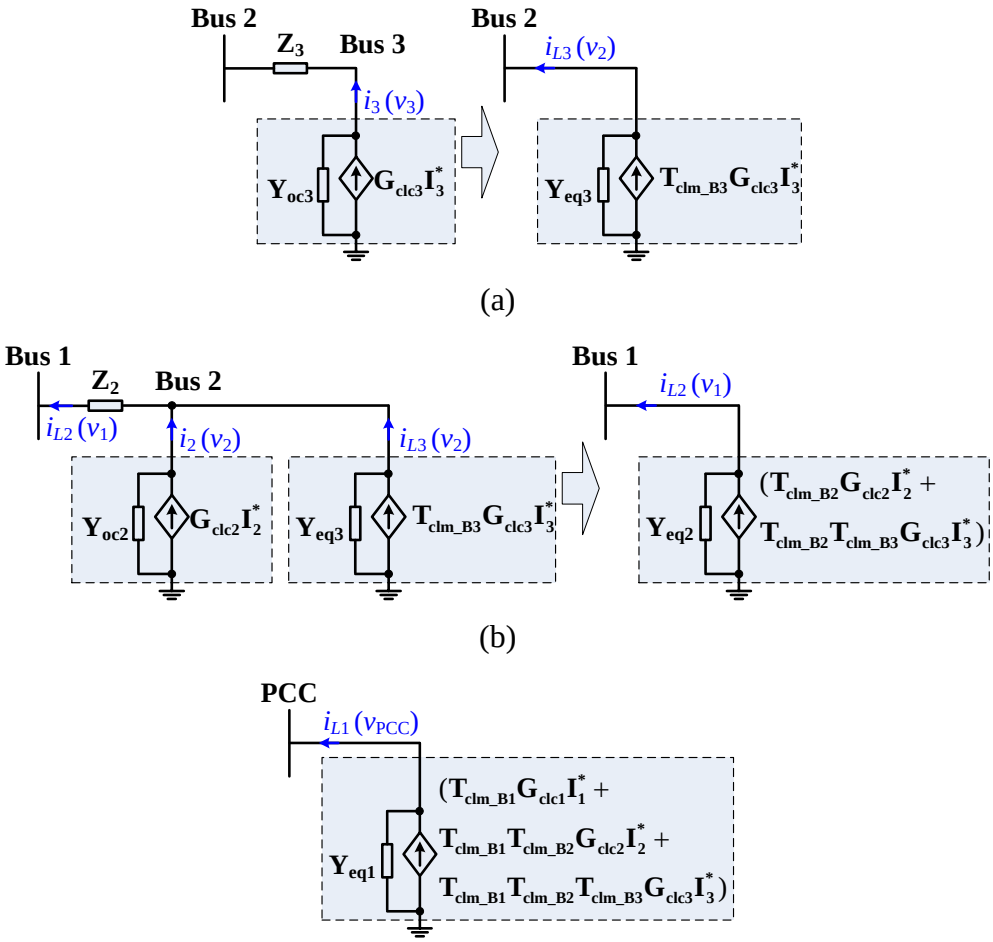

Figure 5-3. Derivation of the equivalent Norton circuit at each bus: (a) Bus 2, (b) Bus 1, (c) Bus PCC.

$$\begin{cases} \mathbf{Y}_{\mathbf{eq3}} = \left(\mathbf{Z}_3 + \mathbf{Y}_{\mathbf{oc3}}^{-1}\right)^{-1} = \mathbf{T}_{\mathbf{clm\_B3}}\mathbf{Y}_{\mathbf{oc3}} \\ \mathbf{Y}_{\mathbf{eq2}} = \left(\mathbf{Z}_2 + \mathbf{Y}_{\mathbf{B2R}}^{-1}\right)^{-1} = \mathbf{T}_{\mathbf{clm\_B2}}\mathbf{Y}_{\mathbf{B2R}} \\ \mathbf{Y}_{\mathbf{PCCR}} = \mathbf{Y}_{\mathbf{eq1}} = \left(\mathbf{Z}_1 + \mathbf{Y}_{\mathbf{B1R}}^{-1}\right)^{-1} = \mathbf{T}_{\mathbf{clm\_B1}}\mathbf{Y}_{\mathbf{B1R}} \\ \mathbf{Y}_{\mathbf{B2R}} = \mathbf{Y}_{\mathbf{oc2}} + \mathbf{Y}_{\mathbf{eq3}} \\ \mathbf{Y}_{\mathbf{B1R}} = \mathbf{Y}_{\mathbf{oc1}} + \mathbf{Y}_{\mathbf{eq2}} \end{cases} \tag{5-10}$$

$$\begin{cases} \mathbf{T_{clm\_B3}} = \left(\mathbf{I} + \mathbf{T_{m\_B3}}\right)^{-1} = \left(\mathbf{I} + \mathbf{Y_{oc3}}\mathbf{Z_3}\right)^{-1} \\ \mathbf{T_{clm\_B2}} = \left(\mathbf{I} + \mathbf{T_{m\_B2}}\right)^{-1} = \left(\mathbf{I} + \mathbf{Y_{B2R}}\mathbf{Z_2}\right)^{-1} \\ \mathbf{T_{clm\_B1}} = \left(\mathbf{I} + \mathbf{T_{m\_B1}}\right)^{-1} = \left(\mathbf{I} + \mathbf{Y_{B1R}}\mathbf{Z_1}\right)^{-1} \\ \mathbf{T_{clm\_PCC}} = \left(\mathbf{I} + \mathbf{T_{m\_PCC}}\right)^{-1} = \left(\mathbf{I} + \mathbf{Y_{PCCR}}\mathbf{Z_g}\right)^{-1} \end{cases} \tag{5-11}$$

$$\mathbf{Z_n} = \begin{bmatrix} L_n s + R_n & -\omega_1 L_n \\ \omega_1 L_n & L_n s + R_n \end{bmatrix} \tag{5-12}$$

According to the GNC, $\mathbf{T_{m\_B3}}$ has no RHP poles. If the characteristic loci of $\mathbf{T_{m\_B3}}$ have zero encirclement around (−1, *j*0), $\mathbf{T_{clm\_B3}}$, $\mathbf{Y_{eq3}}$ and $\mathbf{Y_{B2R}}$ are stable. As a result, $\mathbf{T_{m\_B2}}$ has no RHP poles. The analysis can be extended to other return-ratio matrices. Therefore, if the characteristic loci of all the return-ratio matrices $\mathbf{T_{m\_x}}$ at all buses have zero encirclement around (−1, *j*0), all the transfer function matrices $\mathbf{A}$, $\mathbf{B_1}$, $\mathbf{B_2}$ and $\mathbf{B_3}$ are stable, and thus the grid current $\mathbf{I_g}$ and the total system are stable. Also, there is no need to calculate the poles of the return-ratio matrices. It should be noted that all the inverters are assumed to be stable stand alone, and thus the current closed-loop gains $\mathbf{G_{clcn}}$ and output admittances $\mathbf{Y_{ocn}}$ are stable.

The result can be generalized to the proposed impedance-based sufficient stability criterion of radial-line systems with *N* current-controlled inverters as follows:

(1) Assume PCC is Bus B_0, the ideal grid is Bus B_{-1}, and the grid impedance is $\mathbf{Z_0}$. Define the return-ratio matrix $\mathbf{T_{m\_Bn}}$ at each bus B_n (n=0−*N*) as $\mathbf{T_{m\_Bn}} = \mathbf{Y_{BnR}}\mathbf{Z_n}$, where $\mathbf{Z_n}$ is the line impedance between Bus B_{n-1} and Bus B_n on the left-side and $\mathbf{Y_{BnR}}$ is the total admittance on the right side of Bus B_n.

(2) The checking sequence of the return-ratio matrices at all buses is from the farthest bus B_N to the PCC bus B_0.

(3) If the characteristic loci of each return-ratio matrix have zero encirclement around (−1, *j*0), the total system is stable. If the characteristic loci of the return-ratio matrix at Bus B_n have non-zero encirclement around (−1, *j*0), the total system is probably unstable, and there is no need to check the remaining buses. It should be noted that, if the subsystem checked at Bus B_n is unstable, it is possible that the inclusion of additional inverter and passive components could stabilize the subsystem checked at Bus B_{n-1}. The proposed stability criterion is conservative because it requires all subsystems checked at all buses to be stable.

For the radial-line system with three current-controlled inverters under study in this chapter, assume the grid voltage magnitude is V_g =170 V, and the output currents of all inverters are the same: I_d =10 A, I_q =0 A in their own inverter *d*-*q* frames. According to the steady-state point calculation in Section 5.1, the magnitude and phase angle of each bus in the common *d*-*q* frame aligned with the PCC voltage v_{PCC} are as follows: V_1 =175.91 V, θ_1 =2.83 °; V_2 =176.46 V, θ_2 =4.63 °; V_3 =176.77 V, θ_3 =5.51 °.

The cut-off frequency parameter ω_{ff} of the first-order low-pass filter in the voltage feed-forward gain $\mathbf{G_{ffv}}$, as shown in Figure 3-17, is selected as an example to investigate its effect on the system stability. Three cases are investigated by the proposed stability criterion. Case 1: ω_{ff}=20×2π rad/s; Case 2: ω_{ff}=50×2π rad/s; Case 3: ω_{ff}=300×2π rad/s. The Nyquist plots of the characteristic loci (λ_1 and λ_2) of the return-ratio matrix at each bus are shown in Figure 5-4. For Case 1 and Case 2, all the characteristic loci have zero encirclement around (−1, *j*0), so the system is stable. For Case 3, λ_1 of the return-ratio matrix $\mathbf{T_{m\_B2}}$ at Bus 2 has two encirclements around (−1, *j*0), so the system is probably unstable.

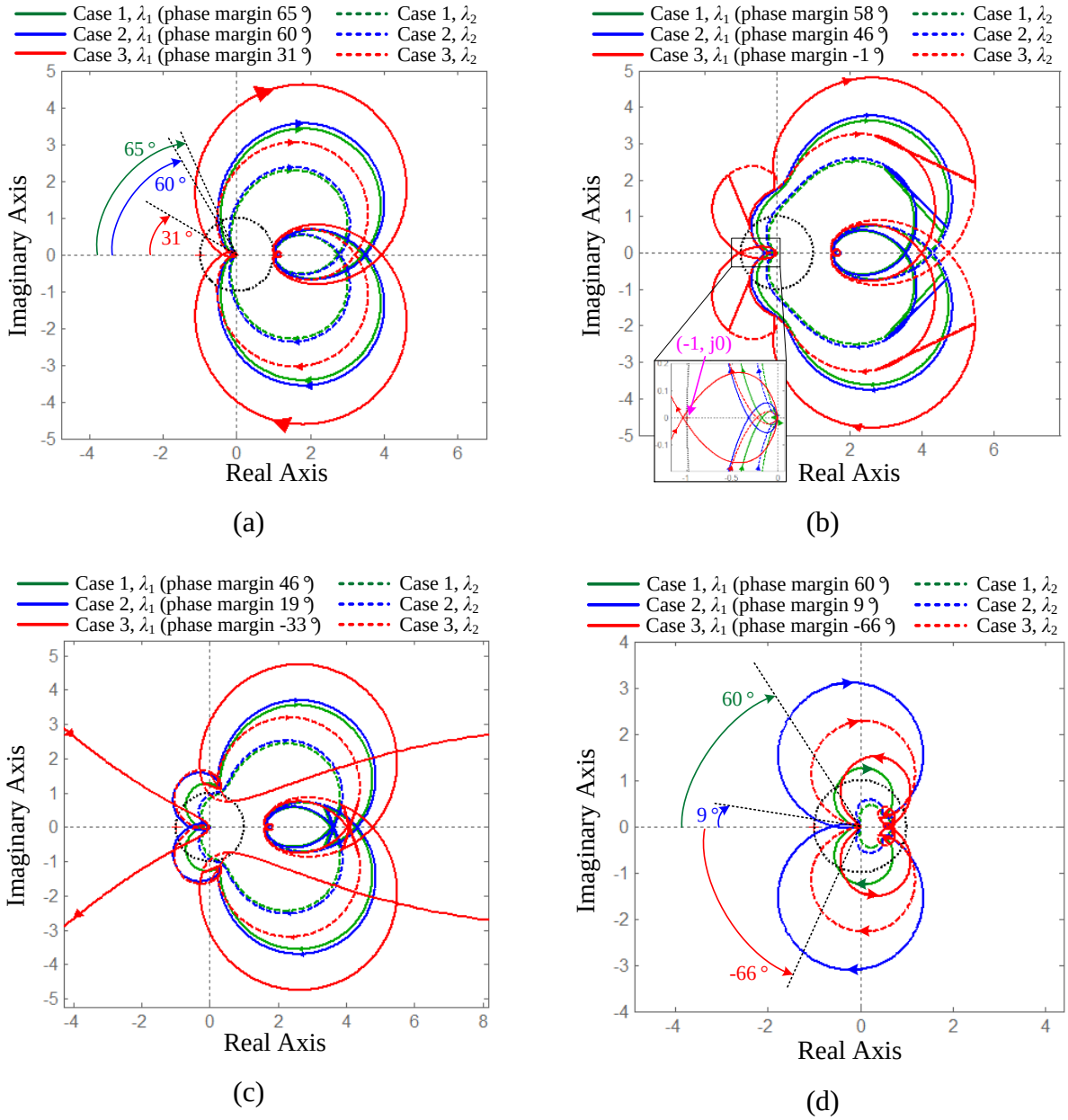

Figure 5-4. The characteristic loci of the return-ratio matrices. (a) $\mathbf{T}_{\mathbf{m\_B3}}$ at Bus 3; (b) $\mathbf{T}_{\mathbf{m\_B2}}$ at Bus 2; (c) $\mathbf{T}_{\mathbf{m\_B1}}$ at Bus 1; (d) $\mathbf{T}_{\mathbf{m\_PCC}}$ at PCC.

5.3 Controller Parameter Design for Stability

5.3.1 Controller Parameter Design for Normal Operation

In addition to the requirement of stable operation, stability margin is also an important concern when designing the controller parameters of the inverters for good system dynamic performance. While using the proposed stability criterion for stability checking, the phase margin ϕ_m of the return-ratio matrix at each bus can also be obtained, which is the angle difference between the unit-circle intersection point and the negative real axis, as shown in Figure 5-4. Considering that there are two characteristic loci (λ_1 and λ_2), the smaller angle of these two intersection points is chosen as ϕ_m. It can be seen from Figure 5-4(d) that Case 1 is a stable case with enough phase margin and good oscillation damping performance, and Case 2 is a stable case with limited phase margin and poor oscillation damping performance, while Case 3 is an unstable case with negative phase margin and resonance.

The impact of the increase of the voltage-feedforward cut-off frequency ω_{ff} on the stability and phase margin ϕ_m at each bus is further investigated, as shown in Figure 5-5. Several characteristics can be observed and used as controller parameter design rules:

(1) With the increase of ω_{ff}, the phase margin of each return-ratio matrix deceases. So, ω_{ff} should be selected sufficiently small to achieve stability and good oscillation damping performance.

(2) The phase margin gradually decreases from the farthest bus (Bus 3) to the nearest bus (Bus 1). When assuming all the line impedances ($\mathbf{Z_1}$–$\mathbf{Z_N}$) are the same and the size and parameters of all the inverters are the same (such as the system under study in this chapter), the decrease of phase margin is generally linear with the bus number (or equivalently the increase in

the number of inverters), as shown in Figure 5-5(b). Therefore, the phase margins (ϕ_{mN} and $\phi_{m(N-1)}$) obtained from the first and second stability checks of return-ratio matrices at Bus B_N and Bus B_{N-1} can be utilized to predict the approximate phase margin ϕ_{m1} at Bus B_1 as (5-13). Conversely, a sufficient phase margin ϕ_{m1} at Bus B_1 (e.g. 30 °) can be required to keep stability at PCC under the grid impedance variation, and then the phase margin ϕ_{mN} at Bus B_N and the controller parameter (ω_{ff}) can be designed. For example, as shown in Figure 5-5(b), when ω_{ff}=300×2π rad/s, the phase margin ϕ_{m2} at Bus 2 is already 0 °, so the system is unstable even when only two inverters are connected to PCC, and ω_{ff} should be re-designed.

$$\phi_{m1} \approx \phi_{mN} - (\mathrm{N}-1)\Delta\phi_m = \phi_{mN} - (\mathrm{N}-1)\left(\phi_{mN} - \phi_{m(N-1)}\right) \tag{5-13}$$

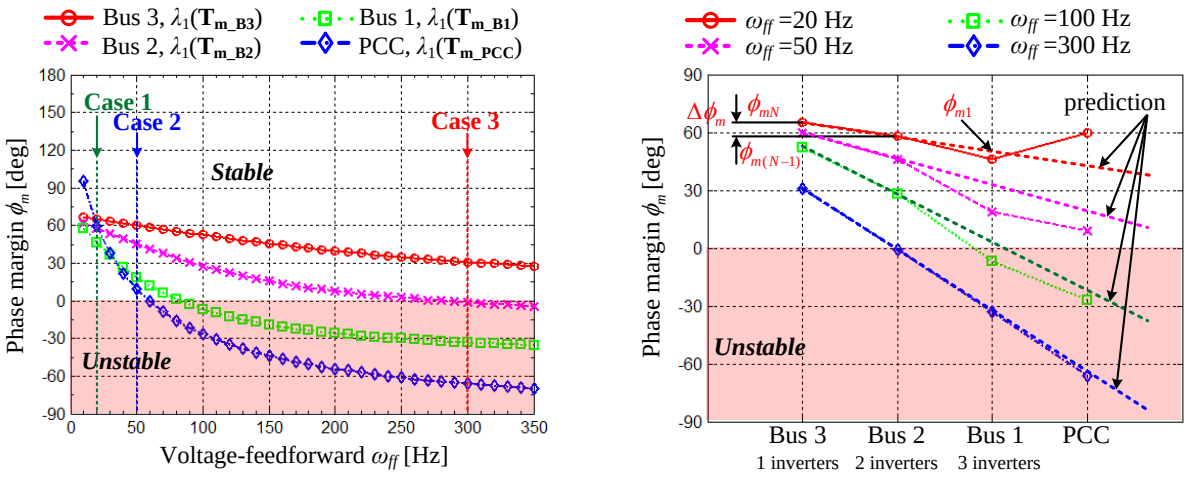

(a) (b)

Figure 5-5. Impact of voltage-feedforward ω_{ff} on stability and phase margin ϕ_m at each bus: (a) ϕ_m versus ω_{ff}; (b) ϕ_m versus Bus number (or the number of inverters).

5.3.2 Design Considering Inverter Disconnection

During the system operation, there is a possibility that one or several inverters are not in service and disconnected from the system, and the system stability and margin might change when still using the designed parameters. Assuming Inverter 2 is disconnected as illustrated in Figure 5-6, the stability and phase margin of the return-ratio matrix at each bus are examined again by applying the stability criterion proposed in Section 5.2, as shown in Figure 5-7.

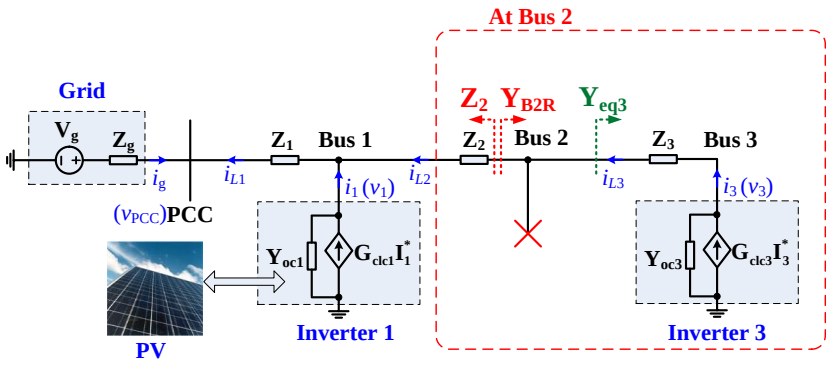

Figure 5-6. Ilustration of the disconnection of Inverter 2.

The phase margins at Bus 2, Bus 3 and PCC are improved under the same controller parameter (ω_{ff}) with Inverter 2 disconnected, compared with Figure 5-5(a). It can be understood in the following way. If Inverter #n is disconnected from Bus B_n, the magnitude of the right-side admittance $\mathbf{Y_{BnR}}$ of Bus B_n is reduced. Then the magnitude interaction between the left-side line admittance $\mathbf{Y_n}$ ($\mathbf{Y_n} = \mathbf{Z_n^{-1}}$) and $\mathbf{Y_{BnR}}$ is weakened, or the magnitude intersection point moves to a higher frequency where the angle of $\mathbf{Y_{BnR}}$ is closer to the passive region (−90°~90°) as shown in Figure 5-8 and the phase difference between $\mathbf{Y_{BnR}}$ and $\mathbf{Y_n}$ at the intersection point is reduced.

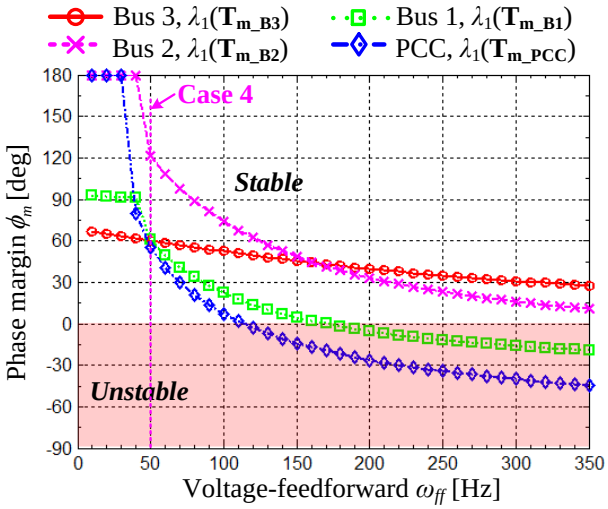

Figure 5-7. Impact of ω_{ff} on stability and phase margin ϕ_m at each bus, when Inverte 2 is disconnected.

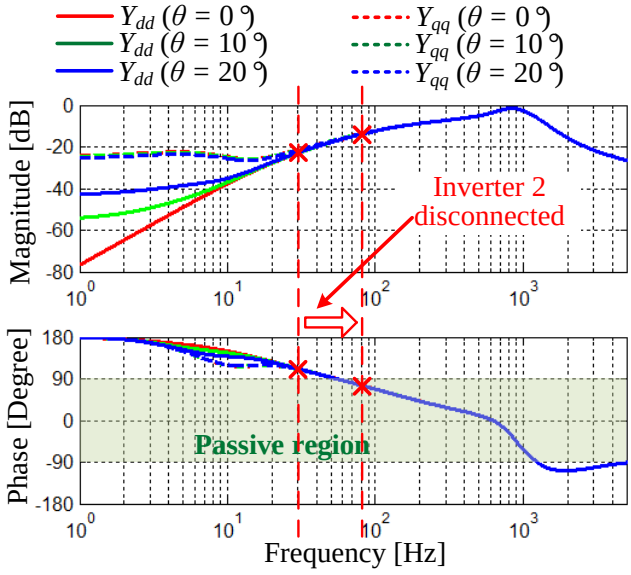

Figure 5-8. Impact of the disconnection of one inverter on the impedance interaction.

Therefore, the proposed controller parameter design method can guarantee the stable operation of the system even with the disconnection of several inverters.

5.3.3 Impact of Operating Point Changes

The system is not always at the rated operating point due to the output power or current variations of the PV inverters as well as the possible disconnection of several inverters. Strictly speaking, for controller parameter design, the system stability should be examined using the proposed criterion multiple times for all the possible operating points. Nevertheless, the operating point changes (such as inverter output current changes and bus voltage angle changes) mainly affect the inverter output admittances in the low frequency range within the PLL bandwidth or outer power control loop bandwidth as shown in Figure 3-18. Therefore, the impact of operating point changes on grid synchronization stability and low frequency oscillation should be considered, while the impact on inner control loop parameter design is small when only the harmonic stability is concerned. The impact and design of other controller parameters (such as current controller bandwidth ω_c, and active damping parameters if *LCL* filters are used) can be analyzed in a similar way.

5.4 Simulation and Experimental Verification

The radial-line system in the above analysis is simulated using MATLAB/Simulink. The aforementioned cases are investigated. Figure 5-9(a) shows that with the change of ω_{ff} from Case 1 to Case 3, the inverter currents change from stable to unstable. Figure 5-9(b) shows that Case 1 has a better oscillation damping performance than Case 2 under the *d*-axis current reference change of Inverter 3 from 5 A to 10 A. Figure 5-9(c) shows that the oscillation damping performance in Case 4 with Inverter 2 disconnected is improved as compared to Case 2.

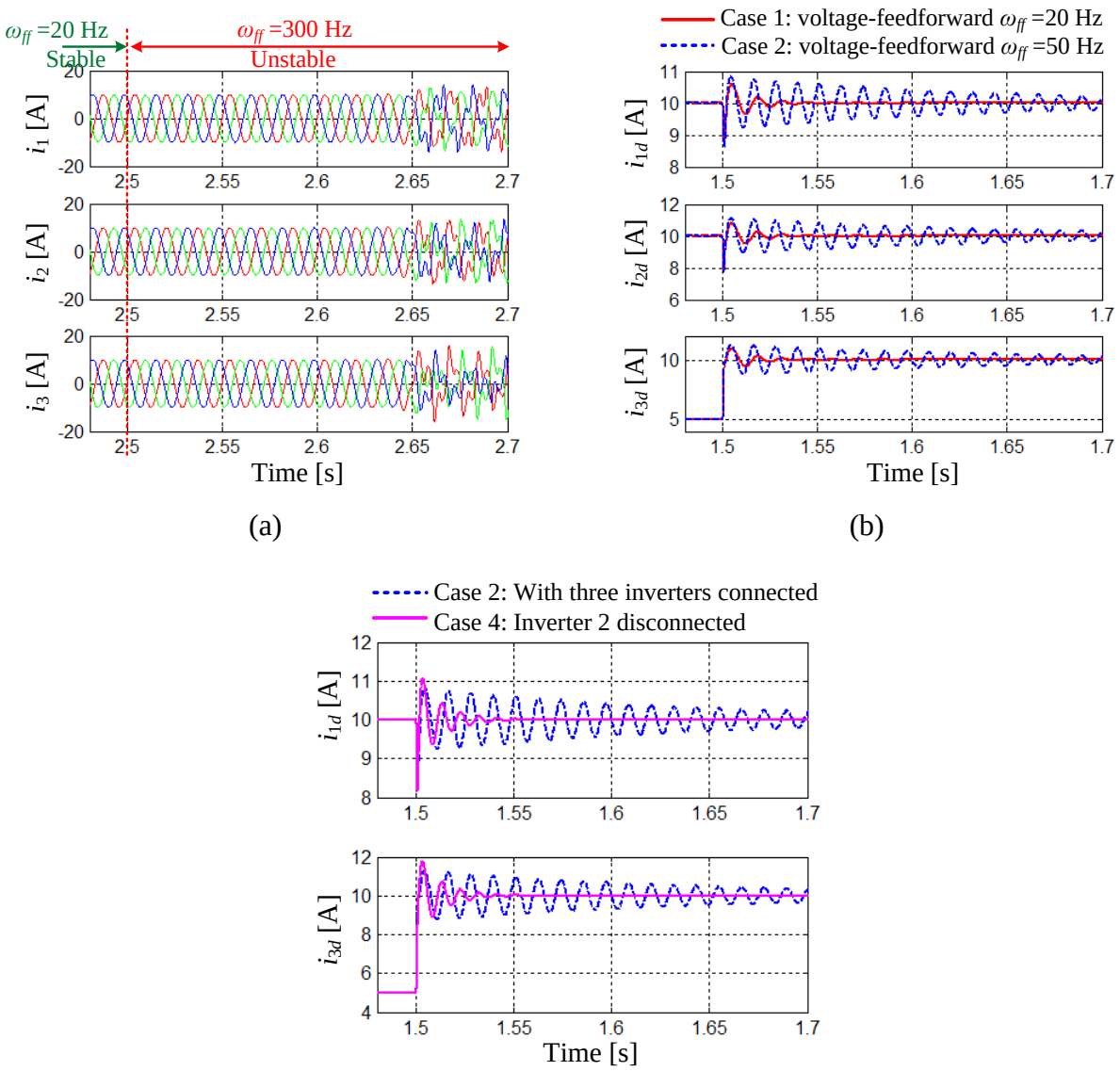

Figure 5-9. Simulation results. (a) Change from Case 1 to Case 3. (b) Comparison between Case 1 and Case 2 under current reference change of Inverter 3. (c) Impact of disconnection of Inverter 2: Case 2 versus Case 4.

The same radial-line system has been set up and investigated in experiments. Figure 5-10 shows that the phase-A currents of three inverters go from stable to unstable when ω_{ff} changes from 20×2π rad/s (Case 1) to 300×2π rad/s (Case 3). Figure 5-11 and Figure 5-12 display the comparison of the phase current and *d*-axis current responses of Case 1, Case 2 and Case 4 under the step change of the Inverter 3 *d*-axis current reference from 5 A to 10 A. With a higher voltage feed-forward cut-off frequency, the current response in Case 2 is worse with a longer oscillation period than that in Case 1. In addition, the disconnection of Inverter 2 results in better oscillation damping performance in Case 4 in contrast to Case 2. These simulation and experimental results have verified the above analysis.

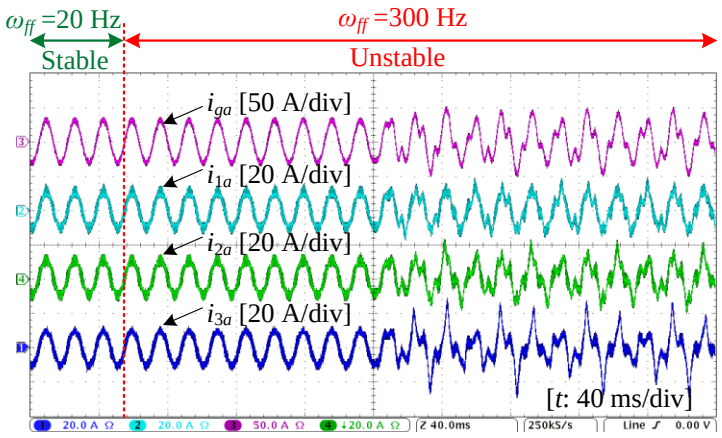

Figure 5-10. Experimental results of the radial-line system with three inverters when ω_{ff} changes from 20×2π rad/s (Case 1) to 300×2π rad/s (Case 3).

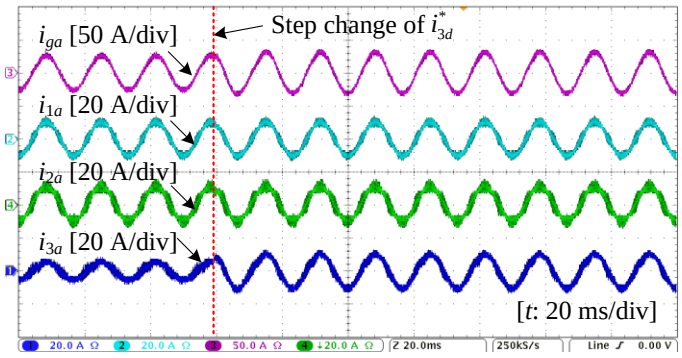

(a)

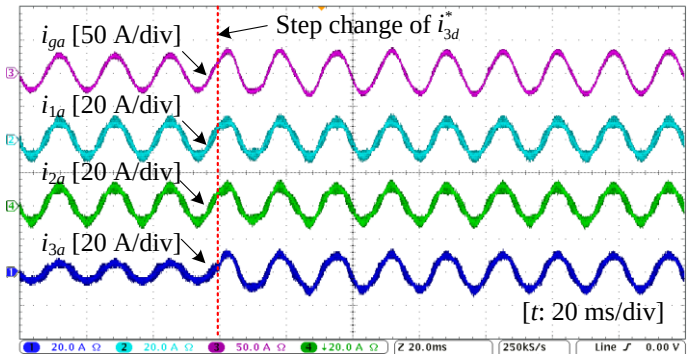

(b)

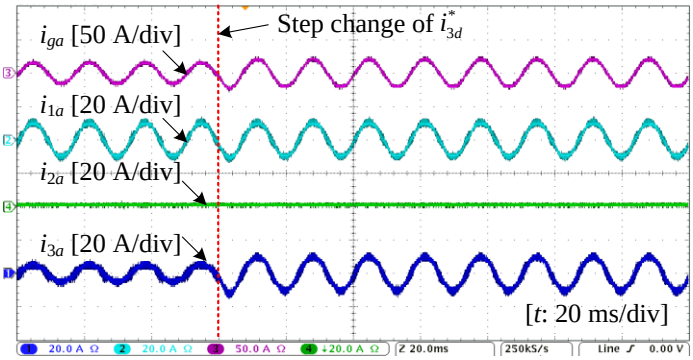

(c)

Figure 5-11. Experimental results of the radial-line system during the step change of the *d*-axis current reference i_{3d}^* of Inverter 3 from 5 A to 10 A. (a) Case 1, $\omega_{ff} = 20\times2\pi$ rad/s; (b) Case 2, $\omega_{ff} = 50\times2\pi$ rad/s; (3) Case 4, $\omega_{ff} = 50\times2\pi$ rad/s.

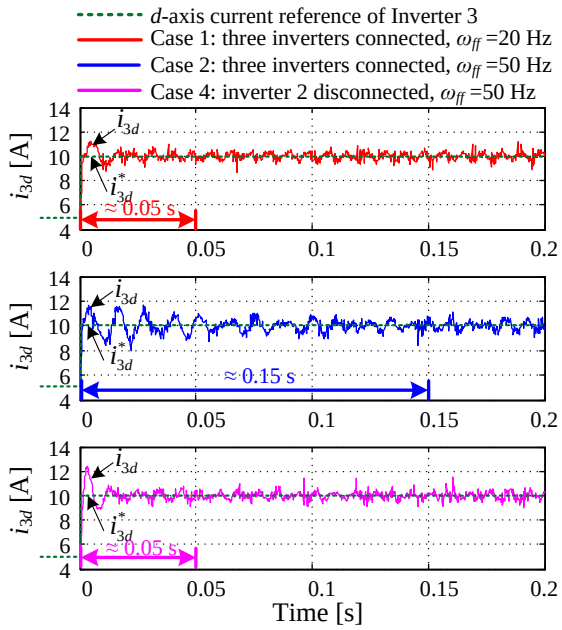

Figure 5-12. Comparison of the Inverter 3 *d*-axis current i_{3d} responses in Cases 1, 2 and 4.

5.5 Conclusion

In this chapter, an impedance-based sufficient stability criterion is proposed to analyze the small-signal stability of radial-line systems with multiple current-controlled inverters in the *d*-*q* domain. The system stability can be examined by checking the encirclements of the point (−1, *j*0) by the characteristic loci of the return-ratio matrix at each bus successively from the farthest bus to the PCC. The pole calculation of return-ratio matrices is avoided, compared to the GNC, while the phase margin of the system can still be obtained. Design rules of inverter controller parameters are also proposed for stable system operation with the consideration of inverter disconnection. The proposed stability criterion and controller parameter design method are verified by simulation and experiments.

6 Sequence Impedance Based Harmonic Stability Analysis and Controller Parameter Design of Multi-Bus Ac Power Systems

Three-phase inverter-based multi-bus ac power systems could suffer from the harmonic instability issue. The existing impedance-based stability analysis method using the Nyquist stability criterion once requires the calculation of right-half-plane (RHP) poles of impedance ratios, which would require the detailed internal control information of inverters and result in a heavy computation burden for complicated systems. In order to analyze the harmonic stability of multi-bus ac systems consisting of both voltage-controlled and current-controlled inverters without the need for RHP pole calculation, this chapter proposes two sequence-impedance-based harmonic stability analysis methods. Based on the summary of all major connection types including mesh, the proposed Method 1 can analyze the harmonic stability of multi-bus ac systems by adding the components one by one from nodes in the lowest level to areas in the highest system level, and accordingly, applying the stability criteria multiple times in succession. The proposed Method 2 is a generalized extension of the Impedance-Sum-Type criterion to be used for the harmonic stability analysis of any multi-bus ac systems based on Cauchy's theorem. The inverter controller parameters can be designed in the forms of stability regions in the parameter space, by repetitively applying the proposed harmonic stability analysis methods. Experimental results of inverter-based multi-bus ac systems validate the effectiveness of the proposed harmonic stability analysis methods and parameter design approach.

6.1 Small-Signal Stability Analysis of Inverter-Based Multi-Bus Systems

6.1.1 System Description

Figure 6-1 depicts the one-line diagram of a two-area system [42], which is a typical system used for power-system related research. Figure 6-2 illustrates a one-line diagram of an inverter-based multi-bus system for scaled-down emulation of the two-area system, where four generators G1–G4 are replaced by four voltage-controlled inverters [8] and two loads L7 and L9 are replaced by two current-controlled inverters [6]. The dc-link voltages of all inverters are regulated as constant by front-end dc power supplies. The parameters of the inverters are the same, which are shown in Table 3-1, Table 3-2 and Table 3-3. The main circuit parameters and operating points of the system are given in Table 6-1 and Table 6-2. It should be noted that only the inner voltage and current control loops of these inverters are considered in this chapter, while the low-bandwidth outer generator emulation and load emulation control loops [6], [8] are neglected.

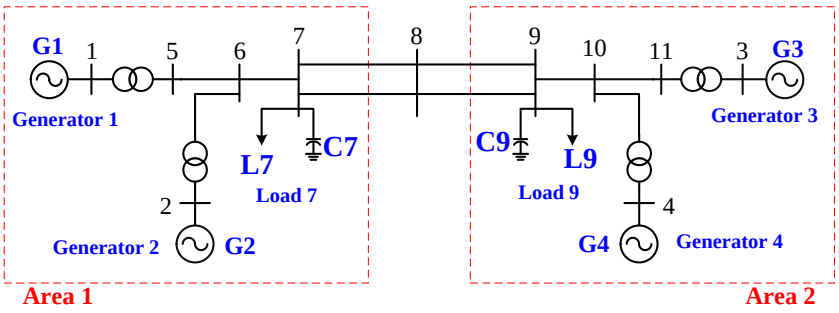

Figure 6-1. One-line diagram of the original two-area system.

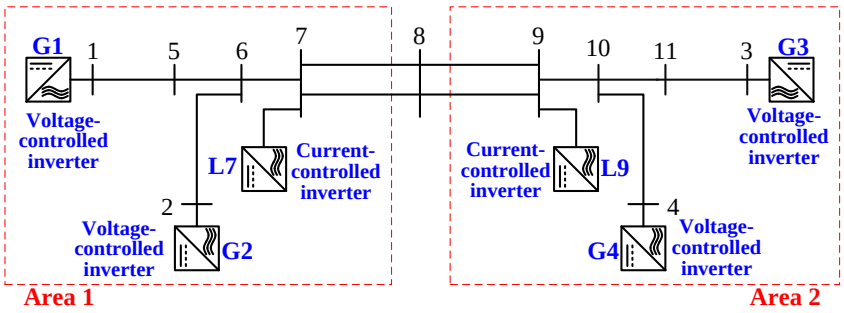

Figure 6-2. One-line diagram of the inverter-based multi-bus ac system for scaled-down emulation of the two-area system.

Table 6-1. Electrical parameters of the scaled-down two-area system.

Electrical Parameters		**Values**
Ac voltage base	V_{base}	50 V (phase peak)
Ac current base	I_{base}	17.36 A (phase peak)
Ac power base	S_{base}	1302 W
Line impedances	$Z_{1\text{-}6}$ ($L_{1\text{-}6}$, $R_{1\text{-}6}$)	2.45 mH, 0.12 Ω
	$Z_{2\text{-}6}$ ($L_{2\text{-}6}$, $R_{2\text{-}6}$)	1.2 mH, 0.04 Ω
	$Z_{6\text{-}7}$ ($L_{6\text{-}7}$, $R_{6\text{-}7}$)	0.7 mH, 0.035 Ω
	$Z_{7\text{-}9}$ ($L_{7\text{-}9}$, $R_{7\text{-}9}$)	10.7 mH, 0.65 Ω
	$Z_{3\text{-}10}$ ($L_{3\text{-}10}$, $R_{3\text{-}10}$)	2.5 mH, 0.12 Ω
	$Z_{4\text{-}10}$ ($L_{4\text{-}10}$, $R_{4\text{-}10}$)	0.7 mH, 0.04 Ω
	$Z_{9\text{-}10}$ ($L_{9\text{-}10}$, $R_{9\text{-}10}$)	0.7 mH, 0.035 Ω

Table 6-2. Operating point of the scaled-down two-area system.

Operating Point		**Values**
Current references of each current-controlled inverter	I_d	−10 A
	I_q	0 A
Voltage references of each voltage-controlled inverter	V_d	50 V
	V_q	0 V

6.1.2 Existing Stability Analysis Method: Using Nyquist Stability Criterion Once

The impedance-based equivalent circuit of the studied inverter-based multi-bus ac system in the sequence domain is shown in Figure 6-3. The multi-bus system can be divided into two subsystems at any bus, where the rank of the controllability and observability matrices is full [34], such as Bus 1 or Bus 7, for harmonic stability analysis using the impedance-based Nyquist stability criterion.

For example, assume the system is divided at Bus 7. The total sequence admittance Y_{B7L} of the left-side subsystem and the total sequence admittance Y_{B7R} of the right-side subsystem can be obtained by forcing the voltage sources and current sources to zero. The expressions of Y_{B7L} and Y_{B7R} are shown in (6-1) and (6-2), the impedance ratio T_{m_B7} (also called the minor loop gain) is expressed in (6-3), and the closed minor loop gain T_{clm_B7} of the impedance ratio is expressed in (6-4). The impedance Z_{lk} of each line is expressed in (6-5) with the line inductance L_{lk} and resistance R_{lk}.

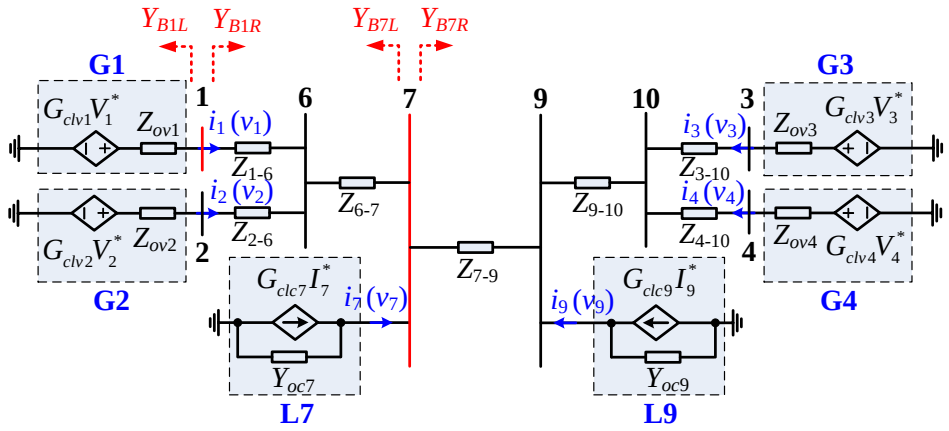

Figure 6-3. Impedance-based equivalent circuit of the studied system in the sequence domain.

$$Y_{B7L} = Y_{oc7} + \cfrac{1}{Z_{6-7} + \cfrac{1}{\cfrac{1}{Z_{ov1}+Z_{1-6}} + \cfrac{1}{Z_{ov2}+Z_{2-6}}}} = \frac{Y_{oc7}\left[Z_{6-7}\left(Z_{ov1}+Z_{1-6}+Z_{ov2}+Z_{2-6}\right)+\left(Z_{ov1}+Z_{1-6}\right)\left(Z_{ov2}+Z_{2-6}\right)\right]+Z_{ov1}+Z_{1-6}+Z_{ov2}+Z_{2-6}}{Z_{6-7}\left(Z_{ov1}+Z_{1-6}+Z_{ov2}+Z_{2-6}\right)+\left(Z_{ov1}+Z_{1-6}\right)\left(Z_{ov2}+Z_{2-6}\right)} \tag{6-1}$$

$$Y_{B7R} = \cfrac{1}{Z_{7-9} + \cfrac{1}{Y_{oc9} + \cfrac{1}{Z_{9-10} + \cfrac{1}{\cfrac{1}{Z_{ov3}+Z_{3-10}} + \cfrac{1}{Z_{ov4}+Z_{4-10}}}}}} \tag{6-2}$$

$$T_{m\_B7} = \frac{Y_{B7R}}{Y_{B7L}} \tag{6-3}$$

$$T_{clm\_B7} = \frac{1}{1+T_{m\_B7}} = \frac{1}{1+\dfrac{Y_{B7R}}{Y_{B7L}}} \tag{6-4}$$

$$Z_{lk} = L_{lk}s + R_{lk} \tag{6-5}$$

Then the system stability can be assessed by applying the Nyquist stability criterion to the impedance ratio, which can be described in

$$P\left(T_{clm\_B7}\right) = Z\left(1+T_{m\_B7}\right) = P\left(T_{m\_B7}\right) - N_{(-1,\,j0)}\left(T_{m\_B7}\right) \tag{6-6}$$

where $P(\ )$ and $Z(\ )$ denote the numbers of RHP poles and zeros respectively, $N_{(-1,\,j0)}(\ )$ is the number of times that the Nyquist trajectory encircles the critical point $(-1, j0)$ in anti-clockwise direction. The system is stable if and only if $Z(1+T_{m\_B7})$ is zero. According to the Nyquist stability criterion, not only the Nyquist diagram but also the RHP poles of the impedance ratio should be examined to evaluate the system stability. Furthermore, since the system is represented by two independent systems in the sequence domains, namely, the positive-sequence system and the negative-sequence system, the stability of both the positive-sequence impedance ratio $T_{m\_B7\_p}(s)$ and the negative-sequence impedance ratio $T_{m\_B7\_n}(s)$ should be examined. The total system is stable only if both sequence systems are stable. It should be noted that the system stability can also be assessed by the RHP poles of the closed-loop gain T_{clm_B7} of the impedance ratio in the both the positive sequence domain $T_{clm\_B7\_p}(s)$ and the negative sequence domain $T_{clm\_B7\_n}(s)$.

The voltage feed-forward control has a potential destabilizing effect on the inverter stability [64], [117], [133], [134]. The cut-off frequency ω_{ffv} of the first-order low-pass filter in the voltage feed-forward gain G_{ffv} of all the current-controlled inverters is selected as an example to investigate the parameter's impact on the system stability. Two cases are investigated by the Nyquist stability criterion in the sequence domain. Case 1: ω_{ffv}=200×2π rad/s; Case 2:

ω_{ffv}=1000×2π rad/s. Figure 6-4 and Figure 6-5 show the Nyquist diagrams of $T_{m\_B7\_p}(s)$ and $T_{m\_B7\_n}(s)$ in the full frequency range (−∞, +∞) and in the positive frequency range (0, +∞), respectively. As mentioned in Section 3.3.2, the Nyquist diagrams of both $T_{m\_B7\_p}(s)$ and $T_{m\_B7\_n}(s)$ are approximately symmetrical in the full frequency range (−∞, +∞). Figure 6-6 shows the pole-zero maps of $T_{m\_B7\_p}(s)$ and $T_{m\_B7\_n}(s)$, respectively. There is zero encirclement of the point (−1, *j*0) in both cases, but there are two RHP poles in Case 2. Therefore, according to the Nyquist stability criterion, the system is stable in Case 1, but unstable in Case 2. The same stability results can be obtained from the pole-zero maps of $T_{clm\_B7\_p}(s)$ and $T_{clm\_B7\_n}(s)$ as shown in Figure 6-7.

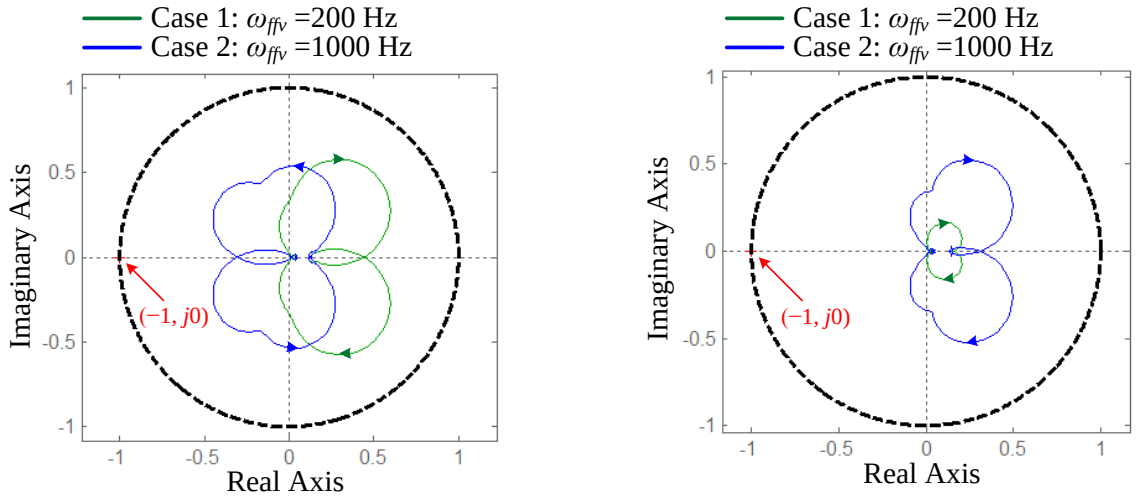

Figure 6-4. Nyquist diagrams of the impedance ratios in Case 1 and Case 2 in the full frequency range: (a) $T_{m\_B7\_p}(s)$ and (b) $T_{m\_B7\_n}(s)$.

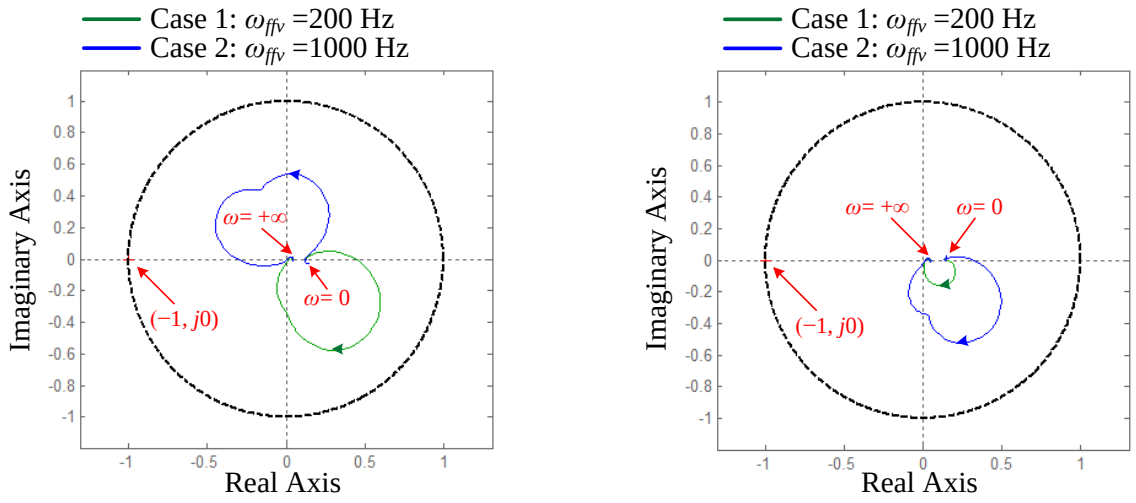

Figure 6-5. Nyquist diagrams of the impedance ratios in Case 1 and Case 2 in the positive frequency range: (a) $T_{m\_B7\_p}(s)$ and (b) $T_{m\_B7\_n}(s)$.

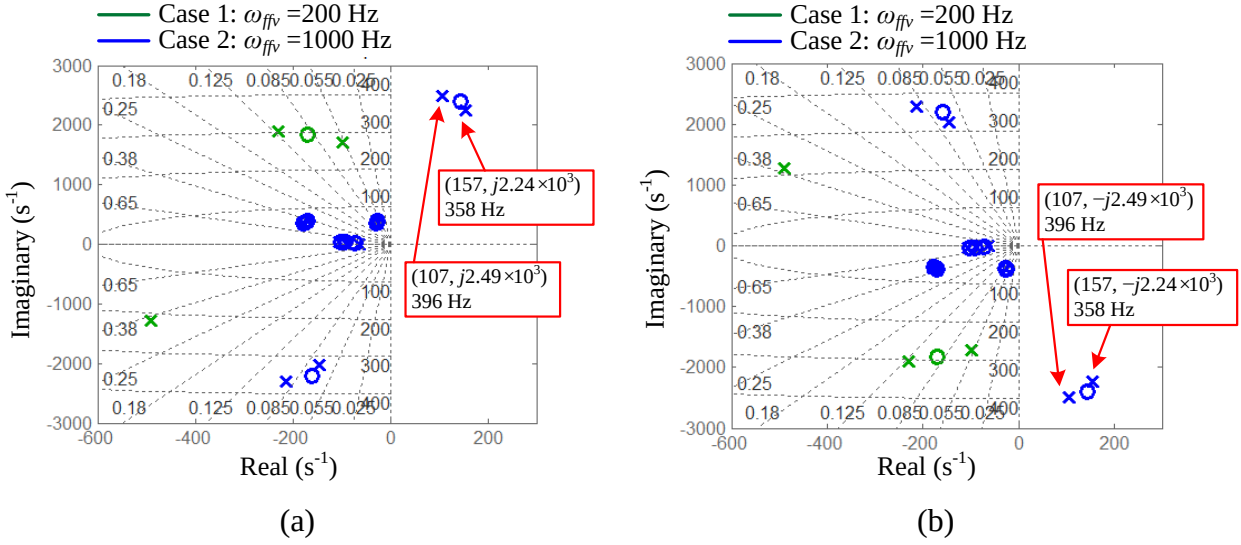

Figure 6-6. Pole-zero maps of the impedance ratios in Case 1 and Case 2: (a) $T_{m\_B7\_p}(s)$ and (b) $T_{m\_B7\_n}(s)$.

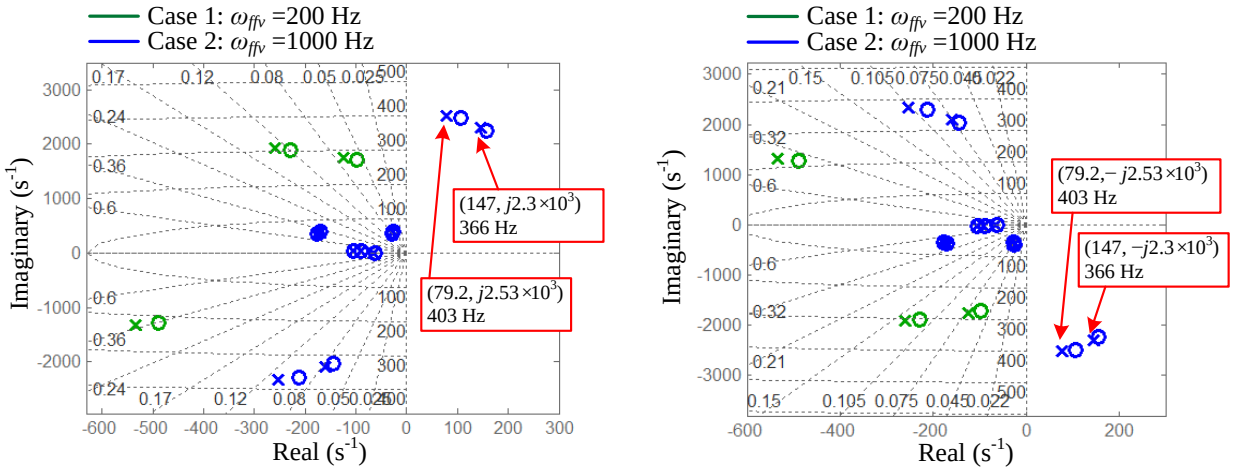

(a) (b)

Figure 6-7. Pole-zero maps of the closed loop gains of impedance ratios in Case 1 and Case 2: (a) $T_{clm\_B7\_p}(s)$ and (b) $T_{clm\_B7\_n}(s)$.

As shown in the above example, the existing impedance-based Nyquist stability criterion is a necessary and sufficient condition, but it requires the examination of the RHP poles of the impedance ratio at the interface between two subsystems, which may need large computation effort when the system order is high or even cannot be obtained when detailed models of inverters are not available due to the lack of internal control information. The latter may cause trouble to system integrators during system stability assessment when the impedances of the adopted inverters can only be measured [29].

6.1.3 Proposed Stability Analysis Method 1: Using Stability Criteria Multiple Times in Succession

Clearly, it is desirable to avoid the examination of the RHP poles of the impedance ratios, for inverter-based multi-bus ac systems with both voltage-controlled and current-controlled

inverters. The first proposed method is to add the system components one by one from nodes in the lowest level to areas in the highest system level and accordingly apply the stability criteria multiple times in succession, and the system is stable if all the stability check results indicate stability.

The terminal characteristics of system components can be classified into two types: impedance (*Z*) type and admittance (*Y*) type [95], [135], [136]. The terminal characteristic of passive components can be considered as *Z*-type in series connections and *Y*-type in parallel or meshed connections.

The terminal characteristics of current-controlled inverters and voltage-controlled inverters can be regarded as *Y*-type and *Z*-type without RHP poles, respectively, when the current and voltage control loops are designed as stable.

Except for mesh-type connections, the majority of the connection among these passive and active components in inverter-based ac systems can be categorized into the following groups.

1) **Type 1: *Y*+*Y* parallel-type connection**. It includes the parallel connection among current-controlled inverters, passive components as well as *Y*-type subsystems, as shown in Figure 6-8(a).

The equivalent admittance of the total subsystem Y_{eqc} is expressed in (6-7). Since the addition operation does not introduce extra RHP poles, *Y*+*Y* parallel-type connection is naturally stable, and the equivalent total subsystem is also *Y*-type as depicted in Figure 6-8(c).

$$Y_{eqc} = Y_l + Y_{oc1} + Y_{oc2} + Y_{sysc1} \tag{6-7}$$

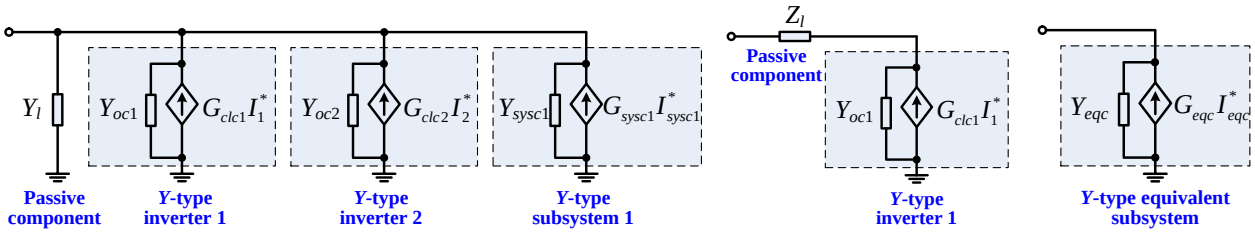

Figure 6-8. System connection and equivalent circuit. (a) *Y*+*Y* parallel-type connection; (b) *Y*+*Z* series-type connection; (c) *Y*-type equivalent subsystem.

2) **Type 2: *Y*+*Z* series-type connection**. It includes the series connection between a current-controlled inverter or a *Y*-type subsystem and a passive component, as shown in Figure 6-8(b). This type of connection is stable if and only if the impedance ratio T_m at the connection interface as expressed in (6-8) meets the Nyquist stability criterion [31]. The equivalent total subsystem is *Y*-type as depicted in Figure 6-8(c), with equivalent admittance Y_{eqc} as expressed in (6-9).

$$T_m = Y_{oc1} Z_l \tag{6-8}$$

$$Y_{eqc} = \frac{Y_{oc1}}{1 + Y_{oc1} Z_l} \tag{6-9}$$

3) **Type 3: *Z*+*Z* series-type connection**. It includes the series connection of a voltage-controlled inverter or a *Z*-type subsystem with a passive component, as shown in Figure 6-9(a). The equivalent impedance of the total subsystem Z_{eqv} is expressed in (6-10). Considering that the addition operation does not introduce extra RHP poles, *Z*+*Z* series-type connection is naturally stable, and the equivalent total subsystem is also *Z*-type as illustrated in Figure 6-9(d).

$$Z_{eqv} = Z_l + Z_{ov1} \tag{6-10}$$

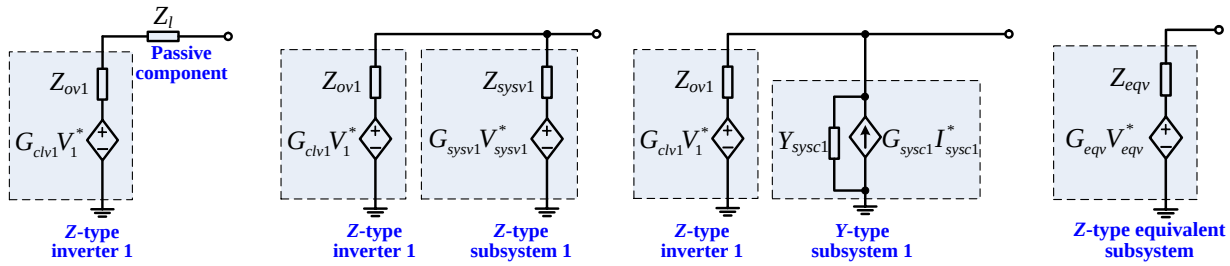

Figure 6-9. System connection and equivalent circuit. (a) *Z*+*Z* series-type connection; (b) *Z*+*Z* parallel-type connection; (c) *Z*+*Y* parallel-type connection; (d) *Z*-type equivalent subsystem.

4) **Type 4: *Z*+*Z* parallel-type connection**. It includes the parallel connection of voltage-controlled inverters and *Z*-type subsystems, as shown in Figure 6-9(b). This type of connection is stable if and only if the sum of the impedances meets the Impedance-Sum-Type Criterion [95], which is briefly described here. The Nyquist stability criterion is based on Cauchy's theorem, which is also called the principle of argument [55]. The impedance ratio T_m at the connection interface is expressed in (6-11), and the closed minor loop gain T_{clm} is expressed in (6-12).

$$T_m = \frac{Z_{ov1}}{Z_{sysv1}} \tag{6-11}$$

$$T_{clm} = \frac{1}{1+T_m} = \frac{Z_{sysv1}}{Z_{ov1} + Z_{sysv1}} \tag{6-12}$$

The system stability is related to the RHP zeros of the denominator of T_{clm}, which can be

estimated by the trajectory of the denominator in the complex plane according to Cauchy's theorem as shown in (6-13) or (6-14):

$$Z\left(1+T_m\right)=P\left(1+T_m\right)-N_{(0,\,j0)}\left(1+T_m\right) \tag{6-13}$$

$$Z\left(Z_{ov1}+Z_{sysv1}\right)=P\left(Z_{ov1}+Z_{sysv1}\right)-N_{(0,\,j0)}\left(Z_{ov1}+Z_{sysv1}\right) \tag{6-14}$$

where $N_{(0,\,j0)}(\ )$ denotes the number of times that the Nyquist trajectory encircles the critical point (0, j0) in anti-clockwise direction, and $N_{(0,\,j0)}(1+T_m)$ is equal to $N_{(-1,\,j0)}(T_m)$. The system is stable if and only if $Z(1+T_m)$ is zero or $Z(Z_{ov1}+Z_{sysv1})$ is zero. The direct application of Cauchy's theorem on (6-13) is equivalent to the application of Nyquist stability criterion on (6-11), which means that the RHP poles of the impedance ratio T_m still need to be checked. However, the application of Cauchy's theorem on (6-14) avoids the RHP pole calculation because $P(Z_{ov1}+Z_{sysv1})$ is 0.

The equivalent total subsystem is also *Z*-type as shown in Figure 6-9(d), and the total equivalent impedance Z_{eqv} is expressed in (6-15).

$$Z_{eqv}=\frac{Z_{ov1}Z_{sysv1}}{Z_{ov1}+Z_{sysv1}} \tag{6-15}$$

5) **Type 5: *Z*+*Y* parallel-type connection**. It includes the parallel connection between a voltage-controlled inverter or a *Z*-type subsystem and a passive component or a current-controlled inverter or a *Y*-type subsystem, as shown in Figure 6-9(c). The connected system is stable if and only if the impedance ratio at the connection interface as described in (6-16) meets the Nyquist stability criterion. The equivalent total subsystem is a *Z*-type subsystem as shown in Figure 6-9(d), and the total equivalent impedance Z_{eqv} is expressed in (6-17).

$$T_m = Y_{sysc1} Z_{ov1} \tag{6-16}$$

$$Z_{eqv} = \frac{Z_{ov1}}{1 + Y_{sysc1} Z_{ov1}} \tag{6-17}$$

The harmonic stability of meshed-type connections can be analyzed by using the proposed Method 2 which will be described in Section 6.1.4 to avoid the RHP pole calculation of impedance ratios, and one example will be given in Section 6.1.5.

Based on the aforementioned summary of all the connection types, the analysis procedure of the proposed Method 1 can be illustrated in Figure 6-10. The analysis is conducted from the lowest level (Level 1) to the highest level (system level). The sequence of adding components on each level is from the farthest terminal to the connection point with the higher level. And the harmonic stability of system-level meshed interconnections can be analyzed by the proposed Method 2 that will be presented in Section 6.1.4.

It should be mentioned that the subsystem assembled in the previous step should be stable before adding the next component. Therefore, the proposed Method 1 is conservative. There is a possibility that the addition of the next component can stabilize an unstable subsystem assembled in the previous step. However, such case can be avoided by the proposed Method 1.

The two-area system under study can be partitioned and re-assembled in five steps, and correspondingly the system harmonic stability can be assessed by five successive stability checks, as illustrated in Figure 6-11. For conciseness, only the stability analysis results in the positive-sequence domain are presented here.

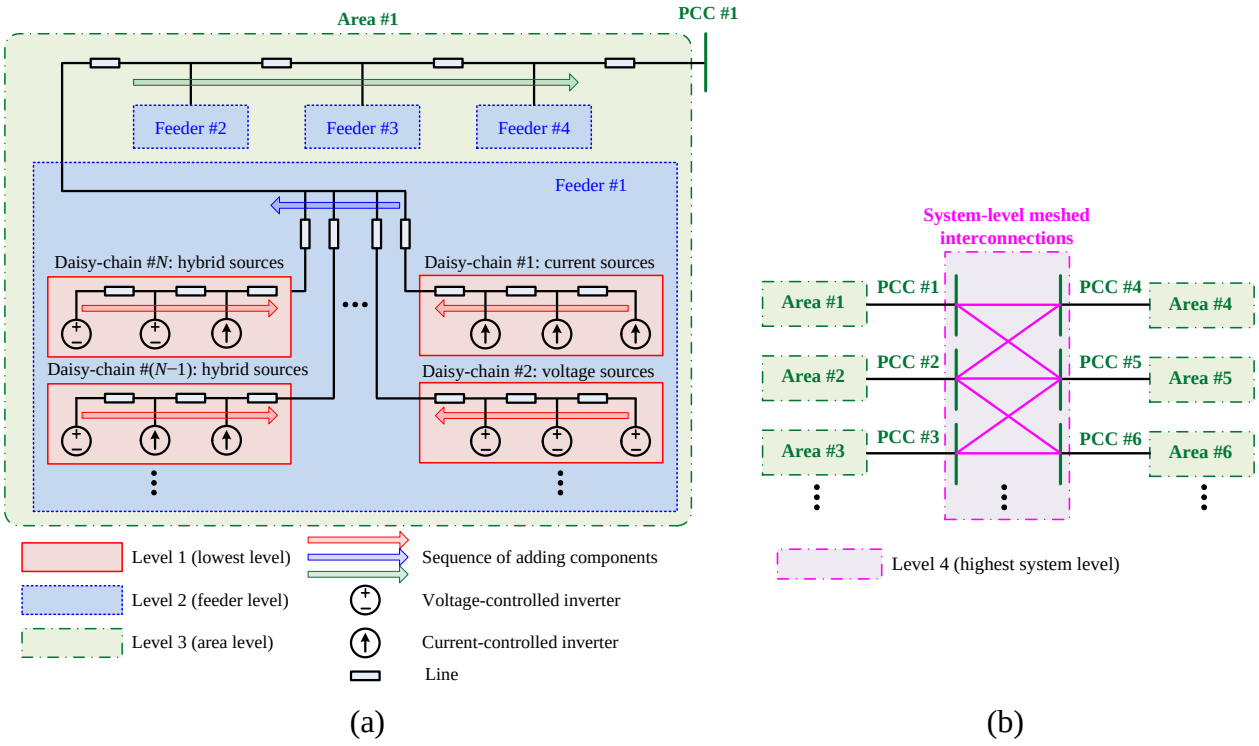

Figure 6-10. Illustration of analysis procedure for a general inverter-based multi-area system: (a) within one area, (b) system level.

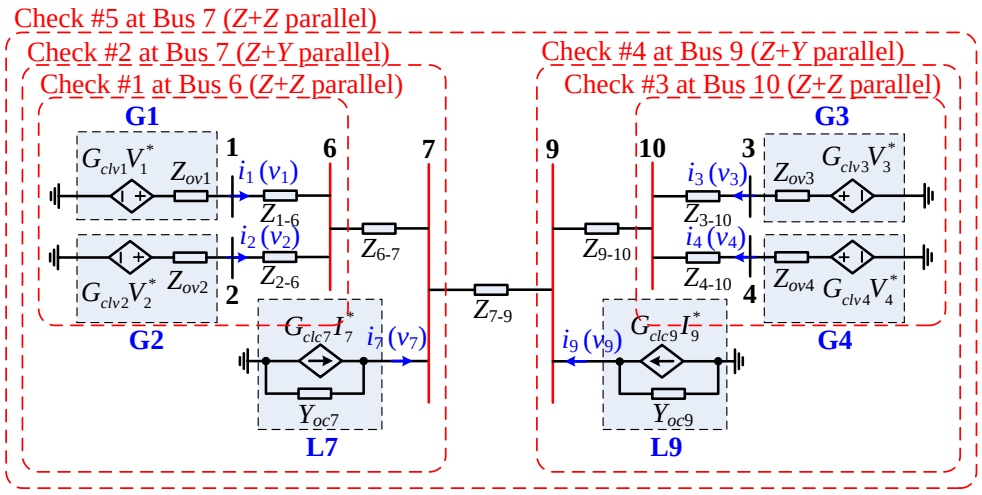

Figure 6-11. Stability analysis of the two-area system by five stability checks in succession.

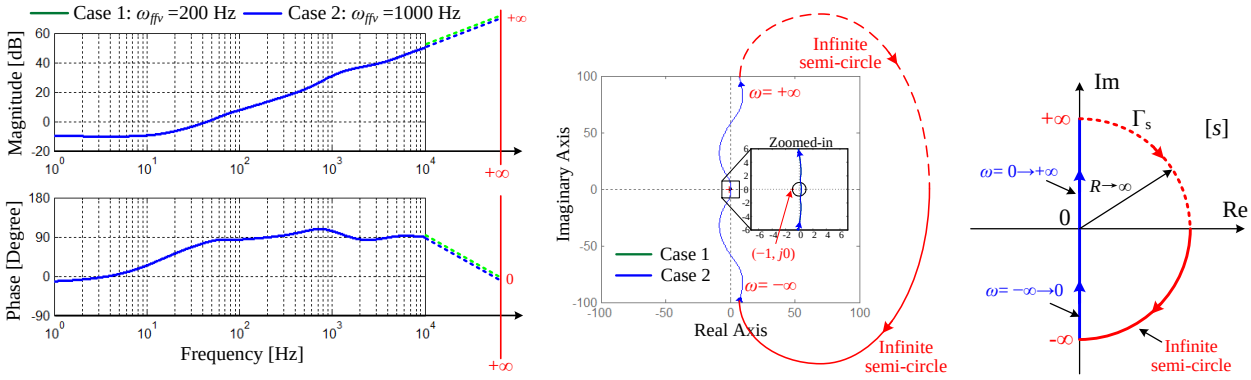

(a) (b) (c)

Figure 6-12. (a) Bode plot and (b) Nyquist diagram of the denominator $D_{clm\_C1\_p}(s)$ in Case 1 and Case 2. (c) Nyquist contour Γ_s in the *s*-plane.

Figure 6-12 shows the Bode plot and Nyquist diagram of the denominator $D_{clm\_C1\_p}(s)$ of the closed minor loop gain $T_{clm\_C1\_p}(s)$ as expressed in (6-18) for Check #1 at Bus 6 in both Case 1 and Case 2. It can be observed that as the frequency ω goes to infinity, the magnitude of $D_{clm\_C1\_p}(s)$ goes to infinity while the phase angle remains around 90 °. This is because the order of the numerator $D^{Num}_{clm\_C1\_p}(s)$ of $D_{clm\_C1\_p}(s)$ is one order higher than that of the denominator $D^{Den}_{clm\_C1\_p}(s)$, as defined in (6-19). For sequence admittances $Y_{oci\_p}(s)$ (i=7, 9) of current-controlled inverters, the order difference between the numerator and the denominator is −1, as seen from the −90° phase in the high frequency range in Figure 4-8(a). Similarly, the order difference is 1 for sequence impedance $Z_{ovj\_p}(s)$ (j=1−4) of voltage-controlled inverters, as observed in Figure 3-9. And the order difference is 1 for the inductive line impedance $Z_{lk\_p}(s)$.

$$T_{clm\_C1\_p}(s) = \frac{N_{clm\_C1\_p}(s)}{D_{clm\_C1\_p}(s)} = \frac{Z_{ov2\_p}(s) + Z_{2-6\_p}(s)}{Z_{ov1\_p}(s) + Z_{1-6\_p}(s) + Z_{ov2\_p}(s) + Z_{2-6\_p}(s)} \qquad (6\text{-}18)$$

$$D_{clm\_C1\_p}(s) = \frac{D_{clm\_C1\_p}^{Num}(s)}{D_{clm\_C1\_p}^{Den}(s)} \tag{6-19}$$

When drawing the Nyquist plot, the Nyquist trajectory segment corresponding to the infinite semi-circle in clockwise direction of the Nyquist contour Γ_s in the *s*-plane ([*s*]) as shown in Figure 6-12(c) should also be considered. When the numerator order is higher than the denominator order, such Nyquist trajectory segment is also an infinite semi-circle in clockwise direction in the Nyquist complex plane, as illustrated in Figure 6-12(b) and also presented as dash lines with phase angle changes of −90° between ω=10^4×2π rad/s and ω=+∞ in the Bode plot in Figure 6-12(a) to assist the explanation. By examining the positive frequency range of the Bode plot, 180 ° increase in the phase angle means encircling the (0, *j*0) point once in anti-clockwise direction while 180 ° decrease in the phase angle means encircling the (0, *j*0) point once in clockwise direction. According to the Bode plot of $D_{clm\_C1\_p}(s)$ in Figure 6-12(a), $N_{(0, j0)}(D_{clm\_C1\_p}(s))$=0 and thus $Z(D_{clm\_C1\_p}(s))$=0 based on Cauchy's theorem. Therefore, the connection at Bus 6 for Check #1 is stable in both Case 1 and Case 2 in the positive-sequence domain.

Figure 6-13(a) shows the Nyquist diagram of the impedance ratio $T_{m\_C2\_p}(s)$ for Check #2 at Bus 7 in the two cases. The trajectory in Case 1 does not encircle the point (−1, *j*0) but the trajectory in Case 2 encircles the point (−1, *j*0) twice in the clockwise direction. Therefore, the connection at Bus 7 for Check #2 is stable in Case 1 but unstable in Case 2 in the positive-sequence domain. According to the Nyquist trajectories, the gain margin is 5.9 dB and phase margin is 9.2° in Case 1, while the gain margin is −11.9 dB and phase margin is −11.6° in Case 2. Similar to Area 1, the Area 2 subsystem is stable in Case 1 but unstable in Case 2. Bode plot of the denominator $D_{clm\_C5\_p}(s)$ of the closed minor loop gain $T_{clm\_C5\_p}(s)$ for Check #5 at Bus 7 has

zero encirclement around the point (0, *j*0) in both cases, as shown in Figure 6-13(b). Therefore, the total two-area system is stable in Case 1 but unstable in Case 2.

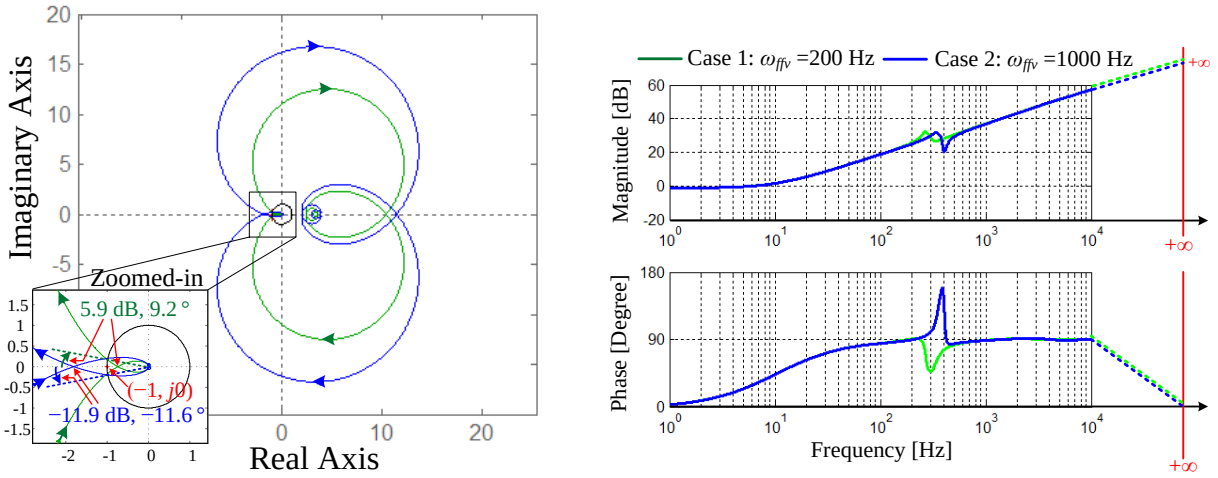

(a) (b)

Figure 6-13. (a) Nyquist diagram of the impedance ratio $T_{m\_C2\_p}(s)$ and (b) Bode plot of the denominator $D_{clm\_C5\_p}(s)$ in Case 1 and Case 2.

In the above harmonic stability analysis of the two-area system by using stability criteria multiple times in succession, calculation of the RHP poles of impedance ratios is avoided, which reduces the computation burden as compared to the stability analysis using the Nyquist criterion once. However, the proposed Method 1 is conservative, due to the requirement that the subsystem for every stability check should be stable. And the multi-step process could be tedious for complicated systems.

6.1.4 Proposed Stability Analysis Method 2: Using Proposed Stability Criterion Based on Cauchy's Theorem Once

A new impedance-based stability criterion is proposed here to assess the harmonic stability of inverter-based multi-bus systems without the need for the examination of the RHP poles of the impedance ratios. And it only needs one stability examination and the consequent stability condition is necessary and sufficient.

The closed minor loop gain T_{clm_B7} can be re-arranged to the form in

$$T_{clm\_B7} = \frac{N_{clm\_B7}\left(Y_{oci}, Z_{ovj}, Z_{lk}\right)}{D_{clm\_B7}\left(Y_{oci}, Z_{ovj}, Z_{lk}\right)} \tag{6-20}$$

where the numerator N_{clm_B7} and the denominator D_{clm_B7} in the modified form are functions of the impedances or admittances of all individual components, including the admittances of current-controlled inverters Y_{oci} (i=7, 9), the impedances of voltage-controlled inverters Z_{ovj} (j=1−4), and the line impedances Z_{lk} . More importantly, these functions only involve multiplication and addition operations. To be clear, examples of this modified form include the second expression of Y_{B7L} in (6-1) and the expression of $T_{clm\_C1\_p}(s)$ in (6-18).

The underlying principle of the impedance-based stability analysis using Cauchy's theorem is explained as follows. Because each inverter is designed to operate stably alone, Y_{oci} and Z_{ovj} are all stable without RHP poles. The line impedances Z_{lk} are passive and thus stable without RHP poles. Since the multiplication and addition operations do not introduce additional RHP poles, both N_{clm_B7} and D_{clm_B7} have zero RHP poles. Therefore, the system stability is determined by the RHP zeros of D_{clm_B7}, which can be estimated by (6-21) based on Cauchy's theorem. The system is stable if and only if $N_{(0,\, j0)}(D_{clm\_B7})$ is zero. By using the modified form of

T_{clm_B7} for stability analysis, the RHP pole calculation is avoided.

$$Z\left(D_{clm\_B7}\right)=P\left(D_{clm\_B7}\right)-N_{(0,j0)}\left(D_{clm\_B7}\right)=-N_{(0,j0)}\left(D_{clm\_B7}\right) \tag{6-21}$$

The previous two cases are analyzed again using the proposed stability criterion. Figure 6-14 displays the Bode plots of the denominators D_{clm_B7} in the modified form in Case 1 and Case 2 in both the positive-sequence domain $D_{clm\_B7\_p}(s)$ and the negative-sequence domain $D_{clm\_B7\_n}(s)$. The corresponding Nyquist diagrams are presented in Figure 6-15. The phase angles of $D_{clm\_B7\_p}(s)$ in Case 1 remain around 270 ° when the frequency is high, because the order of the numerator $D^{Num}_{clm\_B7\_p}(s)$ of $D_{clm\_B7\_p}(s)$, as defined in (6-22), is higher than the order of the denominator $D^{Den}_{clm\_B7\_p}(s)$, and the order difference is 3. The same goes for $D_{clm\_B7\_n}(s)$ in the negative-sequence domain. Considering the infinite semi-circle segments of Nyquist trajectories, the phase angles decrease by 90 °×3=270 ° from $\omega=10^4\times 2\pi$ rad/s to $\omega=+\infty$ in Figure 6-14.

$$D_{clm\_B7\_p}(s)=\frac{D^{Num}_{clm\_B7\_p}(s)}{D^{Den}_{clm\_B7\_p}(s)};\quad D_{clm\_B7\_n}(s)=\frac{D^{Num}_{clm\_B7\_n}(s)}{D^{Den}_{clm\_B7\_n}(s)} \tag{6-22}$$

According to the Bode plots of $D_{clm\_B7\_p}(s)$ in Figure 6-14(a), the overall net phase variations in the frequency range of [0, +∞) are 0° in Case 1 but −180°×4=−720° in Case 2. It means that $N_{(0,\ j0)}(D_{clm\_B7\_p}(s))=0$ and thus $Z(D_{clm\_B7\_p}(s))=0$ in Case 1, while $N_{(0,\ j0)}(D_{clm\_B7\_p}(s))=-4$ and thus $Z(D_{clm\_B7\_p}(s))=4$ in Case 2. As for the Bode plots of $D_{clm\_B7\_n}(s)$ in Figure 6-14(b), $N_{(0,\ j0)}(D_{clm\_B7\_n}(s))=0$ and thus $Z(D_{clm\_B7\_n}(s))=0$ in both Case 1 and Case 2. Therefore, the multi-bus ac system under study is stable in Case 1, while it is unstable in Case 2 and the instability occurs in the positive-sequence system.

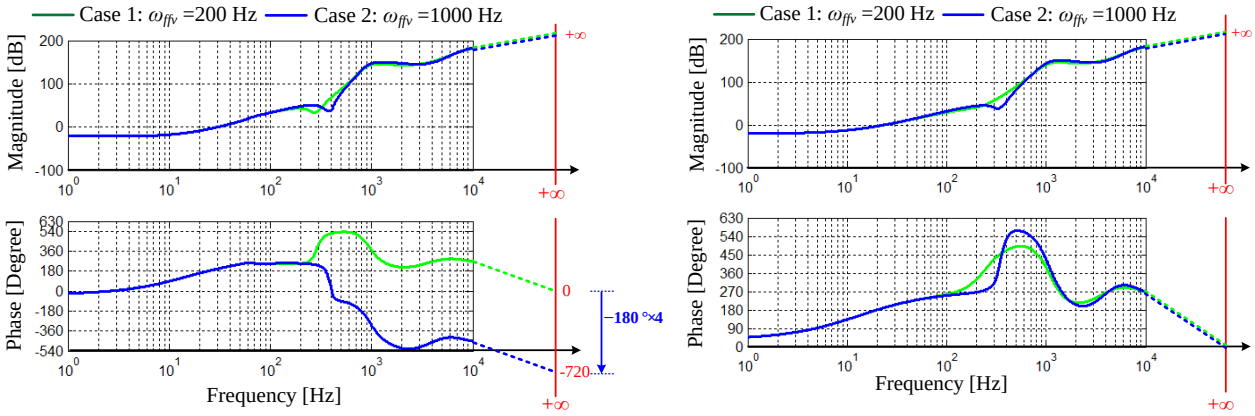

(a) (b)

Figure 6-14. Bode plots of denominators in the modified form in Case 1 and Case 2: (a) $D_{clm\_B7\_p}(s)$ and (b) $D_{clm\_B7\_n}(s)$.

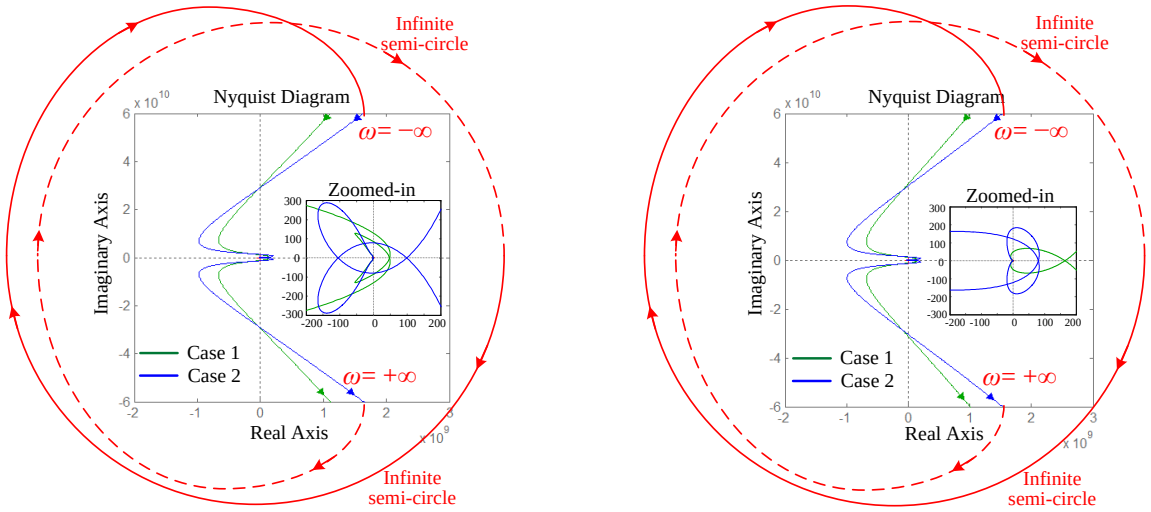

(a) (b)

Figure 6-15. Nyquist diagrams of denominators in the modified form in Case 1 and Case 2: (a) $D_{clm\_B7\_p}(s)$ and (b) $D_{clm\_B7\_n}(s)$.

In summary, the proposed stability criterion based on Cauchy's theorem can be described as follows:

Step 1: Get the frequency responses of stable sequence admittances Y_i or impedances Z_j of all components in the system, which can be obtained by impedance measurement, or from the Bode plots of the transfer functions of the sequence admittances or impedances. Determine the order difference between the numerator and the denominator of each Y_i or Z_j.

Step 2: Divide the total system into two subsystems at any bus, and derive the expression of the closed-loop gain T_{clm} of the impedance ratio T_m as functions of Y_i and Z_j.

Step 3: Change the form of T_{clm} into $T_{clm} = N_{clm} / D_{clm}$, where N_{clm} and D_{clm} are functions of Y_i and Z_j with only multiplication and addition operations.

Step 4: Check the order difference between the numerator and denominator of D_{clm}, by examining each summation term in D_{clm}, in order to determine the phase angle change of D_{clm} corresponding to the infinite semi-circle segments of Nyquist trajectories.

Step 5: Draw the Nyquist or Bode plots of D_{clm} and count the encirclement of the point $(0, j0)$ in anti-clockwise direction, $N_{(0, j0)}(D_{clm})$. The system is stable if and only if $N_{(0, j0)}(D_{clm})$ is zero.

The above steps should be executed in both the positive-sequence domain and the negative-sequence domain. The proposed stability criterion is a necessary and sufficient condition and the RHP poles calculation is avoided, which reduces the computation effort and enables the stability assessment when the component impedances can only be measured. It is worth noting that the reformation in *Step 3* can be done in MATLAB using the `collect` command for symbolic expressions.

6.1.5 Application of Proposed Method 2 to Meshed Systems

In order to demonstrate the effectiveness of the proposed Method 2 in the harmonic stability analysis of meshed systems, one three-bus meshed system is configured with two voltage-controlled inverters G1 and G3 and one current-controlled inverter L2 connected to Bus 1, Bus 3 and Bus 2, respectively, as shown in Figure 6-16(a).

The inverter parameters are the same as those listed in Table 3-1, Table 3-2 and Table 3-3, except the values of ω_{ffv} in Case 11 (ω_{ffv}=200×2π rad/s) and Case 12 (ω_{ffv}=1000×2π rad/s). The impedances of three lines are Z_1=$Z_{1\text{-}6}$, Z_2=$Z_{2\text{-}6}$, and Z_3=$Z_{6\text{-}7}$, respectively, where $Z_{1\text{-}6}$, $Z_{2\text{-}6}$, and $Z_{6\text{-}7}$ are given in Table 6-1. The operating point of the meshed system is the same as that listed in Table 6-2.

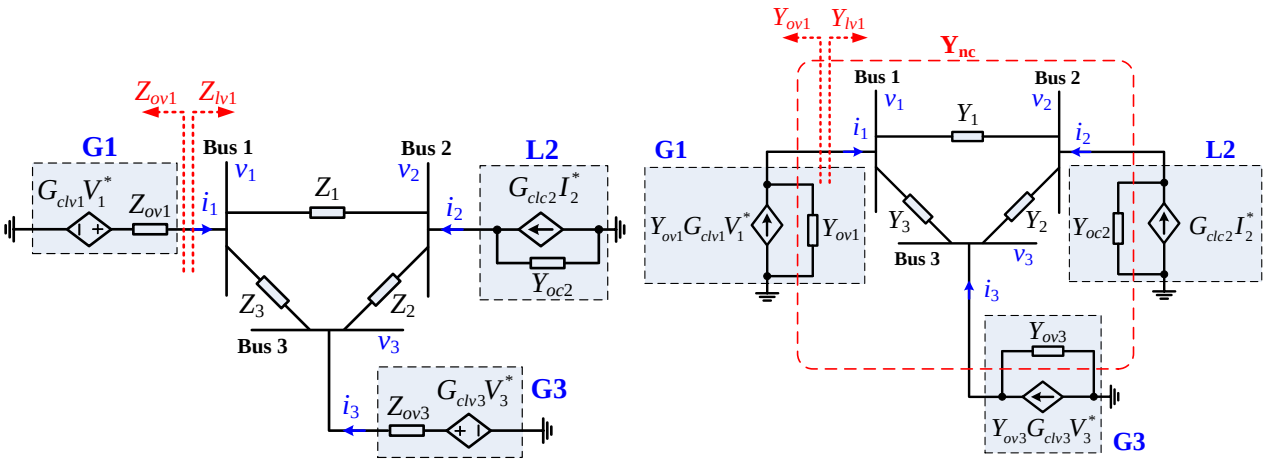

Figure 6-16. Impedance-based circuits of the meshed system: (a) original circuit and (b) equivalent Norton circuit.

The application of the proposed Method 2 is described as follows. For conciseness, only the harmonic stability analysis in the positive-sequence domain is presented.

Step 1: The sequence impedances Z_{ov1} and Z_{ov3} of G1 and G3 and the sequence admittance Y_{oc2} of L2 are described in Section 3.1 and Section 3.2. The sequence impedances of lines are presented in Section 6.1.2.

Step 2: The meshed system is divided into two subsystems with impedances Z_{ov1} and Z_{lv1}, respectively, at Bus 1. The impedance ratio T_{m_B1} and the closed minor loop gain T_{clm_B1} at Bus 1 are expressed in (6-23) and (6-24), which can be derived based on the method developed in [23].

$$T_{m\_B1} = \frac{Z_{ov1}}{Z_{lv1}} = \frac{1}{T_{clm\_B1}} - 1 \tag{6-23}$$

$$T_{clm\_B1} = \frac{1}{1+T_{m\_B1}} = \frac{1}{1+\frac{Z_{ov1}}{Z_{lv1}}} \tag{6-24}$$

By replacing the Thevenin models of G1 and G3 with their equivalent Norton models, the system impedance-based circuit is depicted in Figure 6-16(b) with some variables defined in (6-25) and (6-26).

$$Y_{ov1} = \frac{1}{Z_{ov1}}, Y_{ov3} = \frac{1}{Z_{ov3}} \tag{6-25}$$

$$Y_1 = \frac{1}{Z_1}, Y_2 = \frac{1}{Z_2}, Y_3 = \frac{1}{Z_3}, Y_{lv1} = \frac{1}{Z_{lv1}} \tag{6-26}$$

Based on the system nodal admittance matrix $\mathbf{Y_{nc}}$, T_{clm_B1} can be obtained as (6-27), where Y_{nom} is expressed in (6-28). Then T_{m_B1} can be derived by substituting (6-27) into (6-23).

$$T_{clm\_B1} = \frac{Y_{ov1}\left[Y_1Y_2 + Y_1Y_3 + Y_2Y_3 + \left(Y_2 + Y_3\right)Y_{oc2} + \left(Y_1 + Y_2 + Y_{oc2}\right)Y_{ov3}\right]}{Y_{nom}} \tag{6-27}$$

$$\begin{aligned} Y_{nom} &= \left(Y_1Y_2 + Y_1Y_3 + Y_2Y_3\right)\left(Y_{ov1} + Y_{ov3} + Y_{oc2}\right) \\ &+ \left(Y_1 + Y_2 + Y_{oc2}\right)Y_{ov1}Y_{ov3} + \left[\left(Y_2 + Y_3\right)Y_{ov1} + \left(Y_1 + Y_3\right)Y_{ov3}\right]Y_{oc2} \end{aligned} \tag{6-28}$$

As illustrated in Figure 6-17, although the Nyquist plot of the positive-sequence impedance ratio $T_{m\_B1\_p}(s)$ has zero encirclement of the critical point (−1, *j*0) in both cases, one RHP pole exists in Case 12. It should be noted that another conjugate RHP pole exists in the negative-sequence domain in Case 12. Therefore, the meshed system is stable in Case 11 but unstable in Case 12. According to the pole-zero maps of the positive-sequence closed minor loop gain $T_{clm\_B1\_p}(s)$ as shown in Figure 6-18(a), the unstable frequency of the system RHP pole in Case 12 is 443 Hz in the positive-sequence domain.

Step 3: After substituting (6-25) into (6-27), the closed minor loop gain T_{clm_B1} is reformatted as (6-29), with the numerator N_{clm_B1} and the denominator D_{clm_B1} in the modified forms as expressed in (6-30) and (6-31).

$$T_{clm\_B1} = \frac{N_{clm\_B1}}{D_{clm\_B1}} \tag{6-29}$$

$$N_{clm\_B1} = Y_1 + Y_2 + Y_{oc2} + \left(Y_1Y_2 + Y_1Y_3 + Y_2Y_3\right)Z_{ov3} + \left(Y_2 + Y_3\right)Y_{oc2}Z_{ov3} \tag{6-30}$$

$$\begin{aligned} D_{clm\_B1} &= Y_1 + Y_2 + Y_{oc2} \\ &+ \left(Y_1Y_2 + Y_1Y_3 + Y_2Y_3\right)\left(Z_{ov1} + Z_{ov3} + Y_{oc2}Z_{ov1}Z_{ov3}\right) \\ &+ \left[\left(Y_1 + Y_3\right)Z_{ov1} + \left(Y_2 + Y_3\right)Z_{ov3}\right]Y_{oc2} \end{aligned} \tag{6-31}$$

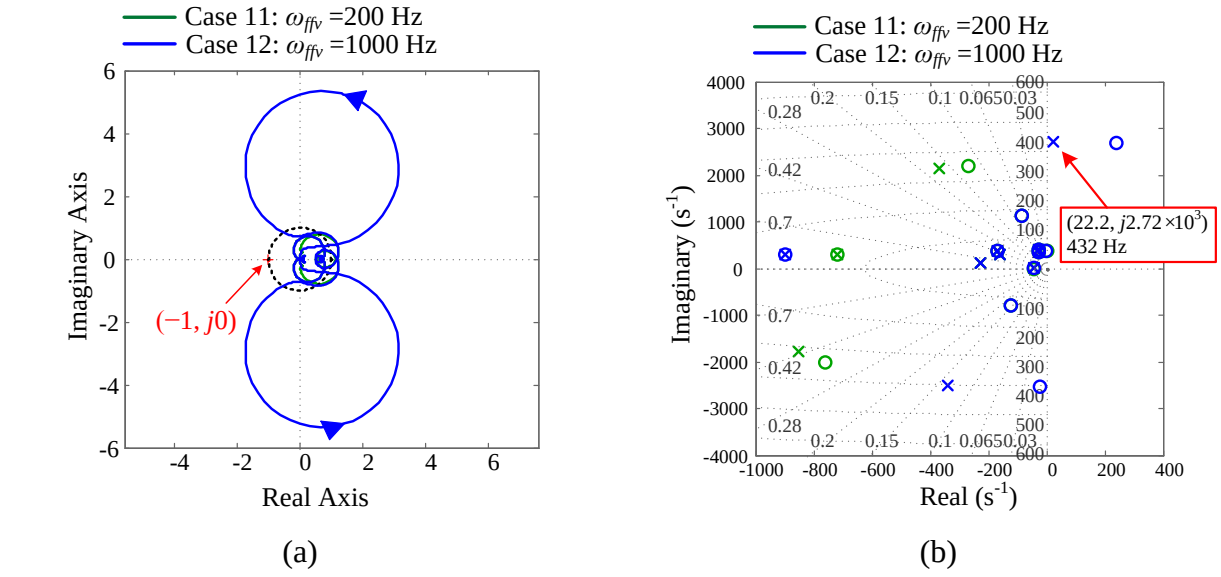

Figure 6-17. (a) Nyquist diagrams and (b) pole-zero maps of the positive-sequence impedance ratios $T_{m\_B1\_p}(s)$ at Bus 1 of the meshed system in Case 11 and Case 12.

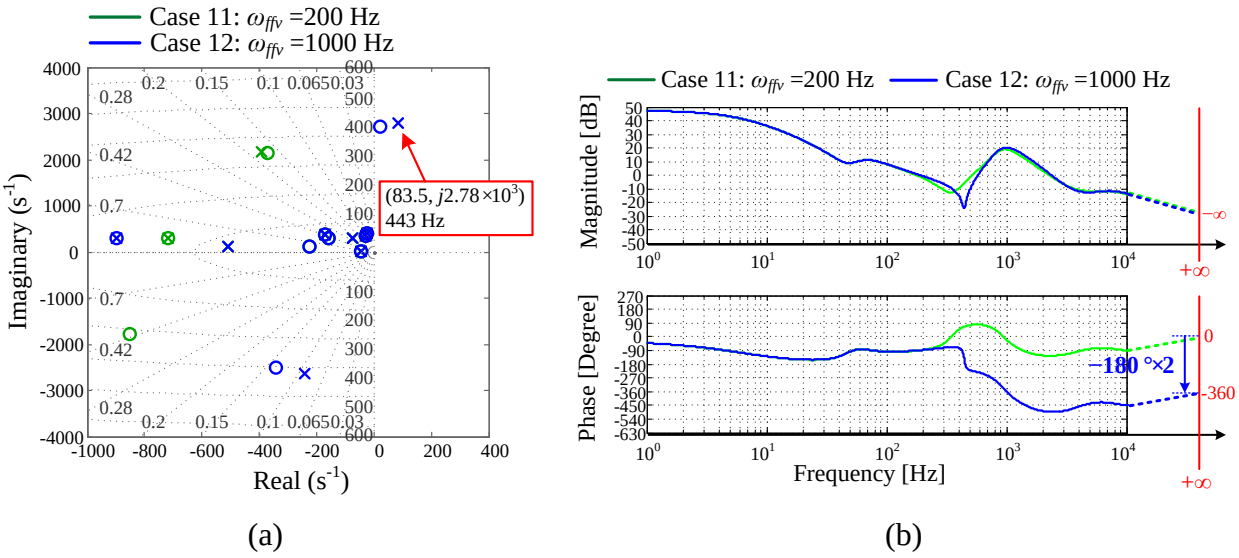

Figure 6-18. (a) Pole-zero maps of the positive-sequence closed-loop gains $T_{clm\_B1\_p}(s)$ and (b) Bode plots of the denominators $D_{clm\_B1\_p}(s)$ in the modified form in Case 11 and Case 12.

Step 4: There is one more *Y*-type variable than *Z*-type variables in each summation term in D_{clm_B1}. Therefore, the order difference between the numerator and the denominator of $D_{clm\_B1}(s)$ is −1, and the phase angle change of $D_{clm\_B1}(s)$ is an increment of 90 °, corresponding to the infinite semi-circle segments of Nyquist trajectories.

Step 5: According to the Bode plots of the positive-sequence denominator $D_{clm\_B1\_p}(s)$ of $T_{clm\_B1\_p}(s)$ as illustrated in Figure 6-18(b), the overall net phase variations in the frequency range of [0, +∞) are 0° in Case 11 but −180°×2=−360° in Case 12. It indicates that $N_{(0, j0)}(D_{clm\_B1\_p}(s))$ is 0 in Case 11 but −2 in Case 12, and the meshed system is stable in Case 11 but unstable in Case 12 with two RHP poles.

The aforementioned analysis shows that the proposed Method 2 can correctly analyze the harmonic stability of meshed systems without the need for the RHP pole calculation of the impedance ratios. The experimental verification will be presented in Section 6.3.4.

6.1.6 Comparison of Stability Analysis Methods

The aforementioned three methods for stability analysis of inverter-based multi-bus systems have been compared regarding 1) necessity and sufficiency, 2) requirement on impedance model details, 3) RHP pole calculation of the impedance ratio, 4) number of stability checks, 5) computation time and 6) stability margins (gain margin and phase margin), as shown in Table 6-3. As compared with the existing method, the proposed Method 1 and Method 2 not only have less strict requirements on the impedance models, which enables the stability assessment using measured impedances, but also take significantly less computation time by avoiding formulating the transfer function of the impedance ratio and calculating the RHP poles of the impedance ratio.

Table 6-3. Comparison of different stability analysis methods.

	Existing method (using Nyquist stability criterion once)	**Proposed Method 1 (using stability criteria multiple times in succession)**	**Proposed Method 2 (using proposed stability criterion based on Cauchy's theorem once)**
Necessity and sufficiency	Necessary and sufficient	Sufficient	Necessary and sufficient
Requirement on impedance model details	Transfer function models of impedances, which require the detailed internal control information of inverters.	Frequency response data of impedances, which can be generated by the transfer function models or measured without the need for internal control details.	Frequency response data of impedances, which can be generated by the transfer function models or measured without the need for internal control details.
RHP pole calculation of the impedance ratio	Required	Avoided	Avoided
Number of stability checks	One	Multiple	One
Computation time*	169.0 s	6.5 s	2.5 s
Stability margins (gain margin and phase margin)	Can tell the stability margins if the Nyquist trajectory intersects the unit circle.	(1) For stability checks using Nyquist criterion: can tell the stability margins if the Nyquist trajectory intersects the unit circle. (2) For stability checks using Cauchy's theorem: cannot tell the stability margins.	Cannot tell the stability margins.

*: Frequency response data: 10000 logarithmically equally spaced points between 10^{-2} Hz and 10^{5} Hz. Computation time listed here is an average value for computation with MATLAB using a second generation Intel® Core™ i7 quad-core CPU.

6.2 Controller Parameter Design of Inverter-Based Multi-Bus Systems

6.2.1 Controller Parameter Design Process

For inverter-based multi-bus ac systems with multiple voltage-controlled and current-controlled inverters, it is not easy to design the controller parameters of each inverter individually because the system stability is determined by the inter-connection of all inverters.

Before interconnecting all inverters to construct the system, each individual inverter should be designed to be stable internally (with ideal external conditions), and the parameter range for *internal stability* of each inverter can be obtained. The aforementioned harmonic stability analysis methods can be repetitively applied for all the parameter sets within the parameters ranges with *internal stability*, in order to obtain the stable regions, unstable regions and stability boundaries in the parameter space for the multi-bus system stability or *external interconnection stability* of all inverters. Considering that the existing method is time-consuming, the proposed Method 1 and Method 2 can be used for this iteration-type design process. It is worth noting that, although the proposed Method 2 cannot tell the traditional gain or phase margins, the achieved stability boundary in the parameter space can still tell the stability margin from a different aspect, that is, the distance from the stability boundary.

For simplicity, it is assumed that all voltage-controlled inverters have same controller parameters and all current-controlled inverters have same controller parameters in the two-area system. And the cut-off frequency ω_{ffv} of the voltage feed-forward control and the current loop bandwidth ω_c of all current-controlled inverters as well as the voltage loop bandwidth ω_v of all voltage-controlled inverters are chosen to be designed. The values of ω_c and ω_v are achieved by setting the PI controller parameters as (6-32).

$$\begin{cases} K_{cp} = \omega_c L_f, \quad K_{ci} = 875 K_{cp} \\ K_{vp} = \omega_v \left(2T_s + \dfrac{1}{\omega_{fv}} \right), \quad K_{vi} = \omega_v \end{cases} \tag{6-32}$$

According to the Bode plots of the stable open-loop gains of the current-controlled inverters, $T_{c\_p}(s)$, and the voltage-controlled inverters, $T_{v\_p}(s)$, in the positive-sequence domain as shown in Figure 6-19, the value of ω_c is confined in the range of [100×2π rad/s, 1000×2π rad/s] for *internal stability* of current-controlled inverters, and the value of ω_v is confined in the range of [50×2π rad/s, 500×2π rad/s] for *internal stability* of voltage-controlled inverters. Since ω_{ffv} only changes the sequence admittances but does not change the current-loop stability of current-controlled inverters, the value of ω_{ffv} is confined in the range of [100×2π rad/s, 1000×2π rad/s].

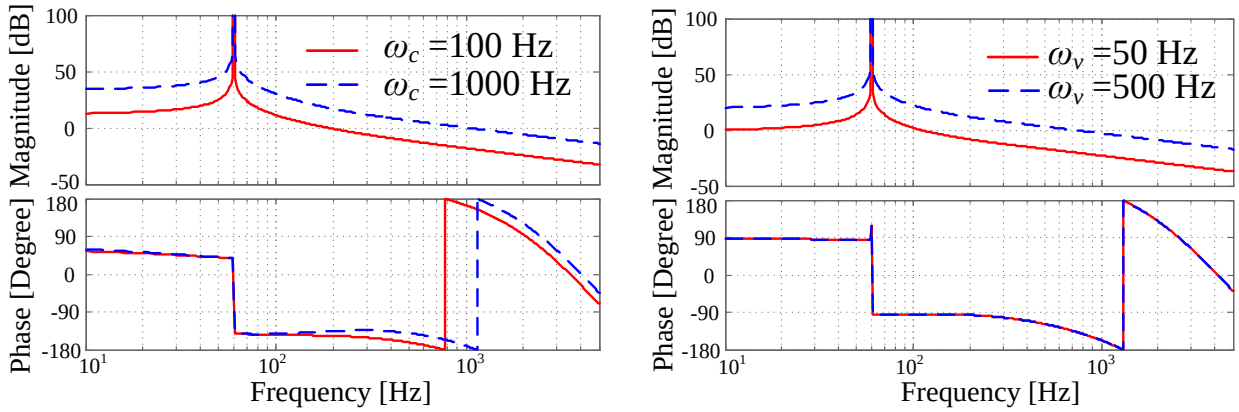

Figure 6-19. Bode plots of the open-loop gains of (a) the current-controlled inverters $T_{c\_p}(s)$ and (b) voltage-controlled inverters $T_{v\_p}(s)$ in the positive-sequence domain.

6.2.2 Design Results of the Two-Area System

The design results of the parameter pair (ω_{ffv} and ω_c) are presented in the two-dimensional maps in Figure 6-20 with ω_v equal to 170×2π rad/s. The design results of the parameter pair (ω_v and ω_c) are shown in Figure 6-21(a) with ω_{ffv} equal to 100×2π rad/s and Figure 6-21(b) with ω_{ffv} equal to 200×2π rad/s.

Since the system in the negative-sequence domain in the selected parameter space happens to be always stable, only the design results for the system in the positive-sequence domain are presented here.

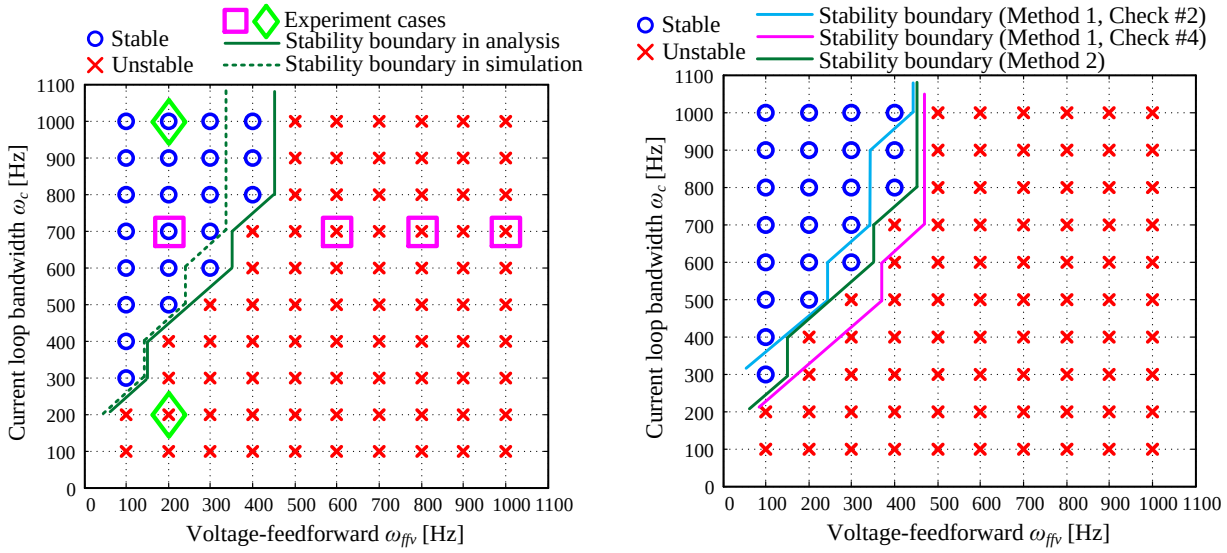

(a) (b)

Figure 6-20. (a) Stability regions and stability boundaries in the map of the parameter pair (ω_{ffv} and ω_c) using the proposed Method 2. (b) Comparison of the stability boundaries generated using the proposed Method 1 and Method 2.

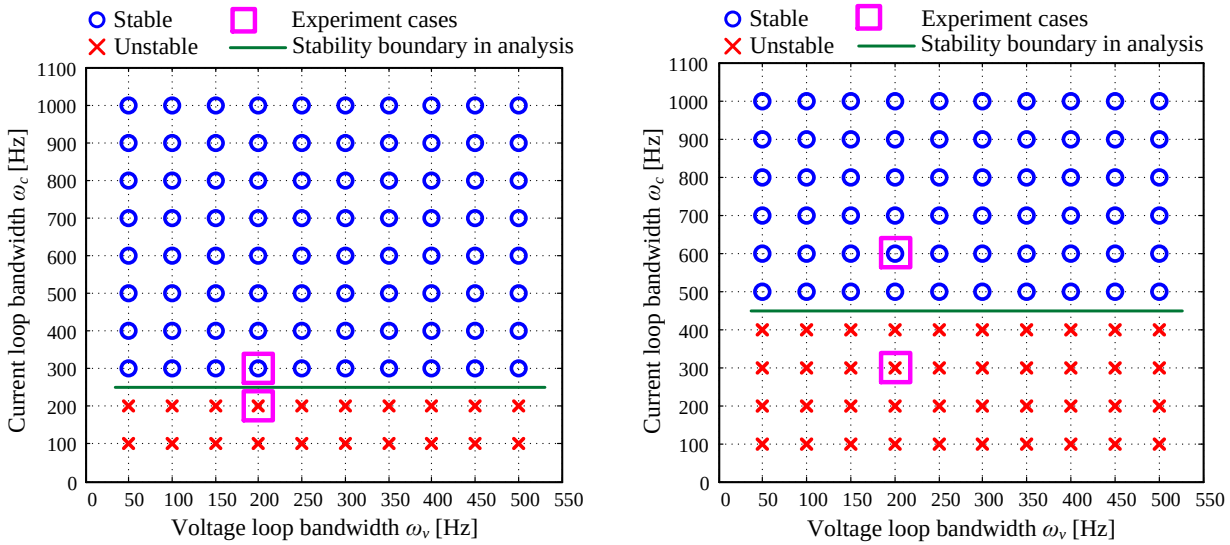

(a) (b)

Figure 6-21. Stability regions and stability boundaries in the map of the parameter pair (ω_v and ω_c) using the proposed Method 2. (a) ω_{ffv} is 100×2π rad/s, (b) ω_{ffv} is 200×2π rad/s.

Figure 6-20(b) shows that the stability region generated using Method 1 (limited by Check #2) is relatively smaller than that generated using Method 2, which exhibits the conservativeness of Method 1. In addition, some general design rules for the studied two-area system can be derived. 1) The cut-off frequency ω_{ffv} of the voltage feedforward control cannot be very large. Larger ω_{ffv} makes the system more prone to instability. 2) The cut-off frequency ω_{ffv} of the voltage feedforward control should be smaller than the current loop bandwidth ω_c. 3) The stability is mainly affected by the parameter ω_{ffv} instead of ω_v.

The stability boundaries obtained from the simulation results using MATLAB/Simulink are also shown in Figure 6-20(a). The small but acceptable discrepancy between the analysis results and the simulation results near the stability boundaries is due to the limitation of the model accuracy described in Section 3.3.

6.3 Experimental Verification

6.3.1 Experimental Setup

The experimental platform for scaled-down emulation of the two-area system using three-phase inverters and inductors has been set up, as shown in Figure 6-22. The three-phase inverter as the emulator consists of the 75 kW-power stage from Vacon company and a customized interface board with TMS320F28335 DSP of Texas Instruments.

In the following experiments, the inverters run under a condition with power lower than their listed power rating. The parameters of the inverters and inductors as well as the system operating points are the same as those listed in Table 3-1, Table 6-1 and Table 6-2.

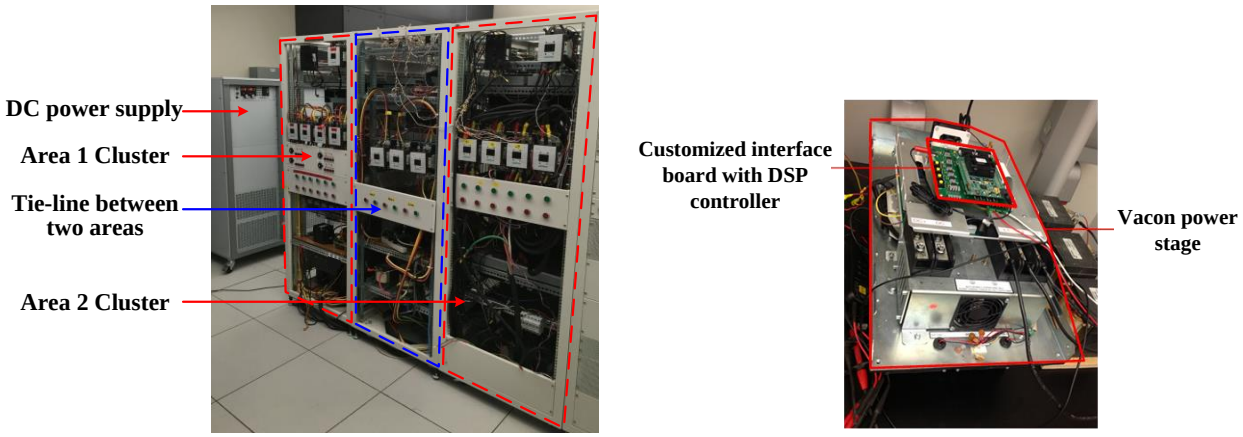

(a) (b)

Figure 6-22. Experimental setup of the inverter-based multi-bus ac system. (a) Photo of the total system. (b) Photo of the three-phase inverter.

6.3.2 Design Verification of the Parameter Pair (ω_{ffv} and ω_c)

In order to verify the design results of the parameter pair (ω_{ffv} and ω_c) presented in the parameter map in Figure 6-20(a), several experimental cases have been carried out, which are also marked as purple squares and green diamonds in Figure 6-20(a).

In the first case group (purple squares), ω_c is 700×2π rad/s and ω_v is 170×2π rad/s, while ω_{ffv} has four different values: 200×2π rad/s (Case 1), 1000×2π rad/s (Case 2), 800×2π rad/s (Case 3) and 600×2π rad/s (Case 4).

Figure 6-23 shows the experimental waveforms of the phase-A currents of G2, G4, L7 and L9 in the two-area system when ω_{ffv} changes from 200×2π rad/s to 1000×2π rad/s. It can be seen that the system changes from a stable state to an unstable state, which verifies the stability analysis in Section 6.1.

Figure 6-24(a) and Figure 6-24(b) display the experimental results of the system in the unstable state when ω_{ffv} is 800×2π rad/s and 600×2π rad/s, respectively, which verifies the parameter design results shown in Figure 6-20(a).

In the second case group (green diamonds), ω_v is 170×2π rad/s and ω_{ffv} is 200×2π rad/s, while ω_c has two different values: 1000×2π rad/s (Case 5) and 200×2π rad/s (Case 6).

Figure 6-25 illustrates the experimental results when ω_c changes from 1000×2π rad/s to 200×2π rad/s. The system changes from a stable state to an unstable state, which verifies the parameter design results shown in Figure 6-20(a).

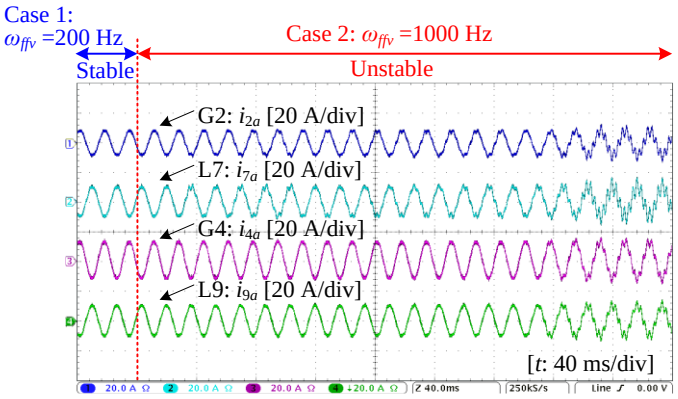

(a)

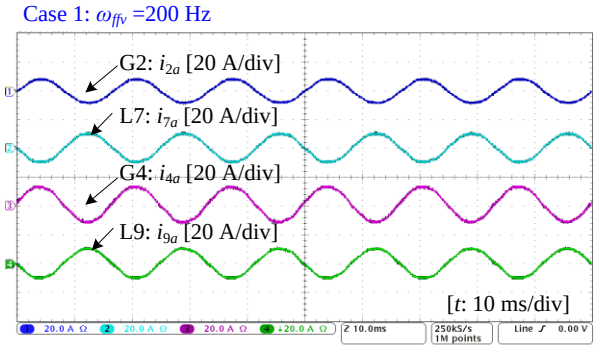

(b)

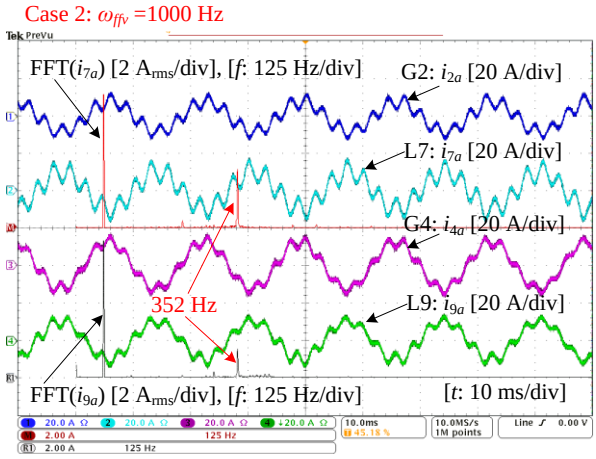

(c)

Figure 6-23. Experimental results when ω_{ffv} changes from 200×2π rad/s to 1000×2π rad/s. (a) System transition from stable state to unstable state. (b) System in stable state when ω_{ffv} is 200×2π rad/s. (c) System in unstable state when ω_{ffv} is 1000×2π rad/s.

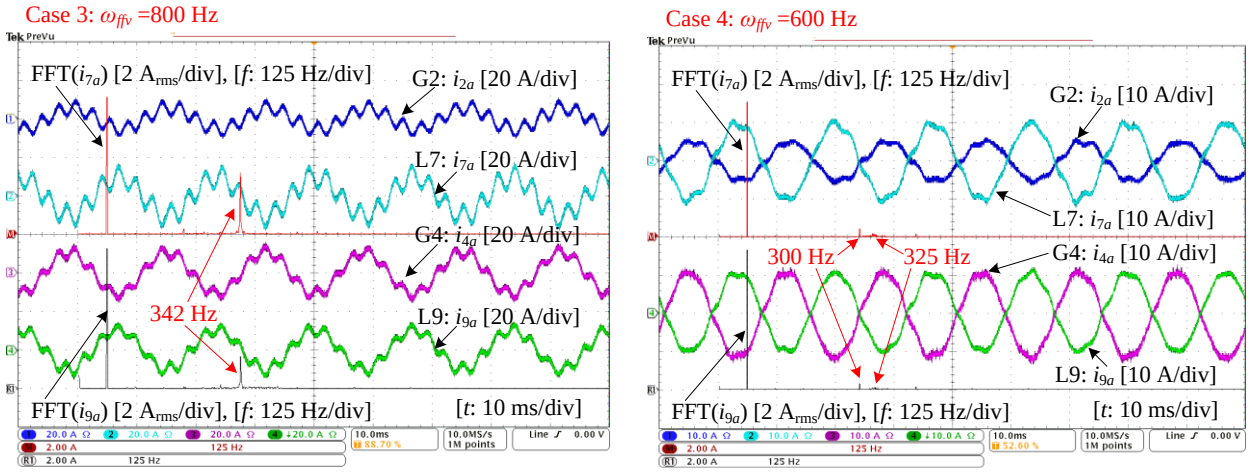

(a) (b)

Figure 6-24. Experimental results of the system in unstable state. (a) ω_{ffv} is 800×2π rad/s. (b) ω_{ffv} is 600×2π rad/s.

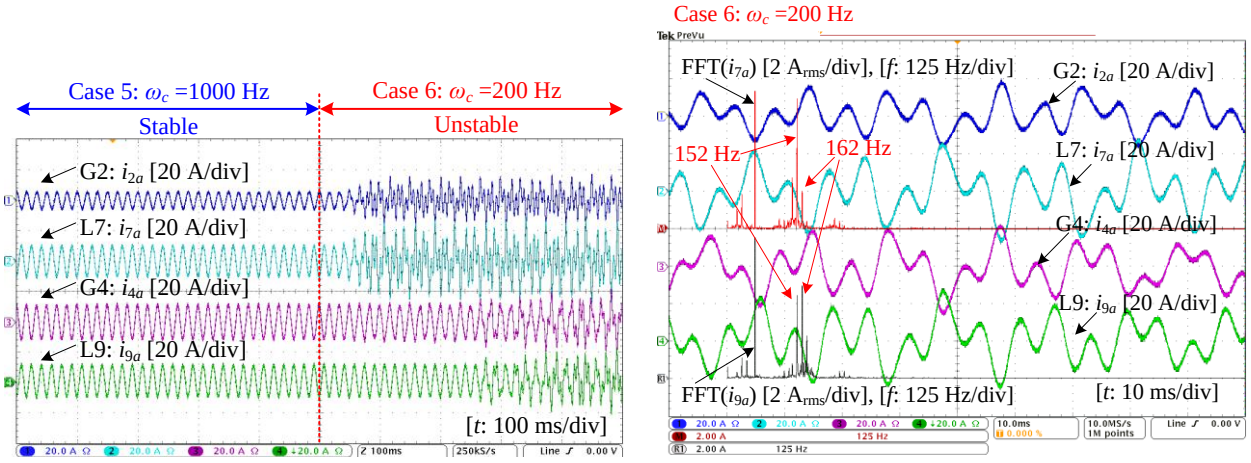

(a) (b)

Figure 6-25. Experimental results when ω_c changes from 1000×2π rad/s to 200×2π rad/s. (a) System transition from a stable state to an unstable state. (b) System in unstable state when ω_c is 200×2π rad/s.

6.3.3 Design Verification of the Parameter Pair (ω_v and ω_c)

Additional four experimental cases, marked as purple squares in Figure 6-21, have been performed to verify the design results of the parameter pair (ω_v *and* ω_c) presented in the parameter maps in Figure 6-21. In the first case group, ω_v is 200×2π rad/s and ω_{ffv} is 100×2π rad/s, while ω_c changes from 300×2π rad/s (Case 7) to 200×2π rad/s (Case 8). The experimental results presented in Figure 6-26(a) show that the system changes from a stable state to an unstable state, which verifies the parameter design results shown in Figure 6-21(a). In the second case group, ω_v is still 200×2π rad/s, but ω_{ffv} is changed to 200×2π rad/s, while ω_c changes from 600×2π rad/s (Case 9) to 300×2π rad/s (Case 10). As illustrated in Figure 6-26(b), the system changes from a stable state to an unstable state, which verifies the parameter design results shown in Figure 6-21(b).

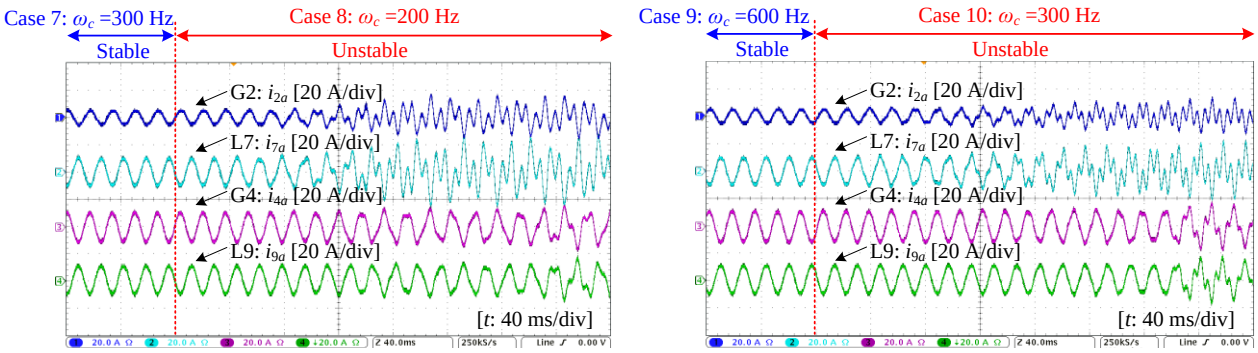

(a) (b)

Figure 6-26. Experimental results of system transition from stable state to unstable state: (a) ω_c changes from 300×2π rad/s to 200×2π rad/s, ω_v is 200×2π rad/s and ω_{ffv} is 100×2π rad/s; (b) ω_c changes from 600×2π rad/s to 300×2π rad/s, ω_v is 200×2π rad/s and ω_{ffv} is 200×2π rad/s.

6.3.4 Verification of the Meshed System

The experimental platform has been reconfigured as the meshed system as depicted in Figure 6-16. Case 11 and Case 12 have been verified in experiments. Figure 6-27 shows the phase-A currents of inverters G1, G3 and L2 in the meshed system. It can be seen that the system changes from a stable state to an unstable state when the parameter ω_{ffv} changes from 200×2π rad/s in Case 11 to 1000×2π rad/s in Case 12.

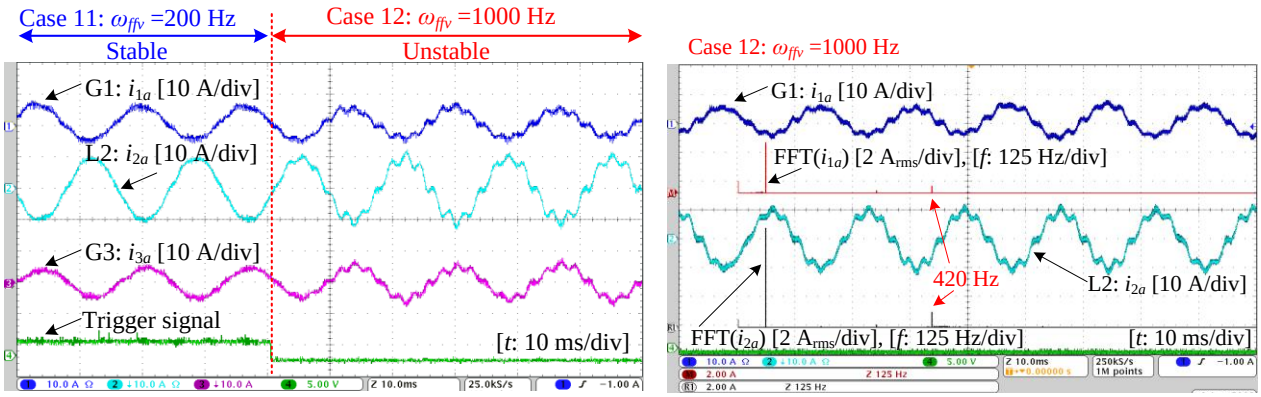

(a) (b)

Figure 6-27. Experimental results of the meshed system when ω_{ffv} changes from 200×2π rad/s to 1000×2π rad/s. (a) Transition from a stable state to an unstable state. (b) Unstable state when ω_{ffv} is 1000×2π rad/s.

6.3.5 Resonance Frequencies in Unstable Cases

When the system transits from a stable state to an unstable state, initially the *d*-*q* currents have small diverging oscillations around the operating points. Then, similar to the phenomenon presented in [91], large diverging currents make the system reach the saturation state with

restricted current oscillation magnitudes due to the saturation of controller outputs, so the resonance frequency could be slightly different from that in the aforementioned small-signal harmonic stability analysis.

The resonance frequencies in unstable cases are summarized in Table 6-4. The differences between the major resonance frequencies in the initial states in simulation and the resonance frequencies in the analysis results are mostly within ±15 Hz, while the differences between the major resonance frequencies in the saturation states in both simulation and experiments and the resonance frequencies in the analysis results are mostly within ±25 Hz.

In summary, the experimental results have verified the harmonic stability analysis methods described in Section 6.1 and the controller parameter design results presented in Section 6.2.

Table 6-4. Electrical parameters of the scaled-down two-area system.

Case No.	**Analysis**	**Major Resonances in Simulation**		**Major Resonances in Experiments in Saturation States**
		In Initial States	**In Saturation State**	
Case 2	366 Hz, 403 Hz	354 Hz	345 Hz, 364 Hz	352 Hz
Case 3	355 Hz, 391 Hz	343 Hz	338Hz, 356 Hz	342 Hz
Case 4	340 Hz	340 Hz	326 Hz, 345 Hz	300 Hz, 325 Hz
Case 6	172 Hz, 183 Hz	171 Hz	169 Hz, 176 Hz	152 Hz, 162 Hz
Case 8	155 Hz	155 Hz	153 Hz	140 Hz
Case 10	197 Hz	197 Hz	195 Hz, 205 Hz	184 Hz
Case 12	443 Hz	420 Hz	405 Hz	420 Hz

6.4 Conclusion

In this chapter, two sequence-impedance-based methods for harmonic stability analysis of three-phase inverter-based multi-bus ac power systems have been proposed to avoid the examination of RHP poles of impedance ratios and reduce the computation effort, as compared with the existing stability analysis method using the Nyquist stability criterion once. The proposed methods also enable the system harmonic stability assessment using only measured sequence impedances of components, without the need for detailed internal control information of them.

The novelty of the proposed Method 1 is: 1) all the major connection types and the meshed connection are summarized, regarding the stability criteria and total equivalent terminal characteristics; 2) a sequential procedure of applying stability criteria to the harmonic stability analysis of general inverter-based multi-area ac systems is proposed to avoid the RHP pole calculation; 3) the proposed Method 1 is applicable to the harmonic stability analysis of any ac systems, which are composed of both current-controlled and voltage-controlled inverters with any structures including all the major connection types and meshed connections.

The novelty of the proposed Method 2 is: 1) the underlying principle of the impedance-based stability analysis using Cauchy's theorem is clearly identified; 2) the proposed Method 2 is a generalized extension of the Impedance-Sum-Type criterion to be used for the harmonic stability analysis of any multi-bus ac systems based on Cauchy's theorem; 3) the approach of using Bode plots in the positive frequency range with the consideration of the order difference between the numerator and denominator to determine the encirclement of the origin point (0, j0) is demonstrated.

Thanks to the low computation burden, the inverter controller parameters of multi-bus ac systems can be designed by repetitively applying the proposed harmonic stability methods, and presented as stability regions in the parameter space. The proposed analysis and design methods are verified by experiments of a two-area system and a meshed system with both voltage-controlled and current-controlled inverters.

7 D-Q Impedance Based Stability Analysis and Controller Parameter Design of Multi-Bus Ac Power Systems

In order to address the low-frequency oscillation issues in three-phase inverter-based ac systems, *d-q* impedances are preferable than sequence impedances for small-signal stability analysis. The impedance-based approach based on the generalized Nyquist stability criterion (GNC) can assess both the harmonic instability and the low-frequency oscillation problems of the systems. However, the GNC involves the right-half-plane (RHP) pole calculation of return-ratio transfer function matrices, which cannot be avoided for stability analysis of complicated ac power systems. Therefore, it necessitates the detailed internal control information of the inverters, which is not normally available for commercial inverters. To address this issue, this chapter introduces the Component Connection Method (CCM) in the frequency domain for stability analysis in the synchronous *d-q* frame, by proposing a method of deriving the impedance matrix of the connection networks of inverter-based ac power systems. Demonstration on a two-area system consisting of inverters with generator and static load emulation shows that: the CCM-enabled approach can avoid the RHP pole calculation of return-ratio matrices and enables the stability analysis by using only the impedances of system components, which could be measured without the need for the internal information. A stability analysis method based on *d-q* impedances, the CCM, and the determinant-based GNC is also proposed to further simplify the analysis process. Inverter controller parameters can be designed as stability regions in parameter spaces, by repetitively applying the proposed stability analysis method. Simulation and experimental results verify the validity of the proposed stability analysis method and the parameter design approach.

7.1 System Description

The same three-phase inverter-based multi-bus ac system for scaled-down emulation of the two-area system as depicted in Figure 6-2 is under study here. The generator emulation using the 4^{th} order model of synchronous generator is enabled in the voltage-controlled inverters G1−G4, and the static ZIP load emulation is enabled in the current-controlled inverters L7 and L9. The system base values and line parameters are listed in Table 6-1. The inductance and resistance parameters of transmission lines are scaled down with same per unit (p.u.) values from the original two-area system [137]. The parameters of the generators G1−G4 are shown in Table 3-7. The generator emulation also includes governor, droop control, automatic generation control (AGC), power system stabilizer (PSS), and excitation system with automatic voltage regulator (AVR) [8], [9]. The static ZIP load parameters are listed in Table 3-6. The operating point of the two-area system is shown in Table 7-1.

As shown in Figure 3-15, each inverter is usually modeled and controlled in its own terminal *d-q* frame with the superscript *c*. The current-controlled inverters with ZIP load emulation synchronize with the grid frequency by using the PLL. The grid frequency synchronization of the voltage-controlled inverters with SG emulation is achieved by the swing equation in the generator mechanical model [8], [9], [138]. In order to facilitate the system stability analysis in the synchronous *d-q* frame, a common *d-q* frame with the superscript *s* is chosen to be aligned with the Bus 1 voltage, that is, the Bus 1 voltage angle is assumed as 0 °. Based on power flow calculation, the voltage magnitudes and angles of buses with direct inverter connections are summarized in Table 7-2.

It should be noted that the emulation of SGs and ZIP loads is implemented by the outer control loops of inverters. Although this inverter-based ac power system is for emulation of

electromechanical phenomena with dynamics of up to 100 Hz in transmission-level power systems [10], [42], the inner voltage and current control loops of inverters still dominate the characteristics of the system in the frequency range above 100 Hz. Therefore, this inverter-based power system under study is significantly different from conventional power systems [139].

Table 7-1. Generator and load operating point in the two-area system.

Parameters	**Values**	**Parameters**	**Values**
G1 active power	0.78 p.u.	L7 active power	1.07 p.u.
G2 active power	0.78 p.u.	L7 reactive power	−0.37 p.u.
G3 active power	0.8 p.u.	L9 active power	1.96 p.u.
G4 active power	0.78 p.u.	L9 reactive power	−0.37 p.u.

Table 7-2. Bus voltage magnitudes and angles in the two-area system.

Bus Number	Bus 1	Bus 2	Bus 3	Bus 4	Bus 7	Bus 9
Voltage Magnitude V (p.u.)	1.03 p.u.	1.01 p.u.	1.03 p.u.	1.01 p.u.	0.99 p.u.	0.97 p.u.
Voltage Angle θ (°)	0 °	−7.0 °	−38.2 °	−48.9 °	−22.4 °	−61.5 °

In addition, the focus of this chapter is on the system-level impedance-based stability analysis. Although a specific inverter-based ac system is studied here, the stability analysis and controller parameter design approaches discussed in this chapter can be readily applied to other inverter-based ac systems, such as distribution systems with photovoltaic (PV) inverters, wind turbine generators and distribution lines or a microgrid with droop-controlled inverters, by simply adapting the *d*-*q* impedance models of inverter components and the connection network.

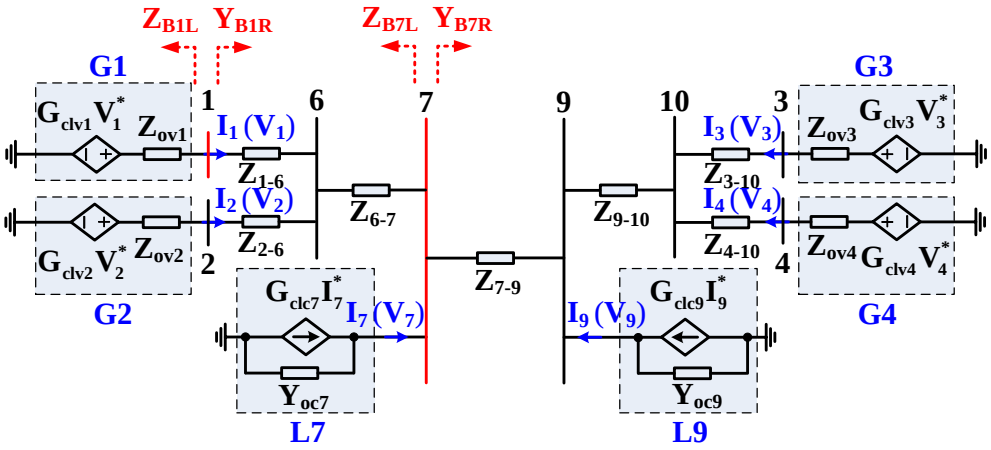

Figure 7-1. Impedance-based equivalent circuit of the two-area system in the common system *d*-*q* frame.

7.2 Stability Analysis Based on the GNC

The impedance-based equivalent circuit of the two-area system in the common system *d*-*q* frame is illustrated in Figure 7-1. Four voltage-controlled inverters G1−G4 with generator emulation are represented by their equivalent Thevenin circuits, where the inverter output

impedance matrices $\mathbf{Z_{ovj}}$ (j=1−4) are derived in Section 3.6 considering only the electrical circuit of the 4th order generator model. Two current-controlled inverters L7 and L9 with static ZIP load emulation are modeled by their equivalent Norton circuits, where the inverter output admittance matrices $\mathbf{Y_{oci}}$ (i=7, 9) are derived in Section 3.5. The voltage and current references of inverters are defined in (7-1) and (7-2), respectively. The *d-q* impedance $\mathbf{Z_{lk}}$ of each transmission line, with inductance L_{lk} and resistance R_{lk} in series, can be modeled by (7-3), where ω_1 is the fundamental angular frequency, and its corresponding *d-q* admittance $\mathbf{Y_{lk}}$ can be expressed by (7-4).

$$\mathbf{V_j^*}(s) = \mathbf{G_{gfj}}\tilde{E}_{fdj} \ (j = 1-4) \tag{7-1}$$

$$\mathbf{I_i^*}(s) = \mathbf{G_{fZIPi}}\mathbf{G_{ZIPi}}\begin{bmatrix} \tilde{P}_i & \tilde{Q}_i \end{bmatrix}^{\mathrm{T}} \ (i = 7,9) \tag{7-2}$$

$$\mathbf{Z_{lk}} = \begin{bmatrix} L_{lk}s + R_{lk} & -\omega_1 L_{lk} \\ \omega_1 L_{lk} & L_{lk}s + R_{lk} \end{bmatrix} \tag{7-3}$$

$$\mathbf{Y_{lk}} = \mathbf{Z_{lk}^{-1}} \tag{7-4}$$

When using the generalized Nyquist stability criterion (GNC) for stability analysis, the multi-bus system can be divided into two sub-systems at any bus, where the rank of the controllability and observability matrices is full [34], such as Bus 1 or Bus 7. If the system is divided at Bus 7, the total impedance $\mathbf{Z_{B7L}}$ of the left-side subsystem and the total admittance $\mathbf{Y_{B7R}}$ (or the inverse of the total impedance $\mathbf{Z_{B7R}}$) of the right-side subsystem can be obtained, as expressed in (7-5) and (7-6). The system return-ratio matrix (or the minor loop gain) $\mathbf{T_{m\_B7}}$ at Bus 7 is defined by the ratio of the left-side subsystem impedance over the right-side subsystem

impedance as shown in (7-7). The return-difference matrix $\mathbf{F_{m\_B7}}$ is defined as the sum of the 2-by-2 identity matrix $\mathbf{I}$ and $\mathbf{T_{m\_B7}}$, as expressed in (7-8). The closed minor loop gain $\mathbf{T_{clm\_B7}}$ of the return-ratio matrix is defined by (7-9).

$$\mathbf{Z_{B7L}} = \left\{ \left\{ \left[\left(\mathbf{Z_{ov1}} + \mathbf{Z_{1\text{-}6}} \right)^{-1} + \left(\mathbf{Z_{ov2}} + \mathbf{Z_{2\text{-}6}} \right)^{-1} \right]^{-1} + \mathbf{Z_{6\text{-}7}} \right\}^{-1} + \mathbf{Y_{oc7}} \right\}^{-1} \tag{7-5}$$

$$\mathbf{Y_{B7R}} = \left\{ \left\{ \left\{ \left[\left(\mathbf{Z_{ov3}} + \mathbf{Z_{3\text{-}10}} \right)^{-1} + \left(\mathbf{Z_{ov4}} + \mathbf{Z_{4\text{-}10}} \right)^{-1} \right]^{-1} + \mathbf{Z_{9\text{-}10}} \right\}^{-1} + \mathbf{Y_{oc9}} \right\}^{-1} + \mathbf{Z_{7\text{-}9}} \right\}^{-1} \tag{7-6}$$

$$\mathbf{T_{m\_B7}} = \mathbf{Y_{B7R}} \mathbf{Z_{B7L}} \tag{7-7}$$

$$\mathbf{F_{m\_B7}} = \mathbf{I} + \mathbf{T_{m\_B7}} \tag{7-8}$$

$$\mathbf{T_{clm\_B7}} = \left(\mathbf{I} + \mathbf{T_{m\_B7}} \right)^{-1} = \mathbf{F_{m\_B7}^{-1}} \tag{7-9}$$

The system stability can be determined by applying the GNC to the return-ratio matrix $\mathbf{T_{m\_B7}}$, as described in

$$P\left(\mathbf{T_{clm\_B7}} \right) = Z\left(\mathbf{I} + \mathbf{T_{m\_B7}} \right) = P\left(\mathbf{T_{m\_B7}} \right) - N_{(-1,\, j0)}\left(\mathbf{T_{m\_B7}} \right) \tag{7-10}$$

where $P(\ )$ and $Z(\ )$ denote the numbers of RHP poles and zeros respectively, $N_{(-1,\, j0)}(\ )$ is the net sum of anticlockwise encirclements of the critical point $(-1, j0)$ by the set of *characteristic loci* (in other words, the Nyquist plots of the *eigenvalues*) of the return-ratio matrix. The system is stable if and only if $P(\mathbf{T_{m\_B7}})$ is equal to $N_{(-1,\, j0)}(\mathbf{T_{m\_B7}})$. According to the GNC, not only the characteristic loci but also the RHP poles of the return-ratio matrix should be examined to evaluate the system stability. Notice that the system stability can also be assessed by the RHP

poles of the closed-loop gain $\mathbf{T}_{\mathbf{clm\_B7}}$ of the return-ratio matrix.

In addition to the aforementioned *eigenvalue-based GNC*, the system stability can also be predicted by applying the *determinant-based GNC* to the to the return-difference matrix $\mathbf{F}_{\mathbf{m\_B7}}$, as expressed in

$$P\left(\mathbf{T}_{\mathbf{clm\_B7}}\right) = P\left(\mathbf{T}_{\mathbf{m\_B7}}\right) - N_{(0,\,j0)}\left(\det\left(\mathbf{F}_{\mathbf{m\_B7}}\right)\right) \tag{7-11}$$

where det($\mathbf{F}_{\mathbf{m\_B7}}$) means the *determinant* of $\mathbf{F}_{\mathbf{m\_B7}}$, and $N_{(0,\ j0)}(\ )$ denotes the number of anticlockwise encirclements of the origin point (0, *j*0) by the Nyquist plot. The system is stable when the encirclements are equal to the number of RHP poles of $\mathbf{T}_{\mathbf{m\_B7}}$.

As discussed in [9], when a single integral controller instead of a PI controller is applied in the voltage-controlled inverters, instability happens in a two-generation system owing to the combination of the 4$^{\text{th}}$-order synchronous generator model and the voltage controller in the inverter. Such instability phenomenon is investigated here for the two-area system. Two cases with different voltage controller parameters are analyzed by the GNC: Case 1 with a PI controller (K_{vp}=1.04 and K_{vi}=325), and Case 2 with an integral controller (K_{vp}=0 and K_{vi}=325).

Figure 7-2(a) shows the characteristic loci of the return-ratio matrix $\mathbf{T}_{\mathbf{m\_B7}}$ for both cases. As shown, none of the characteristic loci encircles the critical point (−1, *j*0). Alternatively, the Bode plots of the determinant of the return-difference matrix $\mathbf{F}_{\mathbf{m\_B7}}$ as illustrated in Figure 7-2(b) exhibit zero net phase change, in other words, zero encirclements around the origin point (0, *j*0). However, the pole-zero map of $\mathbf{T}_{\mathbf{m\_B7}}$ as shown in Figure 7-3(a) indicates that it has zero RHP poles in Case 1 but two pairs of RHP poles in Case 2. Therefore, the system is stable in Case 1 but unstable in Case 2 according to the eigenvalue-based GNC or determinant-based GNC.

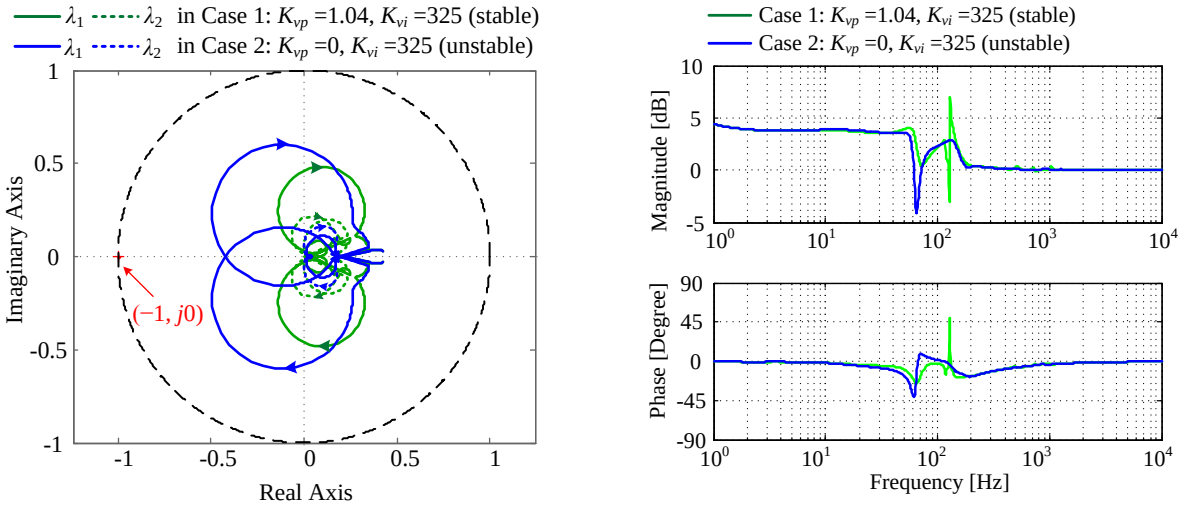

(a) (b)

Figure 7-2. Characteristic loci of $\mathbf{T}_{\mathbf{m\_B7}}$ (a) and Nyquist plot of det($\mathbf{F}_{\mathbf{m\_B7}}$) (b) in both cases.

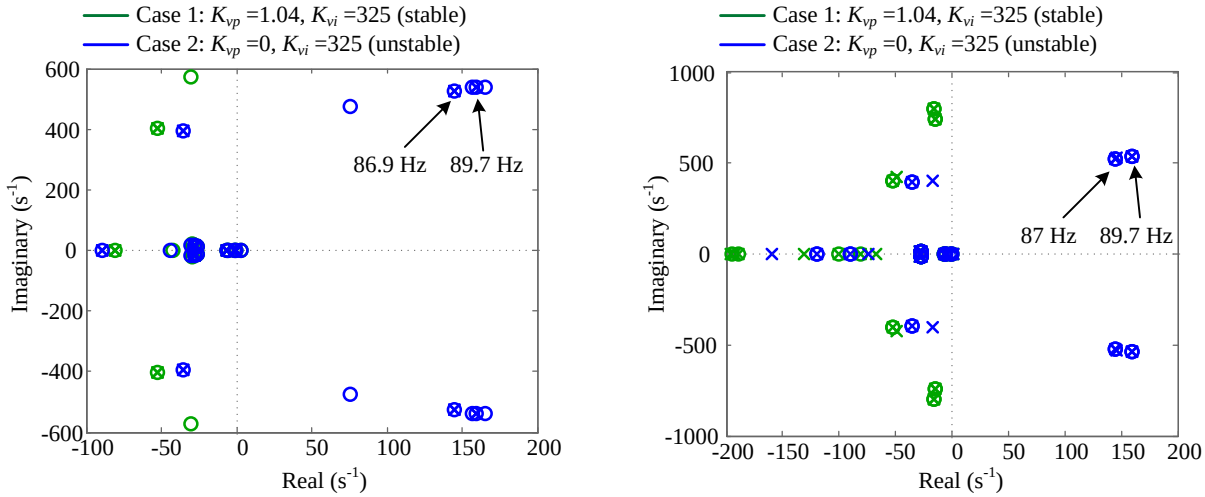

(a) (b)

Figure 7-3. Pole-zero maps of $\mathbf{T}_{\mathbf{m\_B7}}$ (a) and $\mathbf{T}_{\mathbf{clm\_B7}}$ (b) in both Case 1 and Case 2.

The stability analysis results can be confirmed by the pole-zero map of the closed minor loop gain $\mathbf{T}_{\mathbf{clm\_B7}}$ as depicted in Figure 7-3(b), where no RHP pole exists in Case 1 but two pairs of RHP poles with oscillation frequencies of 87 Hz and 89.7 Hz can be found in Case 2.

The above example demonstrates that, when applying the GNC, it is necessary to check the RHP pole of the return-ratio matrix, which cannot be obtained when detailed models of inverters are not available due to the lack of internal control structure and controller parameter information.

7.3 Proposed Stability Analysis Method Based on the CCM

7.3.1 System Model Based on the CCM

Based the Component Connection Method (CCM), the inverter-based two-area system can be decomposed into individual inverter components and the connection network [23], as illustrated in Figure 7-4. The detailed block diagram of the CCM applied to the inverter-based two-area system is depicted in Figure 7-5(a).

The composite model of all inverter components can be expressed as (7-12). The output vector $\mathbf{Y}(s)$, reference vector $\mathbf{U}(s)$ and disturbance vector $\mathbf{D}(s)$ of inverters are expressed in (7-13), respectively. $\mathbf{G_{cl}}(s)$ is the closed-loop transfer function matrix from the reference to the output, as described in (7-14). $\mathbf{G_{cd}}(s)$ is the closed-loop transfer function matrix from the disturbance to the output with inverter output impedances or admittances as the diagonal elements, as shown in (7-15), which can be also seen as the overall impedance matrix model of all inverter components.

$$\mathbf{Y}(s) = \mathbf{G_{cl}}(s)\mathbf{U}(s) - \mathbf{G_{cd}}(s)\mathbf{D}(s) \tag{7-12}$$

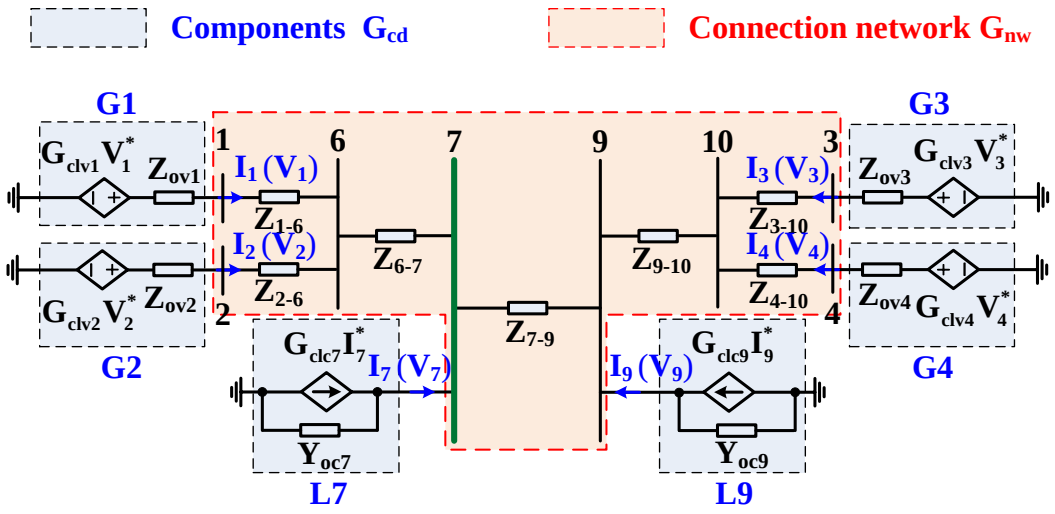

Figure 7-4. Circuit diagram of the CCM applied to the inverter-based two-area system.

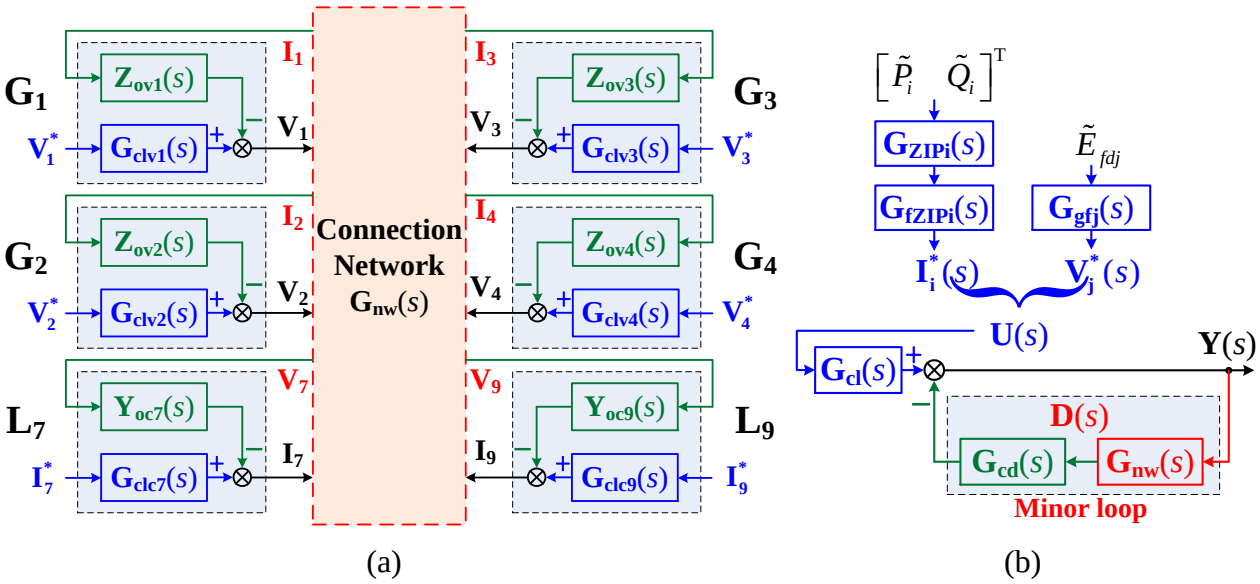

Figure 7-5. Diagrams of the CCM applied to the inverter-based two-area system: (a) detailed diagram, (b) equivalent MIMO feedback system.

$$\begin{cases} \mathbf{Y}(s) = [\mathbf{V}_1(s), \mathbf{V}_2(s), \mathbf{V}_3(s), \mathbf{V}_4(s), \mathbf{I}_7(s), \mathbf{I}_9(s)]^{\mathrm{T}} \\ \mathbf{U}(s) = [\mathbf{V}_1^*(s), \mathbf{V}_2^*(s), \mathbf{V}_3^*(s), \mathbf{V}_4^*(s), \mathbf{I}_7^*(s), \mathbf{I}_9^*(s)]^{\mathrm{T}} \\ \mathbf{D}(s) = [\mathbf{I}_1(s), \mathbf{I}_2(s), \mathbf{I}_3(s), \mathbf{I}_4(s), \mathbf{V}_7(s), \mathbf{V}_9(s)]^{\mathrm{T}} \end{cases} \tag{7-13}$$

$$\mathbf{G}_{\mathbf{cl}}(s) = \mathrm{diag}[\mathbf{G}_{\mathbf{clv1}}(s), \mathbf{G}_{\mathbf{clv2}}(s), \mathbf{G}_{\mathbf{clv3}}(s), \mathbf{G}_{\mathbf{clv4}}(s), \mathbf{G}_{\mathbf{clc7}}(s), \mathbf{G}_{\mathbf{clc9}}(s)] \tag{7-14}$$

$$\mathbf{G}_{\mathbf{cd}}(s) = \mathrm{diag}[\mathbf{Z}_{\mathbf{ov1}}(s), \mathbf{Z}_{\mathbf{ov2}}(s), \mathbf{Z}_{\mathbf{ov3}}(s), \mathbf{Z}_{\mathbf{ov4}}(s), \mathbf{Y}_{\mathbf{oc7}}(s), \mathbf{Y}_{\mathbf{oc9}}(s)] \tag{7-15}$$

In addition, the connection network can be modeled by (7-16) with $\mathbf{G}_{\mathbf{nw}}(s)$ representing the transfer function matrix from the output to the disturbance, which can also be regarded as a multi-input-multi-output (MIMO) impedance matrix model of the connection network. Then, the overall system model can be obtained as (7-17) and it can be regarded as a MIMO negative feedback system as shown in Figure 7-5(b). The transfer functions $\mathbf{G}_{\mathbf{gfj}}(s)$, $\mathbf{G}_{\mathbf{ZIPi}}(s)$ and $\mathbf{G}_{\mathbf{fZIPi}}(s)$ are determined by the emulated SG and ZIP load, so they are stable. Each inverter is designed to be stable individually with ideal external conditions, so $\mathbf{G}_{\mathbf{cl}}(s)$ is stable. Therefore, the system stability is determined by the transfer function matrix $[\mathbf{I}+ \mathbf{G}_{\mathbf{cd}}(s)\mathbf{G}_{\mathbf{nw}}(s)]^{-1}$. For the MIMO feedback system, the open-loop transfer function $\mathbf{L}(s)$ (also called return-ratio matrix or minor loop gain) is expressed in (7-18) and the return-difference matrix $\mathbf{F}(s)$ is expressed in (7-19). Therefore, the system stability can be analyzed by applying the GNC to $\mathbf{L}(s)$ or $\mathbf{F}(s)$. It is worth noting that, when using the traditional analysis method in Section 7.2, the 2-by-2 return-ratio matrix is defined as the ratio of two impedances in the *d-q* frame. Nevertheless, the return-ratio matrix $\mathbf{L}(s)$ derived based on CCM is 12-by-12, defined as the product of the 12-by-12 impedance matrix $\mathbf{G}_{\mathbf{cd}}(s)$ of all components and the 12-by-12 impedance matrix $\mathbf{G}_{\mathbf{nw}}(s)$ of the connection network.

$$\mathbf{D}(s) = \mathbf{G}_{\mathbf{nw}}(s)\mathbf{Y}(s) \tag{7-16}$$

$$\mathbf{Y}(s) = \left[\mathbf{I} + \mathbf{G}_{\mathbf{cd}}(s)\mathbf{G}_{\mathbf{nw}}(s)\right]^{-1}\mathbf{G}_{\mathbf{cl}}(s)\mathbf{U}(s) \tag{7-17}$$

$$\mathbf{L}(s) = \mathbf{G}_{\mathbf{cd}}(s)\mathbf{G}_{\mathbf{nw}}(s) \tag{7-18}$$

$$\mathbf{F}(s) = \mathbf{I} + \mathbf{G}_{\mathbf{cd}}(s)\mathbf{G}_{\mathbf{nw}}(s) \tag{7-19}$$

7.3.2 Proposed Method for Derivation of the Impedance Matrix of Connection Network

A method for derivation of the connection network impedance matrix in multi-bus ac systems composed of both voltage-controlled and current-controlled inverters is developed here to facilitate the CCM-based stability analysis. Each variable is frequency-dependent, but the symbols "(*s*)" or "(*jω*)" are omitted for simplicity. The derivation contains two steps.

Step 1: eliminate the buses without inverter connections (also known as *Kron reduction* [140])

The nodal admittance matrix of the connection work of the two-area system is expressed as a partitioned matrix in (7-20), and simplified as (7-21), by dividing the current vector / voltage vector into the current vector $\mathbf{I_m}$ / voltage vector $\mathbf{V_m}$ for buses with direct connection of inverter components and the current vector $\mathbf{I_n}$ / voltage vector $\mathbf{V_n}$ for buses without direct component connection, as expressed in (7-22) and (7-23), respectively. Considering $\mathbf{I_n}$ =[0, 0]^T, the relationship between $\mathbf{I_m}$ and $\mathbf{V_m}$ can be derived as (7-24) with the admittance matrix $\mathbf{Y_{bus}}$.

Step 2: given $\mathbf{V_v}$ and $\mathbf{I_c}$, solve $\mathbf{I_v}$ and $\mathbf{V_c}$, to obtain $\mathbf{G_{nw}}$

$\mathbf{Y_{bus}}$ can be reformatted as (7-25), by further partitioning $\mathbf{I_m}$ and $\mathbf{V_m}$ into the current vector $\mathbf{I_v}$

/ voltage vector $\mathbf{V_v}$ for buses connected with voltage-controlled inverters and the current vector $\mathbf{I_c}$ / voltage vector $\mathbf{V_c}$ for buses with the connection of current-controlled inverters, as shown in (7-26) and (7-27), respectively. Because $\mathbf{V_v}$ and $\mathbf{I_c}$ are inputs from the inverter components to the connection network, the outputs of the connection network ($\mathbf{I_v}$ and $\mathbf{V_c}$) can be solved from (7-25), as expressed in (7-28), and thus the impedance matrix $\mathbf{G_{nw}}$ of the connection network is derived.

$$\begin{bmatrix} \mathbf{I}_1 \\ \mathbf{I}_2 \\ \mathbf{I}_3 \\ \mathbf{I}_4 \\ \mathbf{I}_7 \\ \mathbf{I}_9 \\ \hdashline \mathbf{I}_6 \\ \mathbf{I}_{10} \end{bmatrix} = \left[\begin{array}{cccccc:cc} \mathbf{Y}_{1\text{-}6} & 0 & 0 & 0 & 0 & 0 & -\mathbf{Y}_{1\text{-}6} & 0 \\ 0 & \mathbf{Y}_{2\text{-}6} & 0 & 0 & 0 & 0 & -\mathbf{Y}_{2\text{-}6} & 0 \\ 0 & 0 & \mathbf{Y}_{3\text{-}10} & 0 & 0 & 0 & 0 & -\mathbf{Y}_{3\text{-}10} \\ 0 & 0 & 0 & \mathbf{Y}_{4\text{-}10} & 0 & 0 & 0 & -\mathbf{Y}_{4\text{-}10} \\ 0 & 0 & 0 & 0 & \mathbf{Y}_{6\text{-}7}+\mathbf{Y}_{7\text{-}9} & -\mathbf{Y}_{7\text{-}9} & -\mathbf{Y}_{6\text{-}7} & 0 \\ 0 & 0 & 0 & 0 & -\mathbf{Y}_{7\text{-}9} & \mathbf{Y}_{7\text{-}9}+\mathbf{Y}_{9\text{-}10} & 0 & -\mathbf{Y}_{9\text{-}10} \\ \hdashline -\mathbf{Y}_{1\text{-}6} & -\mathbf{Y}_{2\text{-}6} & 0 & 0 & -\mathbf{Y}_{6\text{-}7} & 0 & \mathbf{Y}_{1\text{-}6}+\mathbf{Y}_{2\text{-}6}+\mathbf{Y}_{6\text{-}7} & 0 \\ 0 & 0 & -\mathbf{Y}_{3\text{-}10} & -\mathbf{Y}_{4\text{-}10} & 0 & -\mathbf{Y}_{9\text{-}10} & 0 & \mathbf{Y}_{3\text{-}10}+\mathbf{Y}_{4\text{-}10}+\mathbf{Y}_{9\text{-}10} \end{array}\right] \begin{bmatrix} \mathbf{V}_1 \\ \mathbf{V}_2 \\ \mathbf{V}_3 \\ \mathbf{V}_4 \\ \mathbf{V}_7 \\ \mathbf{V}_9 \\ \hdashline \mathbf{V}_6 \\ \mathbf{V}_{10} \end{bmatrix} \tag{7-20}$$

$$\begin{bmatrix} \mathbf{I_m} \\ \hdashline \mathbf{I_n} \end{bmatrix} = \left[\begin{array}{c:c} \mathbf{Y_{mm}} & \mathbf{Y_{mn}} \\ \hdashline \mathbf{Y_{nm}} & \mathbf{Y_{nn}} \end{array}\right] \begin{bmatrix} \mathbf{V_m} \\ \hdashline \mathbf{V_n} \end{bmatrix} \tag{7-21}$$

$$\left[\mathbf{I_m} \;\vdots\; \mathbf{I_n}\right]^{\mathrm{T}} = \left[\mathbf{I_1} \quad \mathbf{I_2} \quad \mathbf{I_3} \quad \mathbf{I_4} \quad \mathbf{I_7} \quad \mathbf{I_9} \;\vdots\; \mathbf{I_6} \quad \mathbf{I_{10}}\right]^{\mathrm{T}} \tag{7-22}$$

$$\left[\mathbf{V_m} \;\vdots\; \mathbf{V_n}\right]^{\mathrm{T}} = \left[\mathbf{V_1} \quad \mathbf{V_2} \quad \mathbf{V_3} \quad \mathbf{V_4} \quad \mathbf{V_7} \quad \mathbf{V_9} \;\vdots\; \mathbf{V_6} \quad \mathbf{V_{10}}\right]^{\mathrm{T}} \tag{7-23}$$

$$\mathbf{I_m} = \left(\mathbf{Y_{mm}} - \mathbf{Y_{mn}}\mathbf{Y_{nn}^{-1}}\mathbf{Y_{nm}}\right)\mathbf{V_m} = \mathbf{Y_{bus}}\mathbf{V_m} \tag{7-24}$$

$$\begin{bmatrix} \mathbf{I}_1 \\ \mathbf{I}_2 \\ \mathbf{I}_3 \\ \mathbf{I}_4 \\ \mathbf{I}_7 \\ \mathbf{I}_9 \end{bmatrix} = \mathbf{Y_{bus}} \begin{bmatrix} \mathbf{V}_1 \\ \mathbf{V}_2 \\ \mathbf{V}_3 \\ \mathbf{V}_4 \\ \mathbf{V}_7 \\ \mathbf{V}_9 \end{bmatrix} \Rightarrow \begin{bmatrix} \mathbf{I_v} \\ \hdashline \mathbf{I_c} \end{bmatrix} = \left[\begin{array}{c:c} \mathbf{Y_{vv}} & \mathbf{Y_{vc}} \\ \hdashline \mathbf{Y_{cv}} & \mathbf{Y_{cc}} \end{array}\right] \begin{bmatrix} \mathbf{V_v} \\ \hdashline \mathbf{V_c} \end{bmatrix} \tag{7-25}$$

$$\mathbf{I}_{\mathbf{m}}^{\mathrm{T}} = \left[\mathbf{I}_{\mathbf{v}} \;\vdots\; \mathbf{I}_{\mathbf{c}}\right]^{\mathrm{T}} = \left[\mathbf{I}_{\mathbf{1}} \quad \mathbf{I}_{\mathbf{2}} \quad \mathbf{I}_{\mathbf{3}} \quad \mathbf{I}_{\mathbf{4}} \;\vdots\; \mathbf{I}_{\mathbf{7}} \quad \mathbf{I}_{\mathbf{9}}\right]^{\mathrm{T}} \tag{7-26}$$

$$\mathbf{V}_{\mathbf{m}}^{\mathrm{T}} = \left[\mathbf{V}_{\mathbf{v}} \;\vdots\; \mathbf{V}_{\mathbf{c}}\right]^{\mathrm{T}} = \left[\mathbf{V}_{\mathbf{1}} \quad \mathbf{V}_{\mathbf{2}} \quad \mathbf{V}_{\mathbf{3}} \quad \mathbf{V}_{\mathbf{4}} \;\vdots\; \mathbf{V}_{\mathbf{7}} \quad \mathbf{V}_{\mathbf{9}}\right]^{\mathrm{T}} \tag{7-27}$$

$$\begin{bmatrix} \mathbf{I}_{\mathbf{v}} \\ \mathbf{V}_{\mathbf{c}} \end{bmatrix} = \begin{bmatrix} \mathbf{Y}_{\mathbf{vv}} - \mathbf{Y}_{\mathbf{vc}}\mathbf{Y}_{\mathbf{cc}}^{-1}\mathbf{Y}_{\mathbf{cv}} & \mathbf{Y}_{\mathbf{vc}}\mathbf{Y}_{\mathbf{cc}}^{-1} \\ -\mathbf{Y}_{\mathbf{cc}}^{-1}\mathbf{Y}_{\mathbf{cv}} & \mathbf{Y}_{\mathbf{cc}}^{-1} \end{bmatrix} \begin{bmatrix} \mathbf{V}_{\mathbf{v}} \\ \mathbf{I}_{\mathbf{c}} \end{bmatrix} = \mathbf{G}_{\mathbf{nw}} \begin{bmatrix} \mathbf{V}_{\mathbf{v}} \\ \mathbf{I}_{\mathbf{c}} \end{bmatrix} \tag{7-28}$$

7.3.3 Stability Analysis Based on the CCM and the Eigenvalue-Based GNC

Reference [100] presented a stability criterion for traditional power systems based on the CCM and the eigenvalue-based GNC, which was applied to the system return-ratio matrix. Likewise, with the derived impedance matrix $\mathbf{G_{nw}}(s)$ of the connection network in Section 7.3.2, the stability of the inverter-based two-area system can also be analyzed by applying the eigenvalue-based GNC to the return-ratio matrix $\mathbf{L}(s)$, as expressed in (7-29).

$$Z\left(\mathbf{F}\right) = P\left(\mathbf{L}\right) - N_{(-1,\,j0)}\left(\mathbf{L}\right) = -N_{(-1,\,j0)}\left(\mathbf{L}\right) \tag{7-29}$$

Because the connection network consists of only passive elements, its impedance matrix $\mathbf{G_{nw}}(s)$ does not have RHP poles, as demonstrated in Figure 7-6. Taking the stable matrix $\mathbf{G_{cd}}(s)$ into account, $\mathbf{L}(s)$ does not have RHP poles, that is, $P(\mathbf{L}) = 0$. Therefore, the system is stable if and only if $N_{(-1,\,j0)}(\mathbf{L}) = 0$. $\mathbf{L}$ has 12 frequency-dependent eigenvalues (λ_1 to λ_{12}). Figure 7-7 and Figure 7-8 illustrate the characteristic loci of $\mathbf{L}$ in Case 1 and Case 2, respectively. Corresponding Bode plots of these eigenvalues for both cases are shown in Figure 7-9. None of the characteristic loci encircles the critical point $(-1,\, j0)$ in Case 1. However, each of the eigenvalues λ_1 and λ_2 encircles the critical point $(-1,\, j0)$ clockwise twice in Case 2.

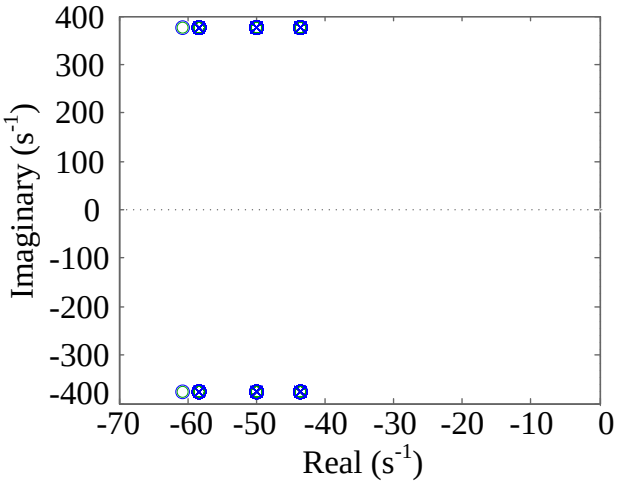

Figure 7-6. Pole-zero map of the impedance matrix $\mathbf{G_{nw}}(s)$.

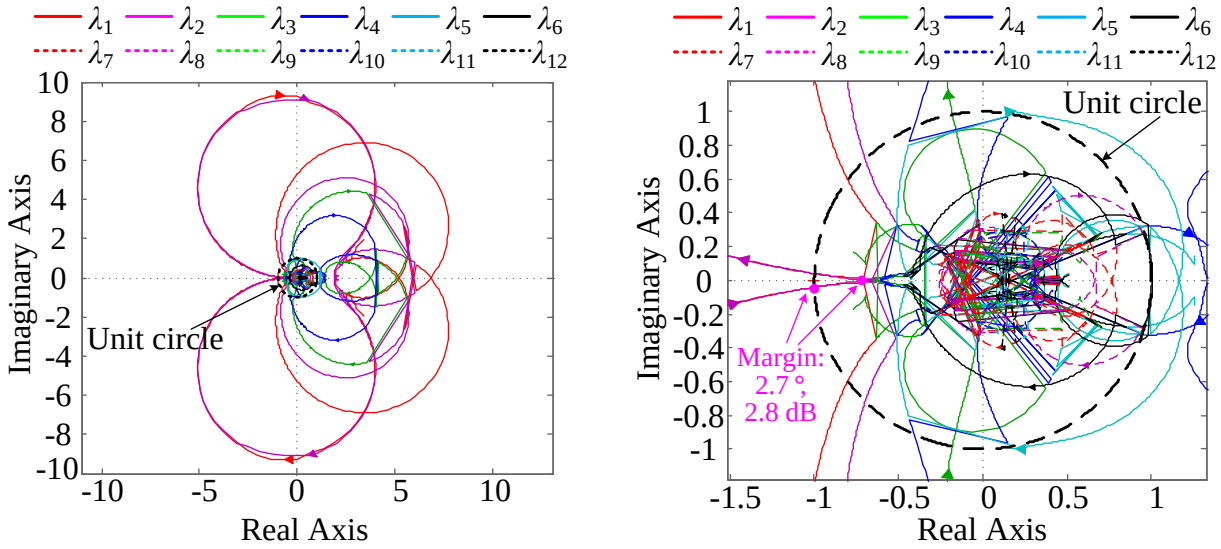

(a) (b)

Figure 7-7. Characteristic loci of **L** in Case 1. (a) Full view; (b) zoomed-in view.

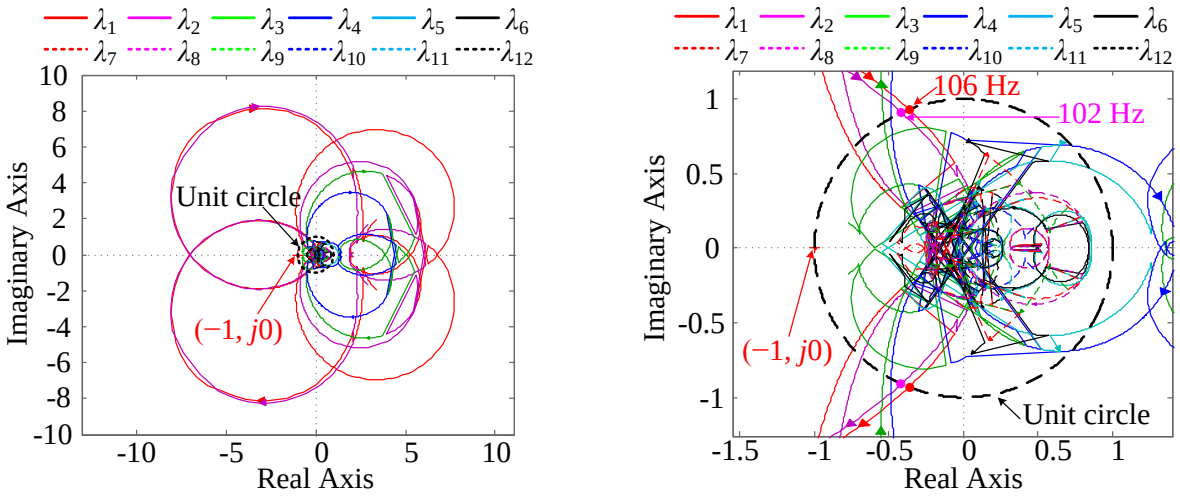

Figure 7-8. Characteristic loci of **L** in Case 2. (a) Full view; (b) zoomed-in view.

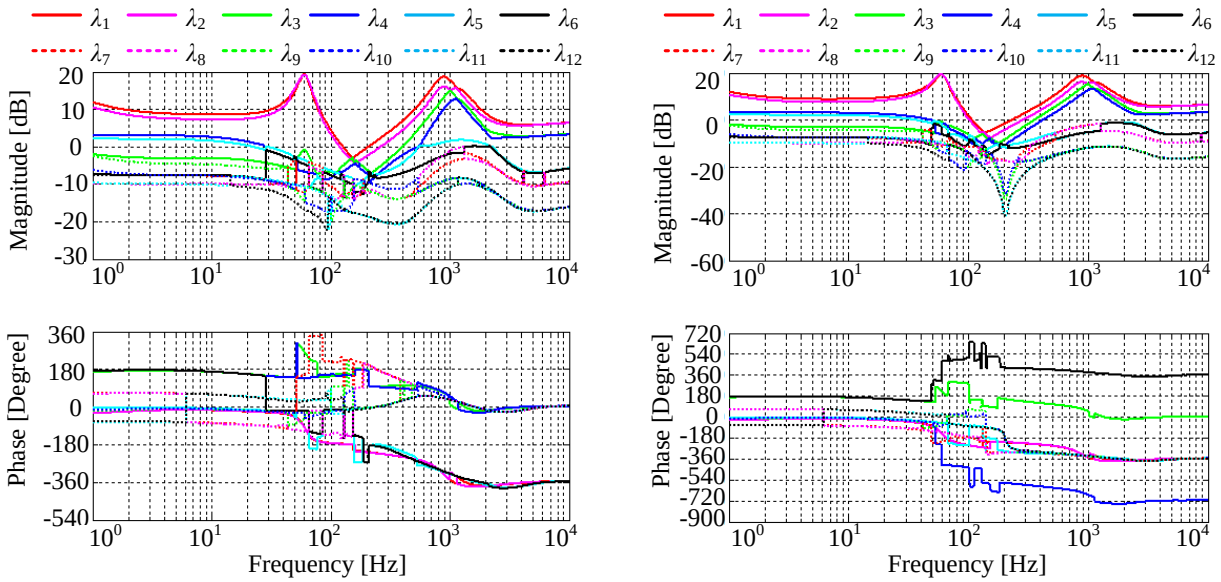

Figure 7-9. Bode plots of eigenvalues of **L** in (a) Case 1 and (b) Case 2.

Therefore, $N_{(-1,\,j0)}(\mathbf{L}) = 0$ and $Z(\mathbf{F}) = 0$ in Case 1, but $N_{(-1,\,j0)}(\mathbf{L}) = -4$ and $Z(\mathbf{F}) = 4$ in Case 2, which indicates that the system has four RHP poles in Case 2. The stability analysis result is the same with that presented in Section 7.2, and the analysis method based on the CCM and the GNC can avoid the examination of the RHP poles of the return-ratio matrix. In addition, it only needs the frequency-dependent impedance characteristics $\mathbf{L}(j\omega)$ instead of the detailed transfer function models $\mathbf{L}(s)$ of the system. Thus, it enables the system integrators to predict the stability of systems by using the measured impedances of purchased commercial inverters.

7.3.4 Proposed Stability Analysis Based on the CCM and the Determinant-Based GNC

For a large system with many inverters, it will be tedious to examine each characteristic locus of **L** when applying the eigenvalue-based GNC. Another stability analysis method for the system model based on the CCM is proposed here, that is, to predict the system stability by applying the determinant-based GNC to the return-difference matrix **F**. The stability criterion is expressed in (7-30). The system is stable if and only if $N_{(0,\,j0)}(\det(\mathbf{F}))$ is 0. Because the determinant of **F**, $\det(\mathbf{F})$, is a frequency-dependent scalar variable, there is only one Nyquist plot to be examined. Thus, the stability judging process using the determinant-based GNC is simpler than that using the eigenvalue-based GNC, which can be demonstrated as follows.

$$Z(\mathbf{F}) = P(\mathbf{L}) - N_{(0,\,j0)}\left(\det(\mathbf{F})\right) = -N_{(0,\,j0)}\left(\det(\mathbf{F})\right) \tag{7-30}$$

Figure 7-10 shows the Nyquist diagrams and Bode plots of $\det(\mathbf{F})$ in both cases. Considering the large magnitude variation, the Bode plot is an easier way than the Nyquist diagram to count the encirclements around the origin (0, *j*0). Note that the Nyquist plot in the full frequency range of $(-\infty, +\infty)$ should be considered. Therefore, considering the symmetrical Nyquist plots, when

only examining the positive frequency range of the Bode plot, 180 ° increase in the phase angle means encircling the (0, *j*0) point once in anti-clockwise direction while 180 ° decrease in the phase angle means encircling the (0, *j*0) point once in clockwise direction. According to the Bode plots, the overall phase variation values in the full positive frequency range are 0 ° in Case 1 but −180°×4=−720° in Case 2. It indicates that $N_{(0,\,j0)}(\det(\mathbf{F})) = 0$ in Case 1 but $N_{(0,\,j0)}(\det(\mathbf{F})) = -4$ in Case 2. Therefore, the closed-loop system is stable in Case 1 but unstable in Case 2 with 4 RHP poles. The analysis result agrees with the results using aforementioned other two methods.

It is worth noting that, although the determinant-based GNC can simplify the analysis, the eigenvalue-based GNC still has some advantages, such as 1) the gain margin and phase margin can be easily observed for stable cases (e.g. 2.8 dB and 2.7 ° in Case 1, as shown in Figure 7-7(b)), and 2) the approximate resonance frequencies can be determined for unstable cases (e.g. 102 Hz and 106 Hz in Case 2, as illustrated in Figure 7-8(d)).

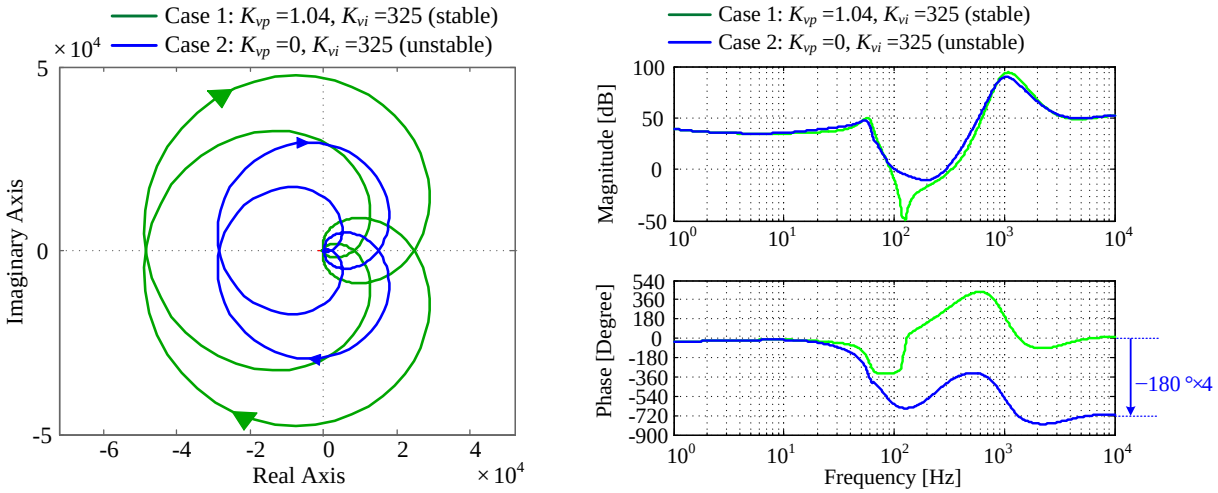

(a) (b)

Figure 7-10. Nyquist diagrams (a) and Bode plots of det(**F**) (b) in both cases.

7.4 Controller Parameter Design

Since the multi-bus system stability can be determined using the aforementioned stability analysis methods given a set of selected controller parameters, the inverter controller parameter can be designed in two steps for the system stability.

Step 1: design each individual inverter to be stable with ideal external conditions, and obtain the parameter range for *internal stability* of each isolated inverter to form parameter spaces.

Step 2: repetitively apply the stability analysis methods for all the parameter sets within the parameters spaces, in order to obtain the stable regions, unstable regions and stability boundaries for *external interconnection stability* of the system.

When using the traditional stability analysis method based on the GNC, the formulation and RHP pole calculation of the return-ratio transfer function matrix $\mathbf{T}_{\mathbf{m\_B7}}(s)$ should be executed for each parameter set, which is cumbersome. On the other hand, when using the stability analysis methods based on the CCM and the GNC, the impedance matrix $\mathbf{G}_{\mathbf{nw}}(j\omega)$ of the connection network only needs calculation once as long as the system topology remains the same, and only the combined impedance matrix $\mathbf{G}_{\mathbf{cd}}(j\omega)$ of all inverters requires an update for each parameter set, which makes the analysis process easier. In addition, considering that the examination of many characteristic loci of the MIMO return-ratio matrix in the method based on the CCM and the eigenvalue-based GNC is still tedious, the proposed stability analysis method based on the CCM and the determinant-based GNC is adopted here for this iteration-type design process.

For simplicity, it is assumed in the following analysis that all voltage-controlled inverters have the same controller parameters and all current-controlled inverters have the same controller parameters. The cut-off frequency ω_{ffv} of the voltage feed-forward control and the current loop

bandwidth ω_c of all current-controlled inverters are chosen to be designed. And the cut-off frequency ω_{fc} of the current filter in the current feed-forward control and the voltage PI control parameters (K_{vp}, K_{vi}) are selected to be designed for all voltage-controlled inverters.

The current PI controller parameters are set as (7-31), where the coefficient 875 is tuned to make the current loop bandwidth as ω_c. The voltage PI control parameters (K_{vp}, K_{vi}) are defined by (7-32), where the coefficients 1.04 and 325 are from Table 3-3 and used in aforementioned Case 1 and Case 2.

$$K_{cp} = \omega_c L_f, \quad K_{ci} = 875 K_{cp} \tag{7-31}$$

$$\begin{cases} K_{vp} = k_{vpgain} \times 1.04 \\ K_{vi} = k_{vigain} \times 325 \end{cases} \tag{7-32}$$

According to the Bode plots of the stable open-loop gains of the current-controlled inverters, $T_{c\_dd}(s)$, and the voltage-controlled inverters, $T_{v\_dd}(s)$, in the *d-d* channel as shown in Figure 7-11, the value of ω_c is confined in the range of [100×2π rad/s, 1000×2π rad/s] for *internal stability* of current-controlled inverters when connected to an ideal voltage source, and the value of k_{vpgain} and k_{vigain} are confined in the range from 0 to 5 for *internal stability* of voltage-controlled inverters with open-circuit.

Since ω_{ffv} and ω_{fc} only change the output admittance or impedance but do not change the stability of the current or voltage loops, the values of ω_{ffv} and ω_{fc} are confined in the ranges of [50×2π rad/s, 1000×2π rad/s] and [100×2π rad/s, 1000×2π rad/s], respectively. Other parameters are the same as those listed in Table 3-1, Table 3-2 and Table 3-3.

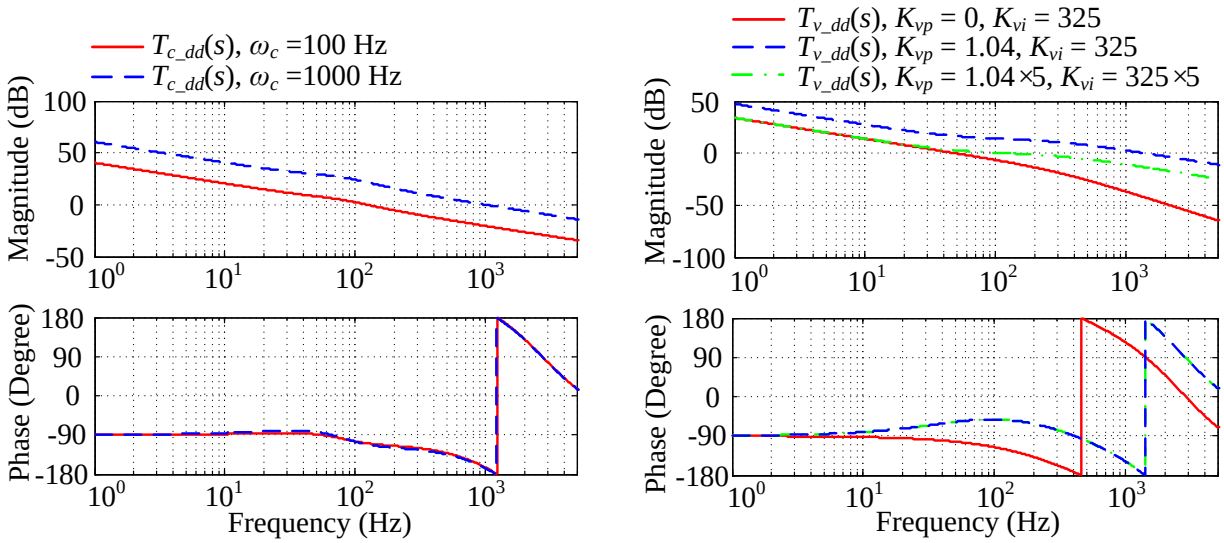

Figure 7-11. Bode plots of open-loop gains of (a) current-controlled inverters $T_{c\_dd}(s)$ and (b) voltage-controlled inverters $T_{v\_dd}(s)$ in the *d*-*d* channel.

7.4.1 Design of Voltage PI Control Parameters (K_{vp}, K_{vi})

The voltage PI control parameters (K_{vp}, K_{vi}) are defined by (7-32) are designed for *external interconnection stability* of the two-area system while keeping ω_c =700×2π rad/s and ω_{ffv} =50×2π rad/s. The parameter design results are presented in the two-dimensional parameter map in Figure 7-12(a). Stable parameter sets are shown as blue circles; unstable parameter sets are shown as red crosses; solid lines represent the analysis stability boundaries, while the dash lines illustrate the stability boundaries obtained from the simulation results of the two-area system using MATLAB/Simulink.

The design results in Figure 7-12(a) show that, for the inverter-based two-area system with generator emulation and static load emulation: 1) the system is unstable with a pure integral

voltage controller in the voltage-controlled inverters; 2) the system is prone to instability when the voltage proportional parameter K_{vp} is low ($k_{vpgain} \leq 1$).

For comparison, the design results for the inverter-based two-area system without generator emulation are presented in Figure 7-12(b), which shows that the system is stable in the whole parameter range. The difference between these two sets of design results is consistent with the conclusion drawn in [9] that the instability with a single integral voltage controller is due to the combination of the 4th-order synchronous generator model and the voltage controller in the inverter.

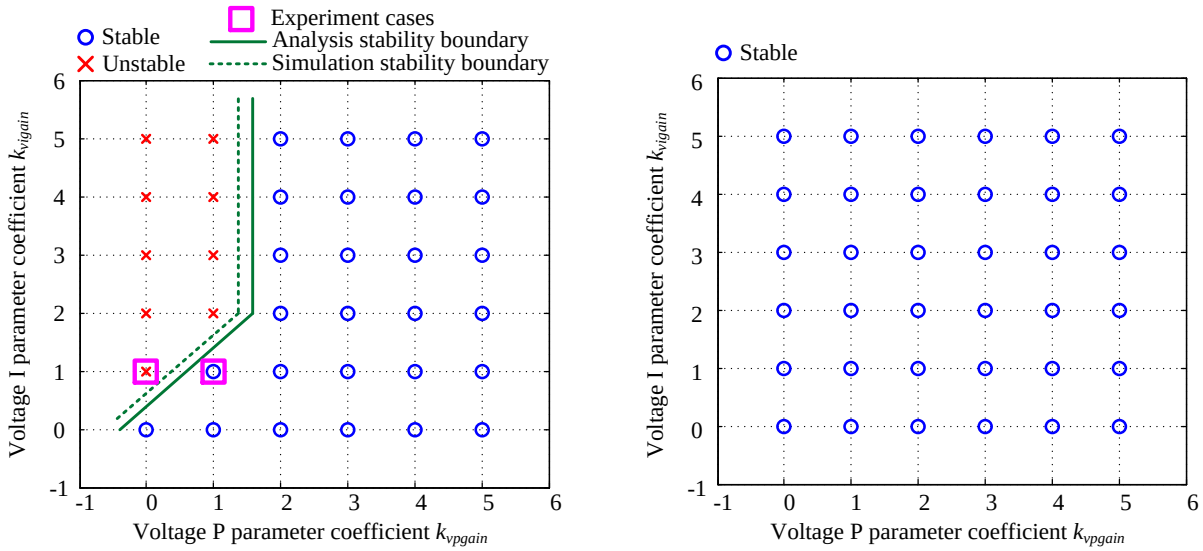

Figure 7-12. Stability regions and boundary in the map of the parameter pair (k_{vpgain} and k_{vigain}): (a) for system with generator emulation; (b) for system without generator emulation.

7.4.2 Design of Current Feed-Forward Parameter ω_{fc}

Assume the voltage PI control parameters (K_{vp}, K_{vi}) are defined by (7-33), where k_{vgain} is an adjustable gain. The parameter pair of the current feed-forward parameter ω_{fc} and the voltage PI parameter gain k_{vgain} is designed here. The value of k_{vgain} is confined in the range from 1 to 5. The value of ω_{fc} is confined in the range of [100×2π rad/s, 1000×2π rad/s] with ten linearly equally spaced points, and the cases without current feed-forward control (CFF) are also considered. All the other parameters of the inverters remain the same as those listed in Table 3-1, Table 3-2 and Table 3-3. The design result is shown in Figure 7-13.

$$\begin{cases} K_{vp} = k_{vgain} \times 1.04 \\ K_{vi} = k_{vgain} \times 325 \end{cases} \tag{7-33}$$

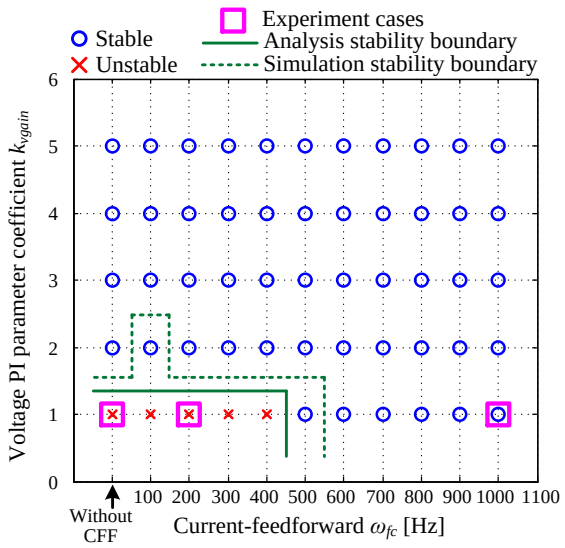

Figure 7-13. Stability regions and boundary in the map of the parameter pair (ω_{fc} and k_{vgain}).

It can be noticed that, when the voltage PI parameters are small, the current feed-forward control of the voltage-controlled inverters should be adopted and the parameter ω_{fc} should be designed high enough to avoid system instability. The small but acceptable discrepancy between the analysis results and the simulation results near the stability boundaries is due to the limitation of the model accuracy.

7.4.3 Design of the Parameter Pair (ω_{ffv}, ω_c)

Figure 7-14 depicts the design result. Some general design rules for the studied system can be derived. 1) The cut-off frequency ω_{ffv} of the voltage feedforward control cannot be very large. Larger ω_{ffv} makes the system more prone to instability. 2) The cut-off frequency ω_{ffv} of the voltage feedforward control should be smaller than the current loop bandwidth ω_c.

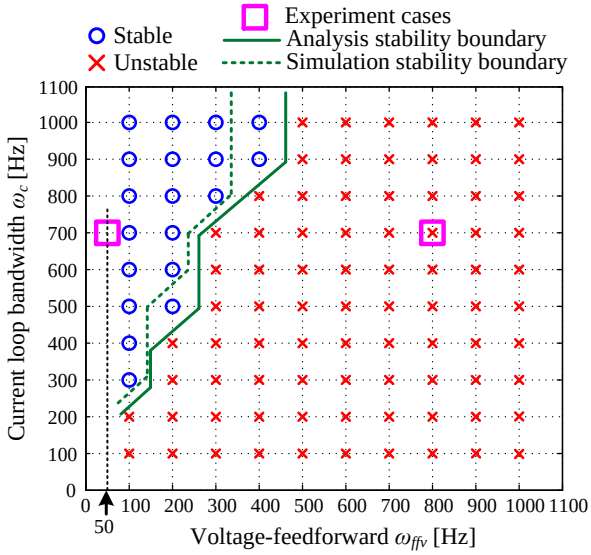

Figure 7-14. Stability regions and boundary in the map of the parameter pair (ω_{ffv} and ω_c).

7.5 Experimental Verification

The same experimental platform for scaled-down emulation of the two-area system is used here, but with generator emulation and static load emulation enabled in the inverters. The system parameters and operating point are the same as those described in Section 7.1. Experiments are carried out to verify the stability analysis presented in Section 7.2 and 7.3 as well as the controller parameter design results given in Section 7.4.

7.5.1 Design Verification of Voltage PI Control Parameters (K_{vp}, K_{vi})

In order to verify the aforementioned stability analysis as well as the design results of the voltage PI control parameters (K_{vp}, K_{vi}) presented in the map of the parameter pair (k_{vpgain} and k_{vigain}) in Figure 7-12(a), two experimental cases (Case 1 and Case 2) have been carried out, which are also marked as purple squares in Figure 7-12(a). Figure 7-15 shows the experimental waveforms of the phase-A currents i_a of inverters (G1, G3, L7 and L9) and line-to-line voltages v_{ab} of inverters (G1−G4) in the two-area system in the stable steady state with parameters (k_{vpgain} =1 and k_{vigain}=1). Since the system is composed of only inverters and inductors without any capacitors, the voltages v_{ab} have large switching-frequency harmonics. Thus, the digital low-pass-filter (LPF) with the cut-off frequency of 2 kHz is enabled in the Teledyne LeCroy oscilloscope, and the filtered line-to-line voltages v_{abf} are also shown in Figure 7-15. Figure 7-16 depicts the response of i_a and v_{abf} when the parameter change of k_{vpgain} from 1 to 0 is triggered. Figure 7-17 shows the corresponding waveforms of inverter currents (i_d and i_q) in their own *d*-*q* frames saved in inverter DSP controllers immediately after the trigger. As observed, the system changes from a stable state to an unstable state. The initial unstable oscillation frequency is about 85 Hz, which matches very well with the analytical results. Then, the large divergent currents cause over-current (OC) protection in inverters G1−G4.

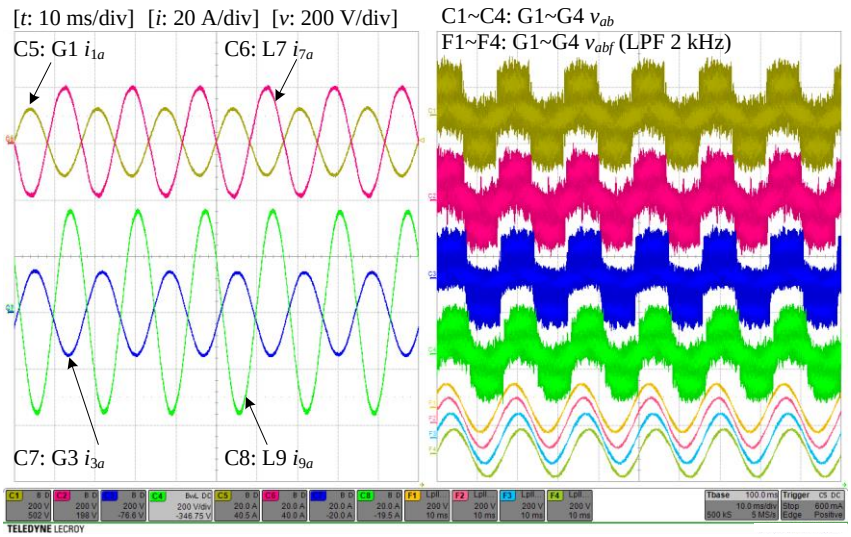

Figure 7-15. Experimental waveforms of the phase-A currents, original and filtered line-to-line voltages of inverters in the two-area system in the stable steady state.

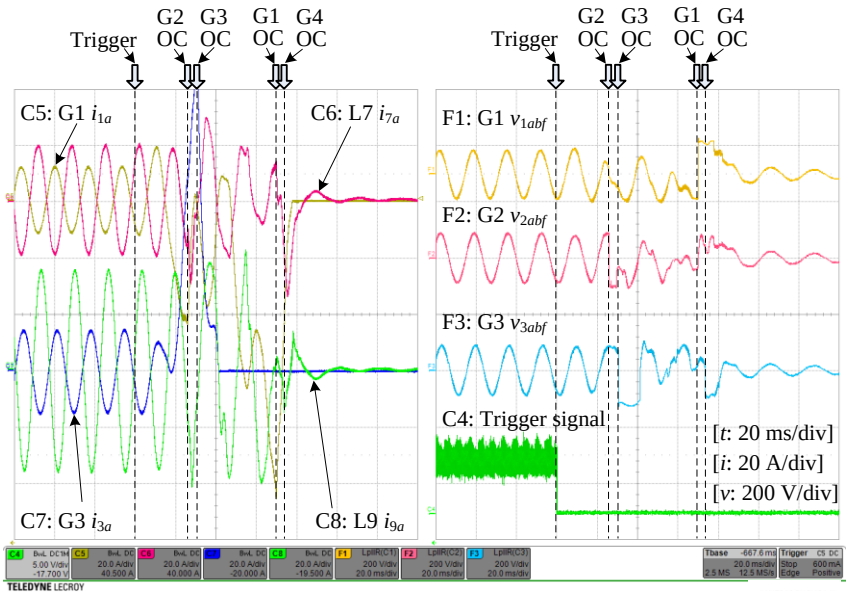

Figure 7-16. Experimental waveforms of the responses of the inverter phase-A currents and filtered line-to-line voltages when the change of k_{vpgain} from 1 to 0 is triggered.

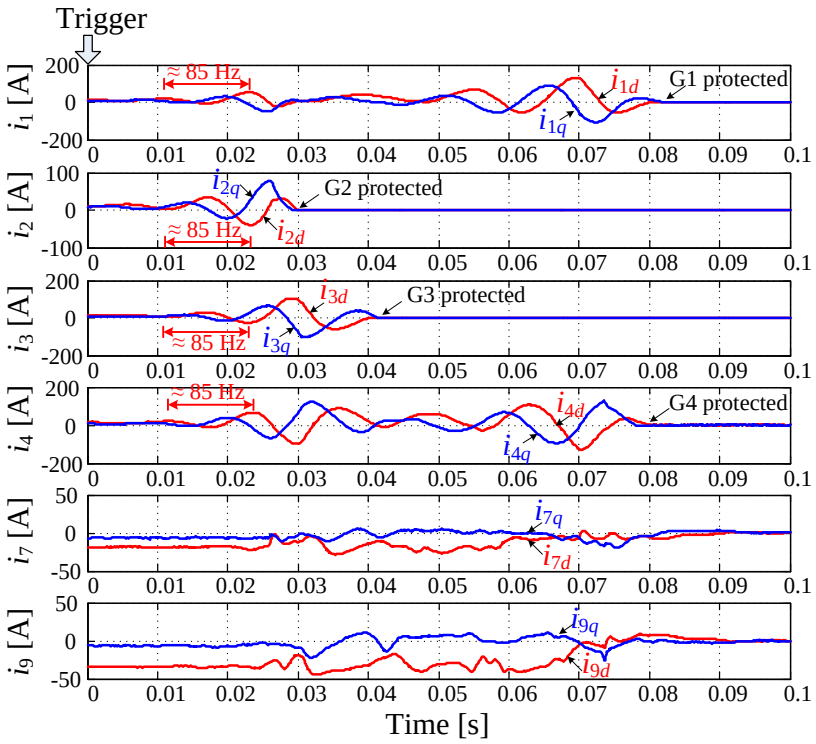

Figure 7-17. DSP-saved data of the *d-q* currents of inverters after the trigger.

7.5.2 Design Verification of Current Feed-Forward Parameter ω_{fc}

Three additional experimental cases are conducted to verify the design results of the current feed-forward parameter ω_{fc} and the voltage PI parameter gain k_{vgain} of inverters G1−G4 presented in the parameter map in Figure 7-13 (marked as purple squares). Case 3: k_{vgain} =1, ω_{fc} =1000×2π rad/s; Case 4: k_{vgain} =1, without current feed-forward control; Case 5: k_{vgain} =1, ω_{fc} =200×2π rad/s.

Figure 7-18 demonstrates the response of the inverter phase-A current i_a and filtered line-to-line voltages v_{abf} when the parameter change from Case 3 to Case 4 is triggered. As seen from the G1 inverter current i_{1a}, the system diverges into the unstable state after the trigger.

Figure 7-19 shows the FFT analysis results of currents and voltages of inverters G1 and G3 in the unstable state without current feed-forward control, which indicates oscillations of 40 Hz and 160 Hz in the phase domain or equivalently 100 Hz in the *d*-*q* frame.

Figure 7-20 illustrates the system response when the parameters change from Case 3 to Case 5, from which obvious oscillations can be observed after the trigger. FFT analysis results of inverter G1 current and voltage in Figure 7-21 display harmonics of 50 Hz and 170 Hz in the phase domain or equivalently 110 Hz in the *d*-*q* frame when current feed-forward parameter ω_{fc} is 200×2π rad/s.

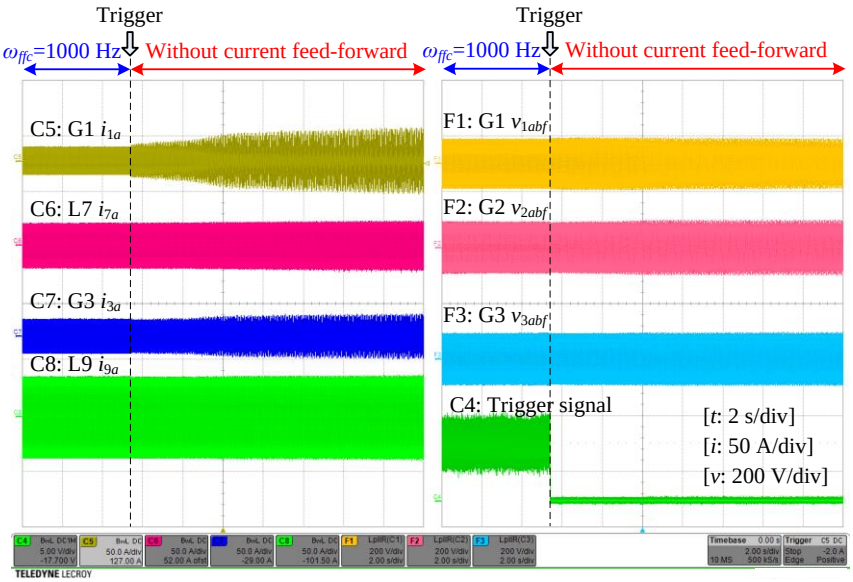

Figure 7-18. Experimental waveforms of the inverter phase-A currents and filtered line-to-line voltages when the disabling of current feed-forward control is triggered.

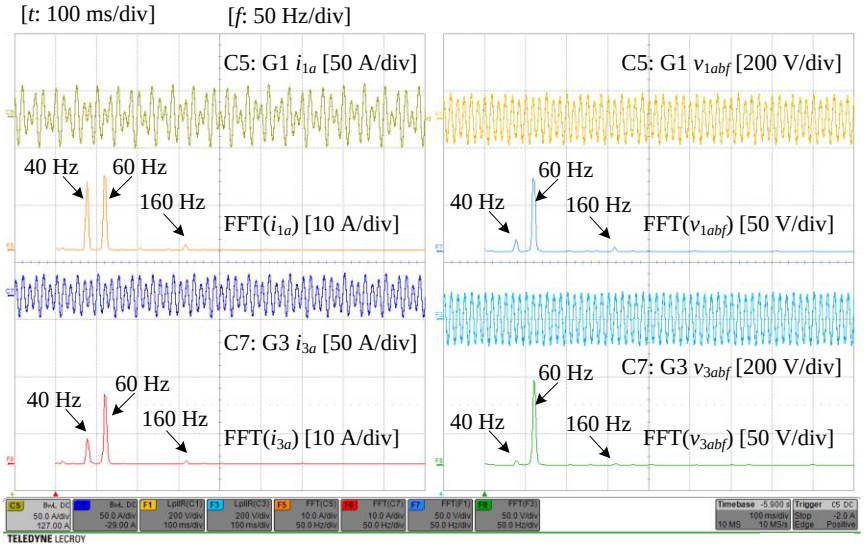

Figure 7-19. FFT analysis of the inverter phase-A currents and filtered line-to-line voltages in the unstable state without current feed-forward control.

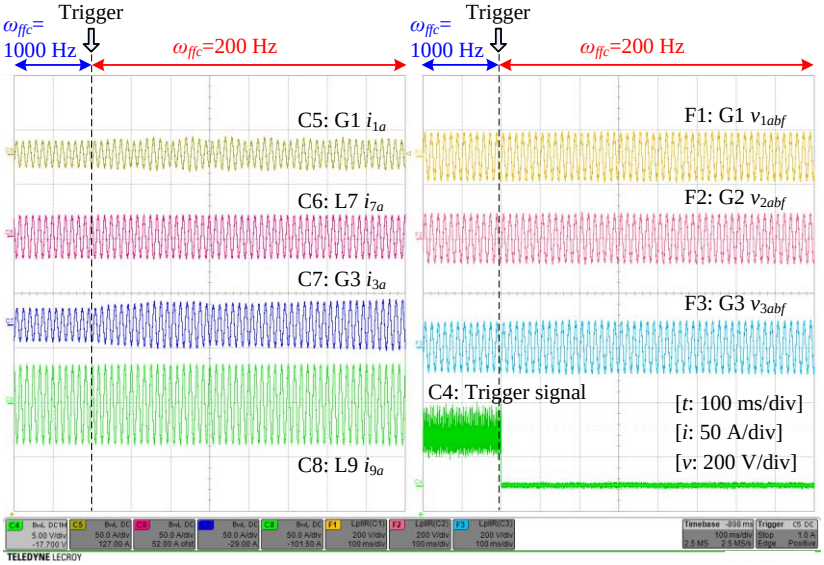

Figure 7-20. Experimental waveforms of the inverter phase-A currents and filtered line-to-line voltages when the change of ω_{fc} from 1000×2π rad/s to 200×2π rad/s is triggered.

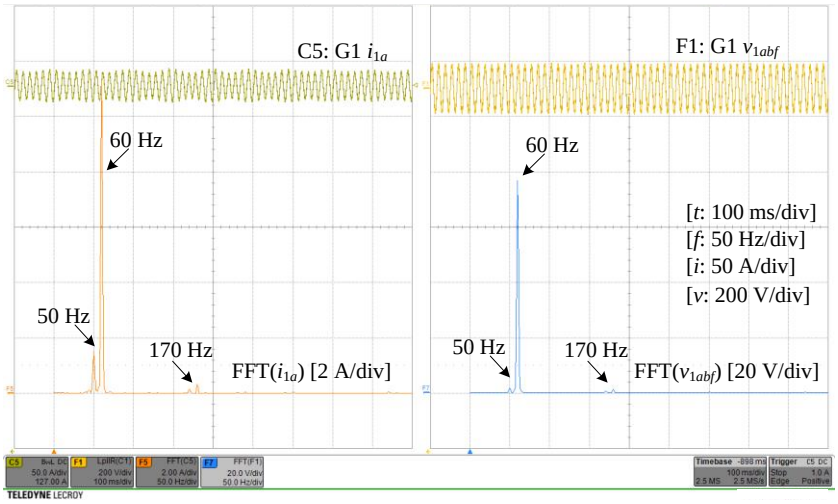

Figure 7-21. FFT analysis of the inverter phase-A currents and filtered line-to-line voltages with current feed-forward parameter ω_{fc} = 200×2π rad/s.

7.5.3 Design Verification of the Parameter Pair (ω_{ffv}, ω_c)

For verification of the design results of the voltage feed-forward parameter ω_{ffv} and the current loop bandwidth ω_c in load-emulation inverters L7 and L9, as shown in Figure 7-14, two more experimental cases (marked as purple squares) are performed. Case 6: ω_{ffv} =50×2π rad/s, ω_c =700×2π rad/s; Case 7: ω_{ffv} =800×2π rad/s, ω_c =700×2π rad/s. As shown in Figure 7-22, the system changes from a stable state to an unstable state after the parameters change from Case 6 to Case 7. According to Figure 7-23, the FFT analysis of phase-A currents of inverters L7 and L9 with voltage feed-forward parameter ω_{ffv} = 800×2π rad/s exhibit oscillations of 202 Hz and 322 Hz in the phase domain or equivalently 262 Hz in the *d*-*q* frame.

In summary, the experimental results have verified the stability analysis methods described in Section 7.2 and 7.3 as well as the controller parameter design results given in Section 7.4.

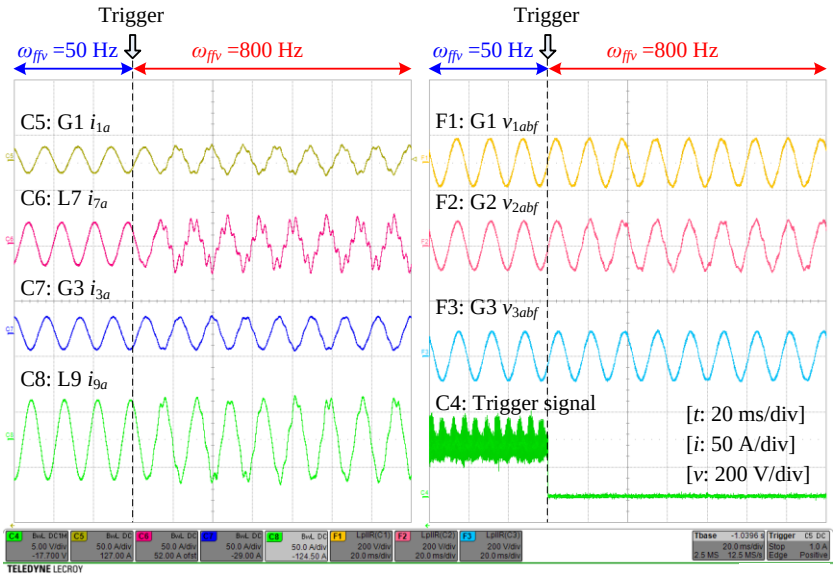

Figure 7-22. Experimental waveforms of the responses of the inverter phase-A currents and filtered line-to-line voltages when ω_{ffv} changes from 50×2π rad/s to 800×2π rad/s.

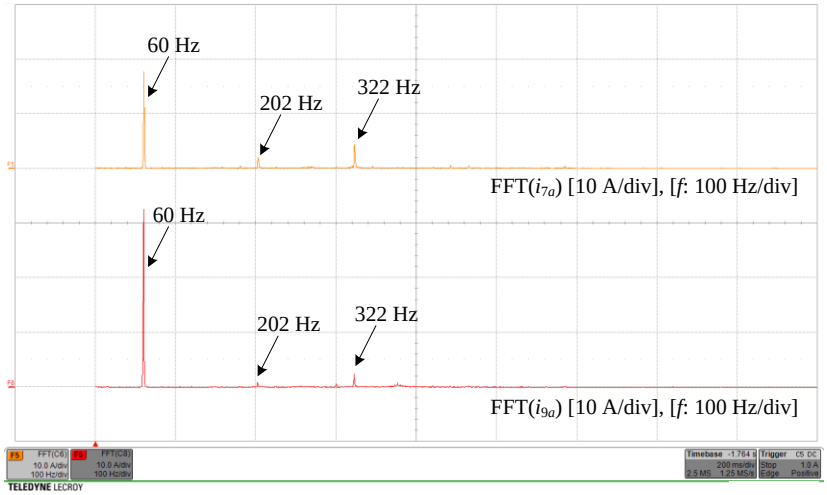

Figure 7-23. FFT analysis of inverter phase-A currents of inverters L7 and L9 with voltage feed-forward parameter ω_{ffv} = 800×2π rad/s.

7.6 Conclusion

This chapter addresses the stability issues and controller parameters design of three-phase inverter-based multi-bus ac systems, including both the harmonic stability and low-frequency stability. This chapter demonstrates, for the first time, the application of the CCM in the frequency domain and *d-q* impedances to the small-signal stability analysis of three-phase inverter-based ac power systems in the *d-q* frame, by proposing a method for deriving the impedance matrix of the connection network for systems with both voltage-controlled and current-controlled inverter components.

Compared with stability analysis using the GNC only, the analysis methods based on the CCM, *d-q* impedances and the GNC do not need to check the RHP poles of the return-ratio matrix. They only need the frequency-dependent impedance characteristics instead of the detailed transfer function models of system components, so system integrators can assess system stability using only the measured impedances of inverters.

Compared with the stability criterion based on the CCM and the eigenvalue-based GNC for conventional power systems, the proposed stability analysis method based on the CCM and the determinant-based GNC, requires only one Nyquist plot examination of the determinant of the return-difference matrix, and thus simplifies the stability judging process.

Controller parameters of both voltage-controlled and current-controlled inverters can be designed by repetitively applying the proposed stability method, and presented as stability regions in the parameter space. The proposed analysis and design method is verified by experiments of a two-area system with four voltage-controlled inverters with generator emulation and two current-controlled inverters with static load emulation.

8 Measured Terminal Characteristics Based Low Frequency Stability Analysis of Islanded Multi-Bus Ac Microgrids

In order to analyze the low-frequency stability of three-phase inverter-based islanded multi-bus ac microgrids when the fundamental frequency is not constant but dynamically regulated, this chapter proposed a stability analysis method based on the measured terminal characteristics of system components. An extended system model based on the CCM is proposed by including the fundamental frequency as an additional variable. The terminal-characteristics matrix of the connection network is also derived. The GNC is applied to the return-ratio or return-difference matrices for stability assessment.

8.1 System Description

In order to investigate the low-frequency unstable oscillation problem in three-phase inverter-based multi-bus ac microgrids in the islanded mode, a microgrid is established by modifying the IEEE 37-bus test system [48], [140] in the islanded mode. As shown in Figure 8-1, the microgrid consists of 4 inverters (VI1−VI4) with inner voltage control loop and outer droop control loop, another 3 inverters (CI1−CI3) with inner current control loop and outer power control loop, 25 *RL* loads and 3 shunt capacitors (C_p). The parameters of the network branches and loads are the same as those listed in Tables V and VI in [140], and thus not presented here. The shunt capacitor parameters are C_{p1}=150 μF, C_{p2}=300 μF and C_{p3}=100 μF, respectively.

Figure 8-2 shows the block diagram of the three-phase inverter with an output *L* filter. i_t is the inverter output current, v_M is the inverter output voltage and v_t is the inverter terminal voltage. The dc-link voltage v_{dc} is regulated by a front-end converter and regarded as a constant value V_{dc}.

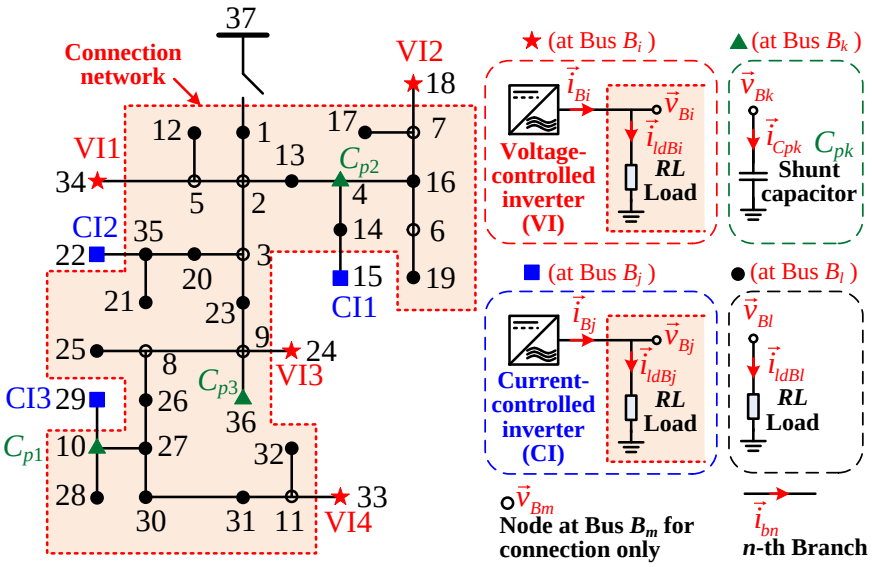

Figure 8-1. One-line diagram of the modified IEEE 37-bus test system in the islanded mode.

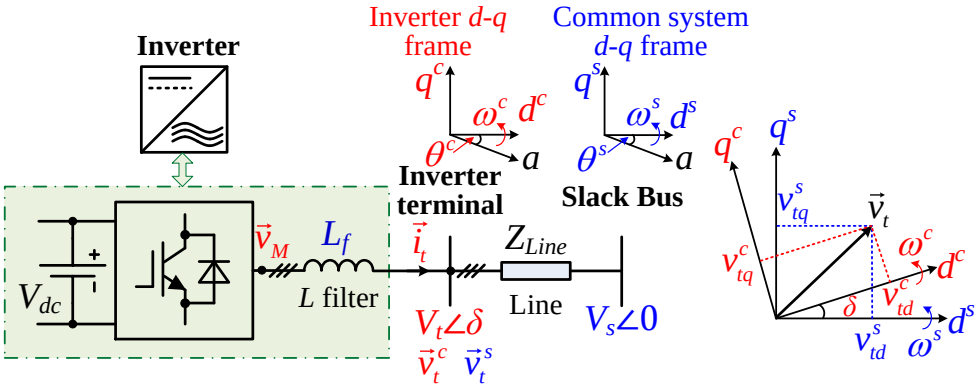

Figure 8-2. Block diagram of a three-phase inverter with an output L filter, and the relationship between different d-q frames.

As shown in Figure 8-2, the inverter terminal *d-q* frame with the superscript *c* is usually adopted for modeling and control of each inverter. The current-controlled inverters utilize the PLL for grid frequency synchronization. The voltage-controlled inverters use the droop controller to synchronize with the grid frequency. For the system stability analysis in the synchronous *d-q* frame, a common *d-q* frame with the superscript *s* is chosen to be aligned with the Bus 34 voltage, as shown in Figure 8-2. δ is the angle between these two *d-q* frames.

Figure 8-3(a) and (b) show the control block diagrams of current-controlled inverters (CI1−CI3) and voltage-controlled inverters (VI1−VI4), respectively. Figure 8-3(c) depicts the detailed diagram of the droop controller adopted by inverters (VI1−VI4). The instantaneous real power *p* and reactive power *q* are calculated from the measured inverter terminal voltage $\vec{v}_t^{\,c}$ and current $\vec{i}_t^{\,c}$ in the inverter *d-q* frame. The average real power *P* and reactive power *Q* are obtained by using the low-pass filters (LPF) with the cut-off frequency $\omega_{fp} = 5\times 2\pi$ rad/s. Then based on the droop equations in (8-1), the inverter frequency reference ω^c and the voltage references (v_{td}^{*c} and v_{tq}^{*c}) in the inverter *d-q* frame are generated, according to the nominal set points of the power (P_0 and Q_0), voltage and frequency (V_0 and ω_0) as well as the droop coefficients (m_P and n_Q) as listed in Table 8-1. The angle difference δ between the individual inverter reference frame and the common reference frame rotating at the common fundamental frequency ω^s can be derived as (8-2). Inverter parameters are the same as those listed in Table 3-1, Table 3-2 and Table 3-3.

$$\omega^c = \omega_0 - m_P\left(P - P_0\right),\ v_{td}^{*c} = V_0 - n_Q\left(Q - Q_0\right),\ v_{tq}^{*c} = 0 \tag{8-1}$$

$$\delta = \int\left(\omega^c - \omega^s\right)dt \tag{8-2}$$

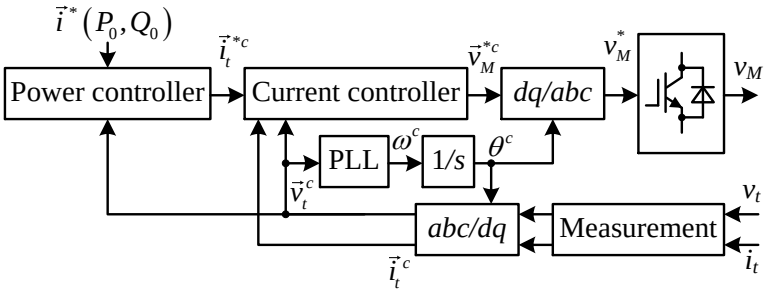

(a)

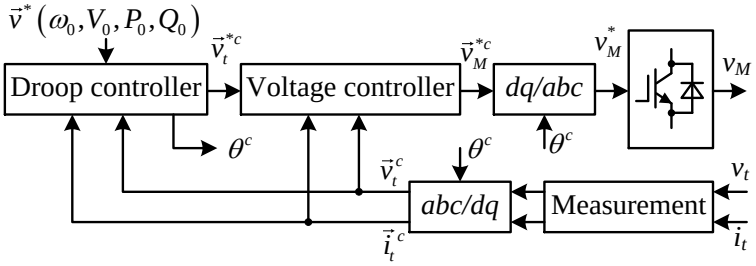

(b)

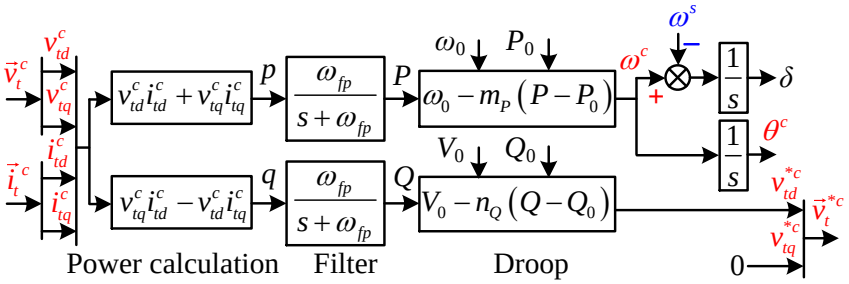

(c)

Figure 8-3. Control block diagrams: (a) inverters with inner current loop and outer power loop, (b) inverters with inner voltage loop and outer droop loop, and (c) the droop controller.

Table 8-1. Parameters of inverters in the modified IEEE 37-bus system.

Inverter	P_0 **(W)**	Q_0 **(Var)**	V_0 **(V)**	ω_0 **(rad/s)**	m_P	n_Q
VI1−VI4	250	0	50	60×2π	0.0025	0.0067
CI1−CI3	250	150	N/A	N/A	N/A	N/A

8.2 Terminal-Characteristics Modeling of Three-Phase Inverters

For three-phase inverter-based ac microgrids in the islanded mode, the fundamental frequency of the system is not a constant value but regulated dynamically and cooperatively by all the droop-controlled inverters. As reported in [75], [76], [104], in order to fully represent the dynamics, especially the low-frequency variation of the fundamental angular frequency ω, of three-phase droop-controlled inverters, the terminal characteristics modeling of inverters should also include a transfer function between the fundamental angular frequency ω and the current or voltage, in addition to the transfer functions (impedance or admittance) between the current and voltage.

By introducing the fundamental angular frequency vector $\vec{\omega}^s$ defined in (8-3), Figure 8-4 depicts the small-signal block diagrams of inverters based on terminal characteristics in the common system *d-q* frame. For the current-controlled inverters (CI1−CI3) with outer power control loop as shown in Figure 8-4(a), the complete small-signal model can be expressed as (8-4), where $\mathbf{G_{clcp}}(s)$ is the current closed-loop gain, $\mathbf{Y_{ocp}}(s)$ is the closed-loop output *d-q* admittance, and $\mathbf{G_{i\omega}}(s)$ is the closed-loop frequency-to-current transfer function matrix, as expressed in (8-5).

$$\vec{\omega}^s = \begin{bmatrix} \omega^s & 0 \end{bmatrix}^{\mathrm{T}} \tag{8-3}$$

$$\vec{\tilde{i}}_t^{\,s} = \mathbf{G_{clcp}}(s)\vec{\tilde{i}}^{*s} - \mathbf{Y_{ocp}}(s)\vec{\tilde{v}}_t^{\,s} - \mathbf{G_{i\omega}}(s)\tilde{\vec{\omega}}^s \tag{8-4}$$

$$\mathbf{Y_{ocp}}(s) = \begin{bmatrix} Y_{ocp\_dd}(s) & Y_{ocp\_dq}(s) \\ Y_{ocp\_qd}(s) & Y_{ocp\_qq}(s) \end{bmatrix}, \quad \mathbf{G_{i\omega}}(s) = \begin{bmatrix} G_{i\omega\_d}(s) & 0 \\ G_{i\omega\_q}(s) & 0 \end{bmatrix} \tag{8-5}$$

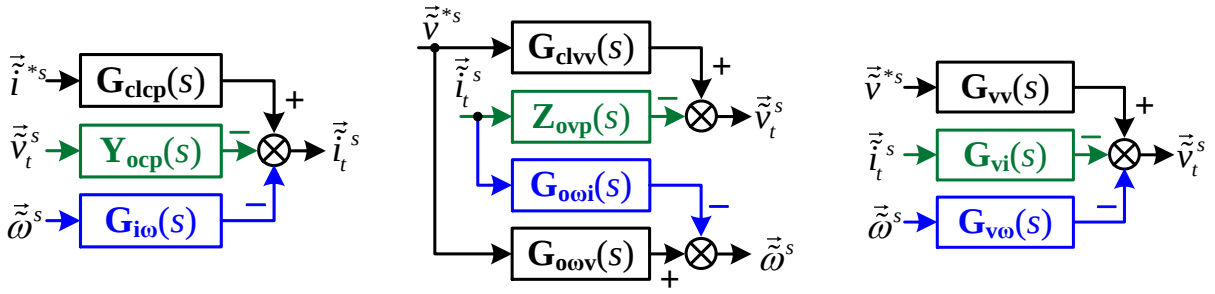

(a) (b) (c)

Figure 8-4. Small-signal diagrams of inverters based on terminal characteristics in the common system *d*-*q* frame: (a) current-controlled inverter, (b) voltage-controlled inverter which provides the common system fundamental frequency ω^s, and (c) other voltage-controlled inverters.

For the voltage-controlled inverter with outer droop control loop (VI1 is selected in this study), which provides the common system fundamental frequency ω^s as shown in Figure 8-4(b), the complete small-signal model can be expressed as (8-6), where $\mathbf{G_{clvv}}(s)$ is the voltage closed-loop gain, $\mathbf{Z_{ovp}}(s)$ is the closed-loop output *d*-*q* impedance, and $\mathbf{G_{o\omega i}}(s)$ and $\mathbf{G_{o\omega v}}(s)$ are the closed-loop current-to-frequency transfer function matrix and the reference-to-frequency transfer function matrix, respectively, as expressed in (8-7).

$$\begin{cases} \vec{\tilde{v}}_t^{\,s} = \mathbf{G_{clvv}}(s)\vec{\tilde{v}}^{*s} - \mathbf{Z_{ovp}}(s)\vec{\tilde{i}}_t^{\,s} \\ \vec{\tilde{\omega}}^{s} = \mathbf{G_{o\omega v}}(s)\vec{\tilde{v}}^{*s} - \mathbf{G_{o\omega i}}(s)\vec{\tilde{i}}_t^{\,s} \end{cases} \tag{8-6}$$

$$\begin{cases} \mathbf{Z_{ovp}}(s) = \begin{bmatrix} Z_{ovp\_dd}(s) & Z_{ovp\_dq}(s) \\ Z_{ovp\_qd}(s) & Z_{ovp\_qq}(s) \end{bmatrix} \\ \mathbf{G_{o\omega i}}(s) = \begin{bmatrix} G_{o\omega i\_d}(s) & G_{o\omega i\_q}(s) \\ 0 & 0 \end{bmatrix}, \quad \mathbf{G_{o\omega v}}(s) = \begin{bmatrix} G_{o\omega v\_d}(s) & G_{o\omega v\_q}(s) \\ 0 & 0 \end{bmatrix} \end{cases} \tag{8-7}$$

For other voltage-controlled inverters (VI2−VI4) with outer droop control loop as shown in Figure 8-4(c), the complete small-signal model can be expressed as (8-8), where $\mathbf{G_{vv}}(s)$ is the voltage closed-loop gain, $\mathbf{G_{vi}}(s)$ is the closed-loop output *d-q* impedance, and $\mathbf{G_{v\omega}}(s)$ is the closed-loop frequency-to-voltage transfer function matrix as expressed in (8-9).

$$\vec{\tilde{v}}_t^{\,s} = \mathbf{G_{vv}}(s)\vec{\tilde{v}}^{*s} - \mathbf{G_{vi}}(s)\vec{\tilde{i}}_t^{\,s} - \mathbf{G_{v\omega}}(s)\vec{\tilde{\omega}}^{s} \tag{8-8}$$

$$\mathbf{G_{vi}}(s) = \begin{bmatrix} G_{vi\_dd}(s) & G_{vi\_dq}(s) \\ G_{vi\_qd}(s) & G_{vi\_qq}(s) \end{bmatrix}, \quad \mathbf{G_{v\omega}}(s) = \begin{bmatrix} G_{v\omega\_d}(s) & 0 \\ G_{v\omega\_q}(s) & 0 \end{bmatrix} \tag{8-9}$$

8.3 Terminal-Characteristics Measurement of Three-Phase Inverters

8.3.1 Measurement Setup and Algorithm

The basic principle of terminal-characteristics measurement is still based on injection of sinusoidal perturbation signals with certain frequency, measurement of responses of the inverter under test, and calculation of frequency responses by using fast Fourier transform (FFT). Figure 8-5(a) shows the setup for terminal-characteristics measurement of current-controlled inverters (CI1−CI3). A three-phase controlled voltage source is adopted not only for generating the three-phase voltage at the fundamental frequency ω^s to establish the desired operating condition for the inverter under test, but also for injecting three perturbation signals, including the voltage perturbation signals (v_{pd}^s and v_{pq}^s) in the common system *d-q* frame and the perturbation signal of the common system fundamental frequency ω_p^s. The terminal voltage v_t and current i_l of the inverter under test are measured and transformed to the values in the common system *d-q* frame, namely, v_{td}^s, v_{tq}^s, i_{ld}^s and i_{lq}^s.

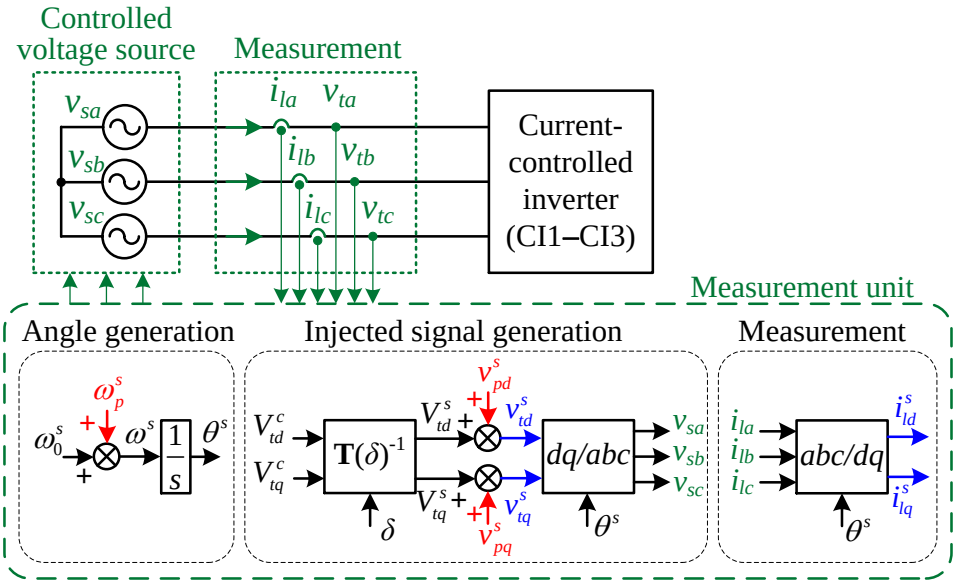

(a)

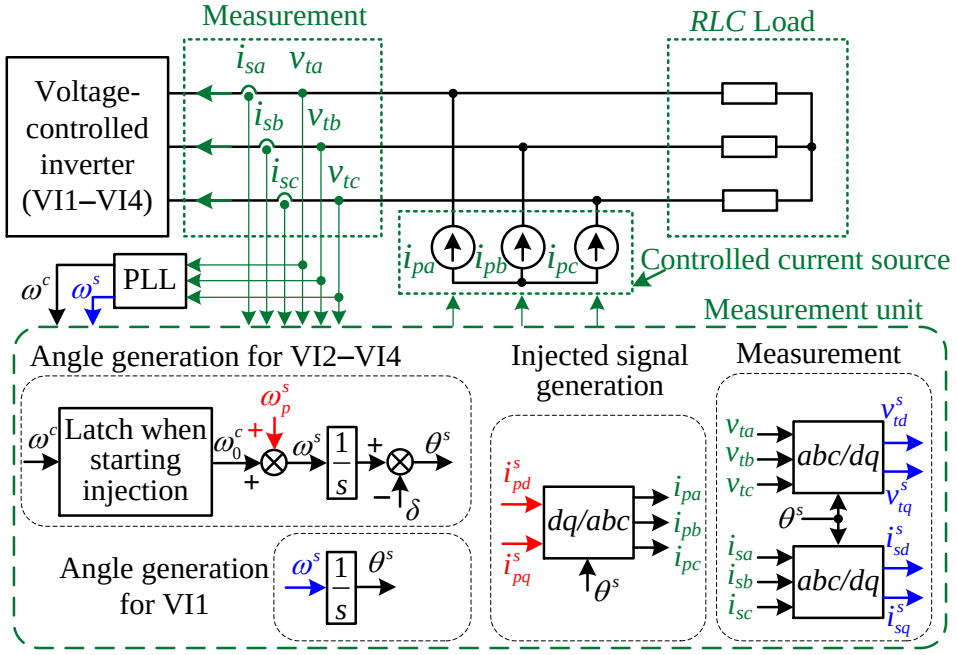

(b)

Figure 8-5. Terminal-characteristics measurement setups: (a) for current-controlled inverters, and (b) for voltage-controlled inverters.

In order to solve the six unknown values in the terminal characteristics $\mathbf{Y_{ocp}}(j\omega)$ and $\mathbf{G_{i\omega}}(j\omega)$ of a current-controlled inverter, three groups of independent perturbations with the subscripts 1, 2 and 3, respectively, are required. Then, the terminal characteristics can be calculated as (8-10). By sweeping the frequency of the injected signals and repeating the measurement process, the frequency response of the terminal characteristics of a current-controlled inverter in the desired frequency range can be obtained.

$$\begin{bmatrix} Y_{ocp\_dd} & Y_{ocp\_dq} & G_{i\omega\_d} \\ Y_{ocp\_qd} & Y_{ocp\_qq} & G_{i\omega\_q} \end{bmatrix} = \begin{bmatrix} i_{ld1}^s & i_{ld2}^s & i_{ld3}^s \\ i_{lq1}^s & i_{lq2}^s & i_{lq3}^s \end{bmatrix} \cdot \begin{bmatrix} v_{td1}^s & v_{td2}^s & v_{td3}^s \\ v_{tq1}^s & v_{tq2}^s & v_{tq3}^s \\ \omega_{p1}^s & \omega_{p2}^s & \omega_{p3}^s \end{bmatrix}^{-1} \tag{8-10}$$

Similarly, Figure 8-5(b) shows the setup for terminal-characteristics measurement of voltage-controlled inverters (VI1−VI4). A three-phase passive *RLC* load is used to make the inverter under test operate in the desired operating point. Another three-phase shunt controlled current source is utilized to inject current perturbations.

For VI1 which provides the common system fundamental frequency ω^s, perturbation signals include the currents (i_{pd}^s and i_{pq}^s) in the common system *d-q* frame. The measured signals include the common system fundamental frequency ω^s and the terminal voltages and currents (v_{td}^s, v_{tq}^s, i_{sd}^s and i_{sq}^s) of the inverter under test in the common system *d-q* frame. Through two independent perturbations, the terminal characteristics of VI1 can be obtained as (8-11). For VI2−VI4, the common system fundamental frequency ω_p^s becomes another perturbation signal, and their terminal characteristics can be solved as (8-12), by three independent perturbations.

$$\begin{bmatrix} Z_{ovp\_dd} & Z_{ovp\_dq} \\ Z_{ovp\_qd} & Z_{ovp\_qq} \\ G_{o\omega i\_d} & G_{o\omega i\_q} \end{bmatrix} = \begin{bmatrix} v_{td1}^s & v_{td2}^s \\ v_{tq1}^s & v_{tq2}^s \\ \omega_1^s & \omega_2^s \end{bmatrix} \cdot \begin{bmatrix} i_{sd1}^s & i_{sd2}^s \\ i_{sq1}^s & i_{sq2}^s \end{bmatrix}^{-1} \tag{8-11}$$

$$\begin{bmatrix} G_{vi\_dd} & G_{vi\_dq} & G_{v\omega\_d} \\ G_{vi\_qd} & G_{vi\_qq} & G_{v\omega\_q} \end{bmatrix} = \begin{bmatrix} v_{td1}^s & v_{td2}^s & v_{td3}^s \\ v_{tq1}^s & v_{tq2}^s & v_{tq3}^s \end{bmatrix} \cdot \begin{bmatrix} i_{sd1}^s & i_{sd2}^s & i_{sd3}^s \\ i_{sq1}^s & i_{sq2}^s & i_{sq3}^s \\ \omega_{p1}^s & \omega_{p2}^s & \omega_{p3}^s \end{bmatrix}^{-1} \tag{8-12}$$

8.3.2 Measurement Results in Simulation

Due to the limitation of the experimental setup, the terminal-characteristics measurement setups are only implemented in simulation by using MATLAB/Simulink. Figure 8-6, Figure 8-7 and Figure 8-8 present the Bode plots of the measured terminal characteristics of the current-controlled inverter CI1, the droop-controlled inverter VI1 and the droop-controlled inverter VI2, respectively.

The impact of the droop controller parameters on the terminal characteristics of voltage-controlled inverters with the outer droop control loop is also investigated. Two cases with different droop controller parameters are considered, namely, Case 1: m_P = 0.0025 and n_Q = 0.0067, and Case 2: m_P = 0.0050 and n_Q = 0.0133.

It can be observed that the droop parameters mainly influence the terminal characteristics of the droop-controlled inverters (VI1 and VI2) in the low-frequency range below 100 Hz. In addition, larger droop parameter values would result in larger magnitudes of the terminal characteristics.

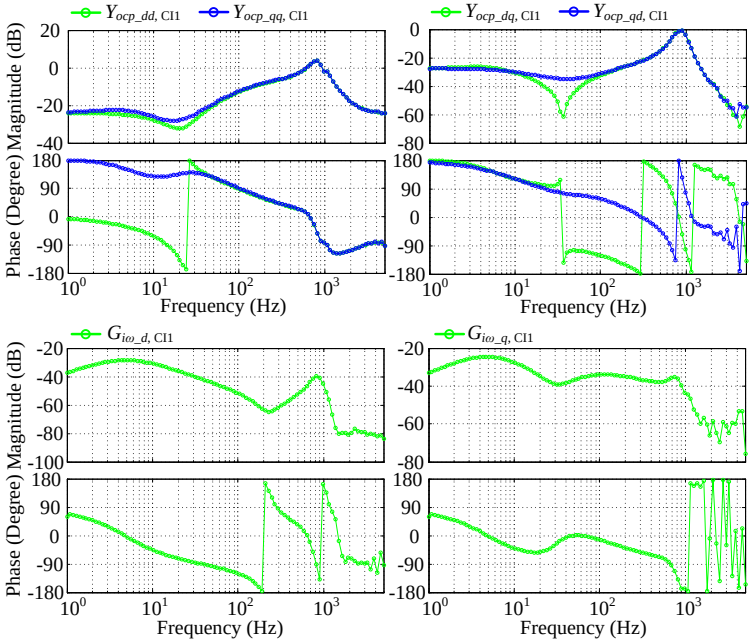

Figure 8-6. Bode plots of the terminal characteristics of the current-controlled inverter CI1.

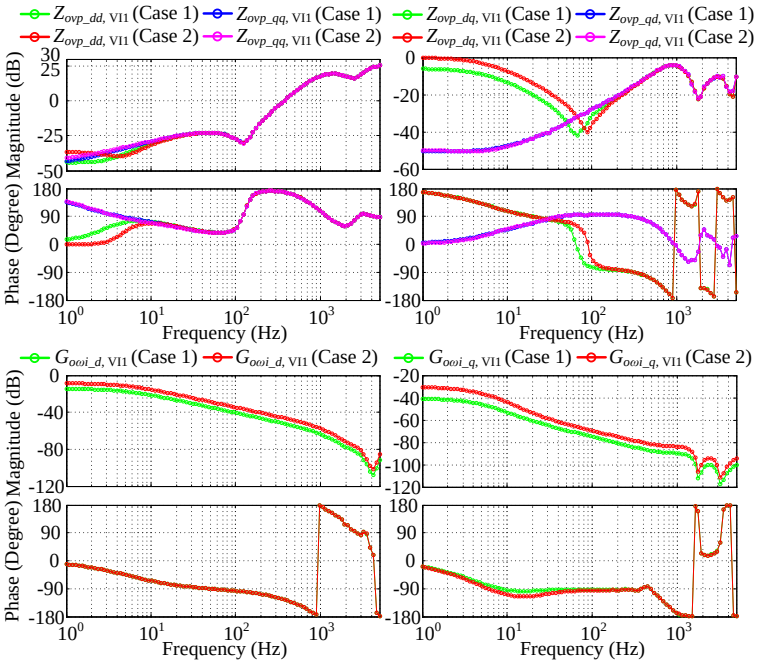

Figure 8-7. Bode plots of the terminal characteristics of the droop-controlled inverter VI1.

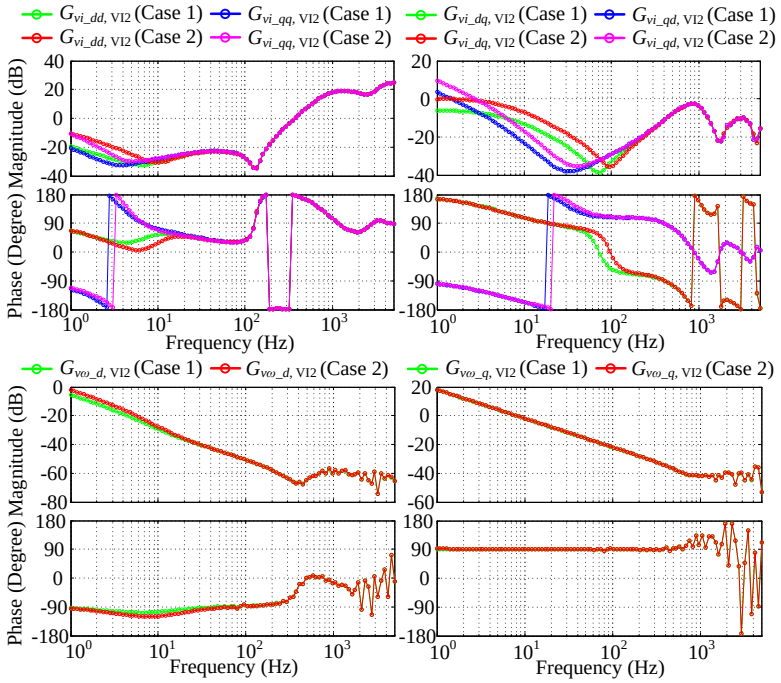

Figure 8-8. Bode plots of the terminal characteristics of the droop-controlled inverter VI2.

8.4 Proposed Stability Analysis Method Based on the CCM

In this section, the proposed stability analysis method based on the CCM and the GNC presented in Chapter 7 is further extended to include the common system fundamental frequency ω^s as an additional variable, in order to facilitate the low-frequency stability assessment of three-phase islanded ac microgrids using only the measured terminal characteristics of system components, without the need for the internal information of the inverters.

8.4.1 Proposed System Model Based on the CCM

Based on the Component Connection Method (CCM), the inverter-based islanded ac microgrid under study can be decomposed into individual inverter components and the connection network [23], as illustrated in Figure 8-1. Only the frequency of one droop-controlled

inverter (VI1) is selected as the common system fundamental frequency, and all other droop-controlled inverters and current-controlled inverters are modeled or measured in the common reference *d-q* frame. Therefore, VI1 can be separated at first to facilitate the modeling, while all other inverters can be modeled in a composite model as expressed in (8-13). The output vector $\vec{Y}(s)$, reference vector $\vec{U}(s)$ and disturbance vector $\vec{D}(s)$ of inverters are expressed in (8-14), respectively. $\mathbf{G_{cl}}(s)$ is the closed-loop transfer function matrix from the reference to the output as described in (8-15). $\mathbf{G_{cd}}(s)$ is the closed-loop transfer function matrix from the disturbance to the output with inverter output impedances or admittances as the diagonal elements, as shown in (8-16). $\mathbf{G_{c\omega}}(s)$ is the closed-loop transfer function matrix from the common system fundamental frequency to the output with the fundamental frequency related terminal characteristics of inverters as the diagonal elements, as shown in (8-17).

$$\vec{Y}(s)=\mathbf{G_{cl}}(s)\vec{U}(s)-\mathbf{G_{cd}}(s)\vec{D}(s)-\mathbf{G_{c\omega}}(s)\vec{\tilde{\omega}}^{s}(s) \tag{8-13}$$

$$\begin{cases}\vec{Y}(s)=[\vec{\tilde{v}}^{\,s}_{t,\mathrm{VI2}}(s),\vec{\tilde{v}}^{\,s}_{t,\mathrm{VI3}}(s),\vec{\tilde{v}}^{\,s}_{t,\mathrm{VI4}}(s),\vec{\tilde{i}}^{\,s}_{t,\mathrm{CI1}}(s),\vec{\tilde{i}}^{\,s}_{t,\mathrm{CI2}}(s),\vec{\tilde{i}}^{\,s}_{t,\mathrm{CI3}}(s)]^{\mathrm{T}}\\ \vec{U}(s)=[\vec{\tilde{v}}^{\,*s}_{\mathrm{VI2}}(s),\vec{\tilde{v}}^{\,*s}_{\mathrm{VI3}}(s),\vec{\tilde{v}}^{\,*s}_{\mathrm{VI4}}(s),\vec{\tilde{i}}^{\,*s}_{\mathrm{CI1}}(s),\vec{\tilde{i}}^{\,*s}_{\mathrm{CI2}}(s),\vec{\tilde{i}}^{\,*s}_{\mathrm{CI3}}(s)]^{\mathrm{T}}\\ \vec{D}(s)=[\vec{\tilde{i}}^{\,s}_{t,\mathrm{VI2}}(s),\vec{\tilde{i}}^{\,s}_{t,\mathrm{VI3}}(s),\vec{\tilde{i}}^{\,s}_{t,\mathrm{VI4}}(s),\vec{\tilde{v}}^{\,s}_{t,\mathrm{CI1}}(s),\vec{\tilde{v}}^{\,s}_{t,\mathrm{CI2}}(s),\vec{\tilde{v}}^{\,s}_{t,\mathrm{CI3}}(s)]^{\mathrm{T}}\end{cases} \tag{8-14}$$

$$\mathbf{G_{cl}}(s)=\mathrm{diag}[\mathbf{G_{vv},_{VI2}}(s),\mathbf{G_{vv},_{VI3}}(s),\mathbf{G_{vv},_{VI4}}(s),\mathbf{G_{clcp},_{CI1}}(s),\mathbf{G_{clcp},_{CI2}}(s),\mathbf{G_{clcp},_{CI3}}(s)] \tag{8-15}$$

$$\mathbf{G_{cd}}(s)=\mathrm{diag}[\mathbf{G_{vi},_{VI2}}(s),\mathbf{G_{vi},_{VI3}}(s),\mathbf{G_{vi},_{VI4}}(s),\mathbf{Y_{ocp},_{CI1}}(s),\mathbf{Y_{ocp},_{CI2}}(s),\mathbf{Y_{ocp},_{CI3}}(s)] \tag{8-16}$$

$$\mathbf{G_{c\omega}}(s)=\mathrm{diag}[\mathbf{G_{v\omega},_{VI2}}(s),\mathbf{G_{v\omega},_{VI3}}(s),\mathbf{G_{v\omega},_{VI4}}(s),\mathbf{G_{i\omega},_{CI1}}(s),\mathbf{G_{i\omega},_{CI2}}(s),\mathbf{G_{i\omega},_{CI3}}(s)] \tag{8-17}$$

Then, the model of the inverter VI1 can be further combined with the composite model of all other inverters to create the extended composite model of all inverters, by including the common

system fundamental frequency vector $\vec{\tilde{\omega}}^s$ in both the extended output vector $\vec{Y}_{ex}(s)$ and the extended disturbance vector $\vec{D}_{ex}(s)$, and the extended reference vector $\vec{U}_{ex}(s)$ is defined accordingly, as expressed in (8-18). Correspondingly, the extended closed-loop transfer function matrix from the reference to the output $\mathbf{G_{clex}}(s)$ is derived in (8-19), and the extended closed-loop transfer function matrix from the disturbance to the output $\mathbf{G_{cdex}}(s)$ is derived in (8-20).

$$\begin{cases} \vec{Y}_{ex}(s) = [\vec{\tilde{v}}^{s}_{t,\mathrm{VI1}}(s), \vec{Y}(s), \vec{\tilde{\omega}}^{s}(s)]^{\mathrm{T}} \\ \vec{U}_{ex}(s) = [\vec{\tilde{v}}^{*s}_{\mathrm{VI1}}(s), \vec{U}(s), \vec{\tilde{v}}^{*s}_{\mathrm{VI1}}(s)]^{\mathrm{T}} \\ \vec{D}_{ex}(s) = [\vec{\tilde{i}}^{s}_{t,\mathrm{VI1}}(s), \vec{D}(s), \vec{\tilde{\omega}}^{s}(s)]^{\mathrm{T}} \end{cases} \tag{8-18}$$

$$\mathbf{G_{clex}}(s) = \mathrm{diag}[\mathbf{G_{clvv}}(s), \mathbf{G_{cl}}(s), \mathbf{G_{o\omega v}}(s)] \tag{8-19}$$

$$\mathbf{G_{cdex}}(s) = \begin{bmatrix} \mathbf{Z_{ovp}}(s) & \mathbf{0} & \mathbf{0} \\ \mathbf{0} & \mathbf{G_{cd}}(s) & \mathbf{G_{c\omega}}(s) \\ \mathbf{G_{o\omega i}}(s) & \mathbf{0} & \mathbf{0} \end{bmatrix} \tag{8-20}$$

Next, the connection network can be modeled by (8-21) with $\mathbf{G_{nwex}}(s)$ representing the extended transfer function matrix from the output to the disturbance, which can also be regarded as a MIMO terminal-characteristics matrix model of the connection network. The expression of $\mathbf{G_{nwex}}(s)$ is shown in (8-22), where $\mathbf{G_{nw}}(s)$ is the traditional impedance matrix model of the connection network without considering the variation of the fundamental frequency ω^s, while $\mathbf{G_{nw\omega}}(s)$ is the fundamental-frequency-related terminal-characteristics matrix model of the connection network.

$$\vec{D}_{ex}(s) = \mathbf{G_{nwex}}(s)\vec{Y}_{ex}(s) \tag{8-21}$$

$$\mathbf{G}_{\mathbf{nwex}}(s)=\begin{bmatrix}\mathbf{G}_{\mathbf{nw}}(s) & \mathbf{G}_{\mathbf{nw\omega}}(s)\\ \mathbf{0} & \mathbf{1}\end{bmatrix} \tag{8-22}$$

Then, the overall system model can be obtained as (8-23) and also shown in Figure 8-9. Because each inverter is designed to be stable individually, $\mathbf{G}_{\mathbf{clex}}(s)$ is stable, and the system stability is determined by the transfer function matrix $[\mathbf{I}+\mathbf{G}_{\mathbf{cdex}}(s)\mathbf{G}_{\mathbf{nwex}}(s)]^{-1}$, which can be treated as the closed-loop transfer function matrix of a MIMO negative feedback system with the return-ratio transfer function matrix $\mathbf{L}_{\mathbf{ex}}(s)$ as expressed in (8-24) and the return-difference matrix $\mathbf{F}_{\mathbf{ex}}(s)$ as expressed in (8-25). Therefore, the system stability can be analyzed by applying the GNC to $\mathbf{L}_{\mathbf{ex}}(s)$ or $\mathbf{F}_{\mathbf{ex}}(s)$. The system model is established in the common system *d-q* frame, and there are totally seven inverters. Moreover, the common system fundamental frequency vector $\vec{\tilde{\omega}}^{s}$ is also considered. Therefore, the sizes of both $\mathbf{L}_{\mathbf{ex}}(s)$ and $\mathbf{F}_{\mathbf{ex}}(s)$ are 16-by-16.

$$\vec{Y}_{ex}(s)=\left[\mathbf{I}+\mathbf{G}_{\mathbf{cdex}}(s)\mathbf{G}_{\mathbf{nwex}}(s)\right]^{-1}\mathbf{G}_{\mathbf{clex}}(s)\vec{U}_{ex}(s) \tag{8-23}$$

$$\mathbf{L}_{\mathbf{ex}}(s)=\mathbf{G}_{\mathbf{cdex}}(s)\mathbf{G}_{\mathbf{nwex}}(s) \tag{8-24}$$

$$\mathbf{F}_{\mathbf{ex}}(s)=\mathbf{I}+\mathbf{G}_{\mathbf{cdex}}(s)\mathbf{G}_{\mathbf{nwex}}(s) \tag{8-25}$$

8.4.2 Proposed Method for Derivation of the Terminal-Characteristics Matrix of Connection Network

In order to model the terminal-characteristics matrix of the connection network considering the variation of the fundamental frequency, the terminal characteristics of passive components, such as the branches, *RL* loads and shunt capacitors in the ac microgrids, should also be derived.

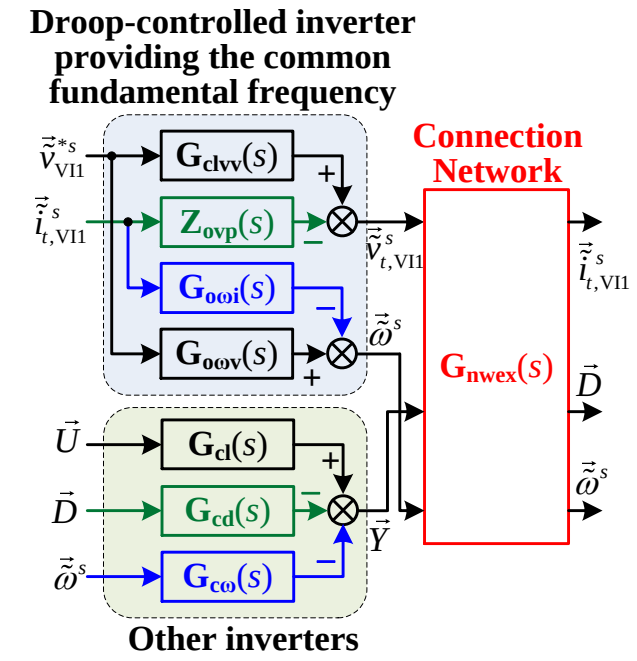

Figure 8-9. Small-signal diagrams of the CCM applied to the inverter-based microgrid: (a) detailed diagram, (b) equivalent MIMO feedback system.

The small-signal block diagrams of passive components in the common system *d-q* frame are illustrated in Figure 8-10. $\mathbf{Y_b}(s)$, $\mathbf{Y_{ld}}(s)$ and $\mathbf{Y_{Cp}}(s)$ are the *d-q* admittance matrices of a branch, a *RL* load and a shunt capacitor, respectively, in the common system *d-q* frame. $\mathbf{G_{i\omega b}}(s)$, $\mathbf{G_{i\omega ld}}(s)$ and $\mathbf{G_{i\omega Cp}}(s)$ are the fundamental-frequency-related terminal-characteristics matrices of a branch, a *RL* load and a shunt capacitor, respectively.

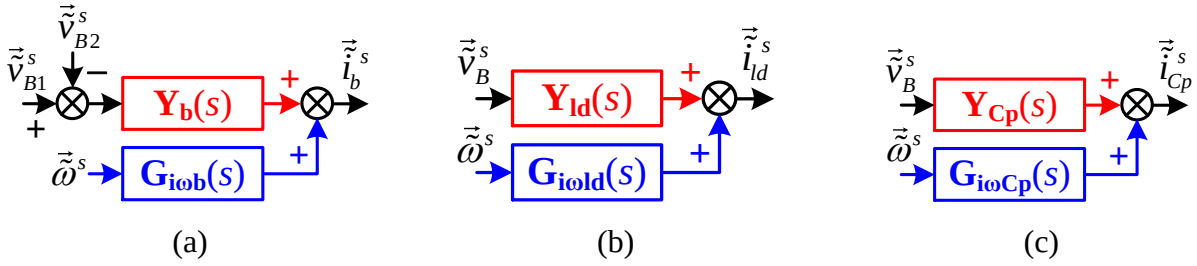

(a) (b) (c)

Figure 8-10. Small-signal block diagrams of passive components in the common system *d-q* frame: (a) a branch, (b) a *RL* load, and (c) a shunt capacitor.

The complete small-signal model of a branch is expressed in (8-26), where L_b and R_b are the inductance and resistance of the branch, respectively, and I^s_{bd} and I^s_{bq} are the steady-state values of the branch current in the common system *d-q* frame. The complete small-signal model of a *RL* load is expressed in (8-27), where L_{ld} and R_{ld} are the inductance and resistance of the load, respectively, and I^s_{ldd} and I^s_{ldq} are the steady-state values of the load current in the common system *d-q* frame. The complete small-signal model of a shunt capacitor is expressed in (8-28), where C_p is the capacitance, and V^s_{Cpd} and V^s_{Cpq} are the steady-state values of the capacitor voltage in the common system *d-q* frame.

$$\begin{cases} \vec{\tilde{i}}^s_b = \mathbf{Y_b}(s)\left(\vec{\tilde{v}}^s_{B1} - \vec{\tilde{v}}^s_{B2}\right) + \mathbf{G_{i\omega b}}(s)\vec{\tilde{\omega}}^s \\ \mathbf{Y_b}(s) = \begin{bmatrix} L_b s + R_b & -\omega^s L_b \\ \omega^s L_b & L_b s + R_b \end{bmatrix}^{-1}, \mathbf{G_{i\omega b}}(s) = \mathbf{Y_b}(s)\begin{bmatrix} L_b I^s_{bq} & 0 \\ -L_b I^s_{bd} & 0 \end{bmatrix} \end{cases} \quad (8\text{-}26)$$

$$\begin{cases} \vec{\tilde{i}}_{ld}^{\,s} = \mathbf{Y_{ld}}(s)\vec{\tilde{v}}_B^{\,s} + \mathbf{G_{i\omega ld}}(s)\vec{\tilde{\omega}}^{s} \\ \mathbf{Y_{ld}}(s) = \begin{bmatrix} L_{ld}s + R_{ld} & -\omega^s L_{ld} \\ \omega^s L_{ld} & L_{ld}s + R_{ld} \end{bmatrix}^{-1}, \mathbf{G_{i\omega ld}}(s) = \mathbf{Y_{ld}}(s)\begin{bmatrix} L_{ld}I_{ldq}^s & 0 \\ -L_{ld}I_{ldd}^s & 0 \end{bmatrix} \end{cases} \tag{8-27}$$

$$\begin{cases} \vec{\tilde{i}}_{Cp}^{\,s} = \mathbf{Y_{Cp}}(s)\vec{\tilde{v}}_B^{\,s} + \mathbf{G_{i\omega Cp}}(s)\vec{\tilde{\omega}}^{s} \\ \mathbf{Y_{Cp}}(s) = \begin{bmatrix} C_p s & -\omega^s C_p \\ \omega^s C_p & C_p s \end{bmatrix}, \mathbf{G_{i\omega Cp}}(s) = \begin{bmatrix} -C_p V_{Cpq}^s & 0 \\ C_p V_{Cpd}^s & 0 \end{bmatrix} \end{cases} \tag{8-28}$$

The extended nodal admittance equation of the connection network is defined in (8-29), where $\mathbf{I_{sys}}$ is the current vector flowing into all the nodes, $\mathbf{V_{sys}}$ is the voltage vector of all the nodes, $\mathbf{Y_{sys}}$ is the nodal admittance matrix of the connection work and $\mathbf{G_{i\omega sys}}$ is the fundamental-frequency-related nodal terminal-characteristics matrix of the connection work. $\mathbf{Y_{sys}}$ can be easily derived as in the normal nodal admittance equation, while $\mathbf{G_{i\omega sys}}$ can be derived in (8-30). Assume the numbers of the nodes, the branches, the *RL* loads and the shunt capacitors are *M*, *N*, *L* and *K*, respectively. The mapping matrix $\mathbf{M_{net}}$ is of size $2M \times 2N$, and it maps the branches onto the nodes of the connection network. The elements of $\mathbf{M_{net}}$ are 2×2 identity matrix **I** for the branch current leaving the node or $-\mathbf{I}$ for the branch current entering the node or 2×2 zero matrix **0** if the specific branch is not connected to the node. The mapping matrix $\mathbf{M_{load}}$ of size $2M \times 2L$ maps the loads onto the nodes, and its elements are **I** if the specific load is connected to the node or **0** if the specific load is not connected to the node. The mapping matrix $\mathbf{M_{cap}}$ of size $2M \times 2K$ maps the shunt capacitors onto the nodes, and its elements are similar to those in $\mathbf{M_{load}}$.

$$\mathbf{I_{sys}} = \mathbf{Y_{sys}}(s)\mathbf{V_{sys}} + \mathbf{G_{i\omega sys}}(s)\vec{\tilde{\omega}}^{s} \tag{8-29}$$

$$\begin{cases} \mathbf{G}_{\mathbf{i\omega sys}}(s) = \mathbf{M}_{\mathbf{net}}\mathbf{G}_{\mathbf{i\omega bN}}(s) + \mathbf{M}_{\mathbf{load}}\mathbf{G}_{\mathbf{i\omega ldL}}(s) + \mathbf{M}_{\mathbf{cap}}\mathbf{G}_{\mathbf{i\omega CpK}}(s) \\ \mathbf{G}_{\mathbf{i\omega bN}}(s) = [\mathbf{G}_{\mathbf{i\omega b}1}(s), \mathbf{G}_{\mathbf{i\omega b}2}(s), \cdots, \mathbf{G}_{\mathbf{i\omega b}N}(s)]^{\mathrm{T}} \\ \mathbf{G}_{\mathbf{i\omega ldL}}(s) = [\mathbf{G}_{\mathbf{i\omega ld}1}(s), \mathbf{G}_{\mathbf{i\omega ld}2}(s), \cdots, \mathbf{G}_{\mathbf{i\omega ld}L}(s)]^{\mathrm{T}} \\ \mathbf{G}_{\mathbf{i\omega CpK}}(s) = [\mathbf{G}_{\mathbf{i\omega Cp}1}(s), \mathbf{G}_{\mathbf{i\omega Cp}2}(s), \cdots, \mathbf{G}_{\mathbf{i\omega Cp}K}(s)]^{\mathrm{T}} \end{cases} \tag{8-30}$$

Similar to the derivation method of the impedance matrix of the connection network presented in Section 7.3.2, the proposed method for the derivation of the terminal-characteristics matrix of the connection network considering the variation of the fundamental frequency also contains two steps.

Step 1: eliminate the buses without inverter connections

$\mathbf{Y}_{\mathbf{sys}}$ and $\mathbf{G}_{\mathbf{i\omega sys}}$ can be expressed as partitioned matrices in (8-31), by dividing the current vector $\mathbf{I}_{\mathbf{sys}}$ / voltage vector $\mathbf{V}_{\mathbf{sys}}$ into the current vector $\mathbf{I}_{\mathbf{m}}$ / voltage vector $\mathbf{V}_{\mathbf{m}}$ for buses with direct connection of inverter components and the current vector $\mathbf{I}_{\mathbf{n}}$ / voltage vector $\mathbf{V}_{\mathbf{n}}$ for buses without component connection. Considering $\mathbf{I}_{\mathbf{n}} = [0, 0]^{\mathrm{T}}$, the relationship between $\mathbf{I}_{\mathbf{m}}$ and $\mathbf{V}_{\mathbf{m}}$ can be derived as (8-32) with the admittance matrix $\mathbf{Y}_{\mathbf{bus}}$ and the fundamental-frequency-related terminal-characteristics matrix $\mathbf{G}_{\mathbf{i\omega bus}}$.

$$\mathbf{I}_{\mathbf{sys}} = \mathbf{Y}_{\mathbf{sys}}(s)\mathbf{V}_{\mathbf{sys}} + \mathbf{G}_{\mathbf{i\omega sys}}(s)\vec{\tilde{\omega}}^{s} \Rightarrow \left[\begin{array}{c} \mathbf{I}_{\mathbf{m}} \\ \hdashline \mathbf{I}_{\mathbf{n}} \end{array}\right] = \left[\begin{array}{c:c} \mathbf{Y}_{\mathbf{mm}} & \mathbf{Y}_{\mathbf{mn}} \\ \hdashline \mathbf{Y}_{\mathbf{nm}} & \mathbf{Y}_{\mathbf{nn}} \end{array}\right]\left[\begin{array}{c} \mathbf{V}_{\mathbf{m}} \\ \hdashline \mathbf{V}_{\mathbf{n}} \end{array}\right] + \left[\begin{array}{c} \mathbf{G}_{\mathbf{i\omega m}} \\ \hdashline \mathbf{G}_{\mathbf{i\omega n}} \end{array}\right]\vec{\tilde{\omega}}^{s} \tag{8-31}$$

$$\mathbf{I}_{\mathbf{m}} = \left(\mathbf{Y}_{\mathbf{mm}} - \mathbf{Y}_{\mathbf{mn}}\mathbf{Y}_{\mathbf{nn}}^{-1}\mathbf{Y}_{\mathbf{nm}}\right)\mathbf{V}_{\mathbf{m}} + \left(\mathbf{G}_{\mathbf{i\omega m}} - \mathbf{Y}_{\mathbf{mn}}\mathbf{Y}_{\mathbf{nn}}^{-1}\mathbf{G}_{\mathbf{i\omega n}}\right)\vec{\tilde{\omega}}^{s} = \mathbf{Y}_{\mathbf{bus}}\mathbf{V}_{\mathbf{m}} + \mathbf{G}_{\mathbf{i\omega bus}}\vec{\tilde{\omega}}^{s} \tag{8-32}$$

Step 2: given $\mathbf{V}_{\mathbf{v}}$ and $\mathbf{I}_{\mathbf{c}}$, solve $\mathbf{I}_{\mathbf{v}}$ and $\mathbf{V}_{\mathbf{c}}$, to obtain $\mathbf{G}_{\mathbf{nw}}$ and $\mathbf{G}_{\mathbf{nw\omega}}$

$\mathbf{Y}_{\mathbf{bus}}$ and $\mathbf{G}_{\mathbf{i\omega bus}}$ can be reformatted as (8-33), by further partitioning $\mathbf{I}_{\mathbf{m}}$ and $\mathbf{V}_{\mathbf{m}}$ into vectors $\mathbf{I}_{\mathbf{v}}$ / $\mathbf{V}_{\mathbf{v}}$ for buses connected with voltage-controlled inverters and vectors $\mathbf{I}_{\mathbf{c}}$ / $\mathbf{V}_{\mathbf{c}}$ for buses with

the connection of current-controlled inverters, as shown in (8-34) and (8-35), respectively. Because $\mathbf{V_v}$ and $\mathbf{I_c}$ are inputs from the inverter components to the connection network, the outputs of the connection network ($\mathbf{I_v}$ and $\mathbf{V_c}$) can be solved from (8-33), as expressed in (8-36), and thus the impedance matrix $\mathbf{G_{nw}}$ and the fundamental-frequency-related terminal-characteristics matrix $\mathbf{G_{nw\omega}}$ of the connection network are derived.

$$\begin{bmatrix} \mathbf{I_v} \\ \mathbf{I_c} \end{bmatrix} = \begin{bmatrix} \mathbf{Y_{vv}} & \mathbf{Y_{vc}} \\ \mathbf{Y_{cv}} & \mathbf{Y_{cc}} \end{bmatrix} \begin{bmatrix} \mathbf{V_v} \\ \mathbf{V_c} \end{bmatrix} + \begin{bmatrix} \mathbf{G_{i\omega v}} \\ \mathbf{G_{i\omega c}} \end{bmatrix} \vec{\tilde{\omega}}^{s} \tag{8-33}$$

$$\mathbf{I_m^T} = \begin{bmatrix} \mathbf{I_v} & \mathbf{I_c} \end{bmatrix}^{\mathrm{T}} = \begin{bmatrix} \vec{\tilde{i}}^{\,s}_{t,\mathrm{VI1}} & \vec{\tilde{i}}^{\,s}_{t,\mathrm{VI2}} & \vec{\tilde{i}}^{\,s}_{t,\mathrm{VI3}} & \vec{\tilde{i}}^{\,s}_{t,\mathrm{VI4}} & \vec{\tilde{i}}^{\,s}_{t,\mathrm{CI1}} & \vec{\tilde{i}}^{\,s}_{t,\mathrm{CI2}} & \vec{\tilde{i}}^{\,s}_{t,\mathrm{CI3}} \end{bmatrix}^{\mathrm{T}} \tag{8-34}$$

$$\mathbf{V_m^T} = \begin{bmatrix} \mathbf{V_v} & \mathbf{V_c} \end{bmatrix}^{\mathrm{T}} = \begin{bmatrix} \vec{\tilde{v}}^{\,s}_{t,\mathrm{VI1}} & \vec{\tilde{v}}^{\,s}_{t,\mathrm{VI2}} & \vec{\tilde{v}}^{\,s}_{t,\mathrm{VI3}} & \vec{\tilde{v}}^{\,s}_{t,\mathrm{VI4}} & \vec{\tilde{v}}^{\,s}_{t,\mathrm{CI1}} & \vec{\tilde{v}}^{\,s}_{t,\mathrm{CI2}} & \vec{\tilde{v}}^{\,s}_{t,\mathrm{CI3}} \end{bmatrix}^{\mathrm{T}} \tag{8-35}$$

$$\begin{aligned} \begin{bmatrix} \mathbf{I_v} \\ \mathbf{V_c} \end{bmatrix} &= \begin{bmatrix} \mathbf{Y_{vv}} - \mathbf{Y_{vc}}\mathbf{Y_{cc}^{-1}}\mathbf{Y_{cv}} & \mathbf{Y_{vc}}\mathbf{Y_{cc}^{-1}} \\ -\mathbf{Y_{cc}^{-1}}\mathbf{Y_{cv}} & \mathbf{Y_{cc}^{-1}} \end{bmatrix} \begin{bmatrix} \mathbf{V_v} \\ \mathbf{I_c} \end{bmatrix} + \begin{bmatrix} \mathbf{G_{i\omega v}} - \mathbf{Y_{vc}}\mathbf{Y_{cc}^{-1}}\mathbf{G_{i\omega c}} \\ -\mathbf{Y_{cc}^{-1}}\mathbf{G_{i\omega c}} \end{bmatrix} \vec{\tilde{\omega}}^{s} \\ &= \mathbf{G_{nw}} \begin{bmatrix} \mathbf{V_v} \\ \mathbf{I_c} \end{bmatrix} + \mathbf{G_{nw\omega}} \vec{\tilde{\omega}}^{s} \end{aligned} \tag{8-36}$$

8.4.3 Stability Analysis Based on the CCM and the GNC

The impact of droop controller parameters on system stability is analyzed here. The aforementioned two cases, namely Case 1 and Case 2, are considered.

The stability of the islanded ac microgrid can be analyzed by applying the eigenvalue-based GNC to the return-ratio matrix $\mathbf{L_{ex}}(s)$, as expressed in (8-37). The connection network consists of only passive elements, so $\mathbf{G_{nwex}}(s)$ does not have RHP poles. Considering the stable matrix $\mathbf{G_{cdex}}(s)$, $\mathbf{L_{ex}}(s)$ does not have RHP poles, that is, $P(\mathbf{L_{ex}}) = 0$. Therefore, the system is stable if

and only if $N_{(-1,\,j0)}(\mathbf{L_{ex}}) = 0$.

$$Z\left(\mathbf{F_{ex}}\right) = P\left(\mathbf{L_{ex}}\right) - N_{(-1,\,j0)}\left(\mathbf{L_{ex}}\right) = -N_{(-1,\,j0)}\left(\mathbf{L_{ex}}\right) \tag{8-37}$$

Because only $N_{(-1,\,j0)}(\mathbf{L_{ex}})$ is required for stability analysis, the detailed transfer function matrix of $\mathbf{L_{ex}}(s)$ is not needed, and the stability can be readily assessed by the frequency-dependent characteristics $\mathbf{L_{ex}}(j\omega)$. Moreover, $\mathbf{L_{ex}}(j\omega)$ can be obtained by the aforementioned measured terminal characteristics of inverters and the frequency response data $\mathbf{G_{nwex}}(j\omega)$ generated by the terminal characteristics transfer function matrix $\mathbf{G_{nwex}}(s)$ of the connection network, assuming the parameters of the connection network are known. $\mathbf{L_{ex}}(j\omega)$ has 16 frequency-dependent eigenvalues (λ_1 to λ_{16}).

Figure 8-11(a) and (b) illustrate the characteristic loci of $\mathbf{L_{ex}}(j\omega)$ in Case 1. None of the characteristic loci encircles the critical point (−1, *j*0). However, in Case 2 as depicted in Figure 8-12(a) and (b), the characteristic locus λ_3 encircles the critical point (−1, *j*0) clockwise twice. Thus, $N_{(-1,\,j0)}(\mathbf{L_{ex}}) = 0$ and $Z(\mathbf{F_{ex}}) = 0$ in Case 1, but $N_{(-1,\,j0)}(\mathbf{L_{ex}}) = -2$ and $Z(\mathbf{F_{ex}}) = 2$ in Case 2, which indicates that Case 2 is unstable with two RHP poles. In addition, λ_3 intersects the unit circle at about 3.63 Hz in Case 1 and the phase margin is 19.4 °. In Case 2, the frequency of the intersection point is about 8.59 Hz and the phase margin is −4 °.

The microgrid stability can also be evaluated by applying the determinant-based GNC to the return-difference matrix $\mathbf{F_{ex}}(j\omega)$. The stability criterion is expressed in (8-38). The system is stable if and only if $N_{(0,\,j0)}(\det(\mathbf{F_{ex}}))$ is 0.

$$Z\left(\mathbf{F_{ex}}\right) = P\left(\mathbf{L_{ex}}\right) - N_{(0,\,j0)}\left(\det\left(\mathbf{F_{ex}}\right)\right) = -N_{(0,\,j0)}\left(\det\left(\mathbf{F_{ex}}\right)\right) \tag{8-38}$$

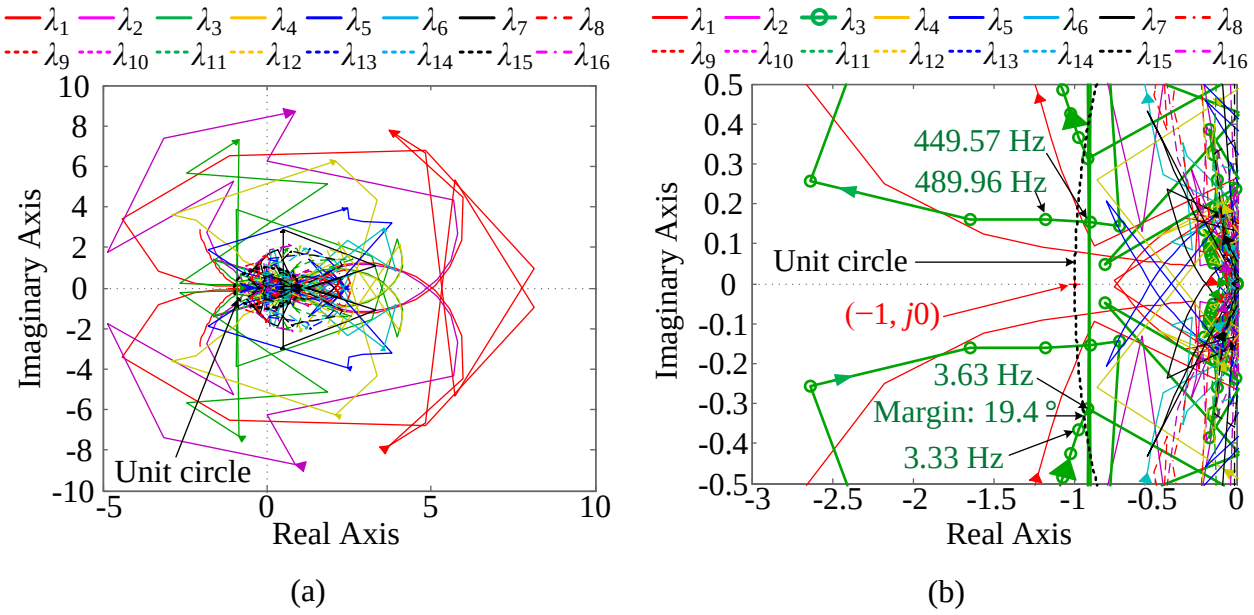

Figure 8-11. Characteristic loci of $\mathbf{L}_{ex}(j\omega)$ in Case 1. (a) Full view; (b) zoomed-in view.

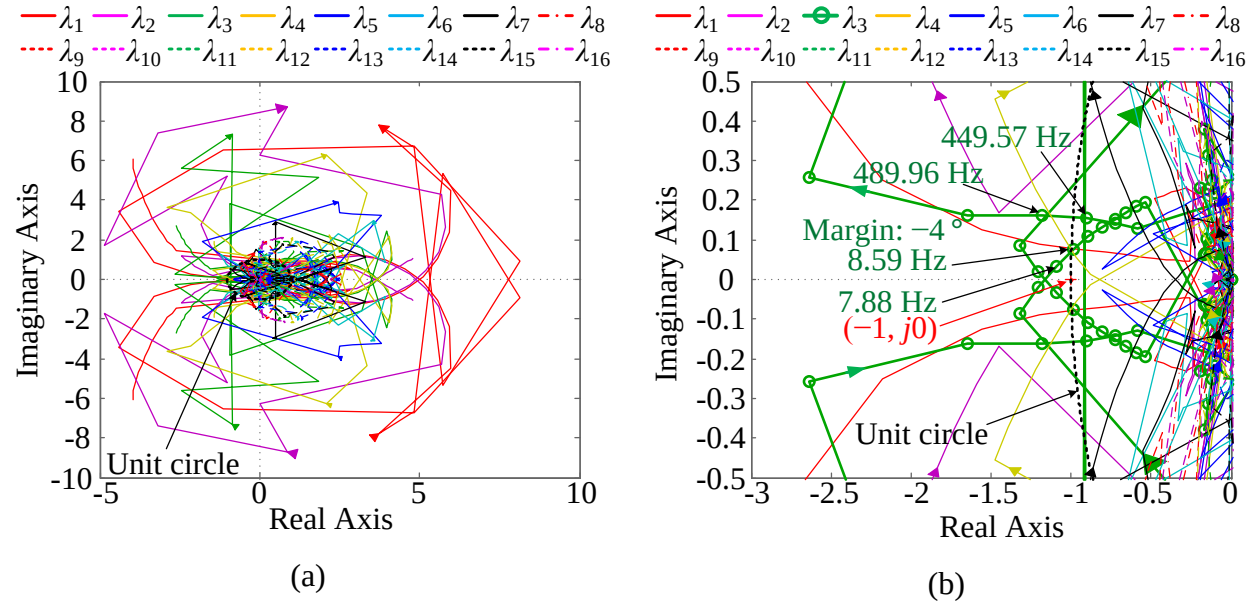

Figure 8-12. Characteristic loci of $\mathbf{L}_{ex}(j\omega)$ in Case 2. (a) Full view; (b) zoomed-in view.

Figure 8-13 shows the Bode plots of det($\mathbf{F_{ex}}$) in both cases. It can be implied that there are three integral elements in the system, so when drawing the Nyquist plot, the Nyquist trajectory segment corresponding to the infinitesimal semi-circle around the origin point in anti-clockwise direction of the Nyquist contour Γ_s in the *s*-plane ([*s*]) as shown in Figure 8-14(a) should also be considered, as illustrated in Figure 8-14(b).

According to the Bode plots in Figure 8-13, the overall phase variation values in the full positive frequency range are 0° in Case 1 but −180°×2=−360 ° in Case 2. It indicates that $N_{(0,\,j0)}(\det(\mathbf{F_{ex}})) = 0$ in Case 1 but $N_{(0,\,j0)}(\det(\mathbf{F_{ex}})) = -2$ in Case 2. Therefore, the system is stable in Case 1 but unstable in Case 2 with 2 RHP poles.

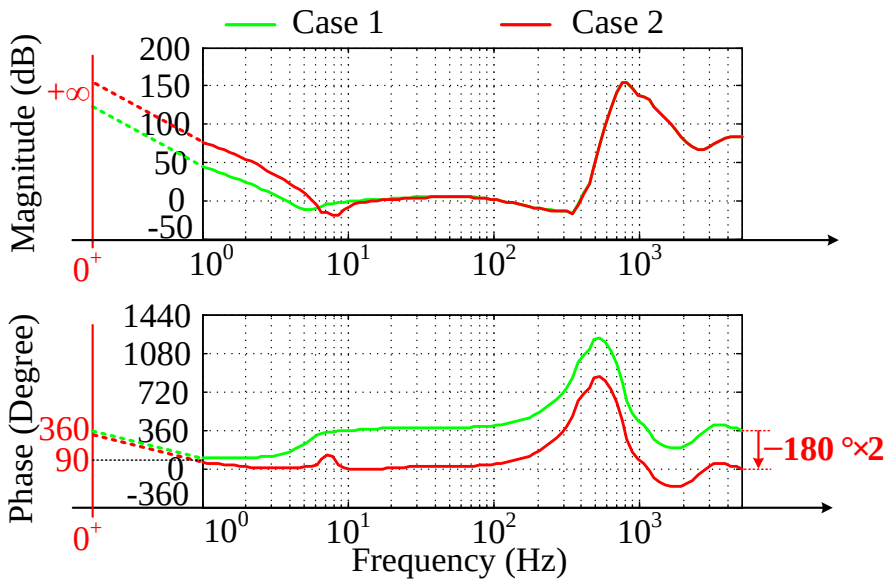

Figure 8-13. Bode plots of det($\mathbf{F_{ex}}$) in both cases.

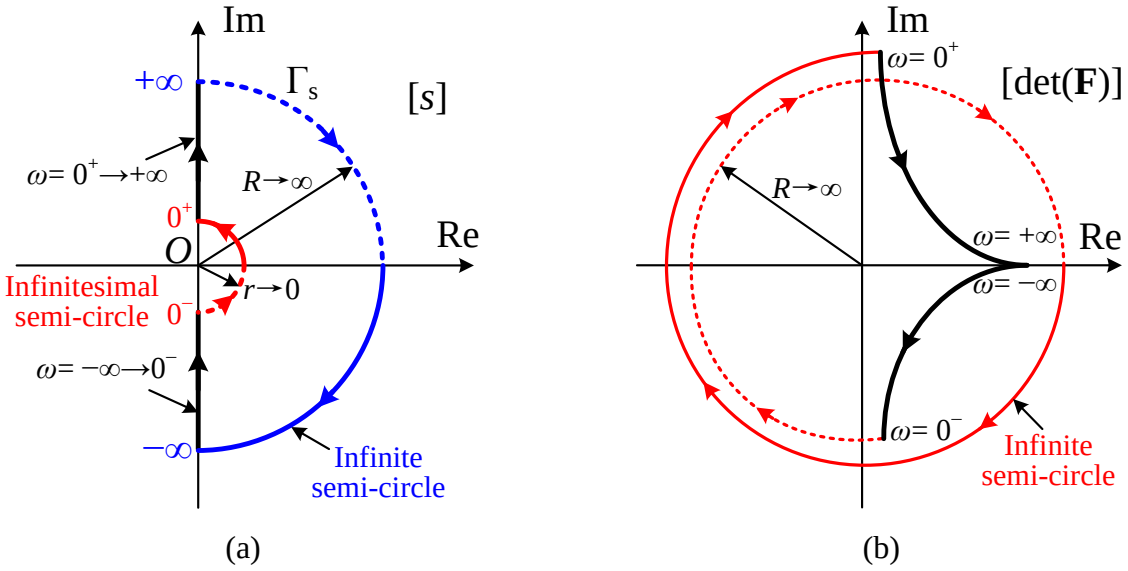

Figure 8-14. (a) Nyquist contour Γ_s in the *s*-plane and (b) Nyquist contour in the plane of det($\mathbf{F_{ex}}$) when there are three integral elements in det($\mathbf{F_{ex}}$).

8.5 Simulation Verification

The simulation model of the islanded microgrid under study has been built in MATLAB/Simulink. Figure 8-15 illustrates the simulation results. Initially, the droop controller parameters are m_P = 0.0025 and n_Q = 0.0067 as in Case 1, and the output power of inverters CI1−CI3 is 0, while only inverters VI1−VI4 share the loads in the microgrid. At t_1=1 s, inverters CI1−CI3 are enabled to track the output power references (P_0 =250 W and Q_0=150 Var), and the output active power of VI1−VI4 drops to equally share the remaining loads, due to the droop control. The dynamic responses of the real power *P*, reactive power *Q*, fundamental frequency *f* and terminal voltage magnitude *V* of each inverter show quickly damped oscillations with a frequency of 3.7 Hz, which matches very well with the analysis result of 3.63 Hz.

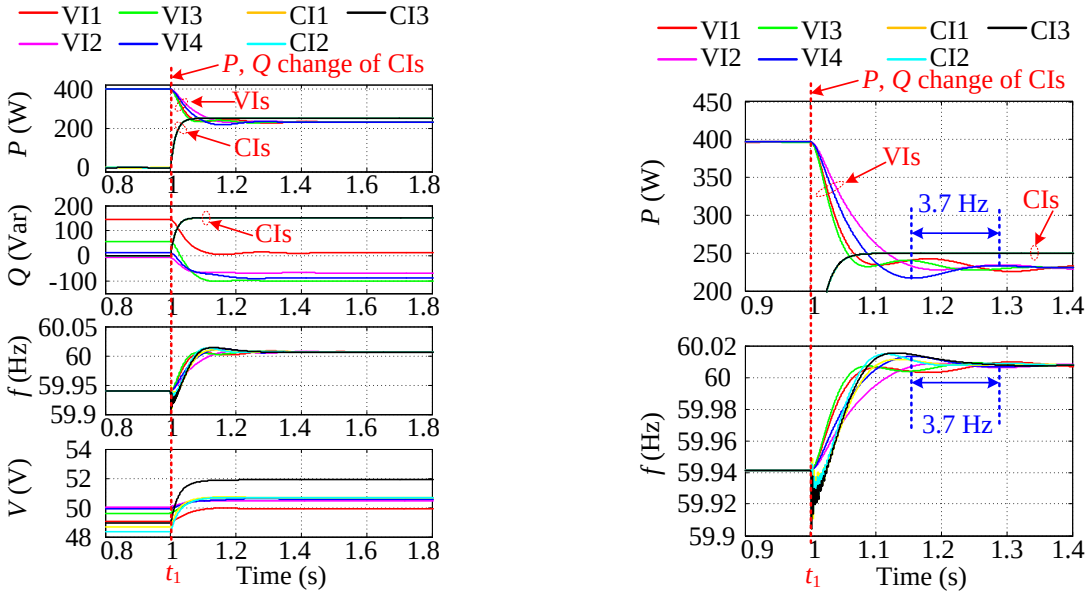

Figure 8-15. Simulation results of the modified IEEE 37-bus system in the islanded mode in Case 1. (a) *P*, *Q*, *f* and *V* of seven inverters during the power change of CIs. (b) Zoomed-in waveforms of *P* and *f* during the power change.

At t_2=2 s, the droop controller parameters became m_P = 0.0050 and n_Q = 0.0133 as in Case 2, and the system becomes unstable. As shown in Figure 8-16, the FFT analysis of *P*, *Q*, *f* and *V* of Inverter VI1 indicates that the major unstable resonance frequencies are 8 Hz and 8.5 Hz in the *d-q* frame. Figure 8-17 further depicts the simulation waveforms of three-phase voltages v_{VI1} and current i_{VI1} of Inverter VI1 (a) in Case 1 and (b) during the change from Case 1 to Case 2. An obvious 8.5 Hz oscillation in the magnitude of phase voltages and currents can be observed in Case 2. This agrees with the analysis results and validates the effectiveness of the proposed low-frequency stability analysis method based on measured terminal characteristics of inverters in the common system *d-q* frame.

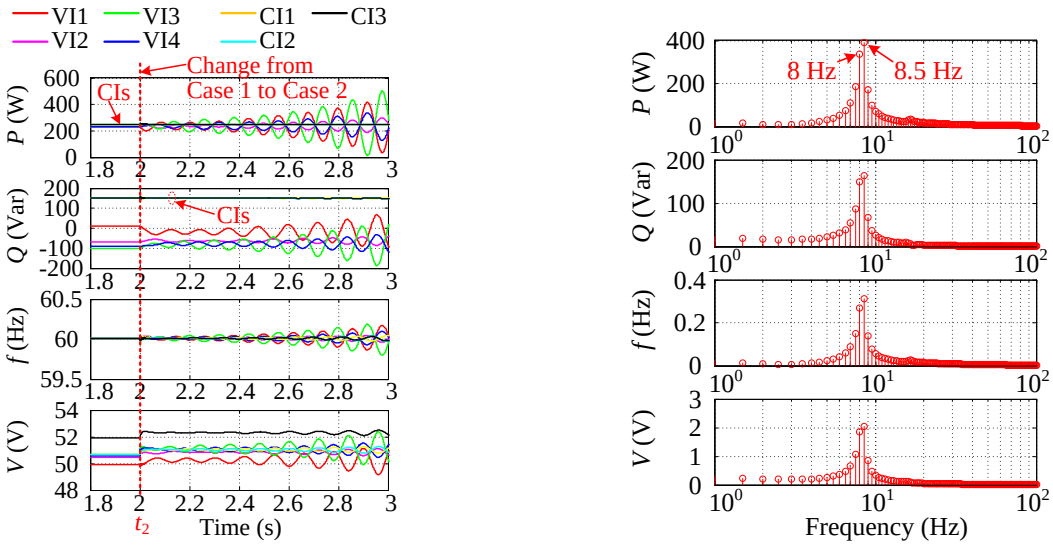

(a) (b)

Figure 8-16. Simulation results during the change from Case 1 to Case 2. (a) *P*, *Q*, *f* and *V* of seven inverters. (b) FFT analysis of *P*, *Q*, *f* and *V* of VI1 in Case 2.

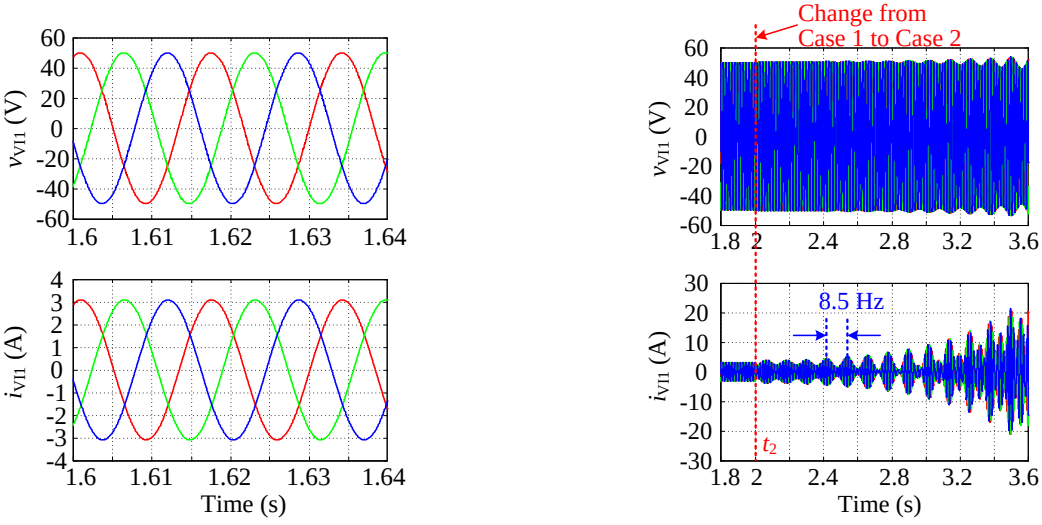

(a) (b)

Figure 8-17. Simulation waveforms of three-phase voltages v_{VI1} and current i_{VI1} of Inverter VI1 (a) in Case 1 and (b) during the change from Case 1 to Case 2.

8.6 Conclusion

This chapter proposed a stability analysis method to analyze the low-frequency oscillation of the fundamental frequency in three-phase inverter-based islanded multi-bus ac microgrids, based on the measured terminal characteristics of system components. The CCM-enabled extended system model is presented by including the fundamental frequency as an additional variable. The derivation of the terminal-characteristics matrix of the connection network is proposed. Simulation results verify that the proposed method can effectively assess the low-frequency stability related with the droop controllers and the system fundamental frequency, by using only the measured terminal characteristics of inverters without the need for their internal information.

9 Impedance-Based Controller Design of Inverters for Stable Integration into an Unknown System

According to the literature review in Section 2.6, it is still a challenge how to design the controller of inverters for stable integration into an unknown system, especially considering the following situations. (1) The voltage feed-forward control is enabled in three-phase current-controlled inverters to improve the voltage disturbance rejection performance. (2) There are existing inverters in operation in the system with unknown information. Due to wideband dynamic interactions among existing inverters, the impedance of the grid or the rest of the system is complicated, and could not be assumed to be simple inductive impedance. So it is not easy to design the inverter controller for stable integration.

This chapter proposes an impedance-based adaptive control strategy of both current-controlled inverters and voltage-controlled inverters for stable integration into an unknown system with the aforementioned two situations. Specifically, two systems are considered: (1) a radial-line renewable energy system with multiple current-controlled interface inverters connected to a weak grid; (2) an islanded inverter-based ac power system.

9.1 Proposed Passivity Compensation of Current-Controlled Inverters

According to the Bode plot of the positive-sequence admittance of a current-controlled inverter with the voltage feed-forward control as shown in Figure 9-1, the voltage feed-forward control could cause the inverter admittance phase to be outside of the passive range [−90°, 90°] within the voltage feed-forward control bandwidth. Therefore, it may trigger low-order harmonic resonances. Note that the PLL is not included in the sequence admittance model in this chapter.

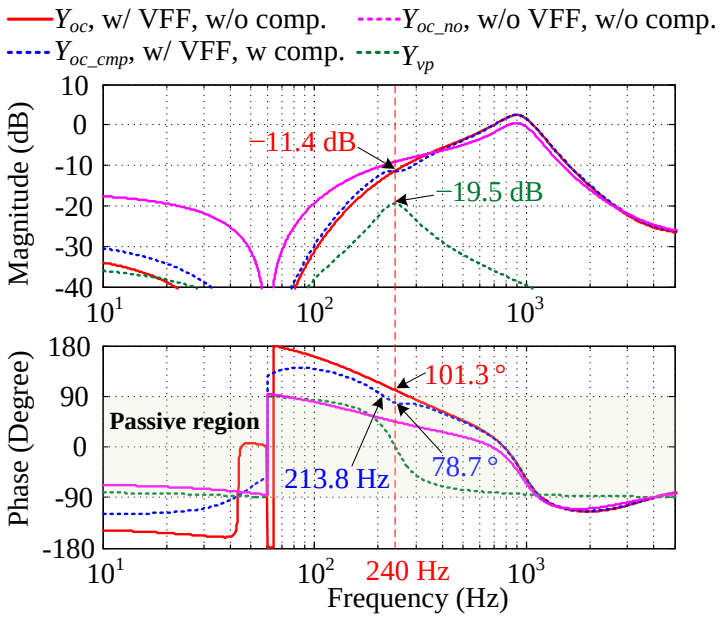

Figure 9-1. Bode plots of the inverter admittance without / with voltage feed-forward (VFF) and compensation.

Due to the adoption of the voltage feed-forward control, it is difficult to design the output admittance of the three-phase current-controlled inverter to be passive within the voltage feed-forward control bandwidth. However, a post remedy measure after the occurrence of instable resonance could be employed to damp the harmonic resonance. A passivity compensation method is proposed here to make the inverter admittance passive at the resonance frequency based on online detection of the resonance frequency. Also, the passivity compensation is achieved by the virtual resistor emulation through an additional band-pass filter (BPF) (G_{cmp}) based voltage feed-forward, as shown in Figure 9-2.

The concept of the passivity compensation for the inverter admittance is illustrated in Figure 9-3, where Y_{oc} is the inverter admittance with the voltage feed-forward (VFF) control but without

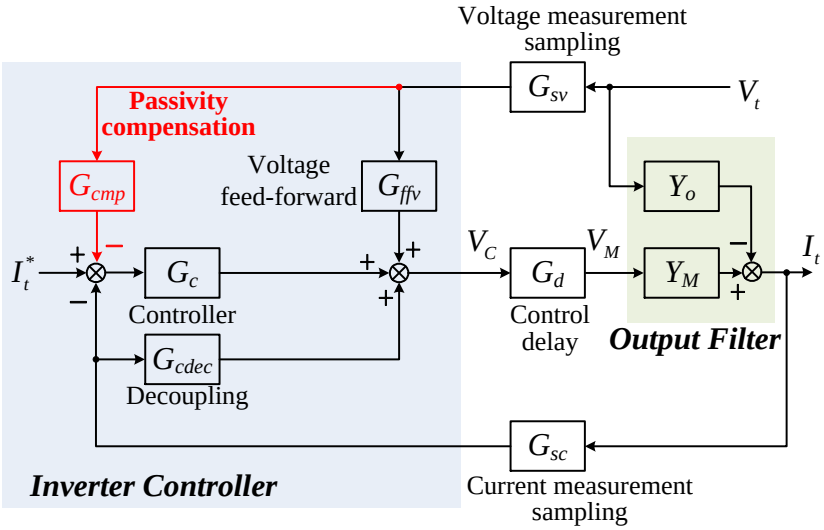

Figure 9-2. Block diagram of the current-control loop with band-pass filter based passivity compensation.

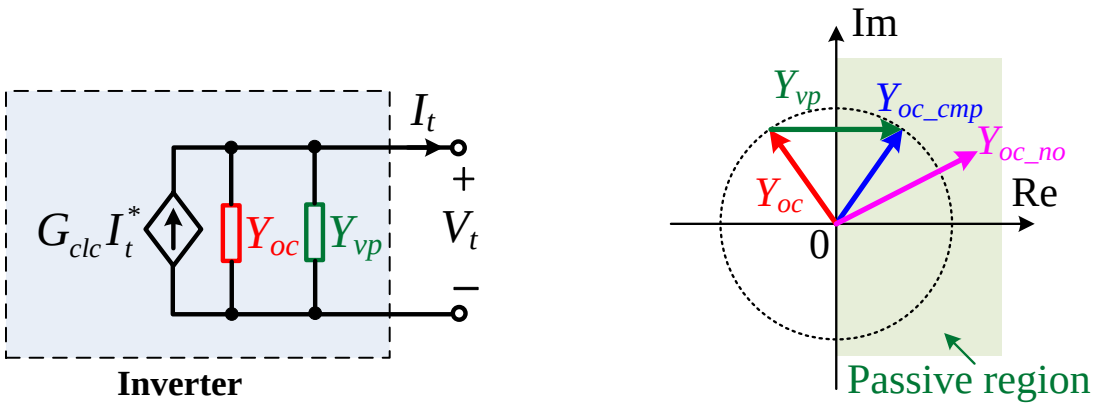

(a) (b)

Figure 9-3. Passivity compensation concept: (a) equivalent impedance-based circuit of the inverter, and (b) the admittances at the resonance frequency in the complex plane.

compensation, Y_{oc_no} is the inverter admittance without the VFF control or compensation, Y_{vp} is the virtual resistance, and Y_{oc_cmp} is the inverter admittance with both the VFF control and the compensation. The magnitude of Y_{vp} is determined by making the magnitudes of Y_{oc_cmp} and Y_{oc} equal to each other at the resonance frequency ω_{res}, while ideally the impedance Y_{oc_cmp} remains the same at other frequencies, as expressed in (9-1), (9-2) and (9-3). Therefore, the phase of the admittance Y_{oc_cmp} can be significantly reduced and shaped into the passive range [−90°, 90°] at the resonance frequency ω_{res}.

$$Y_{oc\_cmp}(j\omega)=\begin{cases}-\mathrm{Re}\left[Y_{oc}(j\omega)\right]+j\,\mathrm{Im}\left[Y_{oc}(j\omega)\right], \omega=\omega_{res}\\ Y_{o}(j\omega), \omega\neq\omega_{res}\end{cases} \tag{9-1}$$

$$\begin{cases}abs\left[Y_{oc\_cmp}(j\omega_{res})\right]=abs\left[Y_{oc}(j\omega_{res})\right]\\ angle\left[Y_{oc\_cmp}(j\omega_{res})\right]=\pi-angle\left[Y_{oc}(j\omega_{res})\right]\end{cases} \tag{9-2}$$

$$Y_{vp}(j\omega)=\begin{cases}-2\,\mathrm{Re}\left[Y_{oc}(j\omega)\right], \omega=\omega_{res}\\ 0, \omega\neq\omega_{res}\end{cases} \tag{9-3}$$

The transfer function of the BPF filter G_{cmp} is expressed in (9-4), where K_{cmp}, ξ_{BPF} and ω_{BPF} are the compensator gain, the damping ratio and the operating frequency of the BPF, respectively. According to the sequence admittance model of a current-controlled inverter presented in Section 3.1, the transfer function of the actual emulated virtual parallel admittance Y_{vp} can be derived as (9-5), where the impact of the current closed-loop gain G_{clc} and the voltage sampling gain G_{sv} is neglected within the current control loop bandwidth. K_{cmp} is set as the absolute value of the virtual resistance and ω_{BPF} is set as the resonance frequency ω_{res}, as expressed in (9-6). Considering that the compensation effect of the BPF would still cause a slight magnitude change

of Y_{oc_cmp} around the resonance frequency ω_{res}, the design rule of ξ_{BPF} is to make the bandwidth of the BPF large enough, so that the phase of the compensated admittance Y_{oc_cmp} is still within the passive range at the frequency of the new intersection point between Y_{oc_cmp} and the admittance of the external system. A conservative design of ξ_{BPF} is to make the phase of Y_{oc_cmp} within the passive range in the frequency range above ω_{res}, as illustrated in Figure 9-1.

$$G_{cmp} = K_{cmp} \frac{2\xi_{BPF}\omega_{BPF}s}{s^2 + 2\xi_{BPF}\omega_{BPF}s + \omega_{BPF}^2} \tag{9-4}$$

$$Y_{vp} = G_{cmp}G_{sv}G_{clc} \approx G_{cmp} \tag{9-5}$$

$$K_{cmp} = -2\,\mathrm{Re}\left[Y_{oc}\left(j\omega_{res}\right)\right], \quad \omega_{BPF} = \omega_{res} \tag{9-6}$$

The corresponding Bode plots of the inverter admittance are shown in Figure 9-1. As observed, the phase of Y_{oc} at the resonance frequency 240 Hz is outside of the passive region ([−90°, 90°]), but the phase of Y_{oc_cmp} at 240 Hz is within the passive range. The magnitude of Y_{oc_cmp} remains the same at 240 Hz while the magnitude change around 240 Hz is small.

9.2 Proposed Phase Compensation of Voltage-Controlled Inverters

Figure 9-4 shows the Bode plot of the positive-sequence impedance of a voltage-controlled inverter with or without the current feed-forward (CFF) control. The phase of the inverter impedance without the CFF control is already outside of the passive range in the majority of the full frequency range. Fortunately, the phase deviation from the passive range is not large. In contrast, with the CFF control, the phase of the inverter impedance is significantly increased and far away from the passive range. It is difficult to compensate the passivity of the inverter impedance at a certain frequency by emulating an additional series resistance based on a BPF.

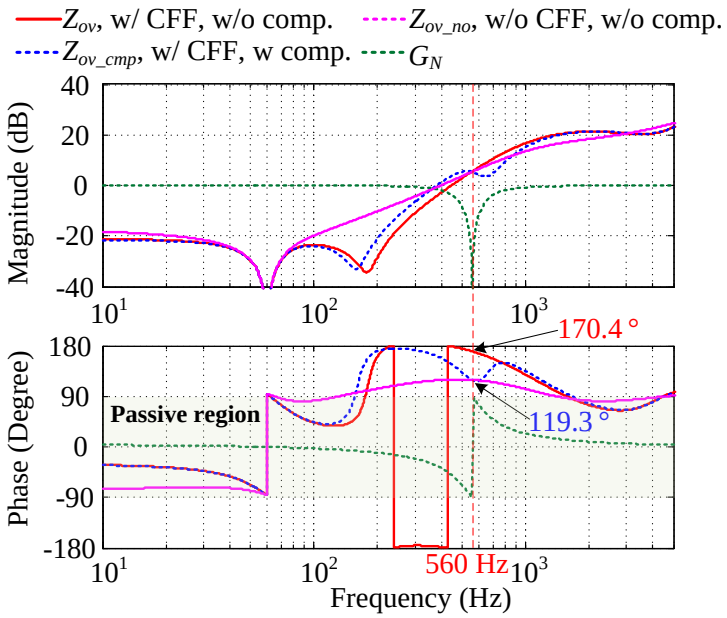

Figure 9-4. Bode plots of the inverter impedance without / with current feed-forward (CFF) and compensation.

Considering that the phase of the inverter impedance without the CFF control has a much smaller deviation from the passive range, as compared with that with the CFF control, it is feasible to disable the effect of the CFF at the resonance frequency, so that the phase of the inverter impedance at the resonance frequency can be moved closer to the passive range and the phase margin of the system can be increased. A phase compensation method is proposed here to make the inverter impedance phase closer to the passive range at the resonance frequency based on online detection of the resonance frequency. Also, the phase compensation is achieved by inserting a notch filter G_N into the current feed-forward path to block the effect of the CFF on the phase of the inverter impedance, as depicted in Figure 9-5. The concept of the proposed strategy for the phase compensation of the inverter impedance is illustrated in Figure 9-6.

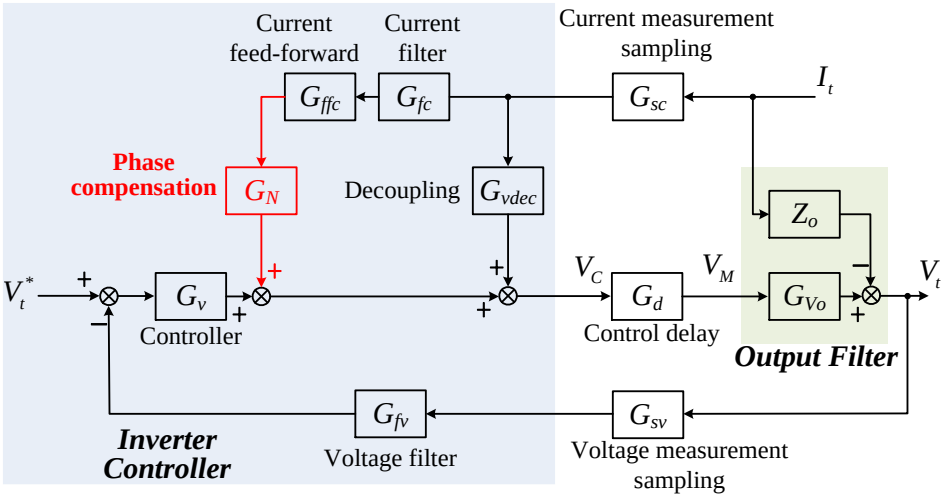

Figure 9-5. Block diagram of the voltage-control loop with notch filter based phase compensation.

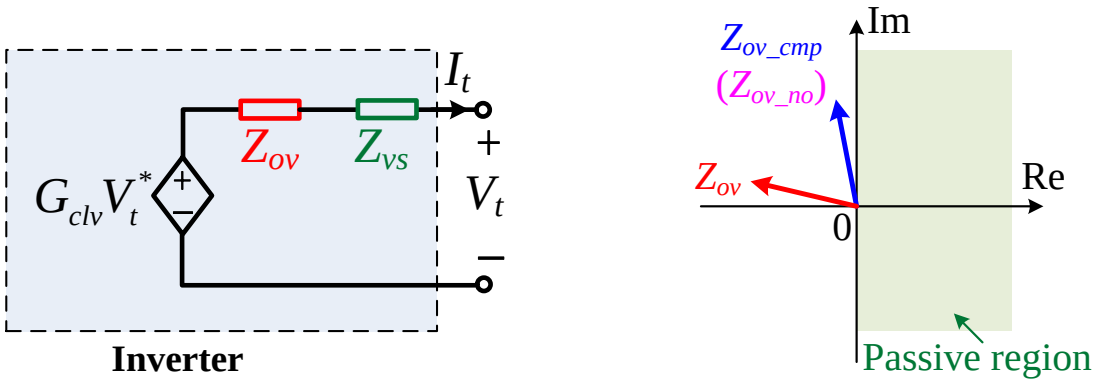

(a) (b)

Figure 9-6. Phase compensation concept: (a) equivalent impedance-based circuit of the inverter, and (b) the impedances at the resonance frequency in the complex plane.

Z_{ov} is the inverter impedance with the CFF control but without compensation, Z_{ov_no} is the inverter impedance without the CFF control or compensation, Z_{ov_cmp} is the inverter impedance with both the CFF control and the compensation, and Z_{vs} is equivalent virtual series impedance introduced by the phase compensation. Both the magnitudes and phases of Z_{ov_cmp} and Z_{ov_no} are identical at the resonance frequency, which means that, equivalently, there is no CFF control at the resonance frequency.

The transfer function of the notch filter G_N is expressed in (9-7), where ξ_N and ω_N are the damping ratio and the operating frequency of the notch filter, respectively. According to the sequence impedance model of a voltage-controlled inverter presented in Section 3.2, the transfer function of Z_{ov_cmp} can be derived as (9-8). The value of ω_N is set as the resonance frequency ω_{res}, as expressed in (9-9). The design of ξ_N is to make the effective frequency range of the compensation large enough to cover the variation in the magnitude of Z_{ov_cmp} around the resonance frequency ω_{res} and the variation of the intersection frequency between Z_{ov_cmp} and the impedance of the external system.

$$G_N = \frac{s^2 + \omega_N^2}{s^2 + 2\xi_N \omega_N s + \omega_N^2} \tag{9-7}$$

$$Z_{ov\_cmp} = \frac{Z_o - G_{sc} G_d G_{Vo} \left(G_{vdec} + G_{fc} G_{ffc} G_N \right)}{1 + T_v} \tag{9-8}$$

$$\omega_N = \omega_{res} \tag{9-9}$$

The corresponding Bode plots of the inverter impedance with the proposed phase compensation are drawn in Figure 9-4. As shown, the phase of Z_{ov} at the resonance frequency 560 Hz is 170.4 °, but the phases of Z_{ov_cmp} and Z_{ov_no} are both 119.3 °at 560 Hz, which is much

closer to the passive range. Aside from the phase compensation, the proposed strategy only brings a slight change in the magnitude of the inverter impedance, so the drift of the magnitude intersection point between the inverter impedance and the external system impedance is small and still within the compensated range.

9.3 Adaptive Compensation Based on Online Resonance Detection

The process of the online resonance detection is depicted in Figure 9-7. The measured inverter *d*-axis currents (i_d) in the *d-q* frame are analyzed by FFT online at a certain execution rate in the DSP controllers of the inverters to detect the magnitude i_{res} and frequency f_{res} of the resonant current component in the *d-q* frame. The resonance frequency f_{res} is set as the operating frequency of the BPF G_{cmp} for passivity compensation and resonance damping of current-controlled inverters, or set as the operating frequency of the notch filter G_N for phase compensation and resonance damping of voltage-controlled inverters.

The effectiveness of the online detection and compensation is illustrated by an example radial-line system with 2 PV inverters as depicted in Figure 9-8. The parameters of both inverters are the same as those listed in Table 3-1 and Table 3-2, except that the cut-off frequency ω_{ffv} of the voltage feedforward control is $300\times2\pi$ rad/s. Inverter 1 is originally connected, while Inverter 2 is connected at time t_1 . The simulation results of inverter currents and resonance detection are shown in Figure 9-9. The FFT executes every 0.25 s. The connection of Inverter 2 at time t_1 results in unstable resonance. 0.25 s later, at time t_2, the resonance frequency is detected as 170 Hz in the *d-q* frame and the BPF-based compensation is enabled in both inverters. Then, the resonance is quickly damped. Another 0.25 s later, at time t_3, the detected resonance magnitude is nearly zero, indicating that the resonance has been completely damped.

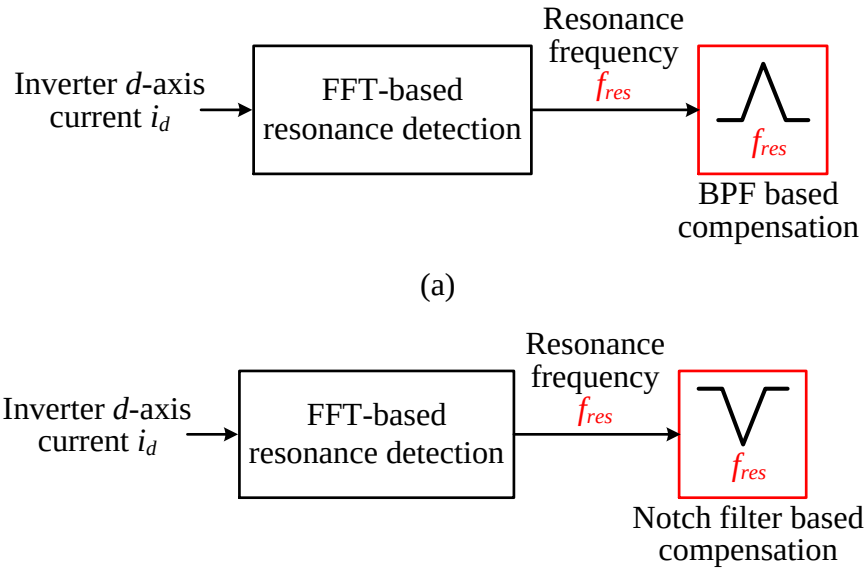

Figure 9-7. Diagrams of online resonance detection for (a) BPF-based passivity compensation, and (b) notch filter based phase compensation.

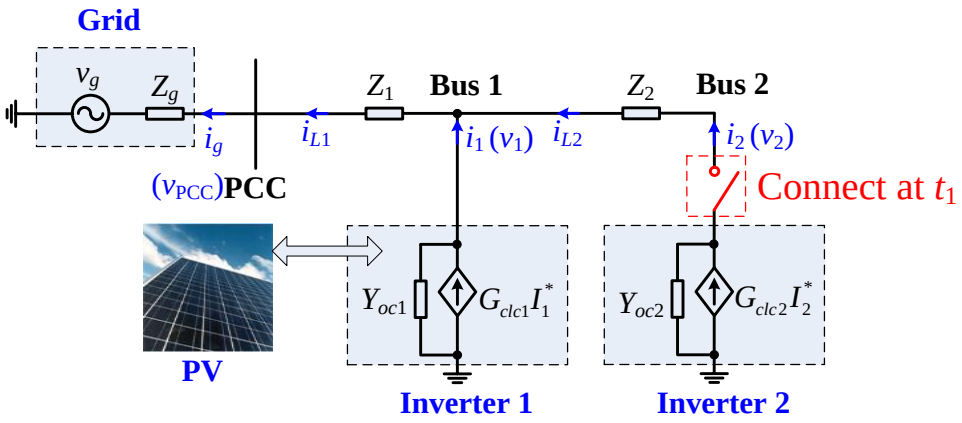

Figure 9-8. Single-line diagram of a radial-line system with 2 PV inverters.

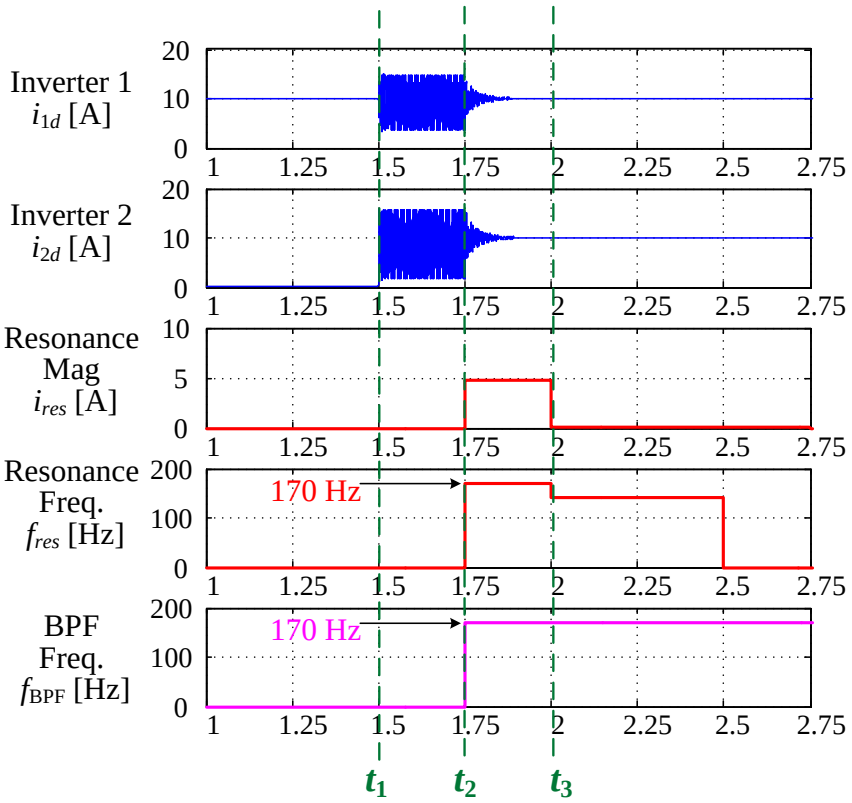

Figure 9-9. Simulation results of inverter currents and resonance detection.

9.4 Experimental Verification

An experimental setup consisting of three three-phase inverters and multiple inductors is established, as shown in Figure 9-10. The experimental setup is configured as two systems: (1) a radial-line renewable energy system with two current-controlled interface inverters (Inverter 1 and Inverter 2) connected to a weak grid; (2) an islanded inverter-based ac power system composed of two voltage-controlled inverter sources (Inverter VI1 and Inverter VI2) and one current-controlled inverter load (Inverter CI1).

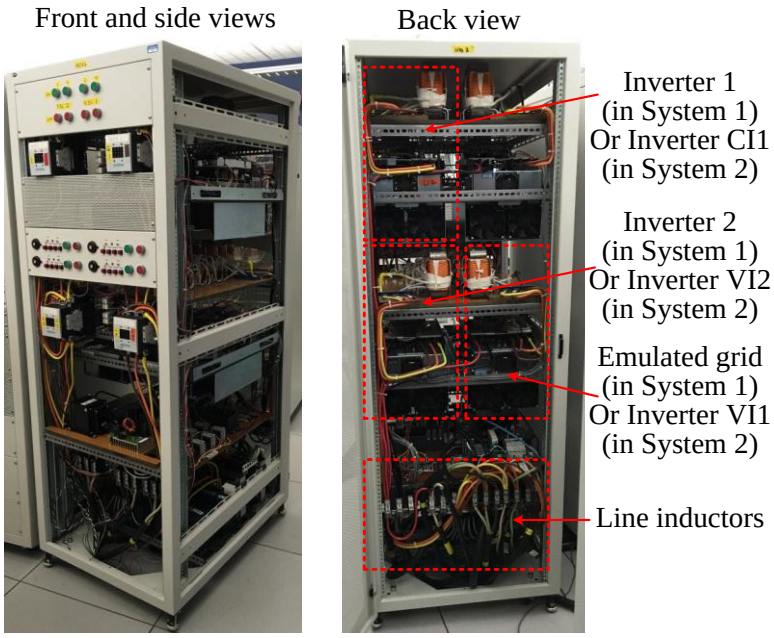

Figure 9-10. Experimental setup.

9.4.1 A Radial-Line Renewable Energy System

The diagram of the system is the same as that in the simulation as shown in Figure 9-8. The parameters of both inverters are the same as those listed in Table 3-1 and Table 3-2, except that ω_{ffv} is 300×2π rad/s. Initially, only the Inverter 1 is connected to the radial line system and in operation. Then, the Inverter 2 is connected to the system at time t_1 and starts increasing the current injection at a ramp rate of 10 A/s. Figure 9-11 shows the experimental waveforms of the phase-A currents of the grid (i_{ga}) and two inverters (i_{1a} and i_{2a}) during the connection of Inverter 2 while the compensation is not enabled. It can be seen that the system is stable without Inverter 2, but the integration of Inverter 2 makes the system unstable with a resonance frequency of 202.5 Hz in the phase domain or equivalently 142.5 Hz in the *d*-*q* frame, as shown in Figure 9-12.

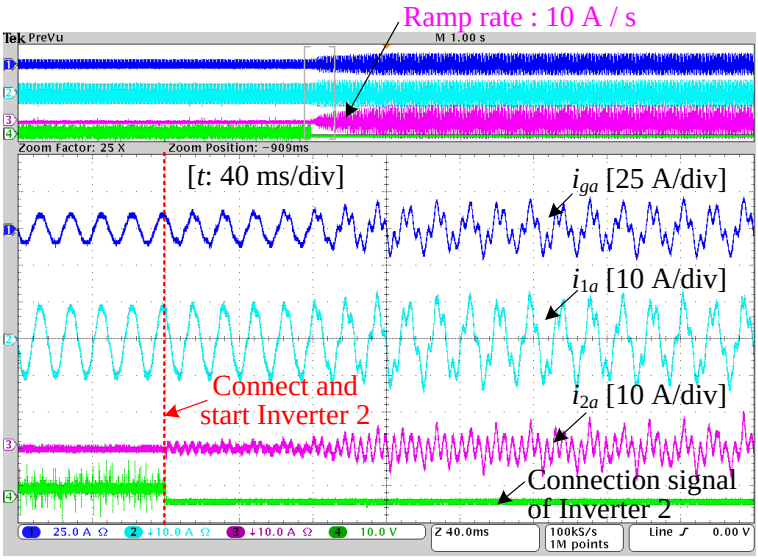

Figure 9-11. Experimental waveforms of the phase-A current of the grid and two inverters during the connection of Inverter 2 while the compensation is not enabled.

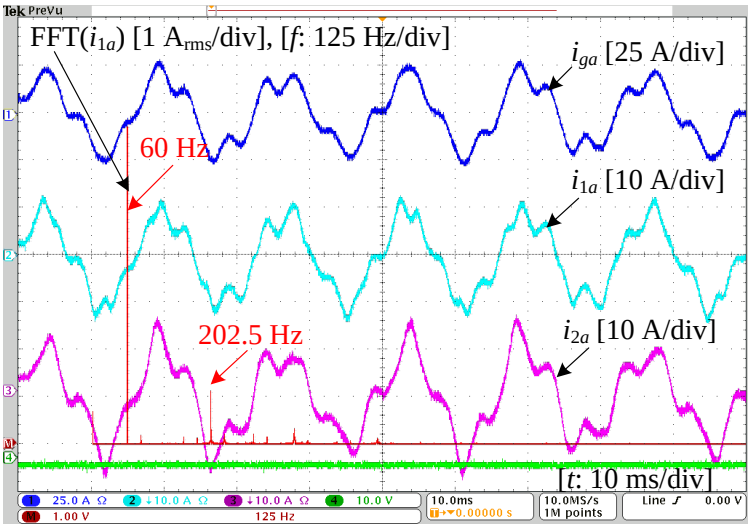

Figure 9-12. Experimental waveforms of the phase-A current of the grid and two inverters in the unstable state.

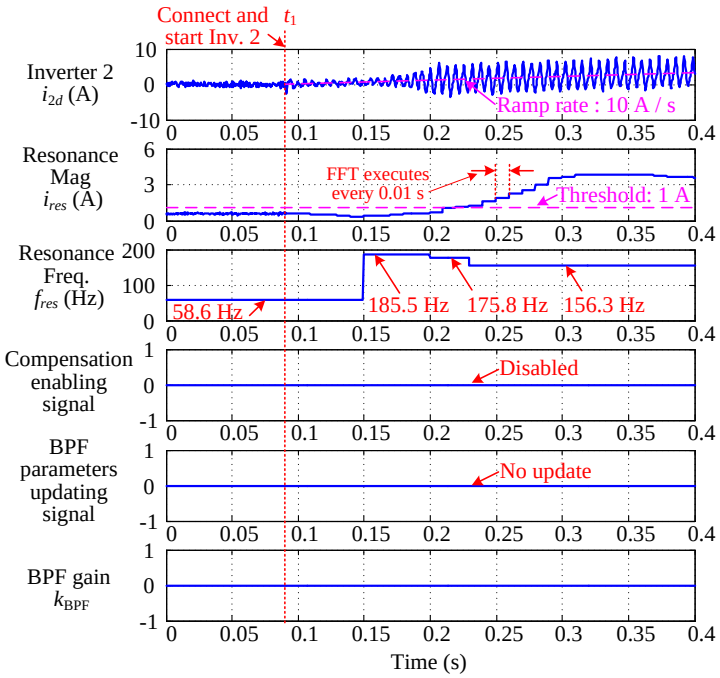

Figure 9-13. Recorded data in the DSP of Inverter 2 during the connection of Inverter 2.

Figure 9-13 illustrates the recorded data in the DSP controller of Inverter 2 during the connection of Inverter 2. By adopting the online FFT executing every 0.01 s in the DSP controller of Inverter 2, it can be seen that the initial resonance frequency f_{res} right after the connection of Inverter 2 is 185.5 Hz, and the resonance frequency gradually becomes 156.3 Hz as the increasing resonance current makes the system reach a saturated state. In addition, without the compensation in Inverter 1 and Inverter 2, the current resonance is much larger than the threshold value (1 A).

For comparison, by enabling the proposed passivity compensation strategy based on online resonance detection in both Inverter 1 and Inverter 2, Inverter 2 can be stably integrated in the existing system, without the need to know the detailed information of the existing system, as

shown in Figure 9-14, Figure 9-15 and Figure 9-16. After connecting the Inverter 2, the system becomes unstable and the resonance current starts increasing. With the online FFT executing every 0.01 s in the DSP controller of Inverter 2, when the detected resonance magnitude i_{res} in the d-axis current i_{2d} reaches the threshold value (1 A), the resonance frequency f_{res} is detected as 175.8 Hz, the parameter of the BPF G_{cmp} are updated as K_{cmp} =0.1145, ξ_{BPF} =0.25, and ω_{BPF} = $2\pi f_{res}$, and the passivity compensation is enabled. Then, the resonance is quickly damped. The whole integration process is only about 0.13 s, and the resonance current magnitude can be restricted below a safe value during the integration process.

Therefore, the effectiveness of the proposed adaptive passivity compensation strategy of current-controlled inverter for stable integration into an unknown system is verified.

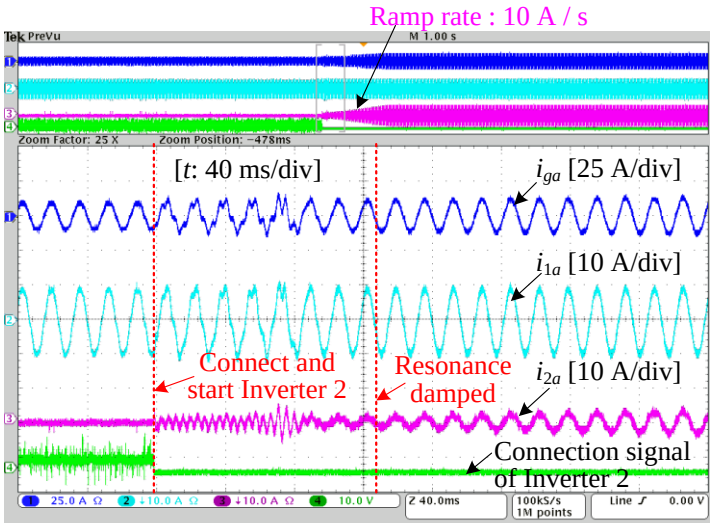

Figure 9-14. Experimental waveforms of the phase-A current of the grid and two inverters during the connection of Inverter 2 while the compensation is enabled.

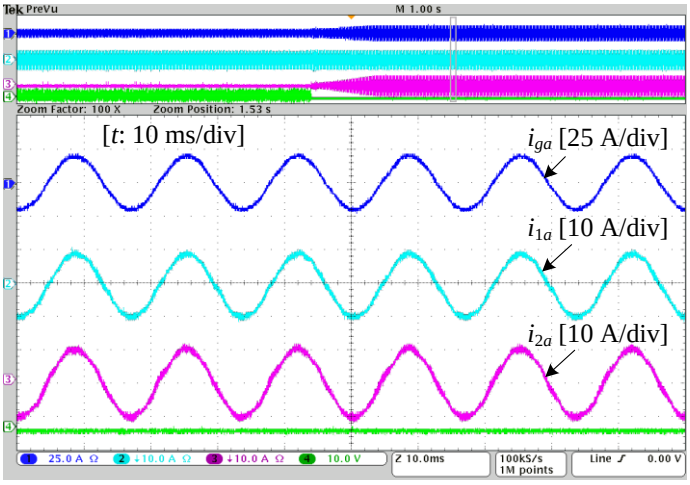

Figure 9-15. Experimental waveforms of the phase-A current of the grid and two inverters in the stable state with the compensation.

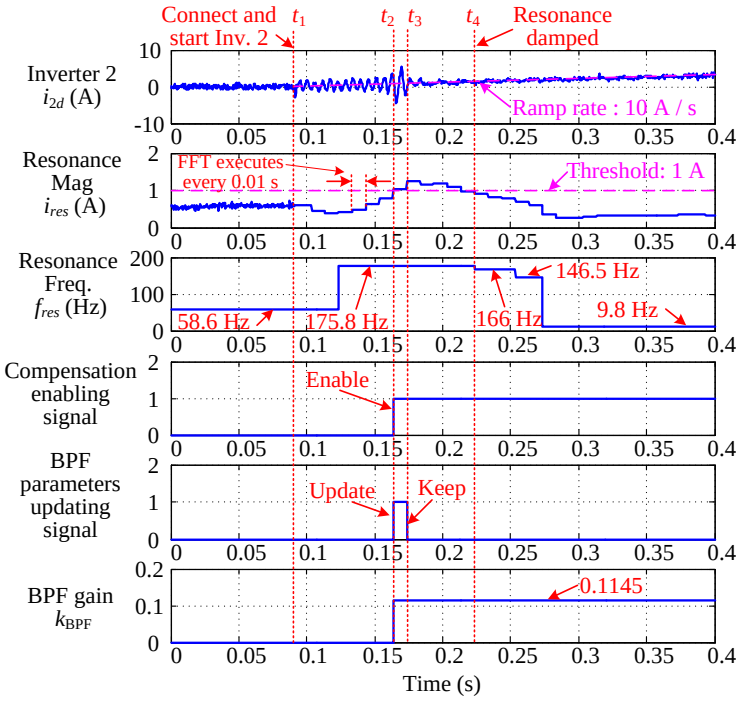

Figure 9-16. Recorded data in the DSP of Inverter 2 with compensation during the connection.

9.4.2 An Islanded Inverter-Based Ac Power System

The diagram of the islanded inverter-based ac power system is shown in Figure 9-17. Initially, the system only consists of the voltage-controlled inverter VI1 as the source and the current-controlled inverter CI1 as the load. Then, at time t_1, another voltage-controlled inverter VI2 connects to the system to share the load with VI1 under the help of droop controllers.

The parameters of these three inverters are the same as the values listed in Table 3-1, Table 3-2 and Table 3-3, except that ω_{ffv} is 25×2π rad/s in Inverter CI1. The *d*-*q* currents of CI1 are i_d= −20 A and i_q=0A. The parameters of the notch filter G_N are set as ξ_N =0.3 and $\omega_N = 2\pi f_{res}$, where f_{res} is the detected resonance frequency by the online FFT executing every 0.01 s in the DSP controllers of Inverter VI1 and VI2.

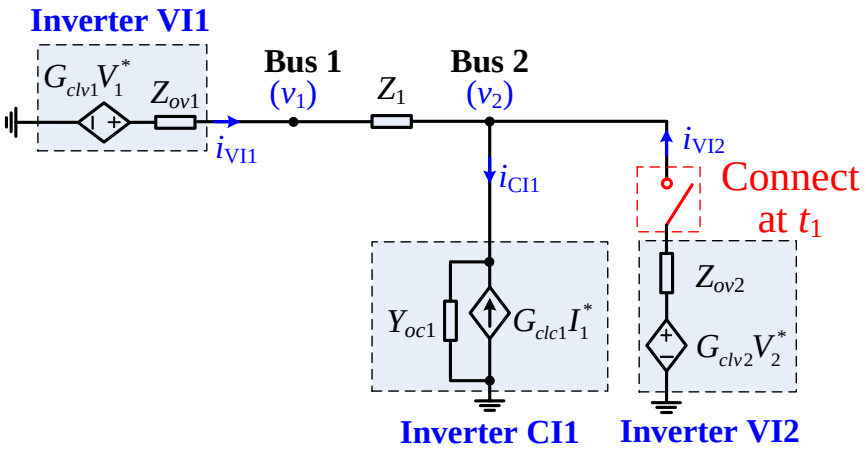

Figure 9-17. Single-line diagram of the islanded inverter-based ac power system, in which Inverter VI2 is connected at time t_1 .

Figure 9-18 shows the experimental waveforms of the phase-A currents of Inverter VI1 (i_{VI1a}), Inverter CI1 (i_{CI1a}) and Inverter VI2 (i_{VI2a}) during the connection of Inverter 2 while the compensation is not enabled. It can be seen that the system is stable without Inverter VI2, but the integration of Inverter VI2 makes the system unstable with a resonance frequency of 560 Hz in the phase domain or equivalently 500 Hz in the *d*-*q* frame, as shown in Figure 9-19. When the proposed adaptive phase compensation is enabled in both Inverter VI1 and Inverter VI2, the oscillation is quickly damped and the system is restored to stability, as shown in Figure 9-20. Therefore, the effectiveness of the proposed adaptive phase compensation strategy of voltage-controlled inverter for stable integration into an unknown system is verified.

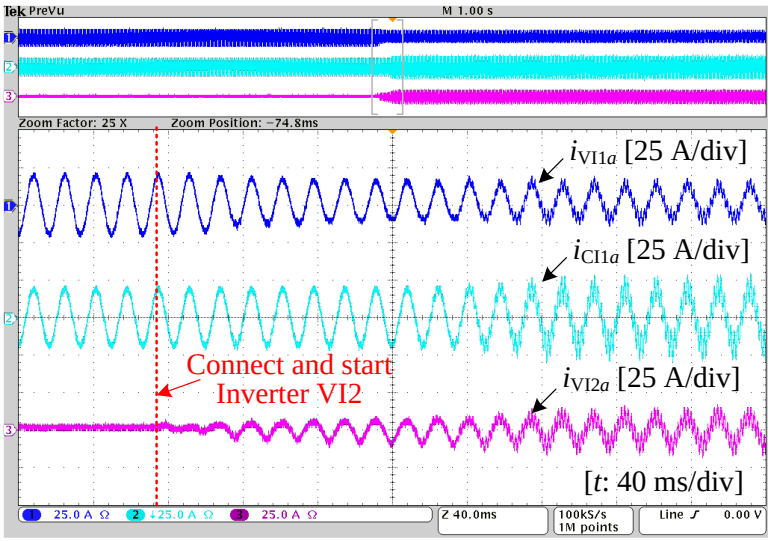

Figure 9-18. Experimental waveforms of the phase-A current of three inverters during the connection of Inverter VI2 while the compensation is not enabled.

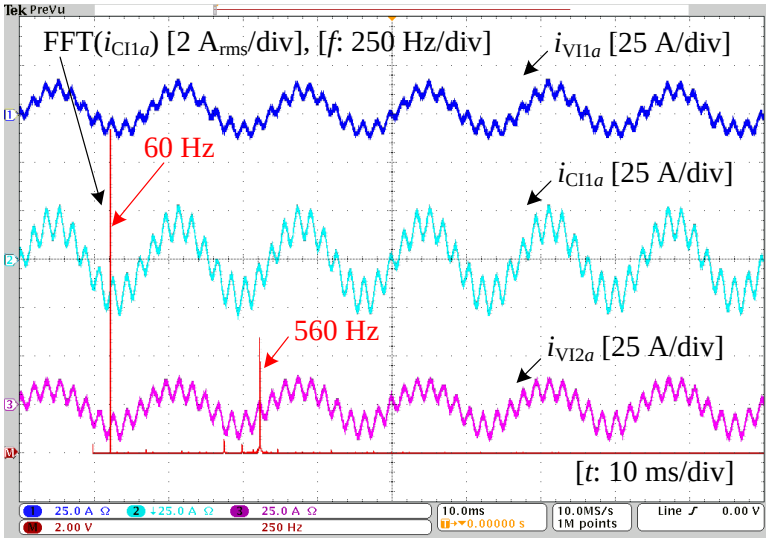

Figure 9-19. Experimental waveforms of the phase-A current of three inverters in the unstable state.

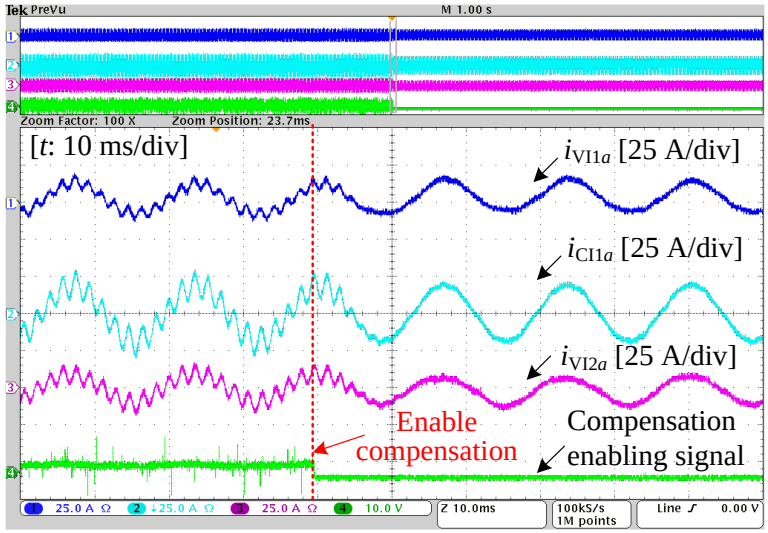

Figure 9-20. Experimental waveforms of the phase-A current of three inverters when the compensation is enabled.

9.5 Conclusion

This chapter proposed an impedance-based adaptive control strategy of both current-controlled inverters and voltage-controlled inverters for stable integration into unknown systems including: (1) a radial-line renewable energy system with multiple current-controlled interface inverters connected to a weak grid; (2) an islanded inverter-based ac power system. The passivity compensation of current-controlled inverters is achieved by the virtual resistor emulation through additional band-pass filter based voltage feed-forward. The phase compensation of voltage-controlled inverters is achieved by inserting a notch filter into the current feed-forward path. Experimental results verify the effectiveness of the proposed adaptive compensation methods based on online resonance detection.

10 Conclusion and Future Work

This chapter summarizes the work in this dissertation and recommends some future work.

10.1 Conclusion

The impedance-based stability analysis and inverter controller design of three-phase inverter-based ac systems have been investigated in this dissertation. The conclusions can be drawn as follows.

- The sequence-admittance model of current-controlled three-phase inverters is improved, considering the voltage feed-forward control in the *d-q* domain and the dead time effect. The sequence-impedance model of voltage-controlled three-phase inverters is developed. The *d-q* admittance model of current-controlled inverters in an arbitrary *d-q* frame is developed with the consideration for static load emulation.
- A method for sequence impedance measurement of three-phase inverters by using another inverter connected in parallel with common-dc and common-ac sides is proposed. The measurement setup is simple, because the inverter as the measurement unit not only injects perturbations but also serves as the voltage source or the current load at the fundamental frequency to create the desired operating conditions for the inverter under test. Zero-sequence circulating current reduction and open-loop voltage compensation improve the measurement accuracy.
- An impedance-based sufficient stability criterion is proposed to analyze the small-signal stability of radial-line systems with multiple current-controlled inverters in the *d-q* domain. The system stability can be examined by checking the encirclements of the

point (−1, *j*0) by the characteristic loci of the return-ratio matrix at each bus successively from the farthest bus to the PCC. The pole calculation of return-ratio matrices is avoided, compared to the generalized Nyquist stability criterion (GNC), while the phase margin of the system can still be obtained for inverter controller parameter design.

- Two methods for harmonic stability analysis of three-phase inverter-based ac power systems are proposed to avoid the examination of RHP poles of impedance ratios and reduce the computation effort, as compared with the existing impedance-based stability analysis method using Nyquist stability criterion once. The proposed stability analysis methods also enable the system stability assessment using only measured component impedance characteristics, without the need for detailed internal control information of the components. The inverter controller parameters of multi-bus ac systems can be designed by repetitively applying the proposed stability methods, and presented as stability regions in the parameter space.
- A stability analysis method, based on the *d-q* impedances, the Component Connection Method (CCM) and the determinant-based GNC, is proposed for assessing both the harmonic stability and low-frequency stability of three-phase inverter-based multi-bus ac systems. The proposed method does not need to check the RHP poles of the return-ratio matrix. It only requires one Nyquist plot examination of the determinant of the return-difference matrix, and thus the stability judging process is simpler than the existing method based on the CCM and the eigenvalue-based GNC. Controller parameters of both voltage-controlled and current-controlled inverters can be designed by repetitively applying the proposed stability methods, and presented as stability regions in the parameter space.

- A low-frequency stability analysis method of three-phase inverter-based islanded multi-bus ac microgrids based on the measured terminal characteristics of system components is proposed. The CCM-enabled extended system model including the terminal-characteristics matrix of the connection network is proposed. The proposed method can effectively assess the low-frequency stability related with the droop controllers and the system fundamental frequency, by using only the measured terminal characteristics of inverters without the need for their internal information.
- An impedance-based adaptive control strategy of both current-controlled inverters and voltage-controlled inverters for stable integration into unknown systems is proposed. The proposed strategy is based on online resonance detection by using online FFT and passivity or phase compensation by integrating a BPF or a notch filter into the control loops of inverters.

10.2 Recommended Future Work

Some recommended future work is listed as follows.

(1) Design of power-electronics-based hardware for resonance mitigation in renewable energy systems

The stability research work in this dissertation focuses on the controller design of the renewable interface inverters to guarantee the stability of renewable energy systems. However, there are still limitations in stability improvement by only changing the inverter controller design, due to some inherent issues of the inverter control, such as the limited control bandwidth and the control time delay. In addition to the control of inverters themselves, it is also possible to use external power-electronics-based hardware to help resonance mitigation and stability

improvement in renewable energy systems. This additional measure creates another degree of freedom, which could overcome the limitation of the inverter control.

(2) Stability analysis and controller design of renewable interface inverters for stable operation under unbalanced conditions

The stability research work in this dissertation only considers the balanced three-phase systems. But it is very common that renewable energy systems sometimes operate under unbalanced conditions, such as unbalanced faults. Therefore, it is important to ensure the stable operation under unbalanced conditions. There are not enough studies on stability under unbalanced conditions in the existing literature. It is challenging to analyze the system stability and design inverter controller for stability under unbalanced conditions.

(3) Design of inverter passive filters and power-electronics-based hardware for power quality improvement in renewable energy systems

Power quality is another major concern in renewable energy systems. There are some existing approaches to improve the power quality in normal power systems, such as passive filters and active power filters. The adoption of high frequency power electronics converters also generates harmonics. These harmonics can be reduced to some extent by introducing harmonic control in renewable interface inverters. For systems with high penetration of renewable energy sources, the harmonic mitigation is more difficult than systems with only a few converters. It is crucial to build design methodology of inverter passive filters and additional power-electronics-based hardware in a coordinated way to improve and optimize the power quality of high-penetration renewable energy systems.

Reference

[1] U.S. number one in the world in wind energy production, AWEA, [Online]. Available: http://www.awea.org/

[2] Wind Vision: A new era for wind power in the United States, US DOE, [Online]. Available: http://www.energy.gov/windvision

[3] US solar market sets new record, installing 7.3GW of solar PV in 2015, Green Tech Media, [Online]. Available: https://www.greentechmedia.com/

[4] R. Lasseter, A. Akhil, C. Marnay, J. Stevens, J. Dagle, R. Guttromson, A. S. Meliopoulous, R. Yinger and Joe Eto "White paper on integration of distributed energy resources: the microgrid concept," CERTS, Apr. 2002.

[5] P. Asmus, D. Liu and A. Dehamna, "Executive summary: microgrid deployment tracker 4Q15," Navigant Research, 2015.

[6] J. Wang, L. Yang, Y. Ma, J. Wang, L. M. Tolbert, F. Wang, and K. Tomsovic, "Static and dynamic power system load emulation in a converter-based reconfigurable power grid emulator," *IEEE Trans. Power Electron.*, vol. 31, no. 4, pp. 3239–3251, Apr. 2016.

[7] J. Wang, "Versatile three-phase power electronics converter based real-time load emulators," Ph.D. dissertation, Dept. Elect. Comput. Eng., The University of Tennessee, Knoxville, TN, USA, 2015.

[8] L. Yang, X. Zhang, Y. Ma, J. Wang, L. Hang, K. Lin, L. M. Tolbert, F. Wang, and K. Tomsovic, "Hardware implementation and control design of generator emulator in multi-converter system," in *Proc. Annu. IEEE Appl. Power Electron. Conf. and Expo.*, 2013, pp. 2316–2323.

[9] L. Yang, "Three-phase power converter based real-time synchronous generator emulation," Ph.D. dissertation, Dept. Elect. Comput. Eng., The University of Tennessee,

Knoxville, TN, USA, 2015.

[10] L. Yang, J. Wang, Y. Ma, J. Wang, X. Zhang, L. M. Tolbert, F. Wang, and K. Tomsovic, "Three-phase power converter based real-time synchronous generator emulation," *IEEE Trans. Power Electron.*, vol. 32, no. 2, pp. 1651–1665, Feb. 2017.

[11] H. Wang, M. Wu, and J. Sun, "Analysis of low-frequency oscillation in electric railways based on small-signal modeling of vehicle-grid system in *dq* frame," *IEEE Trans. Power Electron.*, vol. 30, no. 9, pp. 5318–5330, Sep. 2015.

[12] Z. Chen, Y. Luo, and M. Chen, "Control and performance of a cascaded shunt active power filter for aircraft electric power system," *IEEE Trans. Ind. Electron.*, vol. 59, no. 9, pp. 3614–3623, Sep. 2012.

[13] J. A. Rosero, J. A. Ortega, E. Aldabas, and L. Romeral, "Moving towards a more electric aircraft," *IEEE Aerosp. Electron. Syst. Mag.*, vol. 22, no. 3, pp. 3–9, Mar. 2007.

[14] F. Wang, Z. Zhang, T. Ericsen, R. Raju, R. Burgos, and D. Boroyevich, "Advances in power conversion and drives for shipboard systems," in *Proc. IEEE*, vol. 103, no. 12, pp. 2285–2311, Dec. 2015.

[15] X. Feng, K. L. Butler-Purry, and T. Zourntos, "A multi-agent system framework for real-time electric load management in MVAC all-electric ship power systems," *IEEE Trans. Power Syst.*, vol. 30, no. 3, pp. 1327-1336, May 2015.

[16] E. Muljadi, C. P. Butterfield, A. Ellis, J. Mechenbier, J. Hochheimer, R. Young, N. Miller, R. Delmerico, R. Zavadil, and J. C. Smith, "Equivalencing the collector system of a large wind power plant," in *Proc. IEEE Power Engineering Society General Meeting*, 2006, pp. 1–9.

[17] Y. Zhou, H. Li, and L. Liu, "Integrated autonomous voltage regulation and islanding

detection for high penetration PV applications," *IEEE Trans. Power Electron.*, vol. 28, no. 6, pp. 2826–2841, Jun. 2013.

[18] J. M. Guerrero, M. Chandorkar, T. Lee, and P. C. Loh, "Advanced control architectures for intelligent microgrids—Part I: decentralized and hierarchical control," *IEEE Trans. Ind. Electron.*, vol. 60, no. 4, pp. 1254–1262, Apr. 2013.

[19] F. Blaabjerg and X. Wang, "Stability and damping of grid-connected voltage-source converters," Professional education seminar, in *Proc. Annu. IEEE Appl. Power Electron. Conf. and Expo.*, 2016.

[20] J. H. R. Enslin and P. J. M. Heskes, "Harmonic interaction between a large number of distributed power inverters and the distribution network," *IEEE Trans. Power Electron.*, vol. 19, no. 6, pp. 1586–1593, Nov. 2004.

[21] P. Brogan, "The stability of multiple, high power, active front end voltage sourced converters when connected to wind farm collector system," in *Proc. EPE Wind Energy Chapter Seminar*, 2010, pp. 1–6.

[22] C. F. Jensen, Energinet.dk, "Harmonic assessment in modern transmission network," Harmony Symposium, Aalborg, Aug. 2015.

[23] X. Wang, F. Blaabjerg, and W. Wu, "Modeling and analysis of harmonic stability in an ac power-electronics-based power system," *IEEE Trans. Power Electron.*, vol. 29, no. 12, pp. 6421–6432, Dec. 2014.

[24] A. A. A. Radwan and Y. A.-R. I. Mohamed, "Modeling, analysis, and stabilization of converter-fed ac microgrids with high penetration of converter-interfaced loads," *IEEE Trans. Smart Grid*, vol. 3, no. 3, pp. 1213–1225, Sep. 2012.

[25] X. Wang, F. Blaabjerg, M. Liserre, Z. Chen, J. He, and Y. Li, "An active damper for

stabilizing power-electronics-based ac systems," *IEEE Trans. Power Electron.*, vol. 29, no. 7, pp. 3318–3329, Jul. 2014.

[26] F. Wang, J. L. Duarte, M. A. M. Hendrix, and P. F. Ribeiro, "Modeling and analysis of grid harmonic distortion impact of aggregated DG inverters," *IEEE Trans. Power Electron.*, vol. 26, no. 3, pp. 786–797, Mar. 2011.

[27] N. Bottrell, M. Prodanovic, and T. C. Green, "Dynamic stability of a microgrid with an active load," *IEEE Trans. Power Electron.*, vol. 28, no. 11, pp. 5107–5119, Nov. 2013.

[28] C. Wan, M. Huang, C. K. Tse, and X. Ruan, "Effects of interaction of power converters coupled via power grid: a design-oriented study," *IEEE Trans. Power Electron.*, vol. 30, no. 7, pp. 3589–3600, Jul. 2015.

[29] B. Wen, D. Dong, D. Boroyevich, R. Burgos, P. Mattavelli, and Z. Shen, "Impedance-based analysis of grid-synchronization stability for three-phase paralleled converters," *IEEE Trans. Power Electron.*, vol. 31, no. 1, pp. 26–38, Jan. 2016.

[30] M. Salmani, N. Rahbari-Asr, C. S. Edrington, and C. Mo-Yuen, "Online and offline stability analysis methods for the power electronic-based components in design and operational stages," *IEEE Trans. Power Electron.*, vol. 31, no. 4, pp. 3151–3164, Apr. 2016.

[31] J. Sun, "Impedance-based stability criterion for grid-connected inverters," *IEEE Trans. Power Electron.*, vol. 26, no. 11, pp. 3075–3078, Nov. 2011.

[32] J. Sun, "Small-signal methods for ac power electronics systems," Professional education seminar, *in Proc. Annu. IEEE Appl. Power Electron. Conf. and Expo.*, 2013.

[33] J. Sun, "Control and stability analysis of HVDC converters and systems," Professional education seminar, in *Proc. IEEE Energy Convers. Congr. and Expo.*, 2015.

[34] M. Belkhayat, “Stability criterion for AC power systems with regulated loads,” Ph.D. dissertation, Dept. Elect. Comput. Eng., Purdue University, West Lafayette, IN, USA, 1997.

[35] A. G. J. MacFarlane and I. Postlethwaite, “The generalized Nyquist stability criterion and multivariable root loci,” *Int. J. Control*, vol. 25, no. 1, pp. 81–127, Feb. 1977.

[36] J. Sun, “Impedance modeling and analysis of grid-connected three-phase converters,” Professional education seminar, in *Proc. Annu. IEEE Appl. Power Electron. Conf. and Expo.*, 2014.

[37] B. Wen, D. Boroyevich, R. Burgos, P. Mattavelli, and Z. Shen, “Small-signal stability analysis of three-phase ac systems in the presence of constant power loads based on measured d-q frame impedances,” *IEEE Trans. Power Electron.*, vol. 30, no. 10, pp. 5952–5963, Oct. 2015.

[38] A. Riccobono and E. Santi, “Comprehensive review of stability criteria for dc power distribution systems,” *IEEE Trans. Ind. Appl.*, vol. 50, no. 5, pp. 3525–3535, Sep./Oct. 2014.

[39] R. D. Middlebrook, “Input filter considerations in design and application of switching regulators,” in *Proc. IEEE Ind. Appl. Soc. Annu. Meeting*, 1976, pp. 366–382.

[40] S. P. Rosado, “Voltage stability and control in autonomous electric power systems with variable frequency,” Ph.D. dissertation, Dept. Elect. Comput. Eng., Virginia Polytechnic Institute and State University, Blacksburg, VA, USA, 2007.

[41] P. Kundur, J. Paserba, V. Ajjarapu, G. Andersson, A. Bose, G. Canizares, N. Hatziargyriou, D. Hill, A. Stankovic, C. Taylor, T. Van Cutsem, and V. Vittal, “Definition and classification of power system stability IEEE/CIGRE joint task force on stability

terms and definitions," *IEEE Trans. Power Systems*, vol. 19, is. 3, pp. 1387-401, Aug. 2004.

[42] P. Kundur, *Power System Stability and Control*. New York: McGraw- Hill, 1994.

[43] N. Pogaku, M. Prodanovic, and T. C. Green, "Modeling, analysis and testing of an inverter-based microgrid," *IEEE Trans. Power Electron.*, vol. 22, no. 2, pp. 613–625, Mar. 2007.

[44] S. D'Arco, J. A. Suul, and O. B. Fosso, "Automatic tuning of cascaded controllers for power converters using eigenvalue parametric sensitivities," *IEEE Trans. Ind. Appl.*, vol. 51, no. 2, pp. 1743–1753, Mar./Apr. 2015.

[45] A. Kahrobaeian and Y. A.-R. I. Mohamed, "Analysis and mitigation of low-frequency instabilities in autonomous medium-voltage converter-based microgrids with dynamic loads," *IEEE Trans. Ind. Electron.*, vol. 61, no. 4, pp. 1643–1658, Apr. 2014.

[46] S. Iyer, M. Belur, and M. Chandorkar, "A generalized computational method to determine stability of a multi-inverter microgrid," *IEEE Trans. Power Electron.*, vol. 25, no. 9, pp. 2420–2432, Sep. 2010.

[47] V. Mariani, F. Vasca, J. C. Vasquez, and J. M. Guerrero, "Model order reductions for stability analysis of islanded microgrids with droop control," *IEEE Trans. Ind. Electron.*, vol. 62, no. 7, pp. 4344–4354, Jul. 2015.

[48] M. Rasheduzzaman, J. A. Mueller, and J. W. Kimball, "Reduced-order small-signal model of microgrid systems," *IEEE Trans. Sustain. Energy*, vol. 6, no. 4, pp. 1292–1305, 2015.

[49] Y. Wang, X. Wang, F. Blaabjer, and Z. chen, "Harmonic instability assessment using state-space modeling and participation analysis in inverter-fed power systems," *IEEE Trans. Ind. Electron.*, vol. 64, no. 1, pp. 806–816, Jan. 2017.

[50] G. Gaba, S. Lefebver, and D. Mukhedkar, “Comparative analysis and study of the dynamic stability of ac/dc systems,” *IEEE Trans. Power Syst.*, vol. 3, no. 3, pp. 978–985, Aug. 1988.

[51] S. Lefebver and R. Dube, “Control system analysis and design for an aerogenerator with eigenvalue methods,” *IEEE Trans. Power Syst.*, vol. 3, no. 4, pp. 1600–1608, Nov. 1988.

[52] S. Lefebver, “Tuning of stabilizers in multi-machine power systems,” I*EEE Trans. Power App. Syst.*, vol. PAS-102, no. 2, pp. 290–299, Feb. 1983.

[53] S. Lefebvre, D. P. Carroll, and R. A. DeCarlo, “Decentralized power modulation of multiterminal HVDC systems,” *IEEE Trans. Power App. Syst.*, vol. PAS-100, no. 7, pp. 3331–3339, Jul. 1981.

[54] Y. Wang, X. Wang, F. Blaabjerg, and Z. Chen, “Harmonic stability analysis of inverter-fed power systems using component connection method,” in *Proc. IPEMC-ECCE Asia* 2016, pp. 2667–2674.

[55] K. Ogata, *Modern Control Engineering*, 5th ed. Upper Saddle River, NJ, USA: Prentice Hall, 2009.

[56] M. Liserre, F. Blaabjerg, and S. Hansen, “Design and control of an LCL-filter-based three-phase active rectifier,” *IEEE Trans. Ind. Appl.*, vol. 41, no. 5, pp. 1281–1291, Sep. / Oct. 2005.

[57] J. Dannehl, M. Liserre, and F. W. Fuchs, “Filter-based active damping of voltage source converters with LCL filter,” *IEEE Trans. Ind. Electron.*, vol. 58, no. 8, pp. 3623–3633, Aug. 2011.

[58] X. Li, X. Wu, Y. Geng, X. Yuan, C. Xia, and X. Zhang, “Wide damping region for LCL-type grid-connected inverter with an improved capacitor-current-feedback method,” *IEEE*

Trans. Power Electron., vol. 30, no. 9, pp. 5247–5259, Sep. 2015.

[59] R. N. Beres, X. Wang, F. Blaabjerg, M. Liserre, and C. L. Bak, "Optimal design of high-order passive-damped filters for grid-connected applications," *IEEE Trans. Power Electron.*, vol. 31, no. 3, pp. 2083–2098, Mar. 2016.

[60] J. He, Y. W. Li, D. Bosnjak, and B. Harris, "Investigation and active damping of multiple resonances in a parallel-inverter-based microgrid," *IEEE Trans. Power Electron.*, vol. 28, no. 1, pp. 234–246, Jan. 2013.

[61] J. L. Agorreta, M. Borrega, J. Lopez, and L. Marroyo, "Modeling and control of N-paralleled grid-connected inverters with LCL filter coupled due to grid impedance in PV plants," *IEEE Trans. Power Electron.*, vol. 26, no. 3, pp. 770–785, Mar. 2011.

[62] B. Wen, D. Boroyevich, R. Burgos, P. Mattavelli, and Z. Shen, "Inverse Nyquist stability criterion for grid-tied inverters," *IEEE Trans. Power Electron.*, vol. 32, no. 2, pp. 1548–1556, Feb. 2017.

[63] L. Harnefors, L. Zhang, and M. Bongiorno, "Frequency-domain passivity-based current controller design," *IET Power Electron.*, vol. 1, no. 4, pp. 455-465, 2008.

[64] L. Harnefors, M. Bongiorno, and S. Lundberg, "Input-admittance calculation and shaping for controlled voltage-source converters," *IEEE Trans. Ind. Electron.*, vol. 54, no. 6, pp. 3323–3334, Dec. 2007.

[65] L. Harnefors, A. G. Yepes, A. Vidal, and J. Doval-Gandoy, "Passivity-based controller design of grid-connected VSCs for prevention of electrical resonance instability," *IEEE Trans. Ind. Electron.*, vol. 62, no. 2, pp. 702–710, Feb. 2015.

[66] L. Harnefors, X. Wang, A. G. Yepes, and F. Blaabjerg, "Passivity-based stability assessment of grid-connected VSCs—an overview," *IEEE J. Emerg. Sel. Topics Power*

Electron., vol. 4, no. 1, pp. 116–125, Mar. 2016.

[67] Z. Liu, J. Liu, W. Bao, and Y. Zhao, "Infinity-norm of impedance-based stability criterion for three-phase ac distributed power systems with constant power loads," *IEEE Trans. Power Electron.*, vol. 30, no. 6, pp. 3030–3043, Jun. 2015.

[68] J. Sun, "Small-signal methods for ac distributed power systems—a review," *IEEE Trans. Power Electron.*, vol. 24, no. 11, pp. 2545–2554, Nov. 2009.

[69] B. Wen, D. Boroyevich, R. Burgos, P. Mattavelli, and Z. Shen, "Analysis of d-q small-signal impedance of grid-tied inverters," *IEEE Trans. Power Electron.*, vol. 31, no. 1, pp. 675–687, Jan. 2016.

[70] M. Cespedes and J. Sun, "Impedance modeling and analysis of grid-connected voltage-source converters," *IEEE Trans. Power Electron.*, vol. 29, no. 3, pp. 1254–1261, Mar. 2014.

[71] A. A. A. Radwan and Y. A.-R. I. Mohamed, "Analysis and active-impedance-based stabilization of voltage-source-rectifier loads in grid-connected and isolated microgrid applications," *IEEE Trans. Sustain. Energy*, vol. 4, no. 3, pp. 563–576, Jul. 2013.

[72] M. K. Bakhshizadeh, X. Wang, F. Blaabjerg, J. Hjerrild, L. Kocewiak, C. L. Bak, and B. Hesselbek, "Couplings in phase domain impedance modelling of grid-connected converters," *IEEE Trans. Power Electron.*, vol. 31, no. 10, pp. 6792–6796, Oct. 2016.

[73] A. Rygg, M.Molinas, Z. Chen, and X. Cai, "A modified sequence domain impedance definition and its equivalence to the dq-domain impedance definition for the stability analysis of AC power electronic systems," *IEEE J. Emerging Sel. Topics Power Electron.*, vol. 4, no. 4, pp. 1383–1396, Dec.2016.

[74] A. A. A. Radwan and Y. A.-R. I. Mohamed, "Stabilization of medium-frequency modes in

isolated microgrids supplying direct online induction motor loads," *IEEE Trans. Smart Grid*, vol. 5, no. 1, pp. 358–370, Jan. 2014.

[75] Z. Liu, J. Liu, and D. Boroyevich, "Small-signal terminal characteristics modeling of three-phase boost rectifier with variable fundamental frequency," in *Proc. Annu. IEEE Appl. Power Electron. Conf. and Expo.*, 2016, pp. 739–745.

[76] Z. Liu, J. Liu, D. Boroyevich, R. Burgos, and T. Liu, "Small-signal terminal-characteristics modeling of three-phase droop-controlled inverters," in *Proc. IEEE Energy Convers. Congr. and Expo.*, 2016, pp. 1–7.

[77] N. Hoffmann and F. W. Fuchs, "Minimal invasive equivalent grid impedance estimation in inductive-resistive power networks using extended Kalman filter," *IEEE Trans. Power Electron.*, vol. 29, no. 2, pp. 631–641, 2014.

[78] T. Roinila, M. Vilkko, and J. Sun, "Broadband methods for online grid impedance measurement," in *Proc. IEEE Energy Convers. Congr. and Expo.*, 2013, pp. 3003–3010.

[79] M. Cespedes and J. Sun, "Online grid impedance identification for adaptive control of grid-connected inverters." in *Proc. IEEE Energy Convers. Congr. and Expo.*, 2012, pp. 914–921.

[80] Y. A. Familiant, J. Huang, K. A. Corzine, and M. Belkhayat, "New techniques for measuring impedance characteristics of three-phase AC power systems," *IEEE Trans. Power Electron.*, vol. 24, no. 7, pp. 1802–1810, 2009.

[81] J. Huang, K. A. Corzine, and M. Belkhayat, "Small-signal impedance measurement of power-electronics-based AC power systems using line-to-line current injection," *IEEE Trans. Power Electron.*, vol. 24, no. 2, pp. 445–455, 2009.

[82] V. Valdivia, A. Lazaro, A. Barrado, P. Zumel, C. Fernandez, and M. Sanz, "Impedance

identification procedure of three-phase balanced voltage source inverters based on transient response measurements," *IEEE Trans. Power Electron.*, vol. 26, no. 12, pp. 3810–3816, 2011.

[83] M. Cespedes and J. Sun, "Three-phase impedance measurement for system stability analysis," in *Proc. IEEE COMPEL* 2013, pp. 1–6.

[84] X. Yue, Z. Fang, F. Wang, Z. Zhang, and H. Shi, "A novel adaptive frequency injection method for power electronic system impedance measurement," *IEEE Trans. Power Electron.*, vol. 29, no. 12, pp. 6700–6711, 2014.

[85] X. Yue, F. Zhuo, Z. Zhang, H. Shi, X. Bao, and Z. Yang, "A new current injection method for impedance measurement using superposed modulated square pulse," in *Proc. Annu. IEEE Appl. Power Electron. Conf. and Expo.*, 2013, pp. 1452–1456.

[86] D. Martin, I. Nam, J. Siegers, and E. Santi, "Wide bandwidth three-phase impedance identification using existing power electronics inverter," in *Proc. Annu. IEEE Appl. Power Electron. Conf. and Expo.*, 2013, pp. 334–341.

[87] Z. Shen, M. Jaksic, P. Mattavelli, D. Boroyevich, J. Verhulst, and M. Belkhayat, "Design and implementation of three-phase AC impedance measurement unit (IMU) with series and shunt injection," in *Proc. Annu. IEEE Appl. Power Electron. Conf. and Expo.*, 2013, pp. 2674–2681.

[88] Z. Shen, M. Jaksic, P. Mattavelli, D. Boroyevich, J. Verhulst, and M. Belkhayat, "Three-phase AC system impedance measurement unit (IMU) using chirp signal injection," in *Proc. Annu. IEEE Appl. Power Electron. Conf. and Expo.*, 2013, pp. 2666–2673.

[89] G. Francis, R. Burgos, D. Boroyevich, F. Wang, and K. Karimi, "An algorithm and implementation system for measuring impedance in the D-Q domain," in *Proc. IEEE*

Energy Convers. Congr. and Expo., 2012, pp. 3221–3228.

[90] Q. Ye, R. Mo, Y. Shi, and H. Li, "A unified impedance-based stability criterion (UIBSC) for paralleled grid-tied inverters using global minor loop gain (GMLG)," in *Proc. IEEE Energy Convers. Congr. and Expo.*, 2015, pp. 5816–5821.

[91] S. Lissandron, L. D. Santa, P. Mattavelli, and B. Wen, "Experimental validation for impedance-based small-signal stability analysis of single-phase interconnected power systems with grid-feeding inverters," *IEEE J. Emerg. Sel. Topics Power Electron.*, vol. 4, no. 1, pp. 103–115, Mar. 2016.

[92] L. Xu and L. Fan, "Impedance-based resonance analysis in a VSC-HVDC system," *IEEE Trans. Power Del.*,vol. 28, no. 4, pp. 2209–2216, Oct. 2013.

[93] J. Lyu, X. Cai, and M. Molinas, "Frequency domain stability analysis of MMC-based HVDC for wind farm integration," *IEEE J. Emerg. Sel. Topics Power Electron.*, vol. 4, no. 1, pp. 141–151, Mar. 2016.

[94] R. Turner, S. Walton, and R. Duke, "A case study on the application of the Nyquist stability criterion as applied to interconnected loads and sources on grids," *IEEE Trans. Ind. Electron.*, vol. 60, no. 7, pp. 2740–2749, Jul. 2013.

[95] F. Liu, J. Liu, H. Zhang, and D. Xue, "Stability issues of Z + Z type cascade system in hybrid energy storage system (HESS)," *IEEE Trans. Power Electron.*, vol. 29, no. 11, pp. 5846–5859, Nov. 2014.

[96] X. Wang, F. Blaabjerg, and P. C. Loh, "An impedance-based stability analysis method for paralleled voltage source converters," in *Proc. IEEE IPEC* 2014, pp. 1529–1535.

[97] C. Yoon, H. Bai, X. Wang, C. L. Bak, and F. Blaabjerg, "Regional modeling approach for analyzing harmonic stability in radial power electronics based power system," in *Proc.*

IEEE PEDG 2015, pp. 1–5.

[98] F. Liu, J. Liu, H. Zhang, D. Xue, and Q. Dou, "Terminal admittance based stability criterion for multi-module DC distributed system," in *Proc. Annu. IEEE Appl. Power Electron. Conf. and Expo.*, 2014, pp. 580–586.

[99] F. Liu, J. Liu, H. Zhang, and D. Xue, "Generalized stability criterion for multi-module distributed dc system," *J. Power Electron.*, vol. 14, no. 1, pp. 143–155, Jan. 2014.

[100] Z. Yao, P. G. Therond, and B. Davat, "Stability analysis of power systems by the generalized Nyquist criterion," in *Proc. Int. Conf. Control*, Mar. 1994, vol. 1, pp. 739–744.

[101] Z. Yao, and B. Davat, "Stability assessment of power systems by μ-analysis," in *Proc. Conf. Decision and Control*, Dec. 1994, vol. 1, pp. 617-618.

[102] A. Haddadi, B. Boulet, A. Yazdani, and G. Joos, "A μ-based approach to small-signal stability analysis of an interconnected distributed energy resource unit and load," *IEEE Trans. Power Del.*, vol. 30, no. 4, pp. 1715-1726, 2015.

[103] S. Skogestad and I. Postlethwaite, *Multivariable feedback control: analysis and design*. Hoboken, NJ: John Wiley, 2nd edition, 2005.

[104] Z. Liu, J. Liu, D. Boroyevich, and R. Burgos, "Stability criterion of droop-controlled parallel inverters based on terminal-characteristics of individual inverters," in *Proc. IPEMC-ECCE Asia* 2016, pp. 2958–2963.

[105] D. Yang, X. Ruan, and H. Wu, "Impedance shaping of the grid-connected inverter with LCL filter to improve its adaptability to the weak grid condition," *IEEE Trans. Power Electron.*, vol. 29, no. 11, pp. 5795–5805, Nov. 2014.

[106] X. Zhang, X. Ruan, and Q. C. Zhong, "Improving the stability of cascaded dc/dc converter

systems via shaping the input impedance of the load converter with a parallel or series virtual impedance," *IEEE Trans. Ind. Electron.*, vol. 62, no. 12, pp. 7499–7512, Dec. 2015.

[107] A. Rizqiawan, G. Fujita, T. Funabashi, and M. Nomura, "Impact of a virtual resistor on the input admittance of a grid-connected inverter," *IEEJ Transactions on Electrical and Electronic Engineering*, vol. 8, no. 2, pp. 190–198, 2013.

[108] X. Wang, Y. W. Li, F. Blaabjerg, and P. Ch. Loh, "Virtual-impedance-based control for voltage-source and current-source converters," *IEEE Trans. Power Electron.*, vol. 30, no. 12, pp. 7019–7037, Dec. 2015.

[109] M. Cespedes and J. Sun, "Mitigation of inverter-grid harmonic resonance by narrow-band damping," *IEEE J. Emerg. Sel. Topics Power Electron.*, vol. 2, no. 4, pp. 1024–1031, Dec. 2014.

[110] K. Alawasa, Y. Mohamed, and W. Xu, "Active mitigation of subsynchronous interactions between PWM voltage-source converters and power networks," *IEEE Trans. Power Electron.*, vol. 29, no. 1, pp. 121–134, Jan. 2014.

[111] R. Pena-Alzola, M. Liserre, F. Blaabjerg, M. Ordonez, and T. Kerekes, "A self-commissioning notch filter for active damping in a three-phase lcl -filter-based grid-tie converter," *IEEE Trans. Power Electron.*, vol. 29, no. 12, pp. 6754–6761, Dec. 2014.

[112] X. Wang, F. Blaabjerg, and P. C. Loh, "Proportional derivative based stabilizing control of paralleled grid converters with cables in renewable power plants. " in *Proc. IEEE Energy Convers. Congr. and Expo.*, 2014, pp. 4917–4924.

[113] Y. Gu, W. Li, and X. He, "Passivity-based control of dc microgrid for self-disciplined stabilization," *IEEE Trans. Power Syst.*, vol. 30, no. 5, pp. 2623–2632, Sep. 2015.

[114] A. Riccobono and E. Santi, "A novel passivity-based stability criterion (PBSC) for switching converter dc distribution systems." in *Proc. Annu. IEEE Appl. Power Electron. Conf. and Expo.*, 2012, pp. 2560–2567.

[115] M. Cespedes and J. Sun, "Impedance shaping of three-phase grid-parallel voltage-source converters," in *Proc. Annu. IEEE Appl. Power Electron. Conf. and Expo.*, 2012, pp. 754–760.

[116] H. Liu and J. Sun, "Voltage Stability and Control of Offshore Wind Farms With AC Collection and HVDC Transmission," *IEEE J. Emerg. Sel. Topics Power Electron.*, vol. 2, no. 4, pp. 1181-1189, 2014.

[117] W. Cao, X. Zhang, Y. Ma, and F. Wang, "Stability criterion and controller parameter design of radial-line renewable systems with multiple inverters," in *Proc. Annu. IEEE Appl. Power Electron. Conf. and Expo.*, 2016, 2229–2236.

[118] X. Wang, F. Blaabjerg, and M. Liserre, "An active damper to suppress multiple resonances with unknown frequencies," in *Proc. Annu. IEEE Appl. Power Electron. Conf. and Expo.*, 2014, pp. 2184–2191.

[119] X. Wang, Y. Pang, P. C. Loh, and F. Blaabjerg, "A series-LC-Filtered active damper with grid disturbance rejection for ac power-electronics-based power systems," *IEEE Trans. Power Electron.*, vol. 30, no. 8, pp. 4037–4041, Aug. 2015.

[120] C. Yoon, X. Wang, C. L. Bak, and F. Blaabjerg, "Site selection of active damper for stabilizing power electronics based power distribution system." in *Proc. IEEE PEDG* 2015, pp. 1–6.

[121] M. Cespedes and J. Sun, "Adaptive control of grid-connected inverters based on online grid impedance measurements," *IEEE Trans. Sustain. Energy*, vol. 5, no. 2, pp. 516–523,

Apr. 2014.

[122] C. Zheng, L. Zhou, X. Yu, B. Li, and J. Liu, "Online phase margin compensation strategy for a grid-tied inverter to improve its robustness to grid impedance variation," *IET Power Electronics*, vol. 9, no. 4, pp. 611–620, 2016.

[123] G. Liu, X. Cao, T. Shi, and W. Wang, "Research on adaptive control of grid-connected PV inverters in weak grid," in *Proc. IEEE Energy Convers. Congr. and Expo.*, 2015, pp. 4229–4235.

[124] X. Chen, Y. Zhang, S. Wang, J. Chen, and C. Gong, "Impedance-phased dynamic control method for grid-connected inverters in a weak grid," *IEEE Trans. Power Electron.*, vol. 32, no. 1, pp. 274–283, Jan. 2017.

[125] W. Cao, Y. Ma, X. Zhang, and F. Wang, "Sequence impedance measurement of three-phase inverters using a parallel structure," in *Proc. Annu. IEEE Appl. Power Electron. Conf. and Expo.*, 2015, pp. 3031–3038.

[126] S. Ahmed, Z. Shen, P. Mattavelli, D. Boroyevich, M. Jaksic, K. Karimi, and J. Fu, "Small-signal model of a voltage source inverter (VSI) considering the dead-time effect and space vector modulation types," in *Proc. Annu. IEEE Appl. Power Electron. Conf. and Expo.*, 2011, pp. 685–690.

[127] M. Cespedes and J. Sun, "Methods for stability analysis of unbalanced three-phase systems," in *Proc. IEEE Energy Convers. Congr. and Expo.*, 2012, pp. 3090–3097.

[128] Y. Wang, X. Chen, Y. Zhang, J. Chen, and C. Gong, "Impedance modeling of three-phase grid-connected inverters and analysis of interaction stability in grid-connected system," in *Proc. IEEE International Power Electron. and Motion Control Conf.*, 2016, pp. 3606–3612.

[129] Y. Ma, L. Yang, J. Wang, X. Shi, F. Wang, and L. M. Tolbert, "Circulating current control and reduction in a paralleled converter test-bed system", in *Proc. IEEE Energy Convers. Congr. and Expo.*, 2013, pp. 5426–5432.

[130] X. Wang, F. Blaabjerg, and Z. Chen, "Synthesis of variable harmonic impedance in inverter-interfaced distributed generation unit for harmonic damping throughout a distribution network," *IEEE Trans. Ind. Appl.*, vol. 48, no. 4, pp. 1407–1417, 2012.

[131] J. He and Y. W. Li, "Analysis, design, and implementation of virtual impedance for power electronics interfaced distributed generation," *IEEE Trans. Ind. Appl.*, vol. 47, no. 6, pp. 2525–2538, 2011.

[132] B. Bon-Ho and S. Seung-Ki, "A compensation method for time delay of full-digital synchronous frame current regulator of PWM AC drives," *IEEE Trans. Ind. Appl.*, vol. 39, no. 3, pp. 802–810, 2003.

[133] X. Zhang, F. Wang, W. Cao, and Y. Ma, "Influence of voltage feed-forward control on small-signal stability of grid-tied inverters," in *Proc. Annu. IEEE Appl. Power Electron. Conf. and Expo.*, 2015, pp. 1216–1221.

[134] J. Huang and X. Yuan, "Impact of the voltage feed-forward and current decoupling on VSC current control stability in weak grid based on complex variables," in *Proc. IEEE Energy Convers. Congr. and Expo.*, 2015, pp. 6845–6852.

[135] X. Zhang, X. Ruan, and C. K. Tse, "Impedance-based local stability criterion for dc distributed power systems," *IEEE Trans. Circuits Syst. I, Reg. Papers*, vol. 62, no. 3, pp. 916–925, Mar. 2015.

[136] S. Liu, X. Liu, and Y. Liu, "Analysis on feedback interconnections of cascaded dc-dc converter systems," in *Proc. IEEE Energy Convers. Congr. and Expo.*, 2015, pp. 5160–

5166.

[137] L. Yang, Y. Ma, J. Wang, J. Wang, X. Zhang, L. M. Tolbert, F. Wang, and K. Tomsovic, "Development of converter based reconfigurable power grid emulator," in *Proc. IEEE Energy Convers. Congr. and Expo.*, 2014, pp. 3990–3997.

[138] Y. Ma, W. Cao, L. Yang, F. Wang, and L. M. Tolbert, "Virtual synchronous generator control of full converter wind turbines with short term energy storage," *IEEE Trans. Ind. Electron.*, Early Access Article, 2017.

[139] L. Yang, X. Zhang, Y. Ma, J. Wang, L. Hang, K. Lin, L. M. Tolbert, F. Wang, and K. Tomsovic, "Stability analysis of inverter based generator emulator in test-bed for power systems," in *Proc. IEEE Energy Convers. Congr. and Expo.*, 2013, pp. 5410–5417.

[140] L. Luo and S. V. Dhople, "Spatiotemporal model reduction of inverter-based islanded microgrids," *IEEE Trans. Energy Convers.*, vol. 29, no. 4, pp. 823–832, Dec. 2014.

Vita

Wenchao Cao received the B.S. degree in automation and the M.S. degree in control theory and control engineering from Huazhong University of Science and Technology, Wuhan, China, in 2008 and 2011, respectively. He received the Ph.D. degree in electrical engineering in 2017 in the Center for Ultra-Wide-Area Resilient Electric Energy Transmission Networks (CURENT), Department of Electrical Engineering and Computer Science, College of Engineering, The University of Tennessee, Knoxville, TN, USA.